UNIVERSIDADE FEDERAL DE PERNAMBUCO
CENTRO DE CIÊNCIAS EXATAS E DA NATUREZA
PROGRAMA DE PÓS-GRADUAÇÃO EM FÍSICA

Danilo da Silva Almeida

Quantum Phase Transitions and Emergent Phases in Ladder Systems

Recife

2025

Danilo da Silva Almeida

Quantum Phase Transitions and Emergent Phases in Ladder Systems

Tese apresentada ao Programa de Pós-Graduação em Física da Universidade Federal de Pernambuco, como requisito parcial para a obtenção do título de Doutor em Física.

Área de Concentração: Física Teórica e Computacional

Orientador (a): Prof. Dr. Renê Rodrigues Montenegro Filho

Recife

2025

.Catalogação de Publicação na Fonte. UFPE - Biblioteca Central

Almeida, Danilo da Silva.
Quantum Phase Transitions and Emergent Phases in Ladder Systems / Danilo da Silva Almeida. - Recife, 2025.
177f.: il.

Tese (Doutorado) - Universidade Federal de Pernambuco, Centro de Ciências Exatas e da Natureza, Programa de Pós-Graduação Física, 2025.
Orientação: Renê Rodrigues Montenegro Filho.
Inclui referências e apêndices.

1. Quantum Phase Transitions; 2. Spin Ladders; 3. Frustrated Systems; 4. Quantum Magnetism; 5. DMRG. I. Montenegro Filho, Renê Rodrigues. II. Título.

UFPE-Biblioteca Central

DANILO DA SILVA ALMEIDA

QUANTUM PHASE TRANSITIONS AND EMERGENT PHASES IN LADDER SYSTEMS

Tese apresentada ao Programa de Pós-Graduação em Física da Universidade Federal de Pernambuco, como requisito parcial para a obtenção do título de Doutor em Física.

Área de Concentração: Física Teórica e Computacional

Data de aprovação: 27/05/2025.

BANCA EXAMINADORA

Prof. Dr. Renê Rodrigues Montenegro Filho
Orientador
Universidade Federal de Pernambuco

Prof. Dr. Antônio Murilo Santos Macêdo
Examinador Interno
Universidade Federal de Pernambuco

Prof. Dr. Ernesto Carneiro Pessoa Raposo
Examinador Interno
Universidade Federal de Pernambuco

Prof. Dr. Marcelo Leite Lyra
Examinador Externo
Universidade Federal de Alagoas

Prof. Dr. Rodrigo Gonçalves Pereira
Examinador Externo
Universidade Federal do Rio Grande do Norte

I dedicate this work to my parents, Cláudio and Edevani, for their unwavering support since the beginning of my academic journey, from undergraduate studies to my doctorate. Without their help, I would not have reached this point.

ACKNOWLEDGEMENTS

I am deeply grateful to my family and to all those who supported me throughout my academic journey—especially my parents and my wife—for their unwavering love and encouragement.

I extend my sincere thanks to Professor Renê for his guidance and for leading me with dedication along this path.

I also thank the Physics Department and all its members for the infrastructure and institutional support that were fundamental to the development of this work.

Finally, I acknowledge CAPES for the essential financial support that made this research possible.

”If I have seen further it is by standing on the shoulders of giants”. (Isaac Newton, 1675)

RESUMO

Esta tese investiga as propriedades do estado fundamental e os diagramas de fase quânticos de sistemas de spin de baixa dimensionalidade, com foco em cadeias do tipo escada de spin–1/2 e modelos relacionados. Esses sistemas oferecem um terreno fértil para explorar a interação entre frustração magnética, correlações quânticas, topologia e campos externos. Combinando métodos numéricos avançados, principalmente o grupo de renormalização da matriz densidade (DMRG), com abordagens analíticas, analisamos como diferentes geometrias de acoplamento e campos magnéticos dão origem a fases quânticas distintas, incluindo platôs de magnetização, fases topológicas e protegidas por simetria, e transições de primeira ordem. O estudo abrange escadas uniformes e alternadas, bem como sistemas de escadas acopladas que interpolam entre comportamentos unidimensionais e bidimensionais. Em particular, examinamos como a frustração influencia a estabilidade dos estados coletivos de spin e como os acoplamentos entre escadas podem induzir transições entre estados de valência ressonante (RVB), fases de Haldane e fases triviais com excitações coletivas de spin. Embora modelos analíticos aproximados, como mapeamentos para bósons duros e teoria de ondas de spin, captem certos aspectos qualitativos desses sistemas, nossos resultados destacam suas limitações na descrição precisa de fenômenos críticos e fronteiras de fase, reforçando a importância de análises numéricas de alta precisão.

Palavras-chaves: Transições de Fase Quânticas. Escadas de Spin. Sistemas Frustrados. Magnetismo Quântico. DMRG.

ABSTRACT

This thesis investigates the ground-state properties and quantum phase diagrams of low-dimensional spin systems, with a focus on spin–1/2 ladder chains and related models. These systems provide a fertile ground for exploring the interplay between magnetic frustration, quantum correlations, topology, and external fields. By combining advanced numerical methods, primarily the density matrix renormalization group (DMRG), with analytical approaches, we analyze how different coupling geometries and magnetic fields give rise to distinct quantum phases, including magnetization plateaus, symmetry-protected and topological phases, and first-order transitions. The study covers both uniform and alternating ladders, as well as coupled ladder systems that interpolate between one- and two-dimensional behavior. In particular, we examine how frustration influences the stability of collective spin states, and how interladder couplings can drive transitions between resonating valence bond (RVB) states, Haldane phases, and trivial phases hosting collective spin excitations. Although approximate analytical models, such as hard-core boson mappings and spin-wave theory, capture some qualitative aspects of these systems, our results highlight their limitations in accurately describing critical behavior and phase boundaries, reinforcing the importance of high-precision numerical analysis.

Keywords: Quantum Phase Transitions. Spin Ladders. Frustrated Systems. Quantum Magnetism. DMRG.

LIST OF FIGURES

LISTINGS

LIST OF TABLES

LIST OF ABBREVIATIONS AND ACRONYMS

1D	*One-Dimensional*
2D	*Two-Dimensional*
AFM	*Antiferromagnetic*
AKLT	*Affleck-Kennedy-Lieb-Tasaki*
ALPS	*Algorithms and Libraries for Physics Simulations*
CBC	*Cylindrical Boundary Condition*
CD	*Columnar Dimer*
DMRG	*Density Matrix Renormalization Group*
FBZ	*Folded Brillouin Zone*
FP	*Fully Polarized*
HAF	*Heisenberg Antiferromagnetic*
KT	*Kosterlitz-Thouless*
LL	*Luttinger Liquid*
MPO	*Matrix Product Operator*
MPS	*Matrix Product State*
NRG	*Numerical Renormalization Group*
OBC	*Open Boundary Condition*
PBC	*Periodic Boundary Condition*
PEPS	*Projected Entangled Pair State*
PM	*Paramagnetic*
QCP	*Quantum Critical Point*
QSL	*Quantum Spin Liquid*
RG	*Renormalization Group*
RS	*Rung-Singlet*
RT	*Rung-Triplet*

RVB	*Resonating-Valence-Bond*
SD	*Staggered Dimer*
SPT	*Symmetry-Protected Topological*
SVD	*Singular Value Decomposition*
UBZ	*Unfolded Brillouin Zone*
VBS	*Valence-Bond Solid*

CONTENTS

1 INTRODUCTION

Magnetism has long attracted scientific interest, with its earliest documentation linked to lodestones—naturally magnetized minerals known for their ability to attract iron. Prior to the 19th century, electricity and magnetism were regarded as unrelated phenomena. This perspective changed in 1820 when Hans Christian Ørsted demonstrated that an electric current can deflect a magnetic compass needle [1], revealing a fundamental connection between electric and magnetic fields and initiating the development of classical electromagnetism.

Despite this progress, the microscopic origin of magnetism remained elusive for much of the 19th century. James Clerk Maxwell's formulation of the electromagnetic field equations in the 1860s provided a unified description of electric and magnetic phenomena [2]. These equations describe how time-varying electric and magnetic fields give rise to one another and accurately capture the macroscopic behavior of electromagnetic fields. However, they do not account for the microscopic sources of magnetism, such as the spontaneous alignment of magnetic domains observed in ferromagnetic materials like lodestones.

Lodestones, primarily composed of magnetite ($\mathrm{Fe_3O_4}$), are known to exhibit permanent magnetization. Although classical electromagnetism can describe the field generated by such materials, it lacks a mechanism for explaining the internal alignment of atomic magnetic moments. This limitation pointed to the necessity of a microscopic theory of magnetism.

The advent of quantum mechanics in the early 20th century provided the necessary framework. The discovery of the electron in 1897 [3], followed by the development of atomic models such as that of Bohr in 1913 [4], highlighted the inadequacy of classical physics in describing atomic-scale phenomena. A key conceptual advance was the introduction of the electron's intrinsic angular momentum, or spin, which plays a central role in magnetic behavior.

The quantization of angular momentum was first observed experimentally in the Stern–Gerlach experiment of 1922 [5], which demonstrated that silver atoms possess discrete magnetic moment orientations. While initially interpreted in terms of orbital angular momentum, later developments clarified that spin is the primary source of the observed quantization. This finding established spin as the fundamental microscopic origin of magnetism.

The macroscopic magnetic properties of materials arise from interactions between the spins of individual electrons. Depending on the nature and geometry of these interactions, different types of magnetic ordering can emerge:

- **Ferromagnetism**: characterized by parallel alignment of spins, leading to a net magnetic moment (e.g., magnetite).
- **Antiferromagnetism**: involves alternating spin orientations, resulting in zero net magnetization.
- **Ferrimagnetism**: similar to antiferromagnetism but with unequal opposing moments, yielding a net magnetization (e.g., hematite).
- **Paramagnetism**: unpaired electron spins tend to align with an external magnetic field but become disordered by thermal agitation in its absence.

These types of magnetic order are schematically illustrated in Fig. 1.

Figure 1 – Examples of magnetic ordering: (FM) Spins align parallel in the same direction. (AFM) Spins alternate in opposing directions. (FiM) Spins oppose with unequal magnitudes. (PM) Spins orient randomly.

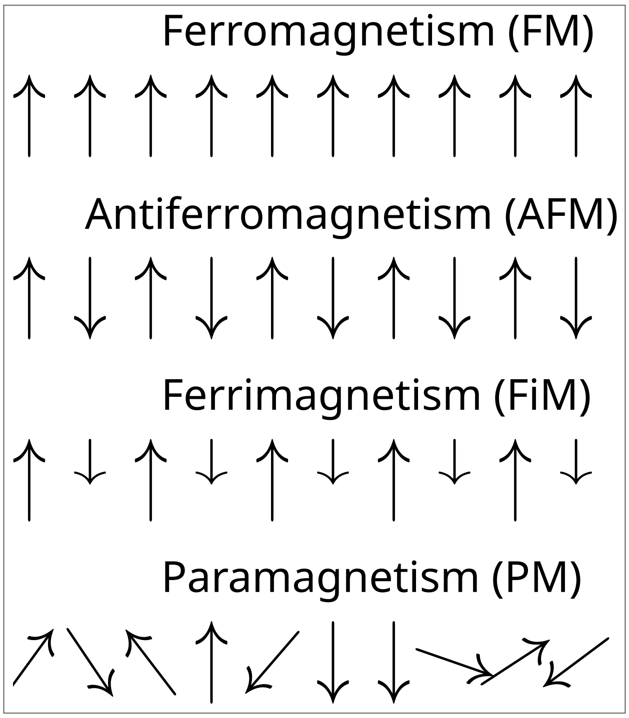

Source: The author (2025)

Magnetic properties are also sensitive to external conditions, particularly temperature and pressure. In 1895, Pierre Curie discovered that ferromagnetic materials exhibit spontaneous magnetization only below a specific temperature, now known as the Curie temperature [6]. Above this threshold, thermal fluctuations overcome spin alignment, and the material enters a paramagnetic state. This phenomenon provided early insight into magnetic phase transitions and remains a cornerstone in the study of magnetic materials.

1.1 SPIN MODELS AND PHASE TRANSITIONS

Spin models are fundamental to understanding magnetic systems and their associated phase transitions. Among the earliest and most influential is the Ising model, introduced by Wilhelm Lenz in the 1920s [7] and solved in one dimension by Ernst Ising [8]. In its classical formulation, the Ising model describes spins as discrete variables ($s_i = \pm 1$), interacting with their nearest neighbors. Despite its simplicity, it serves as a cornerstone in the study of magnetic ordering and critical phenomena. Its Hamiltonian, including a coupling to an external magnetic field h, is given by

$$\mathcal{H} = -\sum_{\langle i,j\rangle} J_{ij} s_i s_j - h \sum_i s_i, \quad s_i = \pm 1, \tag{1.1}$$

where J_{ij} denotes the coupling constant: positive for ferromagnetic ($J_{ij} > 0$) and negative for antiferromagnetic ($J_{ij} < 0$) interactions. The second term represents the Zeeman energy due to the external field. In one dimension, thermal fluctuations inhibit long-range order at finite temperature, precluding a phase transition due to entropic dominance.

In two dimensions, however, the model undergoes a continuous phase transition at a finite critical temperature T_c. Lars Onsager's exact solution for the zero-field case ($h = 0$) in 1944 [9], employing transfer matrix techniques, revealed the emergence of spontaneous magnetization below T_c, signaling a transition from a disordered *Paramagnetic* (PM) phase to an ordered ferromagnetic phase. This seminal result, illustrated in Fig. 2, firmly established the Ising model as a prototypical framework for studying criticality.

The three-dimensional Ising model remains analytically unsolved due to its inherent complexity. Numerical approaches, particularly Monte Carlo simulations [10, 11] and *Renormalization Group* (RG) methods, provide valuable insights. Monte Carlo techniques yield statistical estimates for thermodynamic quantities such as magnetization and susceptibility, while RG analyses uncover universal behavior and critical exponents, in agreement with experimental results for materials such as iron and nickel.

Figure 2 – Magnetization per spin, m, as a function of the dimensionless temperature, k_BT/J, for the Ising model on a 32×32 square lattice in the absence of an external magnetic field. Simulations were performed using the demon algorithm. Due to the symmetry of the system, two degenerate ferromagnetic states are possible: one with all spins aligned up and the other with all spins aligned down.

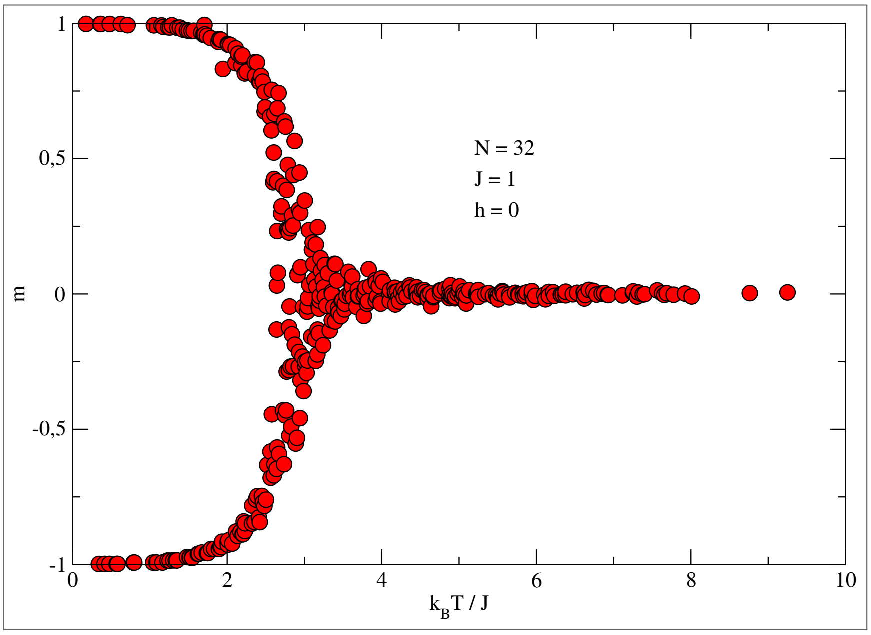

Source: The author (2025)

Extending beyond discrete spin variables, vector spin models offer a more general description. In the classical Heisenberg model, spins are treated as continuous vectors $\vec{S} = (S^x, S^y, S^z)$ with components constrained to lie on a unit sphere. The quantum Heisenberg model generalizes this further by introducing spin operators $\hat{S}^\alpha$, satisfying the angular momentum commutation relations:

$$[\hat{S}^\alpha, \hat{S}^\beta] = i\epsilon_{\alpha\beta\gamma}\hat{S}^\gamma, \tag{1.2}$$

where $\epsilon_{\alpha\beta\gamma}$ is the Levi-Civita symbol. The corresponding Hamiltonian is

$$\hat{\mathcal{H}} = \sum_{\alpha\in\{x,y,z\}} \sum_{\langle i,j\rangle} J_\alpha \hat{S}_i^\alpha \hat{S}_j^\alpha, \tag{1.3}$$

which includes, as special cases, the isotropic Heisenberg (XXX) model ($J_x = J_y = J_z$), the anisotropic XXZ model ($J_x = J_y \neq J_z$), and the fully anisotropic XYZ model ($J_x \neq J_y \neq J_z$).

In classical *Two-Dimensional* (2D) systems with continuous symmetry, the Mermin–Wagner theorem [12] forbids spontaneous symmetry breaking at finite temperatures. This result arises from the divergence of low-energy fluctuations (Goldstone modes), which destabilize long-range order. Nonetheless, certain 2D systems exhibit unconventional transitions. A prominent example is the 2D XY model, where spins are confined to a plane. This model undergoes a topological phase transition, known as the *Kosterlitz-Thouless* (KT) transition, at a critical temperature T_{KT} [13]. Unlike conventional transitions, it is not associated with spontaneous symmetry breaking, but rather with the unbinding of vortex–antivortex pairs. Below T_{KT}, the system enters a quasi-long-range ordered phase characterized by algebraically decaying spin correlations. In contrast, three-dimensional systems can exhibit true long-range order through conventional continuous symmetry breaking.

Quantum extensions of these models replace classical spins with discrete quantum degrees of freedom, introducing quantum fluctuations that are particularly relevant in low-dimensional systems. These fluctuations lead to phenomena such as quantum criticality, where zero-temperature phase transitions occur due to quantum rather than thermal fluctuations.

Classical phase transitions arise from the competition between thermal energy and interaction-induced ordering, and typically occur at finite temperature ($T > 0\,\mathrm{K}$). By tuning external parameters such as pressure or magnetic field, a system may transition between distinct phases—for example, from a PM to a ferromagnetic phase. Above the critical temperature (e.g., the Curie temperature), thermal agitation disrupts spin alignment, while below it, interactions dominate and stabilize ordered configurations.

As temperature approaches absolute zero ($T \to 0\,\mathrm{K}$), thermal fluctuations are suppressed, but quantum fluctuations, arising from the Heisenberg uncertainty principle, remain significant. These drive *quantum phase transitions*, which are governed by a non-thermal control parameter g (e.g., pressure, magnetic field, or chemical doping). The transition occurs at a *Quantum Critical Point* (QCP) located at $g = g_c$. Near the QCP, the system becomes scale-invariant, and physical quantities exhibit power-law scaling. The divergence of the correlation length ξ and characteristic timescale t_c follows

$$\xi \sim |g - g_c|^{-\nu}, \quad t_c \sim |g - g_c|^{-\nu z}, \tag{1.4}$$

where ν is the correlation length exponent and z is the dynamical critical exponent. At the critical point, fluctuations span all spatial and temporal scales, resulting in universal behavior characterized by critical exponents. Although strictly speaking quantum criticality occurs at $T = 0\,\mathrm{K}$, its signatures can be observed experimentally at low temperatures, where quantum and thermal fluctuations coexist. These features are depicted schematically in Fig. 3.

Figure 3 – Field-temperature phase diagram of the spin–ladder compound $(\mathrm{Hpip})_2\mathrm{CuBr}_4$, showing quantum disordered (QD), quantum critical (QC), and spin Luttinger-liquid (LL) phases

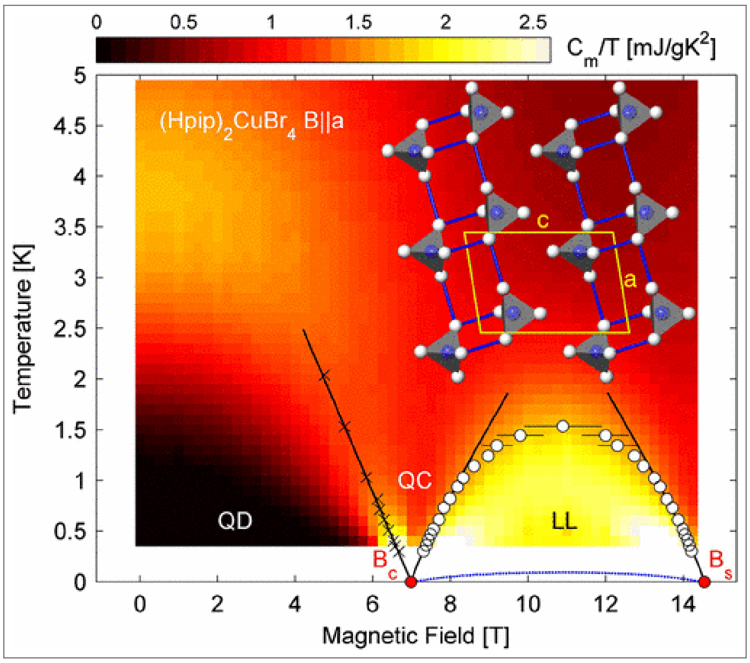

Source: Reference [14]

Accurate analysis of these models—particularly in the quantum regime—relies on numerical techniques. Monte Carlo simulations, despite being hindered by the sign problem in many quantum systems, remain widely used in both classical and quantum contexts. The *Density Matrix Renormalization Group* (DMRG) method [15–17] has become a standard tool for studying *One-Dimensional* (1D) quantum systems, offering highly accurate ground-state and low-energy spectra. A diverse array of numerical methods is available for studying many-body quantum systems, including variational methods, exact diagonalization, tensor networks, and neural quantum states [18].

1.2 LOW-DIMENSIONAL QUANTUM MAGNETISM

Quantum spin models, defined by lattice geometry (e.g., linear chains, ladders, square or Kagome lattices), interaction strengths (J_{ij}), and dimensionality, offer a versatile framework for describing a wide range of physical systems, including real magnetic materials. Among these, the 1D *Heisenberg Antiferromagnetic* (HAF) model plays a foundational role in the study of quantum phenomena. Haldane famously conjectured that the ground state of such systems depends crucially on the spin magnitude: half-odd-integer spin chains $\left(S = \frac{1}{2}, \frac{3}{2}, \dots\right)$ are gapless, whereas integer-spin chains $(S = 1, 2, \dots)$ possess a finite energy gap—the so-called *Haldane gap*—separating the ground state from the lowest excitations [19, 20]. This prediction triggered a surge of interest in low-dimensional spin systems, particularly for $S = 1$, where the resulting *Haldane phase* has been well established both theoretically [21, 22] and experimentally [23–25]. As a topological phase [26], it evades the traditional Landau paradigm of symmetry breaking, featuring hidden string order and characteristic edge states in open chains [22, 27–29]. These traits mirror more general topological phases of matter, such as topological insulators [30], which also exhibit bulk-edge correspondence—insulating bulk behavior coexisting with conducting edge modes.

Spin ladders form an important class of quantum many-body systems that interpolate between 1D chains and 2D lattices. They serve as effective models for several real materials, including $(\mathrm{Hpip})_2\mathrm{CuBr}_4$ [14], $(\mathrm{C}_5\mathrm{H}_{12}\mathrm{N})_2\mathrm{CuBr}_4$ [31], $(\mathrm{VO})_2\mathrm{P}_2\mathrm{O}_7$, and $\mathrm{SrCu}_2\mathrm{O}_3$ [32], all of which realize spin-$\frac{1}{2}$ ladders. The structural and magnetic properties of these compounds—illustrated in Fig. 4—make them ideal platforms for exploring low-dimensional quantum effects.

Figure 4 – (A) Ladder compound $(\mathrm{VO})_2\mathrm{P}_2\mathrm{O}_7$. (B) Schematic representation of a two-leg compound, $\mathrm{SrCu}_2\mathrm{O}_3$, and a three-leg compound, $\mathrm{Sr}_2\mathrm{Cu}_3\mathrm{O}_5$. The black dots represent Cu atoms, the intersections of solid lines represent O atoms, and the dashed lines indicate Cu–O bonds. J denotes the coupling along the ladder, while J' represents the coupling along the rungs.

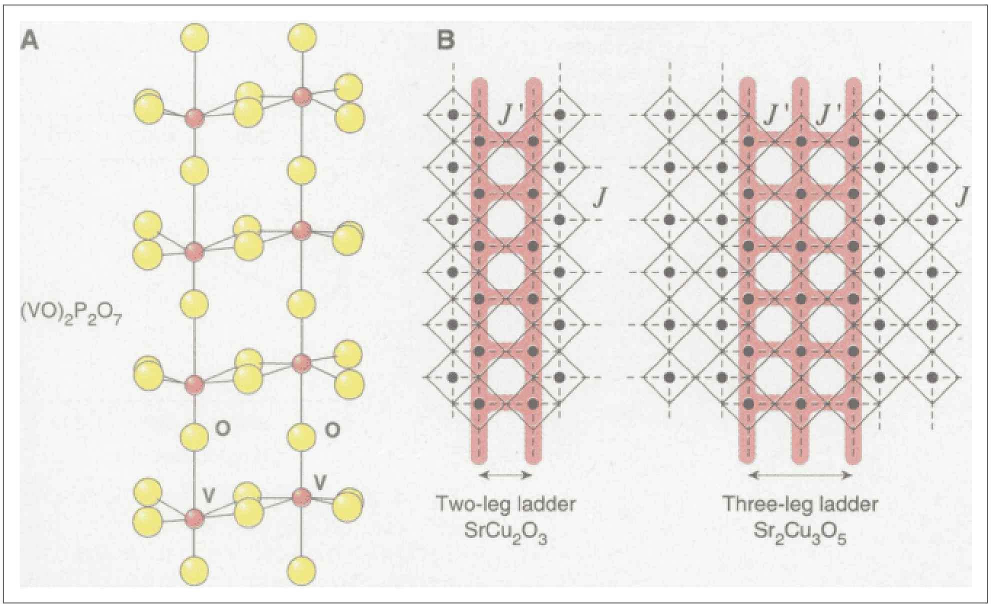

Source: Reference [32]

The ground-state properties of spin ladders depend strongly on the number of legs: **even-leg ladders** typically exhibit a finite spin gap and host gapped spin–liquid phases, while **odd-leg ladders** are generally gapless [33–35]. This even-odd effect is supported by analytical results, such as Lieb-Schultz-Mattis-type theorems [36], and by extensive numerical studies up to four-leg ladders [37–39], scaling analyses [40], and experimental data [32, 41–43]. Ladders with higher spin also attract theoretical and experimental attention. For instance, $Na_2Ni_2(C_2O_4)_3(H_2O)_2$ and β-$CaCr_2O_4$ realize spin–1 [44] and spin–$\frac{3}{2}$ [45, 46] ladders, respectively.

The spin–$\frac{1}{2}$ frustrated two-leg ladder, featuring diagonal couplings, has attracted considerable interest [47–51]. These couplings introduce magnetic frustration, which suppresses full *Antiferromagnetic* (AFM) order. The resulting ground-state phase diagram includes *Rung-Singlet* (RS) and *Rung-Triplet* (RT) phases [49, 51], with the latter often associated with Haldane-like behavior. Frustrated two-leg ladders display several unique phenomena, including equivalence to spin–1 chains under specific exchange patterns [49, 52, 53], fractional magnetization plateaus [48, 54–56], first-order transitions [48, 49, 54], spinon and magnon condensation [48], and KT transitions [55–57].

Nevertheless, only a few materials are known to realize spin–$\frac{1}{2}$ frustrated ladders, limiting experimental validation. $BiCu_2PO_6$ [58] is a rare example, where frustration stems from next-nearest-neighbor couplings along the ladder legs [59]. Another candidate, $Li_2Cu_2O(SO_4)_2$, exhibits $J_\times = J_\parallel$ and a ferromagnetic rung coupling $J_\perp$, along with a strong antiferromagnetic next-nearest-neighbor exchange J_2 [60–63], as illustrated in Fig.5.

In mixed-spin ladders, the interplay between spin arrangement and coupling strengths can give rise to ferrimagnetism, as anticipated by the Lieb-Mattis theorem [64–76]. Similar behavior is found in other 1D ferrimagnetic models [77, 78], such as alternating spin chains with spin–$(\frac{1}{2}, 1)$ and spin–$(\frac{1}{2}, \frac{5}{2})$, which exhibit ferrimagnetic ground states and magnetization plateaus at 1/3 and 2/3, respectively [79–85].

Studies using DMRG have explored the roles of density-dependent magnon hopping, magnon-magnon interactions, and edge-state behavior [86]. In certain anisotropic models, the 1/3 magnetization plateau terminates in a KT transition [87], similar to findings in anisotropic ferrimagnetic chains [88–90]. In contrast, isotropic trimer systems exhibit a 1/3 plateau without a KT transition [91].

Figure 5 – (a) Tetragonal crystal structure of $Li_2Cu_2O(SO_4)_2$ at room temperature. Cu are in blue, O in red, S in yellow, and Li in green. (b) Detail of the atomic structure of the chains running along the c axis. (c) Magnetic model deduced from the atomic structure, with the three dominant interactions along the chain: $J_\perp$ in green, $J = J_\times$ in blue, and J_2 in red. (d) Topologically equivalent frustrated two-leg spin ladder.

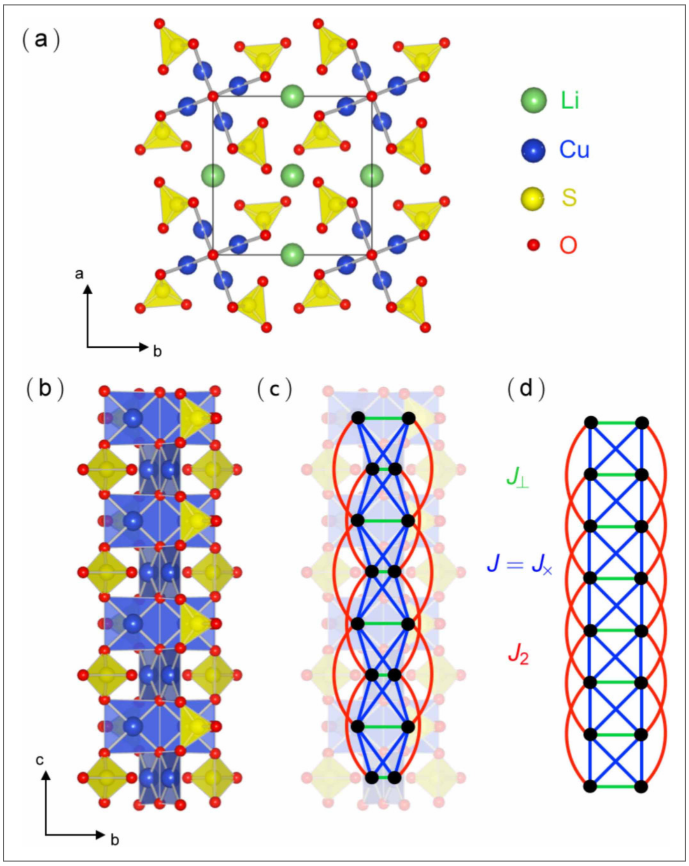

Source: Reference [62]

Extending from 1D to higher dimensions presents significant theoretical and computational challenges. Coupled spin ladders, shown in Fig. 6, offer a practical step toward 2D systems. These have been extensively studied [33, 92–97], and are known to exhibit quantum phase transitions between gapped disordered states and magnetically ordered Néel phases.

One notable compound is Ba_2CuTeO_6 [98–100], which realizes weakly coupled spin–$\frac{1}{2}$ ladders through orbital ordering of Cu^{2+} ions. While isolated ladders would feature a spin–singlet ground state, the system undergoes magnetic ordering at a Néel temperature much lower than the dominant exchange energy scale. This suggests that interladder couplings are weak but sufficient to drive magnetic order, placing the compound near the quantum critical point separating the gapped and ordered phases (see Fig. 7).

Another relevant example is $C_9H_{18}N_2CuBr_4$ [101], a spin–$\frac{1}{2}$ magnetic insulator composed of coupled two-leg ladders. Its low-temperature magnetic behavior and proximity to the quantum critical point have been characterized [102–104].

Figure 6 – Ba2CuTeO6 exhibits a coupled ladder structure, where the exchange interactions J_{rung} and J_{leg} define individual two-leg ladders, and J_{inter} couples these ladders together.

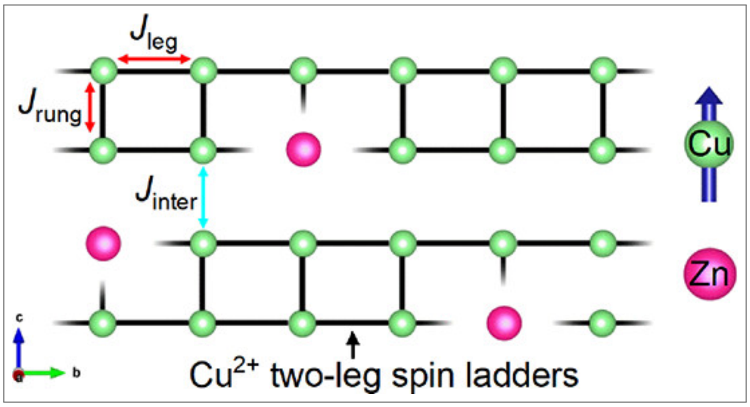

Source: Reference [100]

Figure 7 – (a) Monoclinic structure of Ba_2CuTeO_6 showing the $12R$ hexagonal stacking sequence. The intra-ladder (J_{leg} and J_{rung}) interactions between the $Cu2^+$ cations (colored green) are indicated by the red arrows. The inter-ladder interaction J_{inter} through the face- sharing CuO_6-TeO_6-CuO_6 trimer is indicated by the blue arrow. (b) Two-leg spin ladder structure of $Cu2^+$ cations in Ba_2CuTeO_6 viewed along the a axis. (c) Two-leg spin ladder phase diagram. The red arrow shows that Ba_2CuTeO_6 lies close to the quantum critical point (QCP) on the Néel ordered side of the phase diagram.

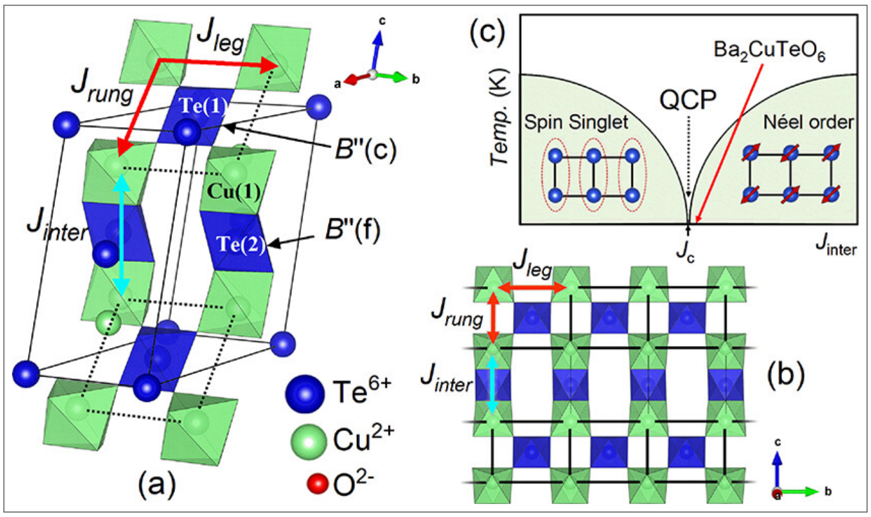

Source: Reference [100]

Frustrated magnetic systems hold greater promise for hosting exotic quantum phases, such as spin liquids and topological states, due to competing interactions. Yet, frustration in coupled ladder systems remains relatively unexplored [105]. While numerical methods like quantum Monte Carlo are powerful for unfrustrated models, they suffer from the sign problem in frustrated systems, especially in 2D, necessitating the use of advanced computational techniques.

Given the success of unfrustrated coupled ladders in modeling quantum materials, the frustrated case is particularly compelling. Frustrated two-leg ladders exhibit rich and complex phase diagrams that go beyond those of unfrustrated systems, providing strong motivation for the present study. The model shown in Fig. 8 offers a promising framework for exploring the interplay of frustration and dimensional crossover in quasi-1D and 2D settings, including the emergence of novel and potentially topological phases.

Figure 8 – Schematic representation of two coupled, frustrated two-leg ladders. Solid lines denote intra-ladder interactions, while dashed lines indicate inter-ladder couplings.

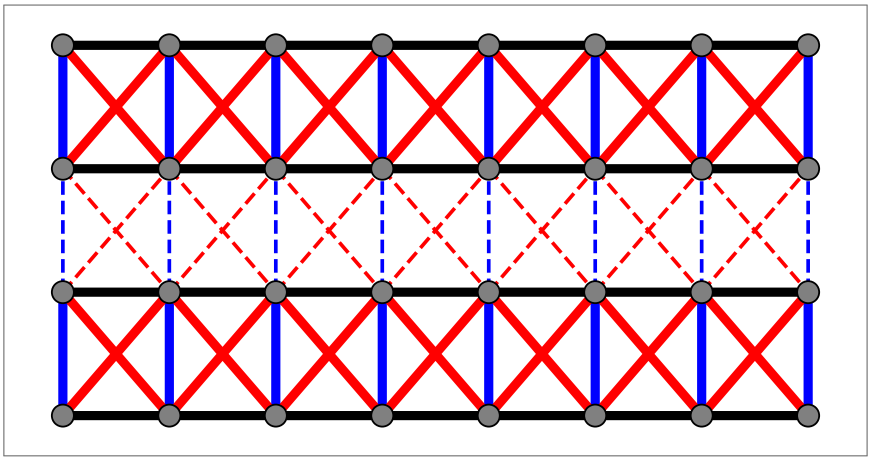

Source: The author (2025)

1.3 THESIS OUTLINE

This thesis is organized as follows:

Chapter 2 introduces the DMRG method, the primary numerical tool used in this work. We present both its traditional formulation and modern *Matrix Product State* (MPS)-based approach, with attention to implementation details. The chapter also describes the computational libraries employed, includes code examples, and outlines the methodology applied throughout the thesis.

Chapter 3 focuses on low-dimensional quantum spin systems. We begin with spin–S chains for $S = \left(\frac{1}{2}, 1, \frac{3}{2}, 2\right)$, presenting DMRG results and discussing the Haldane conjecture and associated topological phases. The chapter concludes with an analysis of spin ladder models, including the ground-state phase diagram of the spin–$\frac{1}{2}$ two-leg ladder.

Chapter 4 analyzes the phase diagram of the spin–$\frac{1}{2}$ frustrated two-leg ladder under an external magnetic field. We examine ground-state properties, identify distinct phases and their boundaries, and estimate KT transition points.

Chapter 5 investigates a Heisenberg two-leg ladder with alternating spins $(\frac{1}{2}, 1)$ in a magnetic field. Combining DMRG and spin–wave theory, we construct the phase diagram, estimate critical points, determine phase boundaries, and compare numerical results with analytical predictions.

Chapter 6 explores systems of coupled spin–$\frac{1}{2}$ two-leg ladders, considering both unfrustrated and frustrated configurations. Using DMRG, we construct phase diagrams, characterize the resulting phases, and extend the study to even-leg systems, with particular emphasis on the four-leg case.

Chapter 7 summarizes the main findings of this thesis and outlines possible directions for future research.

2 DENSITY MATRIX RENORMALIZATION GROUP (DMRG)

The DMRG, introduced by Steven White in 1992 [16, 17], is a powerful numerical method for investigating strongly correlated 1D and quasi-1D quantum systems. A defining feature of such systems is the exponential growth of their Hilbert space with system size, which poses significant obstacles for both analytical approaches and conventional approximation methods, such as perturbation theory or standard variational techniques. The core challenge addressed by DMRG lies in the computational intractability associated with this vast Hilbert space. The method's key innovation is to represent the ground state within an optimally reduced basis, retaining only the most relevant components while discarding less significant contributions. This strategy enables a drastic reduction in the effective Hilbert space dimension while preserving the essential physical properties of the system.

The traditional formulation of DMRG has its roots in the broader context of RG theories, which aim to capture the behavior of many-body systems near criticality. The development of DMRG was motivated by the limitations of the *Numerical Renormalization Group* (NRG) method [106], as critically assessed by White and Noack [107]. While NRG proceeds by iteratively diagonalizing the Hamiltonian and retaining only the lowest-energy eigenstates, it often fails to provide accurate descriptions of low-energy properties in extended systems. In contrast, DMRG improves upon this approach by introducing a two-block scheme (see Fig. 9(b)), which outperforms the single-block strategy employed in NRG (see Fig. 9(a)).

In the NRG framework, one begins with a small block of sites in a 1D system and incrementally adds new sites. To mitigate the exponential growth of the Hilbert space, a maximum number of retained states, denoted by m, is imposed. Once this limit is reached, truncation is performed by discarding states beyond this threshold after each site addition. This iterative procedure continues until convergence of the ground-state energy is achieved. The selection process, commonly referred to as *decimation*, retains states associated with the lowest eigenvalues and thus plays a decisive role in the method's effectiveness. DMRG retains the iterative structure of NRG but enhances its precision by using a two-block architecture, which offers a superior balance between computational efficiency and the fidelity of physical information.

Figure 9 – (a) Representation of an iterative growth process in the NRG method. (b) Representation of an iterative growth process in the DMRG method.

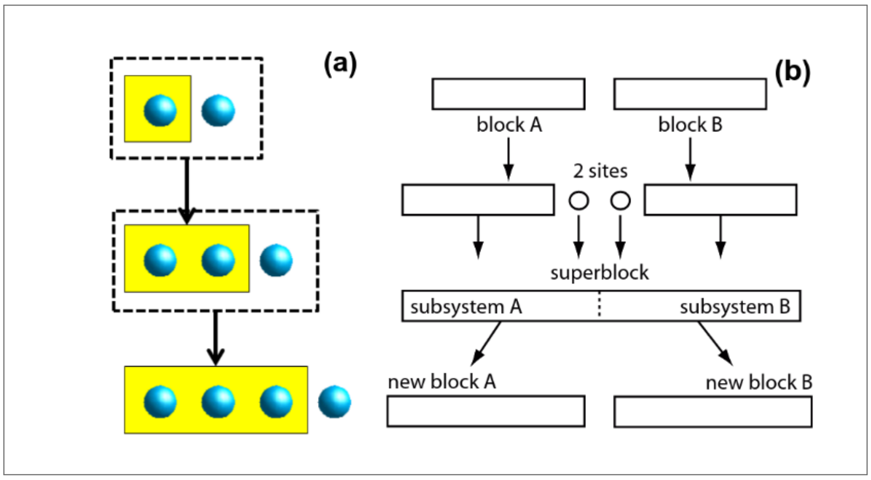

Source: Adapted from [108] and [109].

2.1 FORMULATION

The ground state of the system can be expressed in terms of a bipartite decomposition as

$$|\Psi\rangle = \sum_{i,j} c_{ij}|i\rangle \otimes |j\rangle = \sum_{i,j} c_{ij}|ij\rangle, \tag{2.1}$$

where $|i\rangle$ and $|j\rangle$ form orthonormal bases for subsystems A and B, respectively, and the coefficients c_{ij} are given by $c_{ij} = \langle ij|\Psi\rangle$. It is assumed that the state $|\Psi\rangle$ is normalized, i.e., $\langle\Psi|\Psi\rangle = 1$. When the dimension of the basis for block A reaches a maximum allowed value m, a change of basis is performed through a procedure known as decimation, transforming the basis to $|i'\rangle$. This transformation aims to minimize the squared norm of the difference between the true ground state $|\Psi\rangle$ and its approximation $|\tilde{\Psi}\rangle$:

$$S = \left||\Psi\rangle - |\tilde{\Psi}\rangle\right|^2, \tag{2.2}$$

where the approximate state is defined as

$$|\tilde{\Psi}\rangle = \sum_{i'=1}^{m}\sum_{j} c_{i'j}|i'j\rangle. \tag{2.3}$$

Considering the system illustrated in Fig. 9(b) as a bipartite structure composed of blocks A and B, the Hilbert space of the full system (superblock) is given by $\hat{\mathcal{H}}_{A+B} = \hat{\mathcal{H}}_A \otimes \hat{\mathcal{H}}_B$, with total dimension $\mathcal{D}_{A+B} = \mathcal{D}_A \cdot \mathcal{D}_B$. For a pure state $|\Psi\rangle$, the density matrix is

$$\hat{\rho} = |\Psi\rangle\langle\Psi|. \tag{2.4}$$

The reduced density matrix associated with block A is obtained by tracing out the degrees of freedom of block B:

$$\hat{\rho}^A = \mathrm{Tr}_{\mathrm{B}}|\Psi\rangle\langle\Psi|. \tag{2.5}$$

The matrix elements of $\hat{\rho}^A$ are

$$\hat{\rho}^A_{nm} = \langle n|\hat{\rho}^A|m\rangle = \sum_i \langle ni|\Psi\rangle\langle\Psi|im\rangle = \sum_i c_{ni}c^*_{im}, \tag{2.6}$$

For pure states, the density matrix $\hat{\rho}$ satisfies several key properties:

- **Idempotency:** $\hat{\rho}^2 = \hat{\rho}$,
- **Hermiticity:** $\hat{\rho}^\dagger = \hat{\rho}$,
- **Normalization:** $\mathrm{Tr}\,\hat{\rho} = 1$,
- **Positivity:** all eigenvalues are non-negative.

The eigenvectors $|\rho^A_i\rangle$ of $\hat{\rho}^A$ form an orthonormal basis for the reduced Hilbert space of block A, with associated eigenvalues $\rho^A_i \geq 0$ that satisfy the normalization condition $\sum_i \rho^A_i = 1$. The spectral decomposition of $\hat{\rho}^A$ then takes the form

$$\hat{\rho}^A = \sum_i \rho^A_i |\rho^A_i\rangle\langle\rho^A_i|, \tag{2.7}$$

and a completely analogous decomposition applies to the reduced density matrix of block B.

2.1.1 Singular Value Decomposition

For a general complex matrix $\mathbf{M}$ of dimensions $M \times N$ (with $M > N$), the *Singular Value Decomposition* (SVD) provides a decomposition of the form

$$\mathbf{M} = \mathbf{U}\mathbf{S}\mathbf{V}^\dagger, \tag{2.8}$$

where $\mathbf{U}$ is an $M \times N$ matrix with orthonormal columns ($\mathbf{U}^\dagger\mathbf{U} = \mathbf{I}_N$), $\mathbf{V}$ is an $N \times N$ unitary matrix, and $\mathbf{S}$ is a diagonal $N \times N$ matrix whose non-negative diagonal elements ω_i are known as the singular values of $\mathbf{M}$. Equation (2.8) defines the SVD of $\mathbf{M}$.

Applying this decomposition to the matrix of coefficients c_{ij} appearing in Eq. (2.1), we obtain

$$c_{ij} = \sum_k U_{ik}\omega_k \left(V_{kj}\right)^\dagger = \sum_k U_{ik}\omega_k V^*_{jk}, \tag{2.9}$$

which allows the many-body wavefunction $|\Psi\rangle$ to be re-expressed as

$$\begin{aligned} |\Psi\rangle &= \sum_{i,j,k} U_{ik}\omega_k V^*_{jk}|ij\rangle \\ &= \sum_k \left(\sum_i U_{ik}|i\rangle\right)\omega_k\left(\sum_j V^*_{jk}|j\rangle\right) \\ &= \sum_k \omega_k|a_k\rangle|b_k\rangle, \end{aligned} \tag{2.10}$$

where we define the orthonormal states

$$|a_k\rangle = \sum_i U_{ik}|i\rangle, \quad |b_k\rangle = \sum_j V^*_{jk}|j\rangle. \tag{2.11}$$

In the context of Hilbert spaces, unitary transformations preserve inner products and therefore the norm of vectors, playing an analogous role to rotation operators in Euclidean space $\mathbb{R}^3$. In this framework, the matrices $\mathbf{U}$ and $\mathbf{V}$ serve as change-of-basis operators that rotate the original bases of blocks A and B, respectively, into new orthonormal sets. The resulting vectors $|a_k\rangle$ and $|b_k\rangle$ form orthonormal bases referred to as the *Schmidt basis*.

Thus, the wavefunction $|\Psi\rangle$ can be expressed in Schmidt form as

$$|\Psi\rangle = \sum_k \omega_k|a_k b_k\rangle, \tag{2.12}$$

which highlights the bipartite entanglement structure of the state. In this basis, the reduced density matrices for subsystems A and B take particularly simple diagonal forms:

$$\hat{\rho}^A = \mathrm{Tr}_B|\Psi\rangle\langle\Psi| = \sum_k \omega_k^2|a_k\rangle\langle a_k|, \tag{2.13}$$

$$\hat{\rho}^B = \mathrm{Tr}_A|\Psi\rangle\langle\Psi| = \sum_k \omega_k^2|b_k\rangle\langle b_k|. \tag{2.14}$$

The squared singular values ω_k^2 thus correspond to the eigenvalues of both reduced density matrices. These quantities are central to DMRG, as they determine which basis states contribute most significantly to the entanglement between blocks and guide the truncation process in the renormalization procedure.

2.1.2 The Decimation

Returning to the truncation procedure introduced previously, we now express both the exact ground state $|\Psi\rangle$ and its approximation $|\tilde{\Psi}\rangle$ in terms of the Schmidt decomposition:

$$|\Psi\rangle = \sum_{k=1}^{M} \omega_k |a_k b_k\rangle, \tag{2.15}$$

$$|\tilde{\Psi}\rangle = \sum_{k=1}^{m<M} \omega_k |a_k b_k\rangle. \tag{2.16}$$

where M is the full dimension of the Schmidt decomposition and m is the number of states retained in the truncated basis. The approximation $|\tilde{\Psi}\rangle$ is obtained by keeping only the m Schmidt vectors associated with the largest singular values ω_k.

The error in this approximation can be quantified using the squared norm introduced in Eq. (2.2). In analogy with the Frobenius norm for matrices,

$$||\mathbf{M}||^2 = \mathrm{Tr}(\mathbf{M}^\dagger \mathbf{M}), \tag{2.17}$$

the squared norm for vectors in Hilbert space corresponds to their inner product. Assuming the singular values are ordered such that $\omega_1 \geq \omega_2 \geq \cdots \geq \omega_M \geq 0$, the squared difference between the full and truncated states becomes:

$$\begin{aligned} S &= |||\Psi\rangle - |\tilde{\Psi}\rangle||^2 \\ &= \left| \sum_{k=1}^{M} \omega_k |a_k b_k\rangle - \sum_{k=1}^{m<M} \omega_k |a_k b_k\rangle \right|^2 = \left| \sum_{k=m+1}^{M} \omega_k |a_k b_k\rangle \right|^2 \\ &= \sum_{k,l=m+1}^{M} \omega_k \omega_l \langle a_l b_l | a_k b_k\rangle = \sum_{k,l=m+1}^{M} \omega_k \omega_l \delta_{k,l} \\ &= \sum_{k=m+1}^{M} \omega_k^2, \end{aligned} \tag{2.18}$$

where the last equality follows from the orthonormality of the Schmidt vectors: $\langle a_l b_l | a_k b_k\rangle = \delta_{k,l}$.

From Eqs. (2.13) and (2.14), the squared singular values ω_k^2 are the eigenvalues of the reduced density matrices $\hat{\rho}^A$ and $\hat{\rho}^B$, and the vectors $|a_k\rangle$ and $|b_k\rangle$ are their corresponding eigenvectors. Therefore, Eq. (2.18) gives the sum of the eigenvalues associated with the discarded states in the reduced Hilbert space.

To minimize the truncation error S, **one must retain the eigenvectors corresponding to the largest eigenvalues** of the reduced density matrix, as these carry the dominant weight in the entanglement spectrum. This procedure is the core of the density matrix-based truncation in the DMRG algorithm.

At each renormalization step, the quantity

$$\epsilon = 1 - \sum_{k=1}^{m} \omega_k^2, \tag{2.19}$$

defines the *discarded weight*, representing the loss in norm resulting from the truncation. Since the singular values satisfy the normalization condition $\sum_{k=1}^{M} \omega_k^2 = 1$, Eq. (2.19) directly measures the contribution from the states removed during the decimation. The total discarded weight accumulates throughout the successive truncations and serves as a reliable metric of the approximation quality.

2.1.3 Lanczos Method

A central objective in many numerical algorithms for quantum systems is the diagonalization of the Hamiltonian. The Lanczos method [110] is one of the most widely used techniques for this task, particularly in large Hilbert spaces. It is favored for its **low memory requirements**—storing only three vectors at any given step—and for its **rapid convergence** to extremal eigenvalues, typically limited only by machine precision. Through an iterative process, the Lanczos algorithm generates an orthonormal basis in which the Hamiltonian is represented as a tridiagonal matrix [111].

We begin with an arbitrary normalized vector $|\Psi_0\rangle$ from the Hilbert space. The next vector in the sequence is generated by applying the Hamiltonian $\hat{\mathcal{H}}$ and orthogonalizing via the Gram-Schmidt procedure:

$$|\Psi_1\rangle = \hat{\mathcal{H}}|\Psi_0\rangle - \frac{\langle\Psi_0|\hat{\mathcal{H}}|\Psi_0\rangle}{\langle\Psi_0|\Psi_0\rangle}|\Psi_0\rangle, \tag{2.20}$$

which ensures orthogonality: $\langle\Psi_0|\Psi_1\rangle = 0$. The process continues with

$$|\Psi_2\rangle = \hat{\mathcal{H}}|\Psi_1\rangle - \frac{\langle\Psi_1|\hat{\mathcal{H}}|\Psi_1\rangle}{\langle\Psi_1|\Psi_1\rangle}|\Psi_1\rangle - \frac{\langle\Psi_1|\Psi_1\rangle}{\langle\Psi_0|\Psi_0\rangle}|\Psi_0\rangle, \tag{2.21}$$

which guarantees $\langle\Psi_0|\Psi_2\rangle = \langle\Psi_1|\Psi_2\rangle = 0$.

Generalizing this process, we recursively define the $(n+1)$-th vector in the Krylov subspace as

$$|\Psi_{n+1}\rangle = \hat{\mathcal{H}}|\Psi_n\rangle - a_n|\Psi_n\rangle - b_n^2|\Psi_{n-1}\rangle, \tag{2.22}$$

for $n = 1, 2, \ldots$, with initial conditions $|\Psi_{-1}\rangle = 0$ and $b_0 \equiv 0$. The scalar coefficients a_n and b_n^2 are given by

$$a_n = \frac{\langle \Psi_n | \hat{\mathcal{H}} | \Psi_n \rangle}{\langle \Psi_n | \Psi_n \rangle}, \quad b_n^2 = \frac{\langle \Psi_n | \Psi_n \rangle}{\langle \Psi_{n-1} | \Psi_{n-1} \rangle}, \tag{2.23}$$

In the basis $|\Psi_0\rangle, |\Psi_1\rangle, |\Psi_2\rangle, \ldots$, the Hamiltonian is represented by the tridiagonal matrix:

$$\hat{\mathcal{H}} = \begin{bmatrix} a_0 & b_0 & 0 & 0 & \ldots \\ b_1 & a_1 & b_2 & 0 & \ldots \\ 0 & b_2 & a_2 & b_3 & \ldots \\ 0 & 0 & b_3 & a_3 & \ldots \\ \vdots & \vdots & \vdots & \vdots & \ddots \end{bmatrix}. \tag{2.24}$$

This sparse structure allows for **efficient diagonalization** using standard numerical routines, such as the QR algorithm or specialized methods for tridiagonal matrices.

A key feature of the Lanczos method is its **extreme memory efficiency**. At any given iteration n, only three vectors need to be stored: $|\Psi_{n-1}\rangle$, $|\Psi_n\rangle$, and the result of applying the Hamiltonian, $\hat{\mathcal{H}}|\Psi_n\rangle$. This feature makes the Lanczos algorithm especially attractive for large-scale problems, such as those encountered in exact diagonalization or as part of the DMRG warm-up process.

2.1.4 DMRG Algorithms

Having established how to select the reduced basis, we now describe how DMRG performs numerical calculations using its two core variants: the *infinite-size DMRG* and its enhanced form, the *finite-size DMRG*. Both follow the block growth scheme illustrated in Fig. 9(b), where two blocks are initialized and sites are added iteratively until the system reaches a predefined target size. At each step, the Hilbert space is truncated using the reduced density matrix, and the process repeats until the desired size is attained or the energy error satisfies a prescribed tolerance.

The general procedure is as follows:

- Construct the local operators for each site and the interaction terms between neighboring sites.

- Begin the block growth as depicted in Fig. 9(b).
- When the block dimension exceeds $d \times m$ (where d is the local Hilbert space dimension and m is the maximum number of states retained), perform truncation using the density matrix.
- Diagonalize the superblock Hamiltonian using the Lanczos method to obtain the ground state.
- Compute the reduced density matrices for blocks A and B.
- Retain the m eigenvectors corresponding to the largest eigenvalues.
- Transform the Hamiltonian and operators into the new basis $|a_i\rangle\,|b_i\rangle$.

In the first iteration, the basis transformation reads:

$$|a_i^1\rangle = \sum_k \langle a_k^0 \,| a_i^1\rangle\, |a_k^0\rangle, \quad |b_k^1\rangle = \sum_k \langle a_k^0 \,| b_i^1\rangle\, |a_k^0\rangle, \tag{2.25}$$

where $|a_k^0\rangle\,|b_k^0\rangle$ denotes the initial basis.

In the second iteration, a site $|s_1\rangle$ is added to the right of block A and to the left of block B, leading to

$$|a_i'\rangle = |s_1\rangle \otimes \left|a_i^1\right\rangle = \left|s_1 a_i^1\right\rangle, \quad |b_i'\rangle = |s_1\rangle \otimes \left|b_i^1\right\rangle = \left|s_1 b_i^1\right\rangle. \tag{2.26}$$

The updated basis becomes

$$\left|a_i^2\right\rangle = \sum_{k=1}^{m} \left\langle s_1 a_k^1 \,\middle|\, a_i^2\right\rangle \left|s_1 a_k^1\right\rangle, \quad \left|b_i^2\right\rangle = \sum_{k=1}^{m} \left\langle s_1 b_k^1 \,\middle|\, b_i^2\right\rangle \left|s_1 b_k^1\right\rangle. \tag{2.27}$$

At the n-th iteration, the basis evolves as

$$\left|a_i^n\right\rangle = \sum_{k=1}^{m} \left\langle s_{n-1} a_k^{n-1} \,\middle|\, a_i^n\right\rangle \left|s_{n-1} a_k^{n-1}\right\rangle = \sum_{k=1}^{m} (U_A)_{i,k}^n \left|s_{n-1} a_k^{n-1}\right\rangle, \tag{2.28}$$

$$\left|b_i^n\right\rangle = \sum_{k=1}^{m} \left\langle s_{n-1} a_k^{n-1} \,\middle|\, b_i^n\right\rangle \left|s_{n-1} b_k^{n-1}\right\rangle = \sum_{k=1}^{m} (U_B)_{i,k}^n \left|s_{n-1} b_k^{n-1}\right\rangle, \tag{2.29}$$

where the transformation matrices are defined by

$$(U_A)_{i,k}^n = \left\langle s_{n-1} a_k^{n-1} \,\middle|\, a_i^n\right\rangle, \quad (U_B)_{i,k}^n = \left\langle s_{n-1} b_k^{n-1} \,\middle|\, b_i^n\right\rangle. \tag{2.30}$$

By convention, $|s_0\rangle = \mathbb{I}$. Operators are then rotated into the new basis:

$$\begin{aligned}
\left(\hat{O}_{a_i^n, a_j^n}\right)^n_A &= \langle a_i^n | \hat{O} | a_j^n \rangle \\
&= \sum_{k=1}^{m} \sum_{k'=1}^{m} \left\langle a_i^n \middle| s_{n-1} a_k^{n-1} \right\rangle \left\langle s_{n-1} a_k^{n-1} \middle| \hat{O} \middle| s_{n-1} a_{k'}^{n-1} \right\rangle \left\langle s_{n-1} a_{k'}^{n-1} \middle| a_j^n \right\rangle \\
&= \sum_{k=1}^{m} \sum_{k'=1}^{m} \left(U_A^\dagger\right)^n_{i,k} \left(\hat{O}_{s_{n-1} a_k^{n-1}, s_{n-1} a_{k'}^{n-1}}\right)^n_A (U_A)^n_{j,k'} \,, \qquad (2.31)
\end{aligned}$$

$$\begin{aligned}
\left(\hat{O}_{b_i^n, b_j^n}\right)^n_B &= \langle b_i^n | \hat{O} | b_j^n \rangle \\
&= \sum_{k=1}^{m} \sum_{k'=1}^{m} \left\langle b_i^n \middle| s_{n-1} b_k^{n-1} \right\rangle \left\langle s_{n-1} b_k^{n-1} \middle| \hat{O} \middle| s_{n-1} b_{k'}^{n-1} \right\rangle \left\langle s_{n-1} b_{k'}^{n-1} \middle| b_j^n \right\rangle \\
&= \sum_{k=1}^{m} \sum_{k'=1}^{m} \left(U_B^\dagger\right)^n_{i,k} \left(\hat{O}_{s_{n-1} b_k^{n-1}, s_{n-1} b_{k'}^{n-1}}\right)^n_B (U_B)^n_{j,k'} \,. \qquad (2.32)
\end{aligned}$$

This procedure is repeated until the system reaches the target size or the energy error falls within the desired tolerance. This describes the **infinite-size DMRG** algorithm.

For the **finite-size DMRG**, the process initially mirrors the infinite-size algorithm until the system reaches its maximum size. At that point, an optimization phase known as *sweeping* is introduced (see Fig. 10). Sweeping improves accuracy by refining the basis through a sequence of *right-to-left* and *left-to-right* passes.

Figure 10 – Finite-size DMRG algorithm.

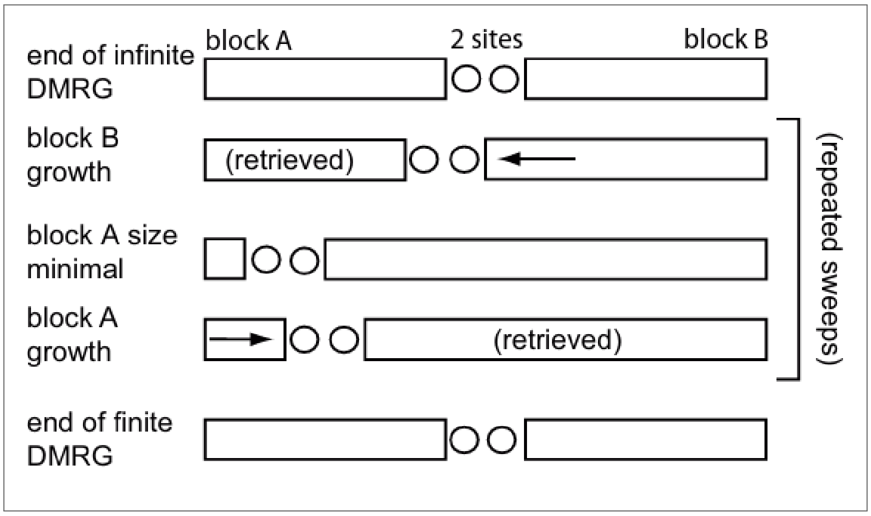

Source: Reference [109].

During a sweep, sites are shifted between the two blocks. In a right-to-left sweep, for example, sites are sequentially moved from block B to block A. At each step, a site from B is added to A, followed by truncation of block A's basis and rotation of all relevant operators. This continues until block B is reduced to a single site. The left-to-right sweep then reverses this process. Sweeping continues until the energy error satisfies the tolerance or a fixed number of sweeps is completed to balance both computational cost and accuracy.

2.1.5 Correlations

During each DMRG sweep iteration, local operators are rotated into a new truncated basis. Consequently, special care must be taken when computing correlation functions involving operators acting on different sites. Let $\hat{O}_i$ and $\hat{O}'_j$ be operators acting on sites i and j, respectively. Depending on the sweep configuration, these sites may belong to the same block or to different blocks. Denote by $|a\rangle$ and $|b\rangle$ orthonormal bases for blocks A and B, respectively. The ground state is written as

$$|\Psi\rangle = \sum_{a,b} c_{ab}|ab\rangle. \tag{2.33}$$

2.1.5.1 Sites in the Same Block

If both sites i and j belong to block A during a particular iteration (see Fig. 11), the correlation function is given by:

$$\begin{aligned}
\langle \hat{O}_i \hat{O}'_j \rangle &= \langle \Psi | \hat{O}_i \hat{O}'_j | \Psi \rangle \\
&= \sum_{a,b} \sum_{a',b'} c_{ab} c^*_{a'b'} \langle a'b' | \hat{O}_i \hat{O}'_j | ab \rangle \\
&= \sum_{a,b} \sum_{a',b'} c_{ab} c^*_{a'b'} \langle b' | b \rangle \langle a' | \hat{O}_i \hat{O}'_j | a \rangle \\
&= \sum_{b} \sum_{a,a'} c_{ab} c^*_{a'b} (\hat{O}_{ij})_{aa'},
\end{aligned} \tag{2.34}$$

where $\hat{O}_{ij} = \hat{O}_i \hat{O}'_j$ is the composite operator acting entirely within block A, and orthonormality of the B basis implies $\langle b' | b \rangle = \delta_{bb'}$.

During the truncation procedure, $\hat{O}_{ij}$ must be rotated into the new reduced basis just like other operators. Importantly, one must **not** compute the product $\hat{O}_i \hat{O}'_j$ after truncating the individual operators, as this yields incorrect results due to loss of information during truncation.

Figure 11 – Case where the operators belong to the same block.

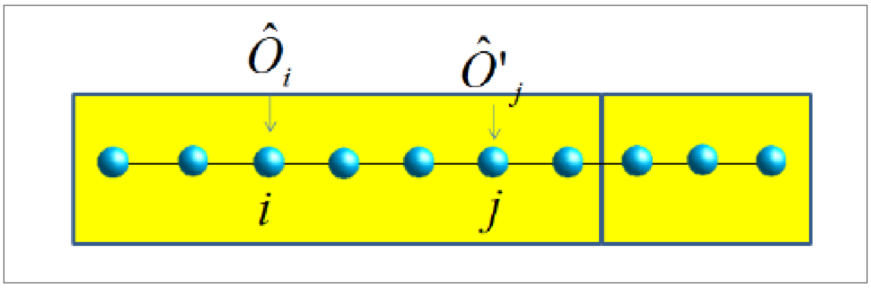

Source: Reference [108].

2.1.5.2 Sites in Different Blocks

When sites i and j belong to different blocks—say, i is in block A and j is in block B (see Fig. 12)—the correlation function becomes:

$$\begin{aligned}\langle \hat{O}_i \hat{O}'_j \rangle &= \langle \Psi | \hat{O}_i \hat{O}'_j | \Psi \rangle \\ &= \sum_{a,b} \sum_{a',b'} c_{ab} c^*_{a'b'} \langle a'b' | \hat{O}_i \hat{O}'_j | ab \rangle \\ &= \sum_{a,b} \sum_{a',b'} c_{ab} c^*_{a'b'} \langle a' | \hat{O}_i | a \rangle \langle b' | \hat{O}'_j | b \rangle \\ &= \sum_{b,b'} \sum_{a,a'} c_{ab} c^*_{a'b'} (\hat{O}_i)_{aa'} (\hat{O}'_j)_{bb'} . \end{aligned} \tag{2.35}$$

Figure 12 – Case where the operators belong to different blocks.

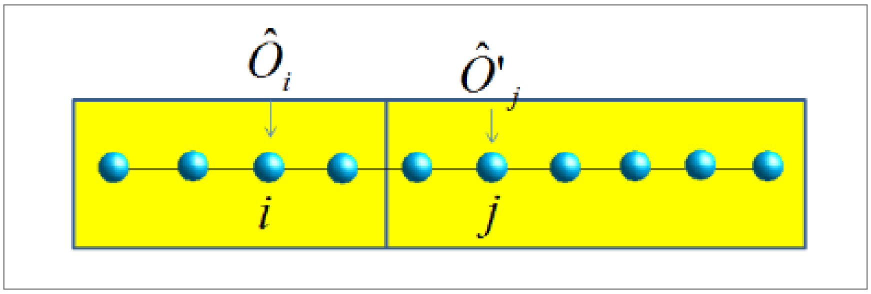

Source: Reference [108].

2.1.6 Theoretical Foundation of DMRG Success

The remarkable efficiency of DMRG for 1D systems with open boundary conditions—contrasting sharply with its limited performance for periodic boundaries and higher dimensions—initially puzzled researchers. This behavior was later elucidated through the lens of quantum information theory: the effectiveness of DMRG is fundamentally linked to the geometry and topology of the system, as these govern the structure of *quantum entanglement*—a measure of the information required to faithfully represent a quantum state. A key quantity capturing this is the *von Neumann entropy.*

In quantum mechanics, entanglement characterizes composite systems in which subsystems cannot be described independently. Consider two spin–$\frac{1}{2}$ particles in the following states:

$$|\Psi_1\rangle = \frac{|\uparrow\downarrow\rangle - |\downarrow\uparrow\rangle}{\sqrt{2}}, \tag{2.36}$$

$$|\Psi_2\rangle = \frac{|\uparrow\uparrow\rangle - |\uparrow\downarrow\rangle + |\downarrow\uparrow\rangle - |\downarrow\downarrow\rangle}{2}. \tag{2.37}$$

The state $|\Psi_2\rangle$ can be factorized, allowing each spin to be described independently:

$$|\Psi_2\rangle = \left(\frac{|\uparrow\rangle_1 + |\downarrow\rangle_1}{\sqrt{2}}\right) \otimes \left(\frac{|\uparrow\rangle_2 - |\downarrow\rangle_2}{\sqrt{2}}\right). \tag{2.38}$$

In contrast, $|\Psi_1\rangle$ cannot be factorized in this way; the state of one particle depends on the state of the other. This inseparability is the hallmark of entanglement.

Entanglement is quantitatively captured by the von Neumann entropy:

$$S = -\mathrm{Tr}\left(\hat{\rho} \ln \hat{\rho}\right), \tag{2.39}$$

where $\hat{\rho}$ is the reduced density matrix of one subsystem. In the Schmidt basis (see Eqs. (2.13) and (2.14)), this entropy becomes:

$$S_A = -\mathrm{Tr}\left(\hat{\rho}^A \ln \hat{\rho}^A\right) = -\sum_k \omega_k \ln \omega_k, \tag{2.40}$$

$$S_B = -\mathrm{Tr}\left(\hat{\rho}^B \ln \hat{\rho}^B\right) = -\sum_k \omega_k \ln \omega_k. \tag{2.41}$$

where ω_k are the Schmidt coefficients. The equality $S_A = S_B \neq 0$ indicates the presence of entanglement between blocks A and B.

Within the DMRG algorithm, truncation is performed by retaining the states with the largest Schmidt coefficients ω_k, which effectively maximizes the von Neumann entropy. This procedure ensures that the most entangled—and thus most physically relevant—states are preserved, while less significant ones are discarded. As a result, DMRG is particularly powerful for strongly correlated systems, such as low-dimensional spin models, where capturing the entanglement structure is essential for an accurate description of the ground state.

2.2 MPS FORMULATION OF DMRG

Over the years, the DMRG method has been recast within the broader formalism of tensor network states, which naturally encode entanglement structures in 1D quantum systems. Among these, the MPS representation has emerged as a central framework, providing both conceptual clarity and computational efficiency. More generally, tensor networks furnish a unifying language for the efficient representation of quantum states in higher dimensions, with notable extensions such as *Projected Entangled Pair State* (PEPS). These developments have established tensor network methods as indispensable tools in modern computational quantum physics, bridging areas such as condensed matter theory, quantum information, and statistical mechanics.

2.2.1 MPS Representation

Consider a quantum system composed of N sites, each associated with a local basis $|s_i\rangle$. The most general pure state of the system can be written as

$$|\Psi\rangle = \sum_{s_1,\ldots,s_N} c_{s_1,\ldots,s_N} |s_1 s_2 \cdots s_N\rangle, \tag{2.42}$$

where, for brevity, we adopt the notation

$$\sum_{\vec{s}} \equiv \sum_{s_1,s_2,\ldots,s_N} . \tag{2.43}$$

Assuming all sites have the same local Hilbert space dimension d, i.e., $\dim(|s_i\rangle) = d$ for all i, the state coefficients $c_{s_1,\ldots,s_N}$ can be viewed as entries of a rank-N tensor. To begin constructing a MPS, we reshape $|\Psi\rangle$ into a matrix $\tilde{\Psi}$ of dimension $d \times d^{N-1}$, with the mapping

$$\tilde{c}_{s_1,(s_2,\cdots,s_N)} = c_{s_1,\cdots,s_N}, \tag{2.44}$$

Performing a SVD on this matrix yields

$$\tilde{c}_{s_1,(s_2,\ldots,s_N)} = \sum_{k_1}^{r} U_{s_1,k_1} S_{k_1 k_1} V^{\dagger}_{k_1,s_2\ldots s_N}. \tag{2.45}$$

where $r_1 \leq d$ is the rank of $\tilde{\Psi}$. The matrix U can be interpreted as a collection of d row vectors A^{s_1}, with components $A^{s_1}_{k_1} = U_{s_1,k_1}$. The product $SV^{\dagger}$ is then reshaped into a new matrix $\tilde{\Psi}_{(k_1 s_2),(s_3 \ldots s_N)}$ of dimension $r_1 d \times d^{N-2}$, giving

$$c_{s_1,\ldots,s_N} = \sum_{k_1=1}^{r_1} A_{k_1}^{s_1} \tilde{\Psi}_{(k_1 s_2),(s_3 \ldots s_L)}. \tag{2.46}$$

Applying another SVD to $\tilde{\Psi}$ and continuing this process iteratively, we obtain

$$c_{s_1,\ldots,s_N} = \sum_{\vec{k}} A_{k_1}^{s_1} A_{k_1,k_2}^{s_2} \cdots A_{k_{N-2},k_{N-1}}^{s_{N-1}} A_{k_{N-1}}^{s_N}, \tag{2.47}$$

which we often write more compactly as a product of matrices:

$$c_{s_1,\ldots,s_N} = A^{s_1} A^{s_2} \cdots A^{s_{N-1}} A^{s_N}. \tag{2.48}$$

Here, the matrices A^{s_i} are site-dependent and indexed by the local physical index s_i, while the auxiliary *bond indices* k_i encode the entanglement between adjacent sites. If necessary, dummy indices of dimension one can be introduced at the boundaries to treat all tensors uniformly as matrices.

The state is now exactly represented in the MPS form:

$$|\Psi\rangle = \sum_{\vec{s}} A^{s_1} A^{s_2} \cdots A^{s_{N-1}} A^{s_N} |s_1, \cdots, s_N\rangle. \tag{2.49}$$

In the exact construction above, the bond dimensions grow rapidly, reaching a maximum of $d^{N/2}$ in the middle of the chain. More precisely, the dimensions of the intermediate tensors scale as $(1 \times d)$, $(d \times d^2)$, ..., $(d^{N/2-1} \times d^{N/2})$, ..., $(d^2 \times d)$, $(d \times 1)$ from left to right. This exponential growth in bond dimension renders exact MPS representations impractical for large systems. Truncated SVDs are typically employed to maintain a manageable bond dimension while controlling approximation error.

At each SVD step, the unitarity condition $U^\dagger U = \mathbb{I}$ implies that the corresponding A^{s_n} matrices satisfy

$$\sum_{s_n} (A^{s_n \dagger} A^{s_n})_{k_n k_n'} = \delta_{k_n k_n'}, \tag{2.50}$$

$$\sum_{s_n} A^{s_n \dagger} A^{s_n} = \mathbb{I}. \tag{2.51}$$

Matrices that satisfy this condition are referred to as *left-normalized*, and a state in which all tensors are left-normalized is said to be in the *left-canonical* form. This construction is illustrated schematically in Fig. 13.

Figure 13 – Graphical representation of an iterative construction of an exact MPS representation of an arbitrary quantum state by a sequence of singular value decompositions.

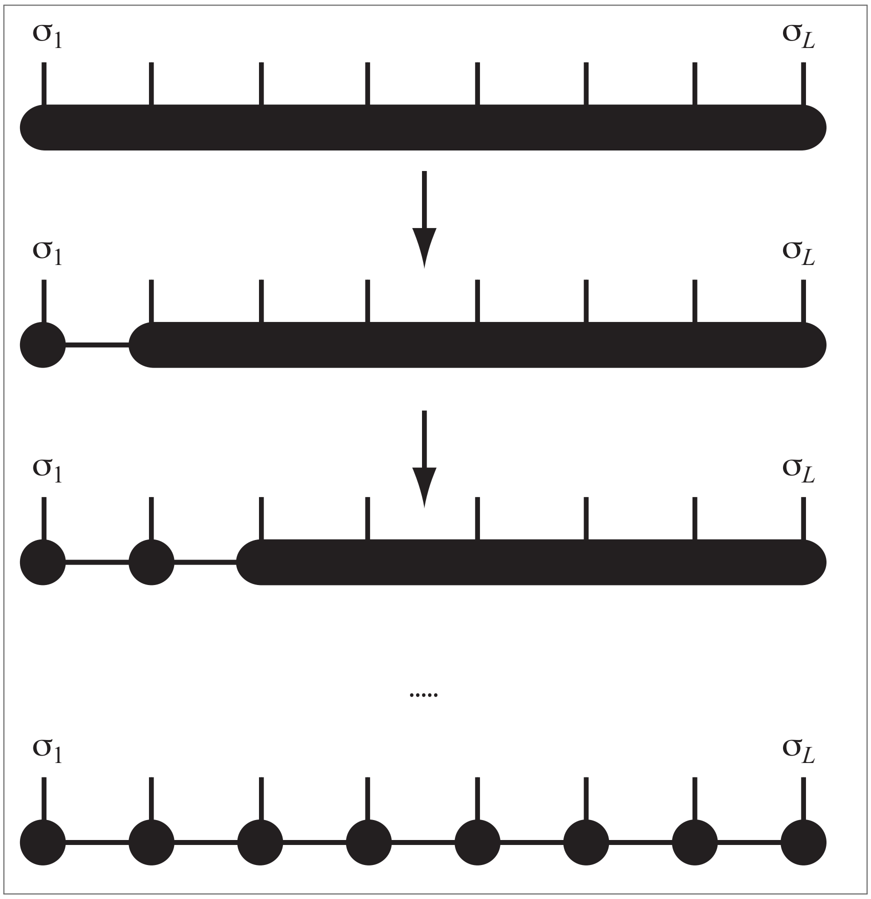

Source: Reference [109].

The choice of starting from the left is arbitrary. An analogous construction starting from the right produces the *right-canonical* form, with tensors satisfying

$$\sum_{s_n} A^{s_n} A^{s_n\dagger} = \mathbb{I}, \tag{2.52}$$

where the A^{s_n} are now *right-normalized.*

Combining these two canonical forms leads to the *mixed-canonical* representation, in which the decomposition is left-normalized up to site i and right-normalized from site $i + 1$ onward:

$$|\Psi\rangle = \sum_{\vec{s_1}} = A^{s_1} \cdots A^{s_i} S B^{s_{i+1}} \cdots B^{s_N} |s_1, \cdots, s_N\rangle, \tag{2.53}$$

where S is a diagonal matrix containing the singular values from the last SVD, and the B tensors are right-normalized, satisfying Eq. (2.52).

The various exact MPS representations discussed above highlight the fact that the MPS form is not unique. In particular, the left-, right-, and mixed-canonical forms each offer specific advantages for algorithmic implementations. Moreover, the MPS structure admits a gauge freedom: for any pair of adjacent tensors A^{s_i} and $A^{s_{i+1}}$ sharing a bond dimension D, we can insert the identity $\mathbb{I} = MM^{-1}$ between them:

$$A^{s_i} A^{s_{i+1}} = A^{s_i} \mathbb{I} A^{s_{i+1}} = A^{s_i} M M^{-1} A^{s_{i+1}}, \tag{2.54}$$

which leaves the overall state unchanged under the transformation

$$A^{s_i} \to A^{s_i} M, \quad A^{s_{i+1}} = M^{-1} A^{s_{i+1}}, \tag{2.55}$$

for any invertible $D \times D$ matrix M. This gauge freedom can be exploited to enforce canonical forms or optimize numerical stability during simulations.

2.2.2 MPO Representation

Operators can be represented analogously to states using *Matrix Product Operators* (MPOs). Consider an arbitrary operator $\hat{O}$ expressed in the local basis as

$$\hat{O} = \sum_{\vec{s},\vec{s}'} C^{s_1',\ldots,s_N'}_{s_1,\ldots,s_N} |s_1 s_2 \cdots s_N\rangle\langle s_1' s_2' \cdots s_N'|, \tag{2.56}$$

Applying successive SVDs to the coefficient tensor yields an exact MPO representation:

$$\hat{O} = \sum_{\vec{s},\vec{s}'} W^{s_1 s_1'} W^{s_2 s_2'} \ldots W^{s_{N-1} s_{N-1}'} W^{s_N s_N'} |s_1 s_2 \cdots s_N\rangle\langle s_1' s_2' \cdots s_N'|, \tag{2.57}$$

where each $W^{s_i s_i'}$ is a matrix associated with site i and physical indices (s_i, s_i').

The action of an MPO on an MPS yields another MPS. Explicitly, for $\hat{O}_{\text{MPO}}$ and $|\Psi\rangle_{\text{MPS}}$, we have:

$$\begin{aligned}
\hat{O}_{\text{MPO}} |\Psi\rangle_{\text{MPS}} &= \sum_{\vec{s},\vec{s}'} W^{s_1 s_1'} W^{s_2 s_2'} \ldots W^{s_N, s_N'} A^{s_1} A^{s_2} \cdots A^{s_N} |s_1 s_2 \cdots s_N\rangle \\
&= \sum_{\vec{s},\vec{s}'} \sum_{\vec{k},\vec{p}} (W^{s_1 s_1'}_{1,p_1} W^{s_2 s_2'}_{p_1,p_2} \cdots A^{s_1}_{1,k_1} A^{s_2}_{k_1,k_2} \cdots) |s_1 s_2 \cdots s_N\rangle \\
&= \sum_{\vec{s},\vec{s}'} \sum_{\vec{k},\vec{p}} (W^{s_1 s_1'}_{1,p_1} A^{s_1}_{1,k_1} W^{s_2, s_2'}_{p_1,p_2} A^{s_2}_{k_1,k_2} \cdots) |s_1 s_2 \cdots s_N\rangle \\
&= \sum_{\vec{s}} \sum_{\vec{k},\vec{p}} \lambda^{s_1}_{(1,1),(p_1,k_1)} \lambda^{s_2}_{(p_1,k_1),(p_1,k_2)} \cdots |s_1 s_2 \cdots s_N\rangle \\
&= \sum_{\vec{s}} \lambda^{s_1} \lambda^{s_2} \cdots |s_1 s_2 \cdots s_N\rangle = |\Phi\rangle_{\text{MPS}},
\end{aligned} \tag{2.58}$$

where the new MPS tensors λ^{s_i} are constructed by contracting the physical indices of $W^{s_i s_i'}$ with the corresponding $A^{s_i'}$. The resulting bond dimension increases to the product of the original MPS and MPO bond dimensions [109].

2.2.3 Tensor Networks in DMRG

The mathematical structure of MPS and MPO can be elegantly formulated using tensor notation. A *tensor* is a mathematical object characterized by a set of indices, where each combination of index values corresponds to a numerical entry. The number of indices defines the *rank* of the tensor: for example, a rank-0 tensor is a scalar, a rank-1 tensor is a vector, and a rank-2 tensor is a matrix. The coefficients in Eq. (2.42) can be regarded as components of a rank-N tensor:

$$T_{s_1,s_2,\ldots,s_N} = c_{s_1,s_2,\ldots,s_N}. \tag{2.59}$$

Up to this point, MPS has been described in terms of one matrix per site. However, for a lattice consisting of N sites, it is advantageous—especially in the context of the DMRG algorithm—to access all $N-1$ possible bipartitions of the system (i.e., into subsystems A and B with a single cut) [112]. To accommodate this, the MPS can be rewritten as a sequence of rank-1 and rank-3 tensors. This representation is commonly referred to as the *tensor-train* form:

$$|\Psi\rangle = \sum_{\vec{s},\vec{\alpha}} \Gamma[1]^{s_1}_{\alpha_1}\Lambda[1]_{\alpha_1}\Gamma[2]^{s_2}_{\alpha_1\alpha_2}\Lambda[2]_{\alpha_2}\Gamma[3]^{s_3}_{\alpha_2\alpha_3}\Lambda[3]_{\alpha_3}\cdots\Gamma[N]^{s_N}_{\alpha_N}|s_1,...,s_N\rangle, \tag{2.60}$$

where s_i indexes the local physical basis at site i (e.g., for a spin-$\frac{1}{2}$ system, $s_i \in \uparrow,\downarrow$ or equivalently $s_i \in 0,1$). The bond index α_i ranges from 1 to the *bond dimension* m, which controls the amount of entanglement retained. The tensor $\Gamma[i]^{s_i}_{\alpha_{i-1}\alpha_i}$ is a rank-3 tensor associated with site i, and $\Lambda[i]_{\alpha_i}$ is a rank-1 tensor containing the Schmidt coefficients between sites i and $i+1$.

Similarly, an MPO can be expressed as:

$$\hat{O} = \sum_{\vec{s},\vec{s}'}\sum_{\vec{\alpha}} \Gamma[1]^{s_1 s'_1}_{\alpha_1}\Lambda[1]_{\alpha_1}\Gamma[2]^{s_2 s'_2}_{\alpha_1\alpha_2}\Lambda[2]_{\alpha_2}\cdots\Gamma[N]^{s_N s'_N}_{\alpha_N}|s_1,\ldots,s_N\rangle\langle s'_1,\ldots,s'_N|. \tag{2.61}$$

Working with a large number of tensors quickly becomes algebraically cumbersome due to the proliferation of indices. To address this, a graphical notation—known as tensor network diagrams—offers an intuitive and powerful visualization tool. The basic rules for this diagrammatic notation are:

- Tensors are represented as shapes (typically filled or shaded), and indices appear as lines extending from these shapes.

- Connecting two index lines represents a contraction, i.e., a summation over the shared index.

Figure 14(a) illustrates examples of tensors represented using diagrammatic notation. Basic tensor operations, such as *contraction*, are shown in Fig. 14(b). A closed loop in these diagrams indicates a trace over a contracted index, as exemplified in Fig. 14(c), which depicts the trace of a single tensor.

Figure 14 – (a) Examples of tensors represented in diagrammatic (graphical) notation, where each leg corresponds to a tensor index. (b) Basic tensor operations such as contraction, represented by joining legs corresponding to summed indices. (c) A closed loop indicating a trace operation, exemplified by tracing over a single tensor's indices.

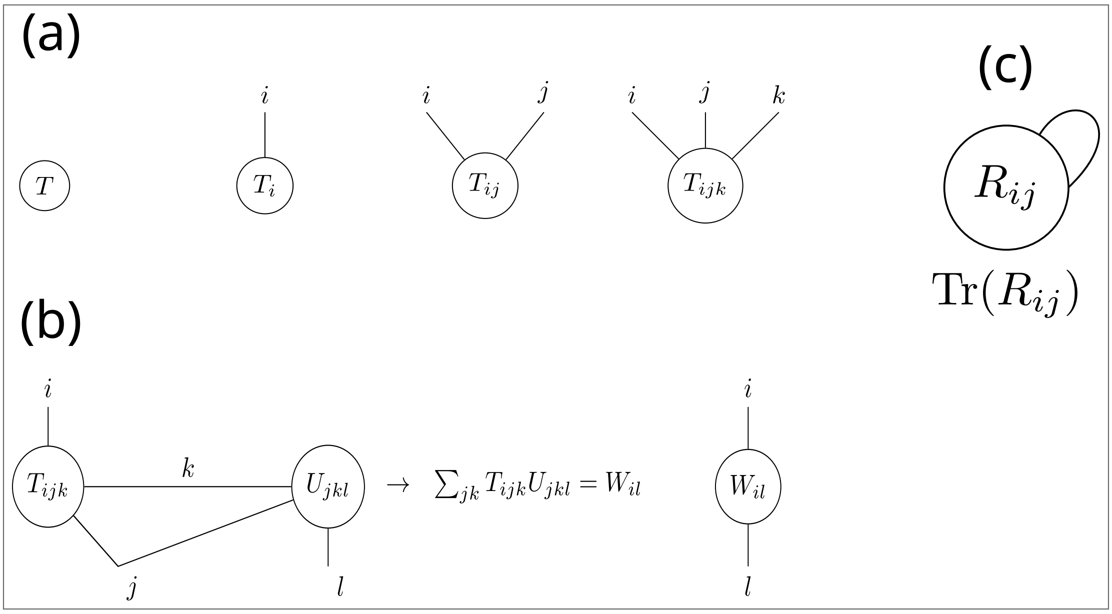

Source: The author (2025).

2.2.4 The Algorithm

The modern formulation of DMRG is grounded in tensor network theory, particularly through the use of the MPS and MPO representations [109, 113–116]. The objective is to determine the MPS that minimizes the variational energy:

$$E = \frac{\langle\Psi|\hat{\mathcal{H}}|\Psi\rangle}{\langle\Psi|\Psi\rangle}. \tag{2.62}$$

The algorithm proceeds through the following steps:

- **Initialization**

  - Initialize the system with a trial MPS of small bond dimension m.
  - Represent the Hamiltonian $\hat{\mathcal{H}}$ as an MPO.

- **Sweeping Procedure**

  The optimization is performed by successively updating the MPS tensors in a local basis:

  - Select a pair of neighboring sites within the MPS.
  - Contract the surrounding MPS tensors and the MPO to construct an effective Hamiltonian $\hat{\mathcal{H}}_{\mathrm{eff}}$ acting on the selected sites.
  - Solve the eigenvalue problem

    $$\hat{\mathcal{H}}_{\mathrm{eff}}|\Psi_{\mathrm{opt}}\rangle = E_{\mathrm{min}}|\Psi_{\mathrm{opt}}\rangle, \tag{2.63}$$

    typically using iterative methods such as Lanczos or Davidson [117], to obtain the locally optimal state $|\Psi_{\mathrm{opt}}\rangle$.
  - Apply a Schmidt decomposition to $|\Psi_{\mathrm{opt}}\rangle$ using SVD, and retain only the leading Schmidt coefficients to update the MPS tensors.
  - Shift the optimization window to the next site pair and repeat the process, sweeping from left to right and then from right to left (completing a full sweep).
  - Continue the sweeping procedure until the energy E converges within a desired threshold.

The use of the Schmidt decomposition allows for systematic truncation of the bond dimension by discarding small singular values. This adaptive truncation ensures that computational resources are focused on the most relevant entanglement degrees of freedom.

The overall procedure can also be represented diagrammatically. Figure 15 provides a schematic summary of the DMRG algorithm in tensor network notation:

Figure 15 – (a) The left MPS $|\Psi\rangle$ (orange) and the Hamiltonian $\hat{\mathcal{H}}$ as an MPO (blue) are shown as tensor networks, with physical indices d and bond dimensions m_i annotated. (b) The variational problem $\langle\Psi|\hat{\mathcal{H}}|\Psi\rangle = E\langle\Psi|\Psi\rangle$ is represented diagrammatically. (c) Two adjacent sites (green) are selected for local optimization. The problem is reformulated as an eigenvalue equation, and redundant contractions are eliminated by exploiting gauge freedom. (d) Instead of evaluating the full network, left and right environments are pre-contracted, allowing efficient optimization of the two-site tensor (orange) via the Davidson algorithm. (e) The optimized tensor is factorized using SVD, truncated to bond dimension m_j, and the singular values are absorbed according to the sweep direction to preserve orthogonality.

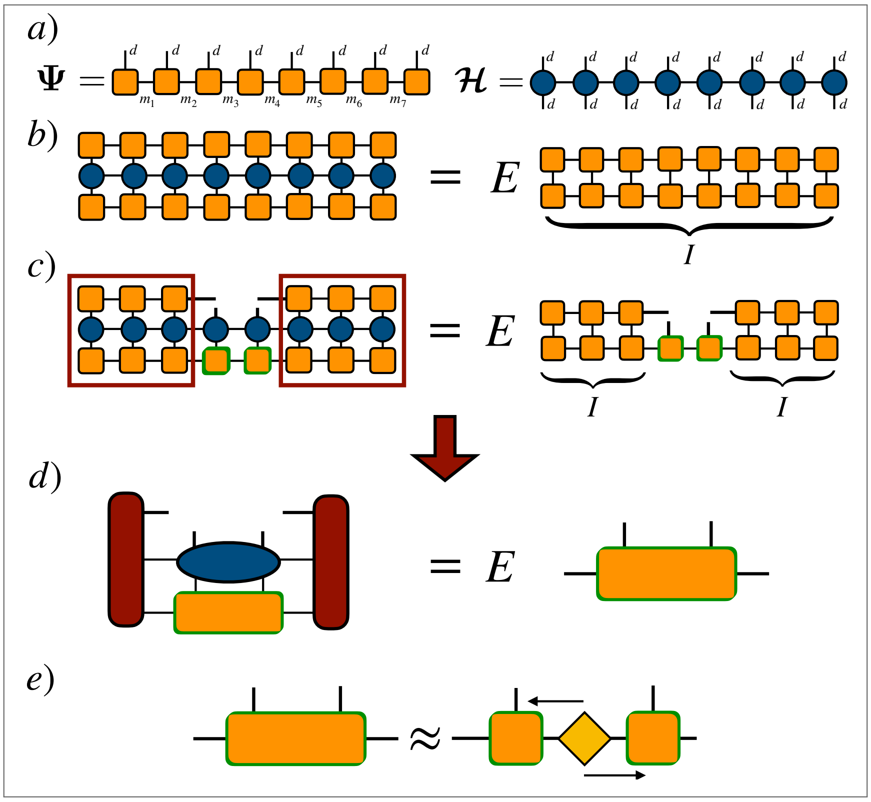

Source: Reference [116]

2.3 APPLYING DMRG TO 2D SYSTEMS

Any 2D spin model can be mapped onto a 1D chain by introducing long-range interactions. This reformulation allows the application of DMRG to 2D systems, albeit with significantly greater computational challenges and typically lower accuracy than in the 1D case. Figure 16 shows two examples of constructing a 1D path within a 2D lattice.

The absence of a unique mapping complicates this extension. Different paths induce different interaction ranges, and the resulting computational cost is highly sensitive to the chosen layout. Optimal mappings depend on both lattice geometry and the structure of interactions.

Despite these challenges, the computational cost of DMRG in 2D scales exponentially

Figure 16 – (a) and (b) represents two forms of make a linear path in a 2D system.

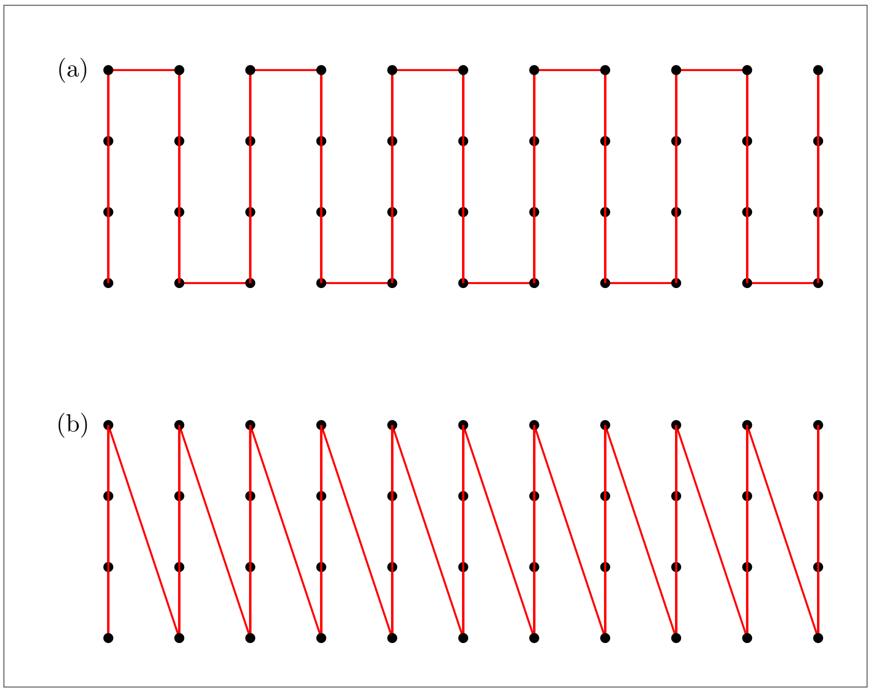

Source: The author (2025).

with the system width—rather than the total number of sites as in exact diagonalization—making moderate-width cylinders or strips feasible. In practice, the scaling prefactor can be favorable. Notably, even in the absence of a sign problem, DMRG often yields results with accuracy comparable to that of *Quantum Monte Carlo* methods [118]. The method has been successfully applied to various 2D lattices, including triangular [118–120], kagome [121, 122], and square lattices [123, 124].

2.3.1 Convergence

A reliable DMRG study of a 2D system requires multiple, independent calculations across different system sizes and parameter regimes. To extract meaningful insight into the true 2D behavior, each ground state must be computed with high precision and thoroughly characterized. Two main factors can prevent DMRG from identifying the true ground state: (i) an insufficient number of retained states after truncation, leading to a poor approximation of the wavefunction; and (ii) convergence to a metastable state due to the variational nature of the algorithm [125].

Convergence is typically assessed by increasing the number of states kept until the energy and key observables stabilize within a chosen tolerance. This can be achieved by fixing the bond dimension m, by imposing a target truncation error, or by combining both. In practice, it is often effective to set a target truncation error alongside a minimum and maximum m. The minimum m is particularly important, as truncation errors can be misleading at low bond dimensions and may result in slow or false convergence.

To mitigate metastability, it is advantageous to initialize the simulation with a wavefunction that closely approximates the true ground state. However, finding such an initial state can be nontrivial, especially for unfamiliar systems. Preliminary calculations on smaller systems or at low m—where DMRG is more controlled—can help identify dominant correlations that guide the construction of an appropriate initial guess.

For systems with conventional symmetry breaking (e.g., antiferromagnets on bipartite lattices), a Néel state often serves as a suitable starting point. For more complex orders, an initial wavefunction can be prepared using a modified Hamiltonian with symmetry-breaking "pinning" fields [126]. For example, to favor a valence bond solid, one can add local terms of the form $\lambda \hat{\mathbf{S}}_i \cdot \hat{\mathbf{S}}_j$ between selected pairs (i, j), as illustrated in Fig. 17. The pinning strength λ is then gradually reduced during the sweeps, allowing the system to relax toward the true ground state.

Figure 17 – Results of a DMRG calculation for the Heisenberg model on a 16 × 8 cylinder with antiferromagnetic order pinned at the open boundaries. To work in the strong pinning limit, it is useful to imagine the finite system embedded within a larger system acted on by an infinitely strong field (shown here as the shaded regions). The pinning fields at the physical edges are determined by the Hamiltonian bonds connecting the real and fictitious system.

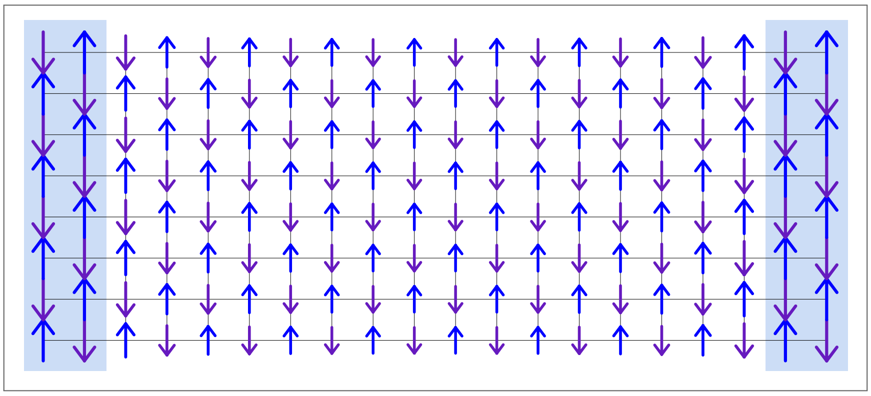

Source: Reference [126]

For complex lattices or phases with large unit cells, exploring alternative DMRG paths can reduce the risk of metastability and the required bond dimension. Since DMRG more efficiently captures entanglement along bonds that remain short-range in the 1D mapping, the choice of path significantly influences performance. In favorable cases, a well-designed path can represent nontrivial initial states, such as valence bond solids, exactly with modest m. Furthermore, observing consistent results across different paths strongly suggests convergence to the true ground state, rather than a metastable configuration.

2.3.2 Gaps and Excited States

In addition to ground state properties, the study of elementary excitations is crucial for phase classification, stability analysis, and the computation of experimentally relevant quantities. A central objective in this context is the determination of the energy gap to the first excited state.

Two main strategies exist for computing excited states and energy gaps within DMRG. When the excited state resides in a different quantum number sector than the ground state—as in spin gap calculations for magnetic systems—DMRG can directly target the lowest-energy state in the desired sector by exploiting quantum number conservation. This method is generally preferred unless the excitation becomes localized at the system's boundaries, which can be verified by inspecting local observables. In such cases, alternative techniques such as restricted sweeping may be more suitable.

For excitations within the same quantum number sector as the ground state (e.g., singlet excitations), or in systems lacking conserved quantities, DMRG can target multiple low-lying eigenstates simultaneously. This involves maintaining distinct superblock wavefunctions for each state while sharing common boundary blocks. However, accurately representing multiple states within a single truncated basis typically requires a larger bond dimension than for single-state calculations.

In scenarios such as topological phases with large ground state degeneracies and no relevant conserved quantum numbers, these standard methods can become inefficient. In such cases, the flexibility of the MPS and MPO formalisms proves advantageous. By representing states as MPSs, one can compute full wavefunctions and perform overlap calculations between independently obtained states, enabling a more robust exploration of the low-energy manifold.

2.3.3 Boundary Conditions

Boundary conditions play a crucial role in determining local observables, such as the site-resolved magnetization $\langle \hat{S}_i^z \rangle$. *Open Boundary Condition* (OBC), the most commonly used scheme, introduces finite-size effects due to the absence of neighbors at the edges, leading to asymmetric interactions. To mitigate such edge effects, *Periodic Boundary Condition* (PBC) can be employed by connecting the first and last sites, thereby preserving translational invariance. This makes PBC more suitable for studying bulk properties and performing reliable finite-size extrapolations, even in smaller systems.

A compromise between these two extremes is offered by *Cylindrical Boundary Condition* (CBC), which applies periodicity in one direction while keeping the other open. This is particularly effective for ladder or quasi-1D geometries, as it reduces edge effects while limiting entanglement growth, thus remaining more computationally tractable than full PBC. Although CBC still retains some boundary influence, it often yields more accurate bulk properties than OBC.

Nevertheless, both PBC and CBC come with increased computational cost. Reaching the same level of accuracy as with OBC typically requires a significantly larger bond dimension m, often scaling as m^2 [109, 127], due to the need to capture nonlocal entanglement—particularly between distant sites connected by periodicity. In practice, CBC demands a smaller m than PBC, though the precise scaling depends on the specific model and system size.

Boundary conditions also influence the physical interpretation of numerical results. In systems exhibiting spontaneous symmetry breaking, OBC can stabilize symmetry-broken states through boundary-induced asymmetry, facilitating their detection. In contrast, PBC enforces global symmetry, which may obscure such phases or mix degenerate ground states. The effectiveness of CBC in revealing symmetry breaking is system dependent; it may either preserve or suppress such features, depending on the geometry and correlations of the model under study.

2.4 COMPUTATIONAL METHODOLOGY

Implementing the DMRG algorithm from scratch is no longer necessary, thanks to several efficient and well-tested library implementations. These frameworks streamline DMRG simulations to the task of specifying the appropriate model and computational parameters. This section outlines the tools employed in this work.

2.4.1 ALPS

The *Algorithms and Libraries for Physics Simulations* (ALPS) project [128–130] provides a comprehensive software suite for simulating correlated quantum systems. It supports a variety of numerical methods, including Classical and Quantum Monte Carlo, Exact Diagonalization, and DMRG.

To define a simulation, the following components must be specified:

- **Lattice**: The geometric structure of the system.
- **Degrees of Freedom**: The local Hilbert space and the operators acting on it.
- **Model**: The Hamiltonian, defined in terms of the available operators.
- **Measurements**: The observables to be computed.
- **Simulation Parameters**: Numerical settings controlling the simulation.

Standard lattices and Hamiltonians are predefined in the `lattices.xml` and `models.xml` files. Once the system is specified via the ALPS interface, a standardized input file is generated. This file can then be used with various ALPS solvers, including Exact Diagonalization, DMRG, and Quantum Monte Carlo. Additionally, ALPS provides tools for data analysis and visualization, along with a graphical interface via *VisTrails*, which improves transparency and reproducibility.

While many parameters are shared across ALPS applications, DMRG simulations require several specific inputs:

- **NUMBER_EIGENVALUES**: The number of eigenstates and energies to compute (default is 1; set to 2 when computing energy gaps).
- **SWEEPS**: The number of DMRG sweeps to perform.
- **MAXSTATES**: The maximum number of retained states. The bond dimension increases with each sweep up to this limit.
- **CONSERVED_QUANTUMNUMBERS**: The set of quantum numbers conserved by the model. These allow matrix block-diagonalization for improved performance. If not specified, the simulation assumes a grand canonical ensemble.

Additional parameters exist but typically require no modification. A practical example of defining and running a DMRG simulation using ALPS is provided in Code 1.

Code 1 – A typical Python setup script for running DMRG simulations in ALPS.

```python
import pyalps
import numpy as np
import matplotlib.pyplot as plt
import pyalps.plot

#prepare the input parameters
parms = [{
        'LATTICE'                     : "open ladder frustrated",
        'MODEL'                       : "spin",
        'CONSERVED_QUANTUMNUMBERS'    : 'N,Sz',
        'Sz_total'                    : 0,
        'J0'                          : 1,
        'J1'                          : 0.55,
        'J2'                          : 0.44,
        'SWEEPS'                      : 10,
        'NUMBER_EIGENVALUES'          : 1,
        'MAXSTATES'                   : 500,
        'L'                           : 128
    } ]


input_file = pyalps.writeInputFiles('parm_local_mag_open_frustrated64_44',parms)
res = pyalps.runApplication('dmrg',input_file,writexml=True)
```

Source: The author (2025)

2.4.2 ITensor

ITensor [113] is a tensor library inspired by tensor diagram notation. Its design philosophy emphasizes translating tensor diagrams directly into code, minimizing the need for auxiliary concepts. For instance, summing two ITensors requires only that they share the same indices—regardless of order—with index matching and contraction handled automatically.

Unlike ALPS, which operates largely as a black box with predefined lattices and models, ITensor provides greater flexibility, allowing detailed customization of models and simulations. It includes DMRG implementations based on the MPS formalism and supports both C++ and Julia. This work uses the Julia version.

The DMRG parameters from ALPS carry over to ITensor with some renaming—for example, “max states kept” corresponds to the “maximum bond dimension.” A typical DMRG simulation in ITensor involves defining lattice sites, constructing the Hamiltonian, specifying algorithmic parameters, and executing the code.

As an illustrative example, consider a 1D spin–$\frac{1}{2}$ chain of N sites governed by the Heisenberg Hamiltonian:

$$\hat{\mathcal{H}} = J \sum_{i=1}^{N-1} \hat{\mathbf{S}}_i \cdot \hat{\mathbf{S}}_{i+1} = J \sum_{i=1}^{N-1} \left[\hat{S}_i^z \hat{S}_{i+1}^z + \frac{1}{2} \left(\hat{S}_i^+ \hat{S}_{i+1}^- + \hat{S}_i^- \hat{S}_{i+1}^+ \right) \right]. \tag{2.64}$$

The workflow in ITensor typically consists of the following steps:

- **Create Sites**: Use `siteinds("S=1/2", N; conserve_qns=false)` to define N spin–$\frac{1}{2}$ sites. Setting `conserve_qns=false` indicates that quantum numbers such as total S^z are not conserved.

- **Construct the Hamiltonian**: Define the operator sum using ITensor’s `OpSum`/`AutoMPO` system. The `OpSum` interface provides a high-level language to specify sums of local operators, which `AutoMPO` compiles into an MPO representation.

Code 2 – Creation of the Hamiltonian (2.64) using the OpSum system.

```
os = OpSum()

for i = 1:N-1
    os += J, "Sz", j, "Sz", j+1
    os += J/2, "S+", j, "S-", j+1
    os += J/2, "S-", j, "S+", j+1
end
```

Source: The author (2025)

- **Convert to MPO**: Use `MPO(os, sites)` to convert the operator sum into an MPO.

- **Initialize the State**: For simulations without conserved quantities, initialize the state with `randomMPS(sites)`. If quantum number conservation is enabled, use `productMPS(sites, state)` to specify an initial product state explicitly.

- **Set DMRG Parameters and Run**: Define algorithmic parameters such as the number of sweeps and bond dimension, then execute the simulation.

A complete code example is provided in:

Code 3 – The following code provides a basic illustration of setting up a one-dimensional spin-1/2 chain using ITensor in Julia. While this example is simplified for clarity, a typical implementation would include additional commands to compute local quantities and utilize packages to save the output data.

```julia
using ITensors

function heisenberg(J,N,n_sweeps,n_maxdim)
    sites = siteinds("S=1/2",N;conserve_qns = false)
    os = OpSum()
  for j=1:N-1
    os += J,"Sz",j,"Sz",j+1
    os += J/2,"S+",j,"S-",j+1
    os += J/2,"S-",j,"S+",j+1
  end
    H = MPO(os,sites)
    psi0 = randomMPS(sites)
    sweeps = Sweeps(n_sweeps)
    setmaxdim!(sweeps,maxdim)
    setcutoff!(sweeps,1E-10)
    noise!(sweeps,1E-5,1E-5,1E-8,1E-8,1E-10,1E-12,0)
    energy, psi = dmrg(H,psi0, sweeps)
    println(" energy = $energy")
    return energy, psi
end
    energy, psi = heisenberg(J,N,sweeps,maxdim)
```

Source: The author (2025)

A key feature of ITensor is its `OpSum`/`AutoMPO` system, which offers an intuitive and flexible interface for building Hamiltonians. This contrasts with ALPS, which requires editing structured XML files such as `lattices.xml` and `models.xml`. In ITensor, the geometry is implicitly defined by the pattern of site interactions. For example, in the ladder geometry of Fig. 16(a), interactions like $J_{\perp}\hat{\mathbf{S}}_1 \cdot \hat{\mathbf{S}}_2$ (rungs) and $J_{\parallel}\hat{\mathbf{S}}_1 \cdot \hat{\mathbf{S}}_8$ (legs) are defined directly from site indexing.

ITensor provides prebuilt site types such as spin–$\frac{1}{2}$ and spin–1, specified via `"S=1/2"` or `"S=1"` in `siteinds`. For higher spin values or custom models, users must define site objects and operator sets manually. The library also supports a variety of physical degrees of freedom, including electrons, bosons, and fermions; see [113] for further details.

2.4.3 Our Approach

This work employs both ALPS and, primarily, *ITensor* to compute ground-state properties of the studied models. A central element of the methodology is the use of the *cut-off* parameter, which dynamically controls the retained bond dimension during DMRG sweeps. Since the required bond dimension is typically unknown a priori, this adaptive strategy ensures that the simulation maintains the desired accuracy while optimizing computational efficiency.

Another important parameter is the *noise*, which introduces small perturbations during early sweeps to improve convergence, particularly in models with complex energy landscapes. This helps avoid metastable configurations by promoting exploration of the variational space. The noise is initially set to 10^{-5} and progressively reduced over the course of the sweeps [113].

The adopted methodology consists of the following key elements:

- **Bond Dimension and Cutoff**: A maximum bond dimension of 3000 is allowed per sweep. The cutoff parameter ensures that only the minimum number of states necessary to achieve the target accuracy is retained.

- **Cutoff Values**: For low-dimensional systems (e.g., chains and two-leg ladders), cutoff values in the range of 10^{-8} to 10^{-10} are employed. For more complex or effectively higher-dimensional systems, such as multi-leg ladders, the cutoff is relaxed to the range of 10^{-6} to 10^{-7}.

- **Initial State**: A Néel state is typically used as the initial state in AFM models. In some cases, a random initial state is adopted to avoid bias and improve convergence.

- **Extrapolation to the Thermodynamic Limit**: Linear extrapolation is performed using results for systems of lengths L, $3L/2$, and $2L$, providing estimates for the thermodynamic limit.

- **Boundary Conditions**: All simulations are carried out with open boundary conditions.

3 QUANTUM MAGNETISM IN LOW DIMENSIONS

The study of low-dimensional magnetic systems, particularly those constrained to 1D, has evolved into a highly active and insightful area of research. These systems offer a fertile ground for investigating quantum ground states, excitation spectra, exotic phases of matter, and the intricate interplay between quantum and thermal fluctuations. From a theoretical standpoint, 1D magnetism is remarkably rich, serving as an ideal testbed for a broad range of analytical and numerical approaches. These include exact solutions (such as the Bethe ansatz and mappings to fermionic models), quantum field-theoretical techniques (e.g., conformal field theory and bosonization), many-body formulations (including hardcore boson representations), perturbative expansions (notably high-order series techniques), and powerful numerical methods such as exact diagonalization—either via full spectrum computations or restricted to low-lying eigenstates using the Lanczos algorithm—alongside the DMRG and quantum Monte Carlo simulations.

A defining characteristic of 1D magnetism is the profound and sustained synergy between theoretical predictions and experimental observations. The early 1980s marked a pivotal moment in the field with groundbreaking theoretical contributions: Faddeev and Takhtajan revealed the spinon nature of excitations in the spin–$\frac{1}{2}$ HAF chain [131], while Haldane established a fundamental dichotomy between half-integer and integer spin chains, now known as the Haldane conjecture [19, 20]. These seminal works reignited interest in quasi-1D magnetic materials and catalyzed substantial developments in experimental techniques aimed at probing low-dimensional quantum magnets.

3.1 LUTTINGER LIQUID

Quantum magnets confined to one spatial dimension (1D) exhibit a rich interplay between strong correlations and enhanced quantum fluctuations, leading to physical behavior that markedly deviates from that of higher-dimensional systems. A unifying theoretical framework for describing the low-energy properties of such systems is provided by the Tomonaga-Luttinger liquid (*Luttinger Liquid* (LL)) theory [132, 133]. Initially developed in the context of interacting fermions, LL theory has been successfully extended to spin chains through bosonization techniques, whereby spin operators are mapped onto bosonic fields that represent collective excitations.

This formalism accounts for hallmark features of 1D quantum systems, such as power-law decaying correlation functions, fractionalized excitations (e.g., spinons), and universal low-energy behavior that transcends microscopic details. In particular, it captures the critical behavior of paradigmatic models like the spin–$\frac{1}{2}$ HAF chain, where the conventional Fermi liquid theory fails. The LL paradigm thus provides a coherent and robust description of a broad class of gapless 1D quantum fluids, encompassing both fermionic and bosonic systems, as well as spin chains.

3.1.1 Density Operator and Bosonization

Consider a one-dimensional system of particles located at positions x_i. The microscopic density operator is defined as:

$$\rho(x) = \sum_i \delta(x - x_i). \tag{3.1}$$

To describe the system in the continuum limit, we introduce a smooth and monotonically increasing field $\phi(x)$, constrained such that $\phi(x_i) = 2\pi i$ at the particle positions. In terms of this field, the density operator becomes:

$$\rho(x) = \sum_i \delta(\phi(x) - \phi(x_i))|\nabla\phi(x)|. \tag{3.2}$$

Employing the Poisson summation formula, the density can be rewritten as:

$$\rho(x) = \frac{|\nabla\phi(x)|}{2\pi} \sum_p e^{ip\phi(x)}. \tag{3.3}$$

Introducing a field $\Phi(x)$ associated with deviations from a uniform background density ρ_0, we define:

$$\phi(x) = 2(\pi\rho_0 x - \Phi(x)), \tag{3.4}$$

which yields the expression:

$$\rho(x) = \left[\rho_0 - \frac{1}{\pi}\nabla\Phi(x)\right] \sum_p \exp\left(2ip(\pi\rho_0 x - \Phi(x))\right). \tag{3.5}$$

At length scales much larger than the interparticle spacing, oscillatory contributions with $p \neq 0$ average out, leading to the smooth approximation:

$$\rho(x) \approx \rho_0 - \frac{1}{\pi}\nabla\Phi(x). \tag{3.6}$$

Since the density operators at distinct positions commute, it follows that $\Phi(x)$ is a self-commuting bosonic field.

3.1.2 Particle Creation Operators

The particle creation operator in the bosonized description takes the general form:

$$\hat{\psi}^\dagger(x) = \sqrt{\hat{\rho}(x)} e^{-i\hat{O}(x)}, \tag{3.7}$$

where the operator $\hat{O}(x)$ is chosen to ensure that the appropriate (anti)commutation relations are satisfied. For bosonic particles, the canonical commutation relation,

$$[\hat{\psi}_B(x), \hat{\psi}_B^\dagger(x')] = \delta(x - x'), \tag{3.8}$$

requires:

$$\left[\hat{\rho}(x), e^{-i\hat{O}(x')}\right] = \delta(x - x') e^{-i\hat{O}(x')}. \tag{3.9}$$

Using Eq. (3.6), this relation is fulfilled if:

$$\left[\frac{1}{\pi}\nabla\hat{\Phi}(x), \hat{O}(x')\right] = -i\delta(x - x'). \tag{3.10}$$

Thus, the bosonic creation operator becomes:

$$\hat{\psi}_B^\dagger(x) \propto \sqrt{\rho_0 - \frac{1}{\pi}\nabla\hat{\Phi}(x)} \sum_p \exp\left(2ip(\pi\rho_0 x - \hat{\Phi}(x))\right) e^{-i\hat{O}(x)}. \tag{3.11}$$

In the fermionic case, anticommutation relations must be enforced. Exploiting the fact that $e^{i\phi(x)/2}$ alternates in sign at particle positions, the fermionic creation operator is constructed as:

$$\begin{aligned} \hat{\psi}_F^\dagger(x) &= \hat{\psi}_B^\dagger(x) e^{i\phi(x)/2} \\ &\propto \sqrt{\rho_0 - \frac{1}{\pi}\nabla\hat{\Phi}(x)} \sum_p \exp\left(i(2p+1)(\pi\rho_0 x - \hat{\Phi}(x))\right) e^{-i\hat{O}(x)}. \end{aligned} \tag{3.12}$$

These operators effectively describe excitations in the continuum limit and are especially suited for analyzing the asymptotic properties of correlation functions.

3.1.3 Luttinger Liquid Hamiltonian

The universal low-energy physics of gapless one-dimensional systems is captured by the effective Hamiltonian [134]:

$$\hat{\mathcal{H}} = \frac{uK}{2\pi} \int \left[(\pi \Pi(x))^2 + \frac{1}{K^2} (\nabla \Phi(x))^2 \right] dx, \tag{3.13}$$

where $\Phi(x)$ is the bosonic field introduced above, and $\Pi(x)$ is its conjugate momentum. The parameters u and K represent the excitation velocity and the Luttinger parameter, respectively, and fully characterize the low-energy behavior of the system [135]. Analogous to the role of quasiparticle mass and interaction strength in Fermi liquid theory, these parameters encode the effects of interactions and collective behavior in 1D systems.

The LL framework describes systems with a gapless excitation spectrum and power-law correlation functions, whose exponents depend non-universally on the value of K [136, 137]. For a system with average density ρ_0, the density-density correlation function assumes the form [138]:

$$\langle \delta\rho(x,\tau) \delta\rho(0) \rangle = \frac{1}{r^2} + A_2 \cos(2\pi\rho_0 x) \left(\frac{1}{r} \right)^{2K} + A_4 \cos(4\pi\rho_0 x) \left(\frac{1}{r} \right)^{8K} + \cdots, \tag{3.14}$$

where $\delta\rho(x) = \rho(x) - \rho_0$, $r = \sqrt{x^2 + (u\tau)^2}$, and A_n are non-universal, model-dependent amplitudes. This expression highlights the quasi-long-range order and scale-invariant nature of the LL phase, governed entirely by the parameters u and K.

3.2 LINEAR SPIN CHAIN

The linear spin chain is one of the most fundamental models in quantum magnetism, yet it displays a remarkably rich variety of physical phenomena. Despite its apparent simplicity, it captures essential features of strong correlations and quantum fluctuations that also appear in higher-dimensional systems. Linear spin chains serve as paradigmatic platforms for both theoretical investigations and experimental realizations, including implementations in cold-atom setups and magnetic materials.

In this section, we focus on chains with nearest-neighbor AFM interactions. The corresponding Hamiltonian is given by:

$$\hat{\mathcal{H}} = J \sum_i \hat{\mathbf{S}}_i \cdot \hat{\mathbf{S}}_{i+1} = J \sum_i \left(\hat{S}_i^x \hat{S}_{i+1}^x + \hat{S}_i^y \hat{S}_{i+1}^y + \hat{S}_i^z \hat{S}_{i+1}^z \right), \tag{3.15}$$

where $J > 0$ denotes the AFM coupling strength, and the model corresponds to the 1D isotropic Heisenberg chain.

Using the spin ladder operators, $\hat{S}_i^{\pm} = \hat{S}_i^x \pm i\hat{S}_i^y$, the Hamiltonian can be rewritten as:

$$\hat{\mathcal{H}} = J \sum_i \left(\hat{S}_i^z \hat{S}_{i+1}^z + \frac{1}{2} \left(\hat{S}_i^+ \hat{S}_{i+1}^- + \hat{S}_i^- \hat{S}_{i+1}^+ \right) \right), \tag{3.16}$$

subject to the standard angular momentum commutation relations:

$$[\hat{S}_i^z, \hat{S}_j^{\pm}] = \pm \delta_{ij} \hat{S}_j^{\pm}, \quad [\hat{S}_i^+, \hat{S}_j^-] = 2\delta_{ij} \hat{S}_j^z. \tag{3.17}$$

A landmark result for spin chains is Haldane's conjecture (1983) [19, 20], which predicts fundamentally different ground-state properties depending on whether the spin quantum number S is integer or half-integer:

- **Integer spin** ($S = 1, 2, \ldots$): The system possesses a finite excitation gap (the Haldane gap) above the ground state, and spin-spin correlations decay exponentially, indicating short-range magnetic order.

- **Half-integer spin** ($S = \frac{1}{2}, \frac{3}{2}, \ldots$): The spectrum is gapless, with a continuum of low-energy excitations and power-law decaying spin correlations characteristic of critical behavior.

This distinction underscores the role of quantum statistics and topological effects in 1D systems and has profound implications for both theory and experiment. The spin–$\frac{1}{2}$ Heisenberg chain, in particular, serves as a prototype of a gapless quantum critical system described by LL theory (see Section 3.1).

3.2.1 Spin–$\frac{1}{2}$ Chain

For a single spin–$\frac{1}{2}$ site, with $\hbar = 1$, the spin operators in the z-basis are represented by the matrices:

$$\hat{S}^z = \frac{1}{2} \begin{pmatrix} 1 & 0 \\ 0 & -1 \end{pmatrix}, \quad \hat{S}^+ = \begin{pmatrix} 0 & 1 \\ 0 & 0 \end{pmatrix}, \quad \hat{S}^- = \begin{pmatrix} 0 & 0 \\ 1 & 0 \end{pmatrix}, \tag{3.18}$$

which act on the basis states $|\uparrow\rangle$ and $|\downarrow\rangle$ as:

$$\begin{aligned} \hat{S}^z|\uparrow\rangle &= \frac{1}{2}|\uparrow\rangle, \quad \hat{S}^+|\uparrow\rangle = 0, \quad \hat{S}^-|\uparrow\rangle = |\downarrow\rangle, \\ \hat{S}^z|\downarrow\rangle &= -\frac{1}{2}|\downarrow\rangle, \quad \hat{S}^+|\downarrow\rangle = |\uparrow\rangle, \quad \hat{S}^-|\downarrow\rangle = 0. \end{aligned} \tag{3.19}$$

In a chain of L spin-$\frac{1}{2}$ sites, local operators are defined via tensor products, such as $\hat{S}_i^z = \mathbb{I} \otimes \cdots \otimes \hat{S}^z \otimes \cdots \otimes \mathbb{I}$. Consider the fully polarized ferromagnetic state:

$$|\Psi_0\rangle = |\uparrow\uparrow \cdots \uparrow\rangle. \tag{3.20}$$

Under periodic boundary conditions, $\hat{S}_{L+1}^z \equiv \hat{S}_1^z$, the Hamiltonian from Eq. (3.16) yields:

$$\hat{\mathcal{H}}|\Psi_0\rangle = J \sum_i \hat{S}_i^z \hat{S}_{i+1}^z |\Psi_0\rangle = \frac{JL}{4}|\Psi_0\rangle = E_0|\Psi_0\rangle, \quad E_0 = \frac{JL}{4}. \tag{3.21}$$

For AFM coupling ($J > 0$), this state corresponds to the highest-energy eigenstate; conversely, for ferromagnetic coupling ($J < 0$), it represents the ground state.

Excited states with n down spins (magnons) are obtained by applying spin-lowering operators to $|\Psi_0\rangle$:

$$|n_1, n_2, \ldots, n_L\rangle = \prod_i (\hat{S}_i^-)^{n_i} |\Psi_0\rangle, \quad \sum_i n_i = n, \quad n_i \in 0, 1. \tag{3.22}$$

A general n-magnon state takes the form:

$$|\Psi\rangle = \sum_{n_1,\ldots,n_L} C_{n_1,\ldots,n_L} |n_1, n_2, \ldots, n_L\rangle. \tag{3.23}$$

The Bethe Ansatz [139] postulates that the coefficients $C_{n_1,\ldots,n_L}$ follow a plane-wave form. For a single magnon, the trial wavefunction is:

$$|\Psi(p)\rangle = \sum_{n=1}^{L} e^{ipn} |n\rangle, \quad |n\rangle = |0, \ldots, 1_n, \ldots, 0\rangle. \tag{3.24}$$

To evaluate $\hat{\mathcal{H}}|\Psi(p)\rangle$, consider how its components act on $|n\rangle$. The Ising term contributes:

$$\hat{S}_i^z \hat{S}_{i+1}^z |n\rangle = \begin{cases} \frac{1}{4}|n\rangle, & \text{if } i \neq n, n-1, \\ -\frac{1}{4}|n\rangle, & \text{if } i = n-1 \text{ or } i = n. \end{cases} \tag{3.25}$$

Summing over i:

$$\sum_i \hat{S}_i^z \hat{S}_{i+1}^z |n\rangle = \left[(L-2) \cdot \frac{1}{4} - \frac{1}{4} - \frac{1}{4}\right] |n\rangle = \left(\frac{L}{4} - \frac{1}{2}\right) |n\rangle. \tag{3.26}$$

The ladder terms yield:

$$\hat{S}_i^+ \hat{S}_{i+1}^- |n\rangle = \begin{cases} |n+1\rangle, & i = n-1, \\ 0, & \text{otherwise}, \end{cases} \tag{3.27}$$

$$\hat{S}_i^- \hat{S}_{i+1}^+ |n\rangle = \begin{cases} |n-1\rangle, & i = n, \\ 0, & \text{otherwise}. \end{cases} \tag{3.28}$$

Thus,

$$\frac{1}{2}\sum_i \left(\hat{S}_i^+\hat{S}_{i+1}^- + \hat{S}_i^-\hat{S}_{i+1}^+\right)|n\rangle = \frac{1}{2}\left(|n+1\rangle + |n-1\rangle\right). \tag{3.29}$$

Applying the full Hamiltonian:

$$\begin{aligned}\hat{\mathcal{H}}|\Psi(p)\rangle &= J\sum_{n=1}^{L} e^{ipn}\left[\left(\frac{L}{4}-\frac{1}{2}\right)|n\rangle + \frac{1}{2}(|n+1\rangle + |n-1\rangle)\right] \\ &= J\left(\frac{L}{4}-\frac{1}{2}+\cos p\right)\sum_{n=1}^{L} e^{ipn}|n\rangle \\ &= E_1(p)|\Psi(p)\rangle, \end{aligned} \tag{3.30}$$

with energy:

$$E_1(p) = J\left(\frac{L}{4}-\frac{1}{2}+\cos p\right), \quad \varepsilon(p) = E_1(p) - E_0 = J(\cos p - 1). \tag{3.31}$$

For N magnons, the exact solution [139] gives:

$$E_N = -\frac{J}{2}\sum_{j=1}^{N}\frac{1}{\lambda_j^2 + 1/4}, \tag{3.32}$$

where the rapidities λ_j satisfy the Bethe equations:

$$\left(\frac{\lambda_j + i/2}{\lambda_j - i/2}\right)^L = \prod_{\substack{k=1\\k\neq j}}^{N}\frac{\lambda_j - \lambda_k + i}{\lambda_j - \lambda_k - i}, \quad j = 1,\ldots,N. \tag{3.33}$$

In the AFM ground state, the λ_j are real and symmetrically distributed around zero. In the thermodynamic limit ($L \to \infty$), they form a continuous distribution, leading to a gapless excitation spectrum.

The spin–$\frac{1}{2}$ HAF chain exemplifies a LL, exhibiting gapless excitations, power-law spin correlations, and fractionalized spinon excitations. These features are rigorously confirmed through bosonization and conformal field theory, which map the system to a Tomonaga-Luttinger liquid with Luttinger parameter $K = 1/2$ [134].

3.2.2 Numerical Results for Linear Spin Chains

For spin–$S > \frac{1}{2}$ systems, the Bethe Ansatz becomes increasingly intricate, and exact solutions are generally intractable. In such cases, Haldane's conjecture offers critical theoretical guidance. To compute thermodynamic properties of spin–S chains, the DMRG method proves highly effective, allowing accurate analysis of 1D quantum systems with moderate computational resources. Nonetheless, DMRG is limited by the maximum system size it can reliably simulate—typically $L \lesssim 1000$ sites—due to the exponential growth of the Hilbert space.

The Hilbert space dimension per site is $2S + 1$, so for a chain of L sites, the full dimension scales as $(2S + 1)^L$, or 2^L for spin–$\frac{1}{2}$. As DMRG relies on a variational optimization over matrix product states, increasing system size leads to computationally intensive operations.

To address finite-size effects, simulations are performed for various lengths and extrapolated to the thermodynamic limit ($L \to \infty$) via finite-size scaling. A commonly used ansatz for the spin gap is

$$\Delta E(L) = \Delta + \frac{a}{L} + \frac{b}{L^2}, \tag{3.34}$$

where Δ denotes the thermodynamic gap, and a and b are fitting parameters. This approach also applies to other observables such as the correlation length, entanglement entropy, and specific heat. Using Eq. (3.34), we extract the Haldane gap in the thermodynamic limit.

3.2.2.1 The Spin–$\frac{1}{2}$ and Spin–$\frac{3}{2}$ Chains

For half-integer spin chains ($S = \frac{1}{2}, \frac{3}{2}$, with $J = 1$), DMRG simulations yield the thermodynamic spin gap values shown in Fig. 18:

$$\Delta_{1/2} = 0, \quad \Delta_{3/2} = 0. \tag{3.35}$$

These results confirm Haldane's conjecture, which predicts gapless excitations for half-integer spin chains, in contrast with the gapped spectra of integer-spin chains. The gapless nature of the spin–$\frac{1}{2}$ chain is exactly verified by the Bethe Ansatz. Experimental realizations include quasi-1D compounds such as $Cs_4CuSb_2Cl_{12}$ [140], CuPzN [141], and $KCuF_3$ [142] for $S = \frac{1}{2}$, and $AgCrP_2S_6$ [143] and $CsVCl_3$ [144] for $S = \frac{3}{2}$, all belonging to the same universality class [145].

The ground states of both chains exhibit vanishing local magnetization ($\langle \hat{S}_i^z \rangle = 0$, Fig. 19), due to quantum superposition. Half-integer spins lack a $|0\rangle$ eigenstate, preventing a simple classical description. Their excitations are *spinons*—fractional quasiparticles carrying spin$-\frac{1}{2}$ [140, 146]. In the spin$-\frac{1}{2}$ HAF chain, a spin flip disrupts the singlet ground state and fractionalizes into two spinons, each with $\Delta S^z = \frac{1}{2}$. Unlike classical domain walls, spinons are delocalized and propagate freely. In finite systems, spinons appear in pairs to conserve total spin. The spin$-\frac{3}{2}$ chain also supports spinon excitations, consistent with its gapless nature. The low-energy behavior of both systems is described by the $SU(2)_1$ Wess-Zumino-Witten conformal field theory [147], confirming the deconfined spinon picture.

Figure 18 – Spin gap ΔE versus $1/L$ for a linear spin chain with open boundary conditions. Red and blue points represent DMRG results for spin-$\frac{1}{2}$ and spin-$\frac{3}{2}$ chains, respectively. Dashed lines show extrapolations to the thermodynamic limit using Eq. (3.34). The maximum truncation error is $\sim 10^{-8}$.

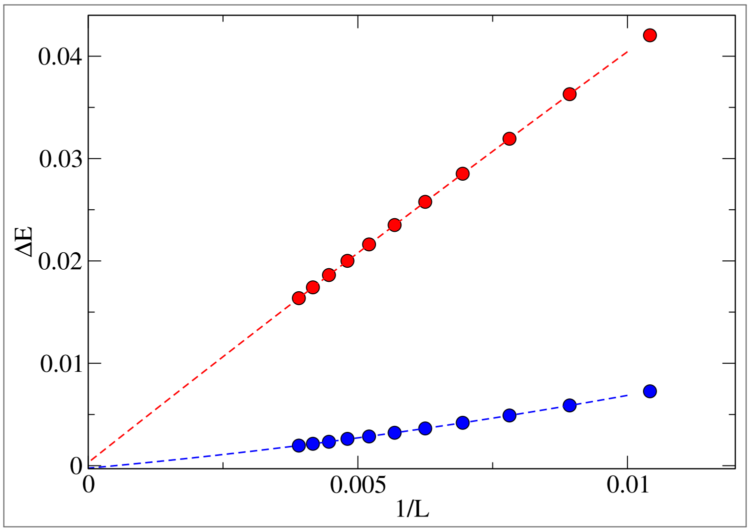

Source: The author (2025)

Figure 19 – Local magnetization of the ground state and the first two magnetic excitations in a linear spin chain with open boundary conditions, computed using DMRG. The magnetization distribution, $\langle \hat{S}^z_i \rangle$, and excitation, $\langle \Delta S^z_i \rangle_k$, are shown for the k-th excitation (e.g., $k = 1$ corresponds to a transition from $S^z_{\text{total}} = 0$ to $S^z_{\text{total}} = 1$). Panels (a.1)–(a.3) depict spin-$\frac{1}{2}$ chain; panels (b.1)–(b.3) depict spin-$\frac{3}{2}$ chain. The maximum truncation error is $\sim 10^{-8}$.

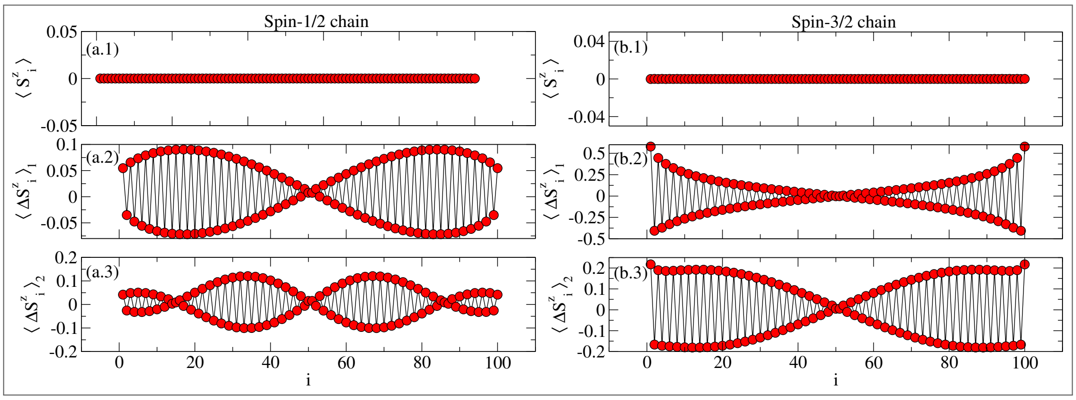

Source: The author (2025)

3.2.2.2 The Spin–1 and Spin–2 Chains

For integer-spin chains ($S = 1, 2$, with $J = 1$), DMRG results in Fig. 20 provide the following thermodynamic gaps:

$$\Delta_1 \approx 0.41, \quad \Delta_2 \approx 0.08. \tag{3.36}$$

The Haldane gap for the spin–1 chain ($\Delta_1 \approx 0.41J$) is a well-established result [148–150], experimentally observed in compounds such as NENP [23, 151, 152]. For the spin–2 chain, the gap is significantly smaller, with early DMRG estimates around $\Delta_2 \approx 0.08J$ [153–155]. The most accurate value to date, $(0.0890 \pm 0.0007)J$, was obtained by Nakano and Sakai [156]. Experimental signatures of the spin–2 Haldane gap have been reported in $\mathrm{MnCl_3(bpy)}$ [157, 158].

Figure 20 – Spin gap ΔE versus $1/L$ for a linear spin chain with open boundary conditions. Panels (a) and (b) represent DMRG results for spin-1 and spin-2 chains, respectively. Dashed lines show extrapolations to the thermodynamic limit using Eq. (3.34). The maximum truncation error is $\sim 10^{-8}$.

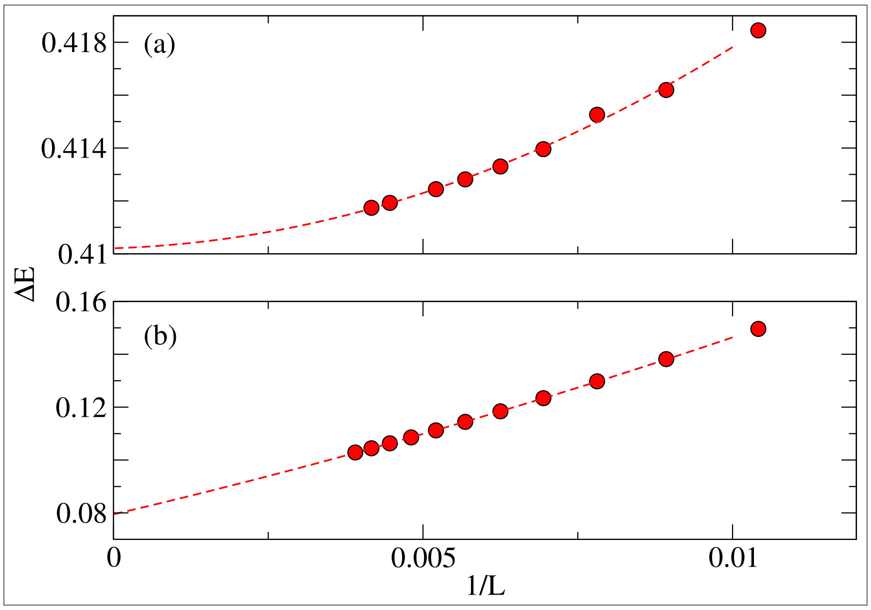

Source: The author (2025)

The spin–1 chain exhibits edge magnetization while remaining non-magnetic in the bulk, as shown in Fig. 21. In the $S^z_{\text{total}} = 0$ sector, two spin–$\frac{1}{2}$ edge states form a doublet (panel a.1). A transition to $S^z_{\text{total}} = 1$ flips one edge spin, producing a localized excitation (panel a.2). These edge states contribute to a fourfold degeneracy across $S^z_{\text{total}} = 0, \pm 1$ in the thermodynamic limit. Bulk excitations are spin–1 magnons—delocalized triplet states—with energy $\Delta_1 \approx 0.41J$, as shown in panel a.3.

Figure 21 – Local magnetization of the ground state and magnetic excitations in a linear spin chain with open boundary conditions, computed using DMRG. The magnetization distribution, $\langle \hat{S}_i^z \rangle$, and excitation, $\langle \Delta S_i^z \rangle_k$, are shown for the k-th excitation. Panels (a.1)–(a.3) depict spin-1 chain; panels (b.1)–(b.3) depict spin-2 chain. The maximum truncation error is $\sim 10^{-8}$.

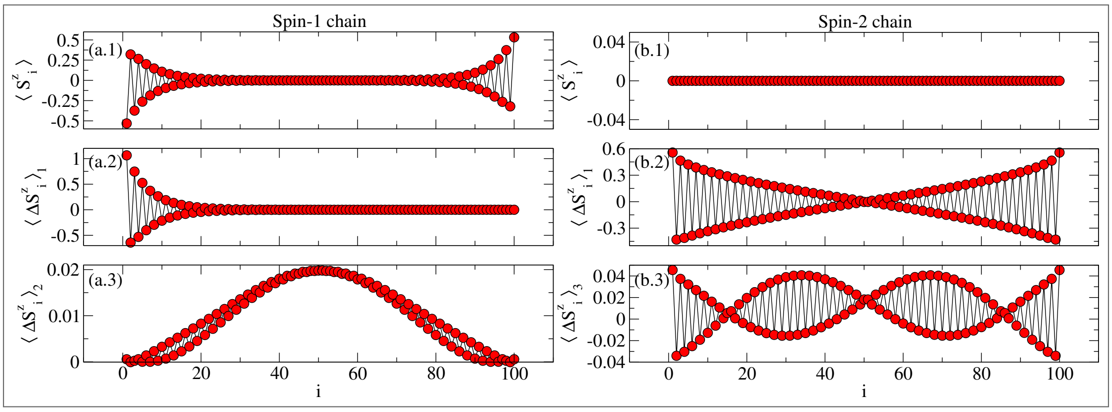

Source: The author (2025)

The ground state of spin–2 chains can differ markedly from that of spin–1 chains. A trivial product state, such as

$$|\psi\rangle = |1\rangle_1 \otimes |0\rangle_2 \otimes \cdots \otimes |-1\rangle_L, \tag{3.37}$$

is unentangled and lacks topological features. In contrast, the spin–1 Haldane phase is a highly entangled quantum state. In the *Valence-Bond Solid* (VBS) picture provided by the *Affleck-Kennedy-Lieb-Tasaki* (AKLT) model [159], each spin–1 site is represented as two symmetrized spin–$\frac{1}{2}$ particles forming singlet bonds with neighboring sites. This results in a gapped *Symmetry-Protected Topological* (SPT) phase, characterized by short-range entanglement and nonlocal string order. Certain spin–2 chains, however, such as trivial AKLT-like configurations, may exhibit ground states that are close to product states, with minimal quantum correlations and no topological order—for instance, with all spins in the $m = 0$ state.

Figure 22 – Illustration of the AKLT state for a spin-1 chain with open boundary conditions. Large shaded circles represent spin-1 sites, each a symmetric combination of two spin-$\frac{1}{2}$ particles (small solid circles). Blue lines indicate singlet bonds between neighboring spin-$\frac{1}{2}$ particles. Under open boundary conditions, an unpaired spin-$\frac{1}{2}$ remains at each boundary, leading to a fourfold degenerate ground state in the thermodynamic limit.

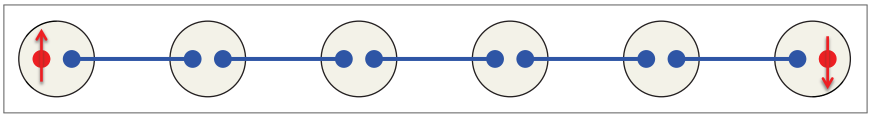

Source: Reference [29]

3.3 TOPOLOGICAL PHASES

Phases of matter are traditionally characterized by an *order parameter*, which quantifies the macroscopic organization of microscopic degrees of freedom and is typically associated with spontaneous symmetry breaking. For instance, in magnetic systems, the magnetization acts as an order parameter, distinguishing between magnetically ordered and disordered phases.

In a broken-symmetry phase, the order parameter acquires a finite expectation value, signaling long-range order. In contrast, it vanishes in the symmetric, disordered phase. A paradigmatic example is the Ising model, whose ordered and disordered phases are separated by a phase transition associated with the breaking of a discrete Z_2 symmetry. In the absence of such a symmetry, the two states can be adiabatically connected, and no true phase transition needs to occur.

Phase transitions may also arise in the absence of symmetry breaking. These are often first-order transitions, terminating at critical endpoints, as exemplified by the liquid-gas transition. More remarkably, certain quantum phases — known as *topological phases* — are distinct despite lacking any local order parameter or conventional symmetry breaking. The classification of such phases, especially in higher dimensions, remains an open problem, with symmetry playing a nuanced role in their stability and distinction.

Topology, in the mathematical sense, concerns properties invariant under continuous deformations. In physical systems, *topological invariants* classify phases according to global features such as connectivity and winding, rather than local order. In the context of quantum matter, topological phases [160] are characterized by entanglement structures that cannot be adiabatically transformed into one another without closing the energy gap or breaking a *protecting symmetry*, such as time-reversal or particle-hole symmetry.

The discovery of the integer [161] and fractional [162] quantum Hall effects in the 1980s provided the first experimental realizations of topological phases. Simultaneously, Haldane's conjecture on integer-spin chains revealed a new class of gapped quantum phases in one dimension, now recognized as SPT phases. These breakthroughs have established topological phases as a central theme in modern condensed matter physics.

3.3.1 The Haldane Phase

The ground state of the spin–1 HAF chain, introduced earlier, is a topological phase known as the *Haldane phase*. This phase lacks a conventional local order parameter, yet it can be characterized by a nonlocal string order parameter. A hallmark of this phase is the presence of fractionalized edge states under OBC, where excitations are localized at the boundaries while the bulk remains gapped — a feature reminiscent of edge currents in the quantum Hall effect.

As illustrated in Fig. 21, the spin–1 chain exhibits a nontrivial ground state, in contrast to the trivial ground state found in the spin–2 chain. In general, topological phases can be categorized as follows:

- *Nontrivial topological phase*: A phase that cannot be adiabatically connected to a trivial product state without either closing the excitation gap or breaking a protecting symmetry. Such phases typically exhibit long-range entanglement and symmetry-protected edge states.
- *Trivial topological phase*: A phase that can be smoothly deformed into a product state without a phase transition, and that lacks topological signatures such as edge modes or string order.

The Haldane $S = 1$ phase is a prime example of a SPT phase [29, 163], meaning it is topologically distinct from a trivial phase only in the presence of certain symmetries, such as lattice translation, time-reversal, and spatial inversion [163]. Its nontrivial character originates from bulk entanglement rather than solely from edge properties. In contrast, the spin–2 ground state is topologically trivial, as it can be adiabatically transformed into a product state in the absence of symmetry constraints. Pollmann *et al.* [21] demonstrated that odd-integer spin chains generically host SPT phases, while even-integer spin chains tend to realize trivial phases.

3.3.2 Order Parameters

Order parameters provide a means to detect magnetic order in quantum spin systems. They assume nonzero values in the presence of a particular type of order and vanish otherwise. For a spin–1 chain, consider the following representative states:

$$|\Psi\rangle_{\text{Ferro}} = |\uparrow\uparrow\cdots\uparrow\rangle, \tag{3.38}$$

$$|\Psi\rangle_{\text{AFM}} = |\uparrow\downarrow\cdots\uparrow\downarrow\rangle, \tag{3.39}$$

where the AFM order parameter satisfies $\langle O_{\text{AFM}}\rangle_{\text{Ferro}} = 0$, $\langle O_{\text{AFM}}\rangle_{\text{AFM}} = 1$.

Common magnetic order parameters include:

- **Ferromagnetic order**
  - *Order parameter*: Magnetization (M)
  - *Definition*: Quantifies the net spin polarization.
  - *Expression*:

$$M = \frac{1}{L}\sum_{i=1}^{L}\langle \hat{S}_i^z\rangle \tag{3.40}$$

  - *Signature*: $M \neq 0$ in ferromagnetic phases; $M = 0$ in PM or AFM phases.
- **Antiferromagnetic order**
  - *Order parameter*: Staggered magnetization (M_s)
  - *Definition*: Measures alternating spin orientation.
  - *Expression*:

$$M_s = \frac{1}{L}\sum_{i=1}^{L}(-1)^i\langle \hat{S}_i^z\rangle \tag{3.41}$$

  - *Signature*: $M_s \neq 0$ in AFM phases; $M_s = 0$ in disordered or ferromagnetic phases.
- **Spin-dimerized order**
  - *Order parameter*: Dimerization (D)
  - *Definition*: Detects alternating bond strengths, indicative of spontaneously dimerized states.
  - *Expression*:

$$D = \frac{1}{L}\sum_{i=1}^{L-1}(-1)^i\langle \hat{\mathbf{S}}_i \cdot \hat{\mathbf{S}}_{i+1}\rangle \tag{3.42}$$

- *Signature*: $D \neq 0$ in dimerized phases; $D = 0$ otherwise.

A finite M_s indicates AFM correlations, although it does not necessarily imply long-range order, especially in finite systems where fluctuations may give rise to a nonzero value even in paramagnetic phases. In the thermodynamic limit, a finite M_s confirms long-range AFM order, while a vanishing M_s suggests short-range correlations. In particular, disordered phases such as spin liquids or VBSs may exhibit short-range spin correlations, yet satisfy $M_s \to 0$ as $L \to \infty$.

3.3.2.1 String Order Parameter

The Haldane phase in spin–1 chains exhibits only short-range AFM correlations and lacks conventional long-range magnetic order. Instead, it is characterized by a nonlocal *hidden order*, captured by the *string order parameter* introduced by Rommelse and den Nijs [164]. For spin–1 systems, this parameter is defined as

$$\mathcal{O}^{\alpha} = \lim_{|j-i|\to\infty} \left\langle \hat{S}_i^{\alpha} \exp\left(i\pi \sum_{k=i+1}^{j-1} \hat{S}_k^{\alpha} \right) \hat{S}_j^{\alpha} \right\rangle , \tag{3.43}$$

where $\alpha = x, z$ denotes the spin component. This nonlocal correlator detects hidden order by effectively filtering out local spin fluctuations through the exponential phase factor, which acts as a string of phase shifts. In the Haldane phase, both longitudinal and transverse components of $\mathcal{O}^z$ are nonzero [164, 165], with $\mathcal{O}^z \approx -0.37$ for $S = 1$ [150].

For arbitrary integer spin S, Oshikawa generalized the string order parameter to account for the broader spin Hilbert space [166]:

$$\mathcal{O}_{\text{str}}^{\alpha} = \lim_{|j-i|\to\infty} \left\langle \hat{S}_i^{\alpha} \exp\left(\frac{i\pi}{S} \sum_{k=i+1}^{j-1} \hat{S}_k^{\alpha} \right) \hat{S}_j^{\alpha} \right\rangle . \tag{3.44}$$

For $S = 2$, the generalized string order parameter is also nonzero, with $\mathcal{O}_{\text{str}}^{z} \approx -0.72$ [153], indicating that a form of hidden order persists despite the absence of conventional magnetic order.

Although the string order parameter is nonzero for both $S = 1$ and $S = 2$, it does not, by itself, guarantee a nontrivial phase. In the $S = 1$ case, nonzero string order reflects a nontrivial SPT Haldane phase, characterized by edge states and a nontrivial projective symmetry action. However, for $S = 2$, the string order parameter remains finite, indicating hidden antiferromagnetic correlations, yet the phase is topologically trivial.

This demonstrates that string order captures certain nonlocal correlations but is not sufficient to distinguish SPT phases: even trivial phases can exhibit nonzero string order in the absence of protected edge modes or projective symmetry representations.

Using ITensor, we compute Eq. (3.44) for finite systems, following Ueda *et al.* [167]. Measurement points are chosen as $i = \lfloor L/3 \rfloor + 1$, $j = \lfloor 2L/3 \rfloor$, ensuring:

- Maximal distance from edges.
- Large correlation distance $|j - i|$.
- Proportional scaling of $|j - i|$ with system size L.

Extrapolating $\mathcal{O}^{\alpha}_{\text{str}}$ across system sizes yields the thermodynamic limit value.

3.4 SPIN LADDERS

A spin ladder consists of N coupled spin chains, each with intrachain coupling $J_{\parallel}$. Interchain coupling $J_{\perp}$ connects corresponding sites across adjacent chains, forming a ladder-like geometry (Fig. 23).

Figure 23 – Schematic of a spin ladder with coupled linear chains. The leg coupling $J_{\parallel}$ governs interactions along each chain, while the rung coupling $J_{\perp}$ connects adjacent chains.

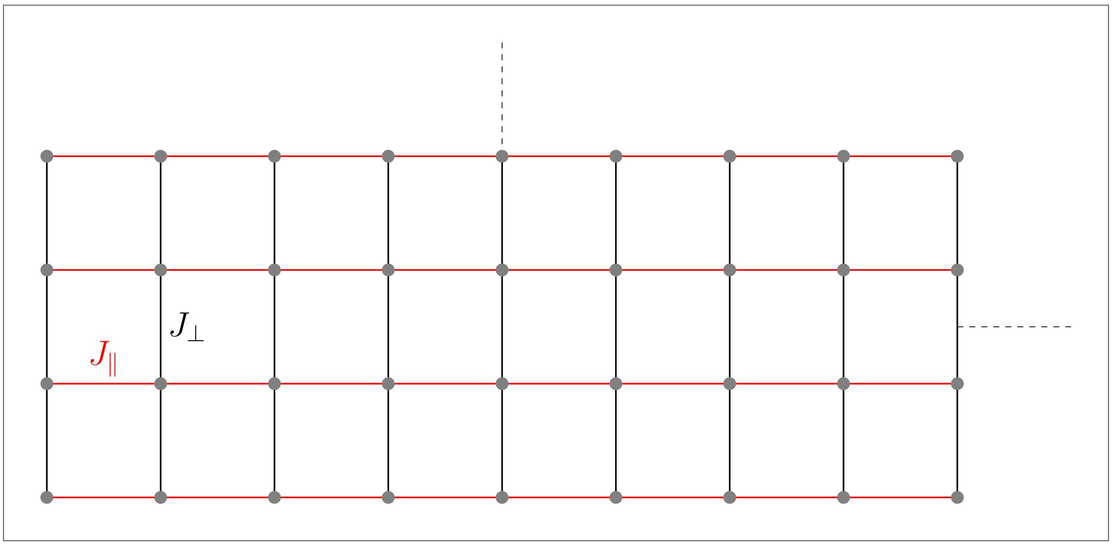

Source: The author (2025)

Spin ladders are quasi-2D systems, characterized by a width N (number of legs) and length L (number of rungs). Typically, $L \gg N$, so ladders retain strong 1D character.

When $L = N$, the geometry approaches that of a square lattice, and 2D effects become more pronounced. Assuming only nearest-neighbor interactions, the Hamiltonian reads:

$$\hat{\mathcal{H}} = J_\perp \sum_{i=1}^{L} \sum_{l=1}^{N-1} \hat{\mathbf{S}}_{i,l} \cdot \hat{\mathbf{S}}_{i,l+1} + J_\parallel \sum_{i=1}^{L-1} \sum_{l=1}^{N} \hat{\mathbf{S}}_{i,l} \cdot \hat{\mathbf{S}}_{i+1,l}, \tag{3.45}$$

where $\hat{\mathbf{S}}_{i,l}$ is the spin operator at rung i, leg l.

For the isotropic case $J_\perp = J_\parallel$, the nature of the ground state depends on the parity of N: ladders with even N form gapped spin–liquid phases, while odd-N ladders are gapless [33–35]. This distinction is supported by Lieb-Schultz-Mattis-type theorems [36], numerical studies up to $N = 6$ [37–39, 168], scaling theory [40], and experimental realizations [32, 41–43].

Sénéchal [169] and Sierra [170] extended Haldane's conjecture to ladder systems, proposing that spin–S, N-leg ladders are gapless when SN is a half-integer and gapped when SN is an integer. This generalized conjecture is well supported for spin–$\frac{1}{2}$ ladders [39, 168, 171], while evidence for $S > 1/2$ remains limited. Using DMRG, Ramos and Xavier [168] provided numerical data for systems with $S \leq 5/2$ and $N \leq 6$, confirming the gap behavior for several combinations of S and N.

White *et al.* [39] proposed a *Resonating-Valence-Bond* (RVB) picture [172] to interpret the qualitative differences between even- and odd-leg ladders. In this framework, the ground state consists of valence bond singlets resonating between different configurations. These resonances, including four-site plaquette flips [173], lower the ground state energy. Two main classes of configurations are considered (Fig. 24): *resonating* configurations, which support quantum fluctuations and minimize energy, and *staggered* configurations, which are energetically unfavorable and suppress resonance.

Figure 24 – Valence bond configurations in spin ladders. (a) Resonating configuration with alternating dimer bonds. (b) Staggered configuration without resonance.

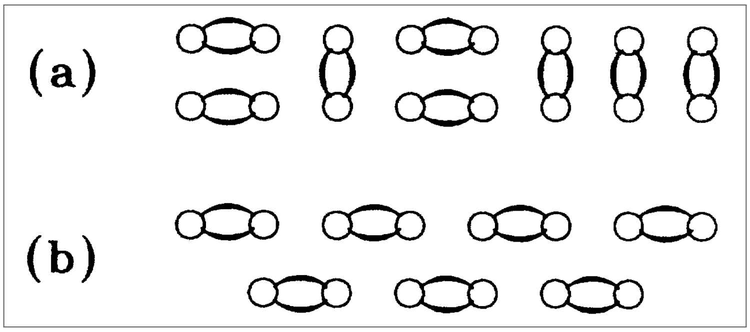

Source: Adapted from [39]

3.4.1 Spin–$\frac{1}{2}$ Two-Leg Ladder

For spin–$\frac{1}{2}$ sites and $N = 2$, Eq. (3.45) describes the two-leg Heisenberg ladder. Assuming $J_\parallel > 0$, the system exhibits distinct regimes depending on the rung coupling $J_\perp$:

- *No rung coupling* ($J_\perp = 0$): The ladder decouples into two independent spin–$\frac{1}{2}$ HAF chains. Each chain is gapless and described by LL theory [134], as discussed in Section 3.2.2.1.
- *Isotropic coupling* ($J_\perp = J_\parallel$): A gapped spin–liquid phase emerges, characterized by short-range correlations and a finite spin gap $\Delta \approx 0.5J_\perp$ [39, 174].
- *Weak rung coupling* ($|J_\perp| \ll J_\parallel$): The legs remain nearly independent, retaining LL behavior similar to a single HAF chain.

In the *strong rung-coupling limit* ($|J_\perp| \gg J_\parallel$), two distinct gapped phases arise:

- *Antiferromagnetic rungs* ($J_\perp > 0$): The ground state consists of rung singlets ($S = 0$), forming a gapped RS phase [175, 176]. The gap corresponds to the energy required to break a singlet bond.
- *Ferromagnetic rungs* ($J_\perp < 0$): Rung triplets ($S = 1$) dominate, leading to a gapped RT phase [49]. This phase can be mapped to an effective spin–1 HAF chain with reduced coupling $J_\parallel/2$.

Early numerical studies suggested a finite critical value $J_\perp$ for gap opening [37, 177]. However, field-theoretical and scaling arguments [40, 178, 179], later confirmed by numerical simulations [180, 181], established that the critical point lies at $J_{\perp,\,\mathrm{c}} = 0$, with the spin gap scaling linearly with $|J_\perp|$ for any nonzero coupling.

3.4.1.1 *Ground-State Phase Diagram of the Spin–$\frac{1}{2}$ Two-Leg Ladder*

We compute the ground-state phase diagram of Eq. (3.45) for the spin–$\frac{1}{2}$ two-leg ladder using DMRG, focusing on rung correlations. The local rung operator is defined as

$$\hat{R}_i = \hat{\mathbf{S}}_{i,1} \cdot \hat{\mathbf{S}}_{i,2}, \tag{3.46}$$

and the average rung correlation is given by

$$R = \frac{1}{L}\sum_{i=1}^{L}\langle \hat{R}_i \rangle = \frac{1}{L}\sum_{i=1}^{L}\langle \hat{\mathbf{S}}_{i,1} \cdot \hat{\mathbf{S}}_{i,2} \rangle. \tag{3.47}$$

The resulting phase diagram, shown in Fig. 25, illustrates the competition between $J_\perp$ and $J_\parallel$. For $J_\perp = 0$, the system consists of two decoupled spin–$\frac{1}{2}$ chains, yielding $R \approx 0$ and a gapless LL phase, as discussed earlier. For $J_\perp > 0$, rung singlets dominate; in the strong-coupling limit, $R \to -0.75$, corresponding to the ideal singlet value and indicating a gapped RS phase. Conversely, for $J_\perp < 0$, rung triplets form with $R > 0$, characteristic of a gapped RT phase. In the weak-coupling regime ($|J_\perp| \ll J_\parallel$), the system behaves similarly to decoupled chains, with $R \approx 0$.

Both regions $J_\perp > 0$ and $J_\perp < 0$ are fully gapped, with the spin gap scaling linearly with $|J_\perp|$. No phase transition occurs for finite $J_\perp$; the only critical point is at $J_{\perp,\,\mathrm{c}} = 0$, where the gap closes and the system becomes critical [178–180].

Figure 25 – Ground-state phase diagram of a spin-$\frac{1}{2}$ two-leg ladder, computed using DMRG as a function of rung coupling $J_\perp$ and leg coupling $J_\parallel$. The color scale represents the average rung correlation R, calculated for $L = 100$ rungs with a truncation error of $\sim 10^{-10}$. At $J_\perp = 0$, $R \approx 0$, indicating two decoupled spin-$\frac{1}{2}$ chains. In the strong rung coupling limit ($|J_\perp| \gg J_\parallel$), $R \to -0.75$ for $J_\perp > 0$ (singlet-dominated RS phase) and $R \to 0.25$ for $J_\perp < 0$ (triplet-dominated RT phase). In the weak rung coupling regime ($|J_\perp| \ll J_\parallel$), $R \approx 0$, reflecting nearly independent legs.

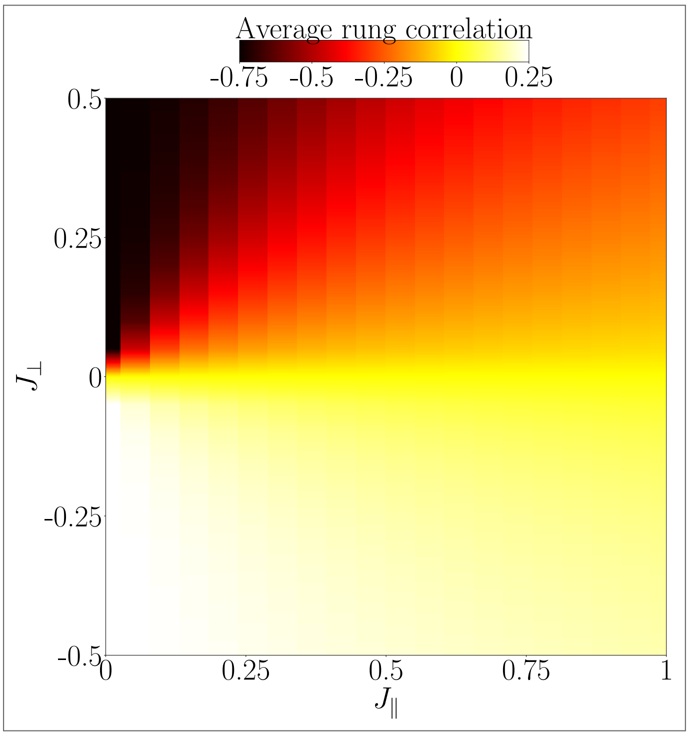

Source: The author (2025)

4 SPIN–$\frac{1}{2}$ FRUSTRATED LADDER

Magnetic frustration arises when competing AFM interactions prevent all spin pairs from simultaneously minimizing their energy. A prototypical example is shown in Fig. 26, where three mutually interacting Ising spins cannot all align antiparallel. This incompatibility leads to a macroscopically degenerate ground state. Under certain conditions, frustration stabilizes exotic quantum phases, such as spin liquids, where spins remain entangled and fluctuate down to zero temperature despite the absence of long-range order [182].

Figure 26 – A triangular arrangement of antiferromagnetically interacting Ising spins, constrained to point either up or down, serves as the simplest example of frustration. In this configuration, it is impossible for all three spins to be fully antiparallel. Consequently, instead of the two ground states expected from Ising symmetry (all spins flipped up or down), the system exhibits six degenerate ground states.

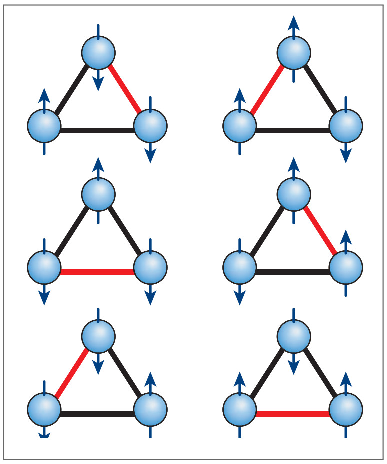

Source: Reference [182]

Frustrated quantum magnets constitute a fertile ground for exploring unconventional critical phenomena [183, 184], including quantum analogs of water's liquid–gas critical point [185], critical endpoints [186], and quantum bicriticality, such as that observed in the heavy-fermion compound YbAgGe [187]. In antiferromagnetic systems, an external magnetic field $\vec{h} = (0, 0, h)$ often acts as a tuning parameter. If the total longitudinal spin component S^z_{total} is conserved, the magnetization,

$$M = g\mu_B \langle \hat{S}^z_{\text{total}} \rangle, \tag{4.1}$$

may exhibit quantized plateaus—regions where $dM/dh = 0$—interspersed with phases of continuously varying magnetization.

Introducing a diagonal AFM coupling $J_\times$ into a spin ladder geometry, as depicted in Fig. 27, generates frustration by introducing competing interactions between spins on opposite legs.

Figure 27 – Schematic representation of a frustrated two-leg ladder. Here, $J_\parallel$ denotes the interactions along the legs, $J_\perp$ along the rungs, and $J_\times$ along the diagonals. The diagonal coupling $J_\times$ introduces magnetic frustration into the antiferromagnetic arrangement.

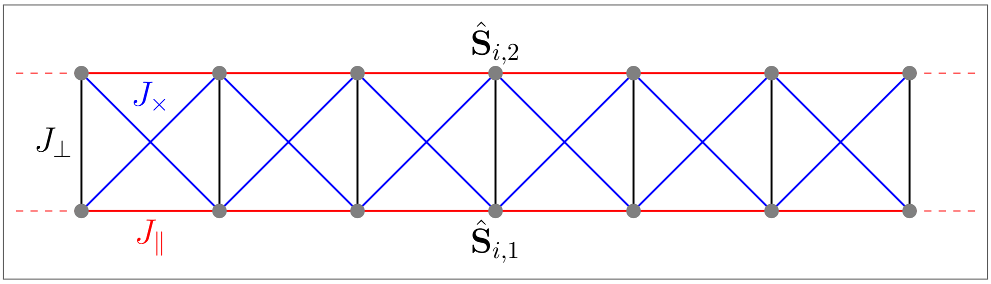

Source: The author (2025)

The Hamiltonian for a spin–$\frac{1}{2}$ frustrated ladder with L rungs and open boundary conditions, restricted to nearest-neighbor interactions, is given by:

$$\hat{\mathcal{H}} = J_\perp \sum_{i=1}^{L} \left[\hat{\mathbf{S}}_{i,1} \cdot \hat{\mathbf{S}}_{i,2} - h \left(\hat{S}^z_{i,1} + \hat{S}^z_{i,2} \right) \right] + J_\parallel \sum_{i=1}^{L-1} \sum_{k=1}^{2} \hat{\mathbf{S}}_{i,k} \cdot \hat{\mathbf{S}}_{i,k} \\ + J_\times \sum_{i=1}^{L-1} \left(\hat{\mathbf{S}}_{i,1} \cdot \hat{\mathbf{S}}_{i+1,2} + \hat{\mathbf{S}}_{i,2} \cdot \hat{\mathbf{S}}_{i+1,1} \right), \tag{4.2}$$

where $\hat{\mathbf{S}}_{i,1}$ and $\hat{\mathbf{S}}_{i,2}$ denote spin–$\frac{1}{2}$ operators at rung i on the lower and upper legs, respectively. The magnetic field h is expressed in energy units, with $g\mu_B \equiv 1$, where g is the Landé factor and μ_B is the Bohr magneton.

It is convenient to define the total and difference spin operators on each rung as:

$$\hat{\mathbf{S}}_i \equiv \hat{\mathbf{S}}_{i,1} + \hat{\mathbf{S}}_{i,2}, \tag{4.3}$$

$$\hat{\mathbf{D}}_i \equiv \hat{\mathbf{S}}_{i,1} - \hat{\mathbf{S}}_{i,2}, \tag{4.4}$$

which yield the inverse relations:

$$\hat{\mathbf{S}}_{i,1} = \frac{\hat{\mathbf{S}}_i + \hat{\mathbf{D}}_i}{2}, \quad \hat{\mathbf{S}}_{i,2} = \frac{\hat{\mathbf{S}}_i - \hat{\mathbf{D}}_i}{2}. \tag{4.5}$$

The operators $\hat{\mathbf{S}}_i$ and $\hat{\mathbf{D}}_i$ satisfy specific commutation relations detailed in Appendix A. Substituting Eq. (4.5) into Eq. (4.2), the Hamiltonian can be recast as:

$$\hat{\mathcal{H}} = J_\perp \sum_{i=1}^{L} \left[\frac{\hat{\mathbf{S}}_i^2 - 2s(s+1)}{2} - h\hat{S}^z_i \right] + \frac{J_\parallel}{2} \sum_{i=1}^{L-1} \left(\hat{\mathbf{S}}_i \cdot \hat{\mathbf{S}}_{i+1} + \hat{\mathbf{D}}_i \cdot \hat{\mathbf{D}}_{i+1} \right) \\ + \frac{J_\times}{2} \sum_{i=1}^{L-1} \left(\hat{\mathbf{S}}_i \cdot \hat{\mathbf{S}}_{i+1} - \hat{\mathbf{D}}_i \cdot \hat{\mathbf{S}}_{i+1} \right). \tag{4.6}$$

For spin$-\frac{1}{2}$ sites ($s = 1/2$), this simplifies to:

$$\hat{\mathcal{H}} = J_\perp \sum_{i=1}^{L} \left(\hat{\mathbf{S}}_i^2/2 - h\hat{S}_i^z \right) + \frac{J_\parallel + J_\times}{2} \sum_{i=1}^{L-1} \hat{\mathbf{S}}_i \cdot \hat{\mathbf{S}}_{i+1} + \frac{J_\parallel - J_\times}{2} \sum_{i=1}^{L-1} \hat{\mathbf{D}}_i \cdot \hat{\mathbf{D}}_{i+1} - \frac{3LJ_\perp}{4}. \tag{4.7}$$

The constant term $-3LJ_\perp/4$ may be omitted for practical purposes. Since $\hat{\mathbf{S}}_i$ represents the total spin of two spin$-\frac{1}{2}$ sites, each rung hosts either a singlet ($S = 0$) or triplet ($S = 1$) configuration, depending on the parameters $J_\perp, J_\parallel, J_\times, h$.

Importantly, the Hamiltonian (4.7) exhibits a symmetry under the exchange $J_\parallel \leftrightarrow J_\times$. The first two terms remain invariant under this transformation, while the third changes sign. However, as shown by the original Hamiltonian (4.2), swapping the spins on each rung, $\hat{\mathbf{S}}_{i,1} \leftrightarrow \hat{\mathbf{S}}_{i,2}$, is a symmetry operation that leaves the system unchanged. This operation effectively inverts $\hat{\mathbf{D}}_i$ or $\hat{\mathbf{D}}_{i+1}$, thereby restoring the invariance of the full Hamiltonian.

4.1 GROUND-STATE PROPERTIES AT ZERO FIELD

The energy spectrum of the Hamiltonian (4.7), denoted as $E(h, J_\perp, J_\parallel, J_\times)$, depends on four parameters, where all exchange couplings ($J_\perp, J_\parallel, J_\times$) are assumed to be AFM. For fixed couplings, the spectrum becomes a function of the magnetic field h, written as $E(h)$. As h increases, spins progressively align, eventually reaching a *Fully Polarized* (FP) ferromagnetic state at sufficiently large fields. Due to the antiferromagnetic nature of the couplings, this fully polarized state corresponds to the highest energy, leading to a monotonically increasing $E(h)$.

At zero field ($h = 0$), the ground state is governed by the Hamiltonian:

$$\hat{\mathcal{H}} = \frac{J_\perp}{2} \sum_{i=1}^{L} \hat{\mathbf{S}}_i^2 + \frac{J_\parallel + J_\times}{2} \sum_{i=1}^{L-1} \hat{\mathbf{S}}_i \cdot \hat{\mathbf{S}}_{i+1} + \frac{J_\parallel - J_\times}{2} \sum_{i=1}^{L-1} \hat{\mathbf{D}}_i \cdot \hat{\mathbf{D}}_{i+1} - \frac{3LJ_\perp}{4}. \tag{4.8}$$

4.1.1 Fully Frustrated Case

In the fully frustrated case ($J_\times = J_\parallel$), the Hamiltonian simplifies to:

$$\hat{\mathcal{H}} = -\frac{3LJ_\perp}{4} + \frac{J_\perp}{2} \sum_{i=1}^{L} \hat{\mathbf{S}}_i^2 + J_\parallel \sum_{i=1}^{L-1} \hat{\mathbf{S}}_i \cdot \hat{\mathbf{S}}_{i+1}. \tag{4.9}$$

In this regime, many eigenstates can be constructed exactly [49]. A rung in a singlet state ($S = 0$) decouples from its neighbors [188]. Thus, any configuration with N_t spatially separated triplet rungs ($S = 1$) embedded in a background of singlets forms an exact eigenstate of Eq. (4.9), with energy:

$$E(N_t) = -\frac{3LJ_\perp}{4} - J_\perp N_t, \quad N_t \leq L/2, \tag{4.10}$$

where $N_t \leq L/2$ ensures sufficient spacing to maintain triplet isolation. For polarized triplets with $S^z = \pm 1$, the total magnetization is $M = N_+ - N_-$, where $N_\pm$ denotes the number of triplets with $S^z = \pm 1$, respectively. These states span all quantum sectors of fixed total spin and have energy:

$$E(m) = \left(m - \frac{3}{4}\right) J_\perp L, \quad \text{for } 0 \leq m \leq 1/2, \tag{4.11}$$

$$E(m) = \left(m - \frac{3}{4}\right) J_\perp L + (2m-1)J_\parallel L, \quad \text{for } 1/2 \leq m \leq 1, \tag{4.12}$$

where $m = M/L$ is the magnetization per rung. In the latter regime, the triplets are no longer separated, and the interaction term $\hat{\mathbf{S}}_i \cdot \hat{\mathbf{S}}_{i+1}$ contributes to the energy.

For large $J_\perp$, the $\hat{\mathbf{S}}_i^2$ term favors singlets, stabilizing the RS phase. Conversely, for small $J_\perp$, the exchange interaction promotes rung triplets, leading to the RT phase [49]. A first-order transition between these two phases occurs at $J_\perp/J_\parallel \approx 1.4$ [49, 51, 189], and this transition remains robust under small deviations from the fully frustrated condition [47, 48, 190, 191].

4.1.2 Haldane Phase

In the limit $J_\perp \ll J_\parallel$, the Hamiltonian (4.9) reduces to:

$$\hat{\mathcal{H}} = J_\parallel \sum_i \hat{\mathbf{S}}_i \cdot \hat{\mathbf{S}}_{i+1}, \tag{4.13}$$

describing an effective spin–1 Heisenberg chain. In this regime, the frustrated ladder enters the RT phase, wherein each rung behaves effectively as a spin–1 degree of freedom. This raises the question: is the RT phase distinct from the Haldane $S = 1$ phase? The answer is no. The spin–$\frac{1}{2}$ HAF ladder maps onto a spin–1 chain and belongs to the same universality class [53], establishing the equivalence between the RT phase and the Haldane phase.

For example, at $J_\perp = 1$ and $J_\parallel = 0.8$, the RS–Haldane phase transition occurs at $J_\times \approx 0.67 \pm 0.01$ [47]. Choosing $J_\times = 0.72$, we analyze the ground-state properties

(Fig. 28). The RT phase exhibits characteristic features of the Haldane phase: spin–$\frac{1}{2}$ edge states (Figs. 28(a) and (b)) and a finite spin gap $\Delta \approx 0.306$ (Fig. 28(d)). In comparison, the spin–1 chain has a gap $\Delta = 0.411J$, implying an effective coupling:

$$J_{\text{eff}} = \frac{0.306}{0.411} \approx 0.74, \tag{4.14}$$

which closely matches the chosen value $J_\times = 0.72$.

Figure 28 – DMRG results for a spin-$\frac{1}{2}$ frustrated ladder with $J_\perp = 1$, $J_\| = 0.8$, $J_\times = 0.72$, $L = 100$ rungs, and open boundary conditions. (a) Spin-$\frac{1}{2}$ edge states, characteristic of a spin-1 chain. (b) First magnetization excitation, confirming the edge-state nature. (c) Local rung correlation, indicating a rung-triplet state. (d) Energy gap $\Delta \approx 0.306$, obtained via linear extrapolation in $1/L$

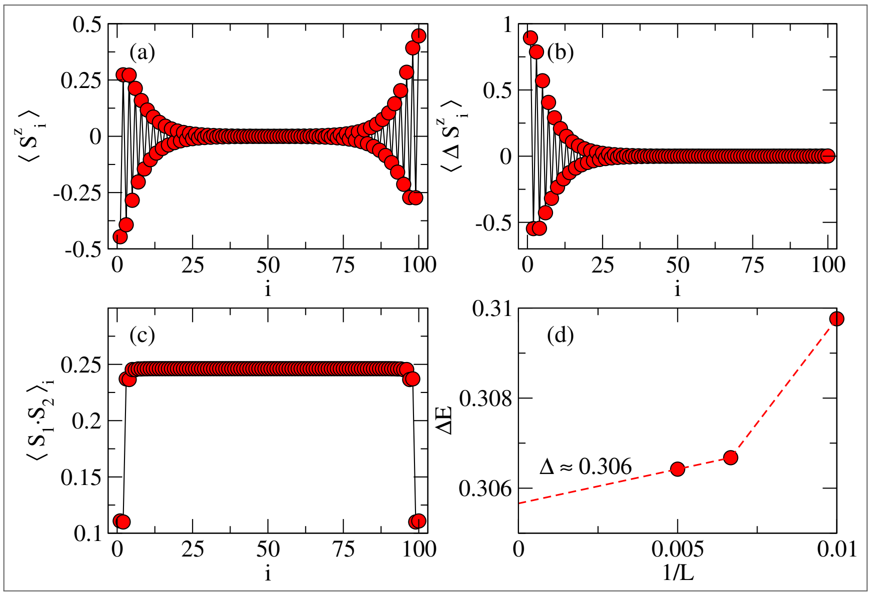

Source: The author (2025)

To further confirm this identification, we compute the string order parameter:

$$\mathcal{O}^z_{\text{str}}(i,j) = \left\langle \left(\hat{S}^z_{1,i} + \hat{S}^z_{2,i}\right) \exp\left(i\pi \sum_{k=i+1}^{j-i} \left(\hat{S}^z_{1,k} + \hat{S}^z_{2,k}\right)\right) \left(\hat{S}^z_{1,j} + \hat{S}^z_{2,j}\right) \right\rangle, \tag{4.15}$$

using ITensor tools. By evaluating $\mathcal{O}^z_{\text{str}}$ for system sizes L, $3L/2$, and $2L$ with $L = 100$, and extrapolating to the thermodynamic limit, we find:

$$\lim_{|j-i|\to\infty} O^z_{\text{str}}(i,j) = -0.37, \tag{4.16}$$

which is nearly indistinguishable from the spin–1 chain value of -0.38 [150, 192].

4.1.3 Weakly Coupled Chain Limit

In the weak-coupling limit ($J_\perp, J_\times \ll J_\parallel$), field-theoretical analysis predicts a phase boundary at $J_\perp = 2J_\times$ separating the RS and Haldane phases [193, 194]. However, the nature of this boundary—whether it marks a direct transition or harbors an intermediate phase—remains a subject of debate.

Starykh and Balents [194] argued that fine-tuning $J_\perp$ and $J_\times$ cannot eliminate all relevant inter-leg couplings. They proposed the emergence of a spontaneously dimerized intermediate phase—either *Columnar Dimer* (CD) or *Staggered Dimer* (SD)—where spin pairs form singlet dimers (Fig. 29). These phases would separate the RS and Haldane regimes.

Figure 29 – Schematic of possible phases in a spin-$\frac{1}{2}$ frustrated ladder: rung-singlet (RS), Haldane, columnar dimerized (CD), and staggered dimerized (SD). The RS and Haldane phases are well-established, but the dimerized phases remain debated

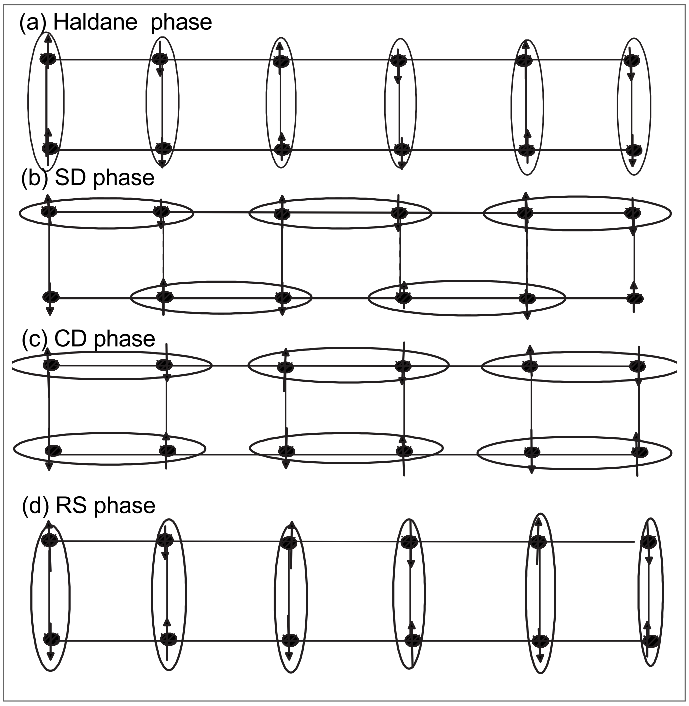

Source: Reference [195]

For $J_\times \ll J_\parallel$, the CD phase is predicted within:

$$2J_\times - \frac{5J_\times^2}{\pi^2} \leq J_\perp \leq 2J_\times - \frac{J_\times^2}{\pi^2} \tag{4.17}$$

Early numerical studies reported no evidence for such an intermediate phase [196, 197]. Although Liu *et al.* [195] suggested a dimerized region for $0.373 \leq J_\perp \leq 0.386$ at $J_\times = 0.2$, their results were inconclusive. Hikihara and Starykh [198] observed tentative signs of dimerization at $J_\perp = 0.38$, $J_\times = 0.2$. However, Barcza *et al.* [199], using high-precision DMRG over $0.36 \leq J_\perp \leq 0.4$, found no such phase. More recent studies agree that the HAF ladder does not host a dimerized phase [200, 201], although such phases may appear with ferromagnetic interactions [198] or next-nearest-neighbor leg couplings [202–204].

4.1.4 Ground-State Phase Diagram

The ground-state phase diagram, derived from numerical methods [47, 51, 190, 191, 195–197, 199, 200], is shown in Fig. 30. The model hosts two distinct phases: the RS phase and the Haldane phase, separated by a quantum phase transition (red line). Fixing $J_\parallel = 1$ as the energy scale, setting $J_\times = 0$ recovers the conventional spin ladder of Section 3.4. Conversely, for $J_\perp = 0$, the system maps to a spin–1 chain with gapped spin–1 magnons. While early studies suggested a first-order transition at all coupling strengths, subsequent work revealed a continuous transition at weak rung couplings, becoming first-order at stronger couplings [190, 196].

Figure 30 – Ground-state phase diagram of the spin-$\frac{1}{2}$ frustrated ladder. The system features two distinct phases, the rung-singlet and the rung-triplet, separated by a quantum phase transition (red line). Purple rungs with ellipses represent rung-singlet spin states, while red rungs with parallel spins represent rung-triplet states. Numbered circles denote specific points in the phase diagram for which thermodynamic results are provided in the source of the figure.

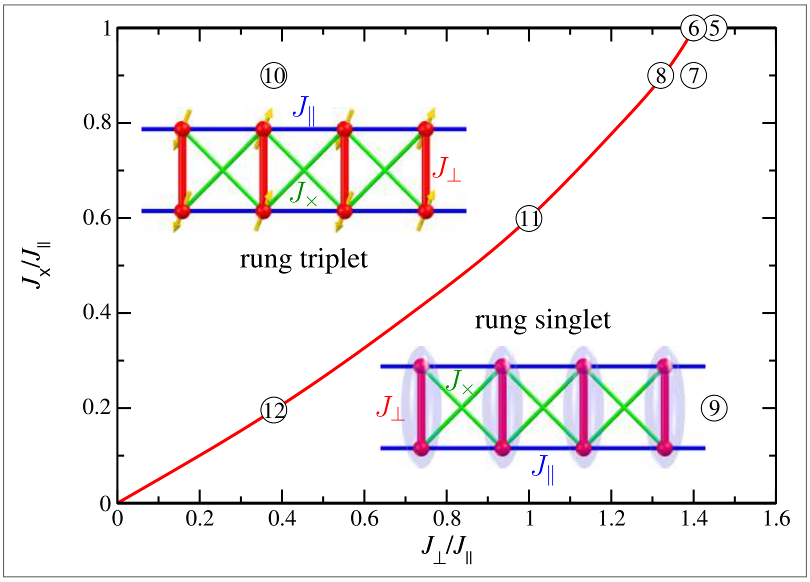

Source: Reference [51]

4.2 FRUSTRATED LADDER IN AN EXTERNAL MAGNETIC FIELD

In the presence of an external magnetic field ($h \neq 0$) and fixing $J_\perp = 1$, the Hamiltonian in Eq. (4.7) can be decomposed into three terms:

$$\hat{\mathcal{H}}_1 = \sum_{i=1}^{L} (\hat{\mathbf{S}}_i^2/2 - h\hat{S}_i^z), \quad \hat{\mathcal{H}}_2 = J\sum_{i=1}^{L-1} \hat{\mathbf{S}}_i \cdot \hat{\mathbf{S}}_{i+1}, \quad \hat{\mathcal{H}}_3 = \frac{\delta J}{2}\sum_{i=1}^{L-1} \hat{\mathbf{D}}_i \cdot \hat{\mathbf{D}}_{i+1}, \tag{4.18}$$

with effective couplings defined as:

$$J = \frac{J_\parallel + J_\times}{2}, \quad \delta J = J_\parallel - J_\times. \tag{4.19}$$

Each term plays a distinct physical role:

- $\hat{\mathcal{H}}_1$ favors rung singlets at low fields ($h < 1$) but promotes triplets at high fields ($h > 1$).
- $\hat{\mathcal{H}}_2$ introduces repulsion between adjacent rung triplets, stabilizing a magnetization plateau at $m = 1/2$, where triplets occupy alternating rungs.
- $\hat{\mathcal{H}}_3$ enables triplet mobility due to the non-commutation of $\hat{\mathbf{D}}_i$ with $\hat{\mathcal{H}}_1$, leading to gapless regions between plateaus.

Previous studies [47–49, 55, 205, 206] predict magnetization plateaus at $m = 0$, $m = 1/2$, and $m = 1$, with intervening gapless LL phases exhibiting square-root singularities at the plateau edges. However, numerical results show deviations: the singularity near $m = 1/2$ is weak, and a magnetization jump is observed between $m = 1/2$ and $m = 1$, as illustrated in Fig. 31.

According to the condition established by Oshikawa, Yamanaka, and Affleck [207], a magnetization plateau at m is allowed only if:

$$(S_u - m_u) = \text{integer}, \tag{4.20}$$

where S_u and m_u are the total spin and magnetization per unit cell, respectively. For a unit cell containing two spin$-\frac{1}{2}$ sites, plateaus preserving translational symmetry can appear at $m = 0$ (the PM state) and $m = 1$ (the FP state), as observed for specific values of $J_\times$ in Fig. 31, with corresponding critical fields h_{PM} and h_{FP}. For moderate $J_\times$, a plateau at $m = 1/2$ is stabilized with a doubled unit cell of four spins. This plateau is bounded by critical fields h_- and h_+, and in finite systems with open boundaries, it manifests two steps associated with domain walls, connected at $h = h_0$.

In the gapless LL phases between plateaus, transverse spin correlations decay as power laws:

$$\Gamma(r) \sim r^{-1/2K}, \tag{4.21}$$

where K is the LL exponent and r is the spin separation along the chain.

Figure 31 – Magnetization per rung, $m = \langle S^z_{\text{total}} \rangle / L$, versus magnetic field h for a ladder with $L = 128$ rungs and $J_{\|} = 0.55$. Shown are the paramagnetic (PM), $m = 1/2$, and fully polarized (FP) plateaus, with critical fields h_{PM}, h_-, h_+, and h_{FP}. The field h_f indicates a magnetization jump, and h_0 marks the finite-size splitting of the $m = 1/2$ plateau into two steps under open boundary conditions.

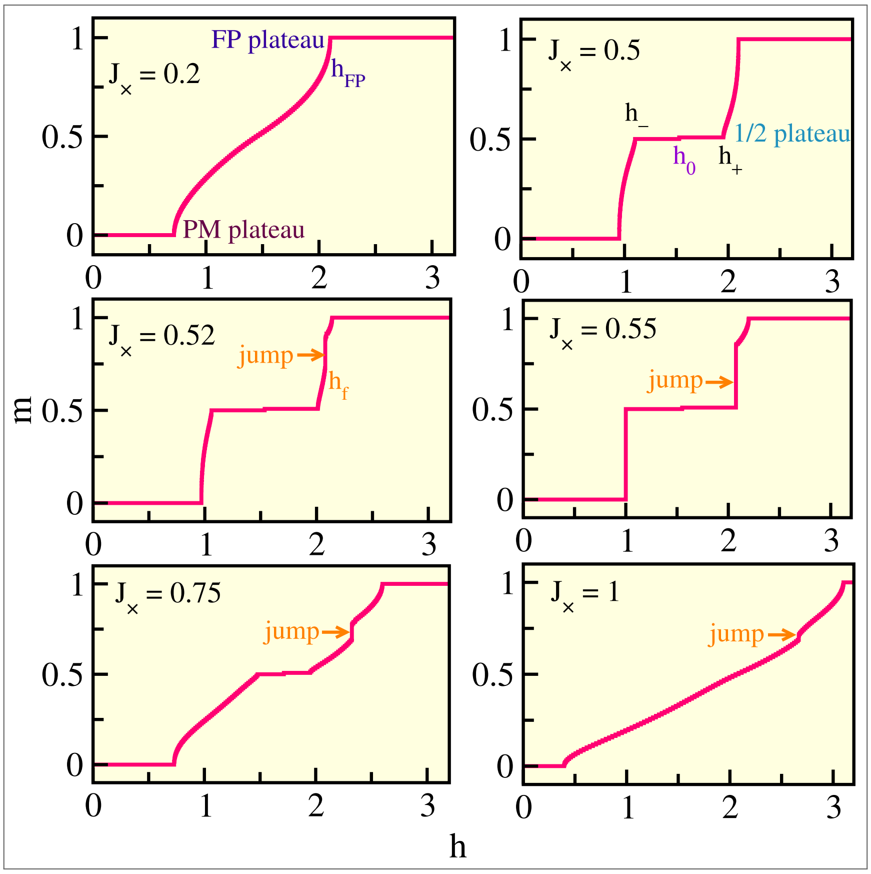

Source: Reference [47]

The nature of elementary excitations varies across the magnetization plateaus:

- At $m = 0$, the lowest-energy excitations are magnons (triplet excitations) with $\Delta S^z = +1$.
- At $m = 1/2$, the excitations are spinons, interpreted as domain walls separating ordered triplets. These carry $\Delta S^z = \pm 1/2$, depending on the field direction.

- At $m = 1$, magnons correspond to singlet states embedded in a polarized background, with $\Delta S^z = -1$.

Quantum phase transitions between gapped plateaus and gapless regions are driven by the condensation of these elementary excitations.

4.2.1 Mapping to the XXZ Chain

In the fully frustrated limit discussed in Section 4.1.1, the total spin on each rung is conserved, and the ground state is exactly known. We now consider a regime in the vicinity of this limit, characterized by:

$$\delta J \ll J \ll 1. \tag{4.22}$$

In this parameter regime, each rung predominantly occupies either the singlet state or the $S^z = 1$ triplet state. The remaining triplet components are energetically unfavorable for any value of the magnetic field. This restriction effectively reduces the Hilbert space to two states per rung. Employing perturbation theory in δJ, we derive an effective Hamiltonian restricted to this low-energy subspace.

By identifying the singlet with a spin-up state and the $S^z = 1$ triplet with a spin-down state, the original ladder model maps onto an spin–$\frac{1}{2}$ AFM XXZ chain with easy-axis anisotropy [48, 55]:

$$\hat{\mathcal{H}}_{\text{xxz}} = \sum_{i=1}^{L-1} \left(j \frac{\hat{s}_i^+ \hat{s}_{i+1}^- + \hat{s}_i^- \hat{s}_{i+1}^+}{2} + j_z \hat{s}_i^z \hat{s}_{i+1}^z \right) - H \sum_{i=1}^{L} \hat{s}_i^z - H_{\text{edge}} (\hat{s}_1^z + \hat{s}_L^z)/2, \tag{4.23}$$

where $\hat{s}_i^\alpha$ are spin–$\frac{1}{2}$ operators, and the effective couplings and fields are given by:

$$j = \delta J + O(\delta J^2), \quad j_z = J + O(\delta J^2), \quad H = h - 1 - J + O(\delta J^2), \quad H_{\text{edge}} = J. \tag{4.24}$$

The edge field H_{edge} breaks the degeneracy between the Néel states, selecting a particular ordering and stabilizing the fractional magnetization plateau where singlets and triplets coexist in a nearly degenerate configuration.

The XXZ chain exhibits a spin gap in the AFM regime ($j_z/|j| > 1$) at zero field [208], yielding a plateau at zero magnetization for $|H| < H_{\text{min}}$. At $H = \pm H_{\text{min}}$, the gap closes and spinons condense, leading to a gapless LL phase. These transition points correspond, in the original ladder, to the boundaries of the $m = 1/2$ magnetization plateau. For

$|H| > H_{\mathrm{min}}$, the system remains in the LL phase until saturation at $|H| = H_{\mathrm{max}}$, marking the transitions to the $m = 0$ and $m = 1$ plateaus.

The critical fields of the XXZ chain are given by [208]:

$$H_{\mathrm{max}} = j_z + |j|, \quad H_{\mathrm{min}} = |j| \mathrm{sihn}\ g \sum_{k=-\infty}^{\infty} \frac{(-1)^k}{\cosh kg}, \tag{4.25}$$

where $\cosh g = j_z/|j|$. Translating back to the original ladder variables, with $h = H + J + 1 + O(\delta J^2)$, we define the following critical fields:

$$h_0 = 1 - |\delta J|, \tag{4.26}$$

$$h_1 = 2J + |\delta J| + 1, \tag{4.27}$$

$$h_{\pm} = 1 + J \left(1 \pm \sum_{k=-\infty}^{\infty} \frac{(-1)^k}{T_k(J/|\delta J|)} \right), \tag{4.28}$$

where $T_k(x)$ denotes the k-th Chebyshev polynomial of the first kind:

$$T_k(x) = \frac{(x + \sqrt{x^2 - 1})^k + (x - \sqrt{x^2 - 1})^k}{2}. \tag{4.29}$$

The phase structure is thus described as:

- $h < h_0$: Gapped $m = 0$ plateau.
- $h_0 < h < h_-$: LL phase.
- $h_- < h < h_+$: Gapped $m = 1/2$ plateau.
- $h_+ < h < h_1$: LL phase.
- $h \geq h_1$: $m = 1$ plateau.

As a concrete example, consider $J_{\|} = 0.2$ and $J_{\times} = 0.18$, which yield $J = 0.19$ and $|\delta J| = 0.02$. Using Eqs. (4.26)–(4.28), the critical fields computed via the XXZ mapping are:

$$h_0 = 0.98 \text{ (XXZ)}, \quad 0.98 \text{ (DMRG)},$$

$$h_- = 1.00 \text{ (XXZ)}, \quad 1.04 \text{ (DMRG)},$$

$$h_+ = 1.38 \text{ (XXZ)}, \quad 1.34 \text{ (DMRG)},$$

$$h_1 = 1.40 \text{ (XXZ)}, \quad 1.40 \text{ (DMRG)}.$$

These results, compared with numerical data from DMRG in Fig. 32, demonstrate the accuracy of the XXZ mapping in the regime defined by Eq. (4.22). However, as $|\delta J|$ increases, higher-order corrections become relevant, and the mapping loses precision. Moreover, since the XXZ chain does not exhibit magnetization jumps, it cannot capture discontinuities observed in the ladder model for larger values of δJ.

Figure 32 – Magnetization per rung $m = \langle S^z_{\text{total}} \rangle / L$ versus external magnetic field h from DMRG calculations for a ladder with $L = 128$ rungs, $J_{\|} = 0.2$, and $J_{\times} = 0.18$. For a finite-size ladder, The small magnetization step in the middle of the $m = 1/2$ plateau occurs when the spinon changes its spin from $\Delta S^z = -1/2$ to $+1/2$. Maximum truncation error is $\sim 10^{-10}$.

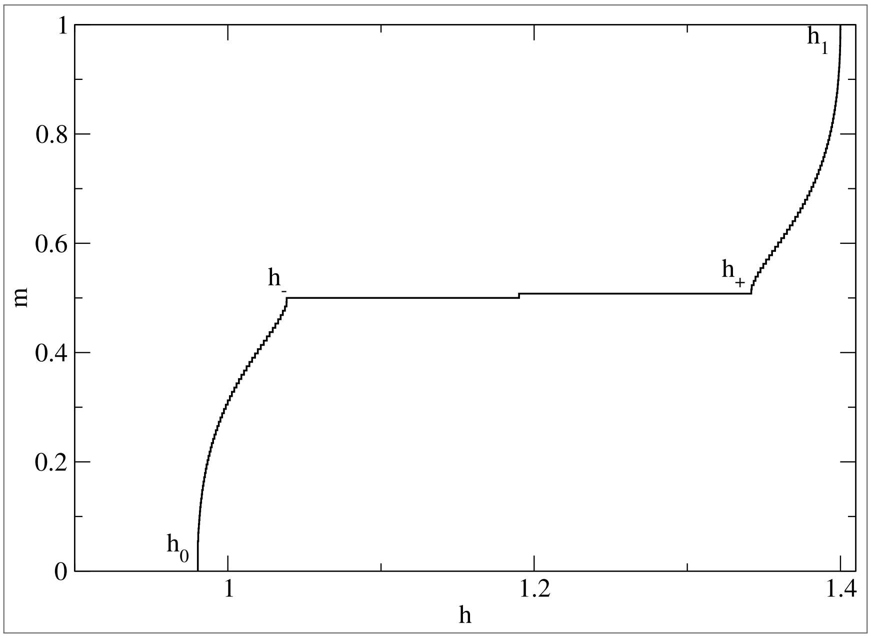

Source: The author (2025)

4.2.2 Hard-Core Boson Mapping

The spin system can be mapped onto hard-core bosons to determine the critical field h_{FP} associated with the transition from the FP state. The mapping is given by:

$$\hat{S}^z_{i,k} = \frac{1}{2} - \hat{a}^\dagger_{i,k}\hat{a}_{i,k}, \tag{4.30}$$

$$\hat{S}^+_{i,k} = \hat{a}_{i,k}, \tag{4.31}$$

$$\hat{S}^-_{i,k} = \hat{a}^\dagger_{i,k}, \tag{4.32}$$

where $\hat{a}_{i,k}$ are hard-core bosonic operators. To preserve the spin commutation relations (Eq. 3.17), these operators satisfy:

$$[\hat{a}^\dagger_{i,k}, \hat{a}_{j,k'}] = \delta_{ij}\delta_{kk'}(1 - 2\hat{a}^\dagger_{i,k}\hat{a}_{i,k}), \quad (\hat{a}_{i,k})^2 = (\hat{a}^\dagger_{i,k})^2 = 0. \tag{4.33}$$

enforcing the hard-core constraint, i.e., at most one boson per site.

Using this mapping, the Hamiltonian in Eq. (4.2) becomes:

$$\hat{\mathcal{H}}_{(\text{free hc})} = \left(J_\parallel + J_\times + h - \frac{1}{2}\right)\hat{N} + \frac{J_\parallel}{2}\sum_i (\hat{a}^\dagger_{i,1}\hat{a}_{i+1,1} + \hat{a}^\dagger_{i,2}\hat{a}_{i+1,2} + \text{h.c}) \\ + \frac{1}{2}\sum_i (\hat{a}^\dagger_{i,1}\hat{a}_{i,2} + \hat{a}^\dagger_{i,2}\hat{a}_{i,1}) + \frac{J_\times}{2}\sum_i (\hat{a}^\dagger_{i,1}\hat{a}_{i+1,2} + \hat{a}^\dagger_{i,2}\hat{a}_{i+1,1} + \text{h.c}), \tag{4.34}$$

where $\hat{N} = \sum_{i,k} \hat{a}^\dagger_{i,k}\hat{a}_{i,k}$ is the total boson number. Interaction terms are neglected for simplicity.

To describe low-energy excitations above the fully polarized background, we define bosonic operators that create singlet and $S^z = 0$ triplet states:

$$\hat{s}^\dagger_i \equiv \frac{\hat{a}^\dagger_{i,1} - \hat{a}^\dagger_{i,2}}{\sqrt{2}}, \tag{4.35}$$

$$\hat{t}^\dagger_{0,i} \equiv \frac{\hat{a}^\dagger_{i,1} + \hat{a}^\dagger_{i,2}}{\sqrt{2}}, \tag{4.36}$$

These operators act on the FP state $|\text{FP}\rangle$, where all spins point up:

$$\hat{s}^\dagger_i|\text{FP}\rangle = \frac{|\downarrow\uparrow\rangle_i - |\uparrow\downarrow\rangle}{\sqrt{2}} = |s\rangle_i, \tag{4.37}$$

$$\hat{t}^\dagger_{0,i}|\text{FP}\rangle = \frac{|\downarrow\uparrow\rangle_i + |\uparrow\downarrow\rangle}{\sqrt{2}} = |t_0\rangle_i. \tag{4.38}$$

Applying a Fourier transform and diagonalizing Eq. (4.34) yields:

$$\hat{\mathcal{H}}_{(\text{free hc})} = \sum_q \varepsilon^s_q \hat{s}^\dagger_q \hat{s}_q + \sum_q \varepsilon^t_q \hat{t}^\dagger_{0,q}\hat{t}_{0,q}, \tag{4.39}$$

with the dispersion relations:

$$\varepsilon^t(q) = (J_\parallel + J_\times)(\cos(q) - 1) + h, \tag{4.40}$$

$$\varepsilon^s(q) = (J_\parallel - J_\times)\cos(q) - (J_\parallel + J_\times) - 1 + h \tag{4.41}$$

The band minima determine the onset of condensation:

$$\varepsilon^t_{\text{min}} = \varepsilon^t(\pi) = h - 2(J_\parallel + J_\times), \tag{4.42}$$

$$\varepsilon^s_{\text{min}} = \begin{cases} \varepsilon^s(\pi) = h - 1 - 2J_\parallel & \text{if } J_\times < J_\parallel, \\ \varepsilon^s(0) = h - 1 - 2J_\times & \text{if } J_\times > J_\parallel. \end{cases} \tag{4.43}$$

The corresponding critical fields are:

$$h^t_c = 2(J_\parallel + J_\times), \tag{4.44}$$

$$h^s_c = \begin{cases} 1 + 2J_\parallel & \text{if } J_\times < J_\parallel, \\ 1 + 2J_\times & \text{if } J_\times > J_\parallel. \end{cases} \tag{4.45}$$

Comparing Eqs. (4.42) and (4.43) allows us to determine which excitation condenses first as a function of $J_\parallel$ and $J_\times$, thus identifying the critical field h_{FP}. The resulting phase boundaries are shown in Fig. 33.

Figure 33 – Critical field h_{FP} for the fully polarized state as a function of $J_\times$ and $J_\parallel$.

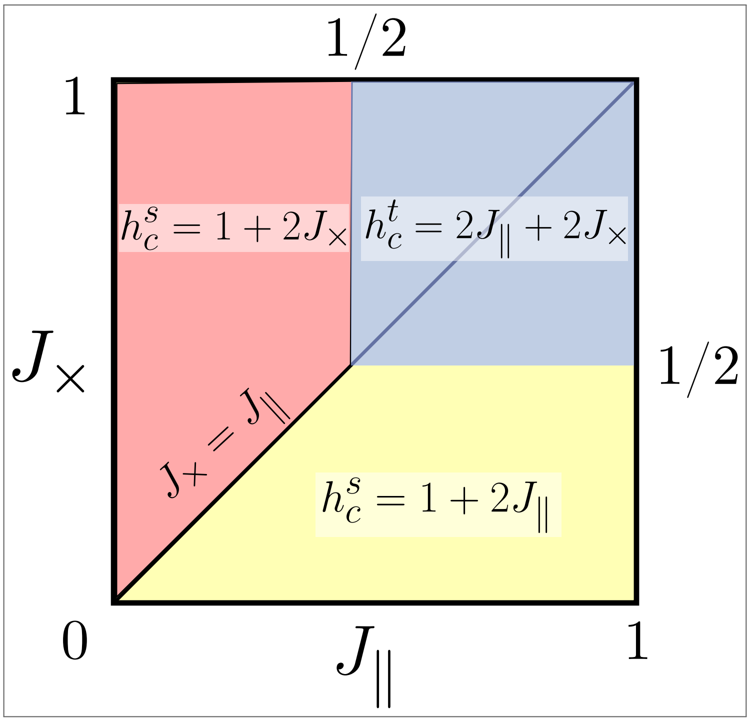

Source: Reference [47]

4.3 PHASE DIAGRAM

Figure 34 shows the phase diagram of the magnetization m as a function of the magnetic field h and the diagonal coupling $J_\times$ for a frustrated ladder with $J_\parallel = 0.55$ and system size $L = 128$ rungs. The color scale indicates the magnetization m, and the boundaries of the magnetization plateaus in the thermodynamic limit are indicated. For fixed $J_\times$, plateaus at $m = 0$, $1/2$, and 1 are generally bounded by second-order quantum phase transitions occurring at the critical fields h_{FP}, h_-, h_+, and h_{PM}. As these transitions are approached from the gapless Luttinger liquid phase [135], the Luttinger parameter K flows to characteristic values: $K \to 1$ at the boundaries of the FP and PM plateaus, and $K \to 1/4$ at the boundaries of the $m = 1/2$ plateau.

Nevertheless, the phase diagram also features first-order transitions. Specifically, for $J_\times = J_\parallel = 0.55$, both the PM-to-$m = 1/2$ and $m = 1/2$-to-FP transitions exhibit discontinuous jumps in the magnetization along the line h_f. This first-order transition line terminates at a bicritical point located at $J_\times = 0.5$, where the two second-order lines associated with the FP plateau merge.

The $m = 1/2$ plateau closes at two KTs transition points, characterized by the Luttinger parameter flowing to $K \to 1/2$ from the gapless side. These transitions occur at

$$(J_{\times,\,\mathrm{KT}_1}, h_{\mathrm{KT}_1}) = (0.255 \pm 0.005,\ 1.467 \pm 0.002), \tag{4.46}$$

$$(J_{\times,\,\mathrm{KT}_2}, h_{\mathrm{KT}_2}) = (0.935 \pm 0.005,\ 1.98 \pm 0.01). \tag{4.47}$$

Figure 34 – DMRG-derived phase diagram of magnetic field h versus frustration $J_\times$ for $J_\parallel = 0.55$ in the thermodynamic limit. Magnetization m is color-coded for a system with $L = 128$ rungs. Gapped plateaus at $m = 1$ (fully polarized, FP), $m = 1/2$, and $m = 0$ (paramagnetic, PM) are bounded by h_{FP}, h_+, h_-, and h_{PM}, respectively. Gapless Luttinger liquid (LL) phases lie between plateaus. The Luttinger parameter K approaches 1 (FP, PM) or 1/4 ($m = 1/2$) at second-order transitions from the LL side and 1/2 at Kosterlitz-Thouless (KT) transitions (●) closing the $m = 1/2$ plateau. A first-order transition line h_f, marked by magnetization jumps, begins at a bicritical point (♦) on h_{FP} and includes two points (●) at $J_\times = J_\parallel$.

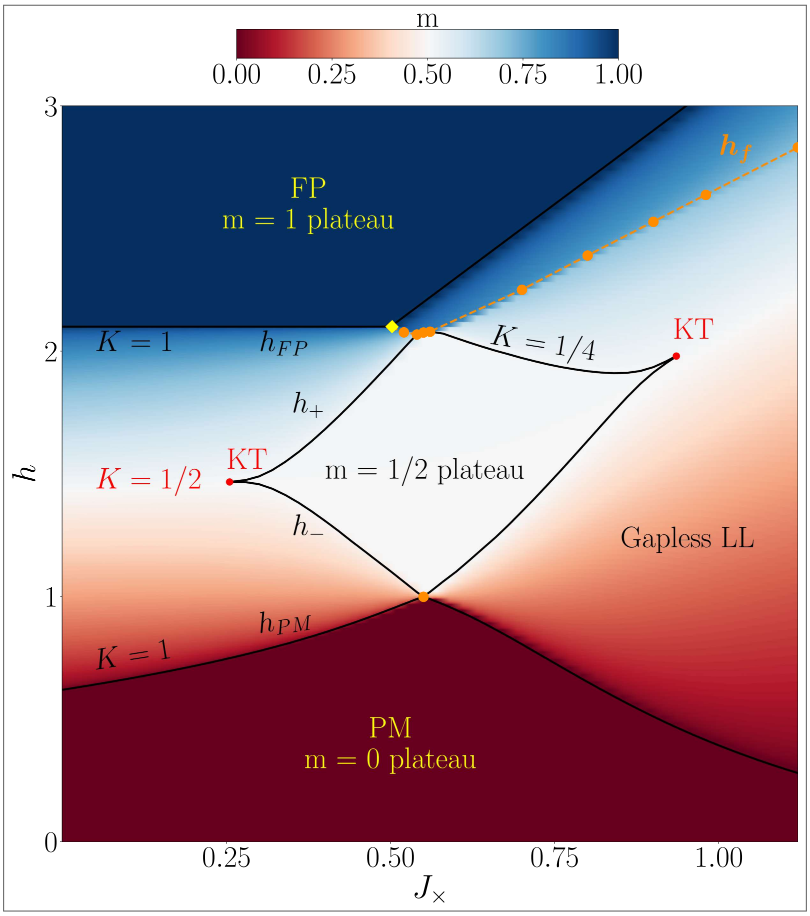

Source: Reference [47]

4.3.1 First-Order Phase Transition

The magnetization jump observed in Fig. 31 indicates a first-order transition between singlet and triplet $|t_0\rangle$ states. The probability densities of singlets and triplets on rung i are given by:

$$\langle \hat{n}_i^s \rangle = \langle \hat{s}_i^\dagger \hat{s}_i \rangle = \frac{1}{4} - \langle \hat{\mathbf{S}}_{i,1} \cdot \hat{\mathbf{S}}_{i,2} \rangle + \langle \hat{n}_{i,1} \hat{n}_{i,2} \rangle \approx \frac{1}{4} - \langle \hat{\mathbf{S}}_{i,1} \cdot \hat{\mathbf{S}}_{i,2} \rangle, \tag{4.48}$$

$$\langle \hat{n}_i^{t_0} \rangle = \langle \hat{t}_{0,i}^\dagger \hat{t}_{0,i} \rangle = \frac{3}{4} - \langle \hat{S}_i^z \rangle + \langle \hat{\mathbf{S}}_{i,1} \cdot \hat{\mathbf{S}}_{i,2} \rangle - \langle \hat{n}_{i,1} \hat{n}_{i,2} \rangle \approx \frac{3}{4} - \langle \hat{S}_i^z \rangle + \langle \hat{\mathbf{S}}_{i,1} \cdot \hat{\mathbf{S}}_{i,2} \rangle, \tag{4.49}$$

where the contribution from $\langle \hat{n}_{i,1} \hat{n}_{i,2} \rangle$ is neglected, which is nonzero if the rung is in the triplet state $|t_{-1}\rangle$, which has a low probability of occurrence.

The corresponding system-wide densities are defined as:

$$\langle \hat{n}_s \rangle = \frac{1}{L} \sum_{i=1}^{L} \langle \hat{n}_i^s \rangle, \quad \langle \hat{n}_{t_0} \rangle = \frac{1}{L} \sum_{i=1}^{L} \langle \hat{n}_i^{t_0} \rangle. \tag{4.50}$$

Figure 35 displays $\langle \hat{n}_s \rangle$ and $\langle \hat{n}_{t_0} \rangle$ as functions of m for $J_\times = 0.75$ (main panel) and $J_\times = 0.4$ (inset), in the range $0.5 < m < 1$.

Figure 35 – DMRG results for singlet $\langle \hat{n}_s \rangle$ and triplet $\langle \hat{n}_{t_0} \rangle$ densities versus magnetization m for $J_\parallel = 0.55$, $J_\times = 0.75$, and $L = 128$. Magnetization states within the jump occur for $0.70 < m < 0.78$. Inset: same parameters except $J_\times = 0.4$

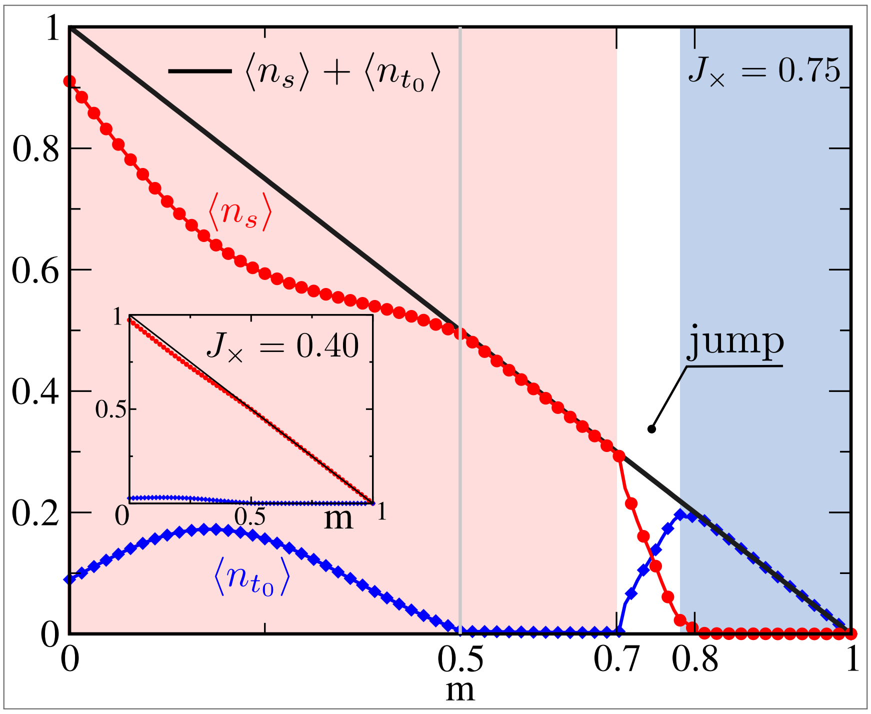

Source: Reference [47]

For $J_\times = 0.75$, a clear first-order transition occurs at $h = h_f$, leading to a discontinuous magnetization jump (see also Fig. 33). In the magnetized phase $m_f \approx 0.78 < m < 1$, the system is fully dominated by triplets, with $\langle \hat{n}_s \rangle = 0$ and $\langle \hat{n}_{t_0} \rangle \neq 0$. Conversely, in the interval $0.5 < m < 0.70$, singlets dominate, with $\langle \hat{n}_s \rangle \neq 0$ and $\langle \hat{n}_{t_0} \rangle = 0$. Within the narrow coexistence window $\Delta m \approx 0.08$, the system exhibits domain separation between singlet-rich and triplet-rich regions. In contrast, for $J_\times = 0.4$, no magnetization jump is observed, and singlet dominance persists throughout, with $\langle \hat{n}_s \rangle \neq 0$ and $\langle \hat{n}_{t_0} \rangle = 0$.

The nature of these phases is further elucidated by examining transverse spin correlations, defined as

$$\Gamma_{ij}(r) = \frac{1}{2} \langle \langle \hat{S}^+_{l,i} \hat{S}^-_{m,j} + \hat{S}^-_{l,i} \hat{S}^+_{m,j} \rangle \rangle_{|m-l|=r}. \tag{4.51}$$

where $\Gamma_{11}(r) = \Gamma_{22}(r)$ corresponds to correlations along the same leg, and $\Gamma_{12}(r) = \Gamma_{21}(r)$ to opposite-leg correlations. These correlators decay algebraically in the critical phases I, I′, and II, as shown in Fig. 36.

Figure 36 – Transverse spin correlations $\Gamma_{11}(r)$ (same leg) and $\Gamma_{12}(r)$ (different legs) near the fully polarized (FP) plateau for $J_\parallel = 0.55$, shown in the bottom panels. In phases I and I′, the singlet density $\langle \hat{n}_s \rangle \neq 0$ and triplet $|t_0\rangle$ density $\langle \hat{n}_{t_0} \rangle \approx 0$, while in phase II, $\langle \hat{n}s \rangle \approx 0$ and $\langle \hat{n}_{t_0} \rangle \neq 0$. The bicritical point (◆) is at $J_\times = 0.5$, $h = 1 + 2J_\parallel = 2.1$. The dashed line h_c^s denotes the singlet condensation critical line for the noninteracting model, and h_f is the first-order transition line from DMRG in the thermodynamic limit.

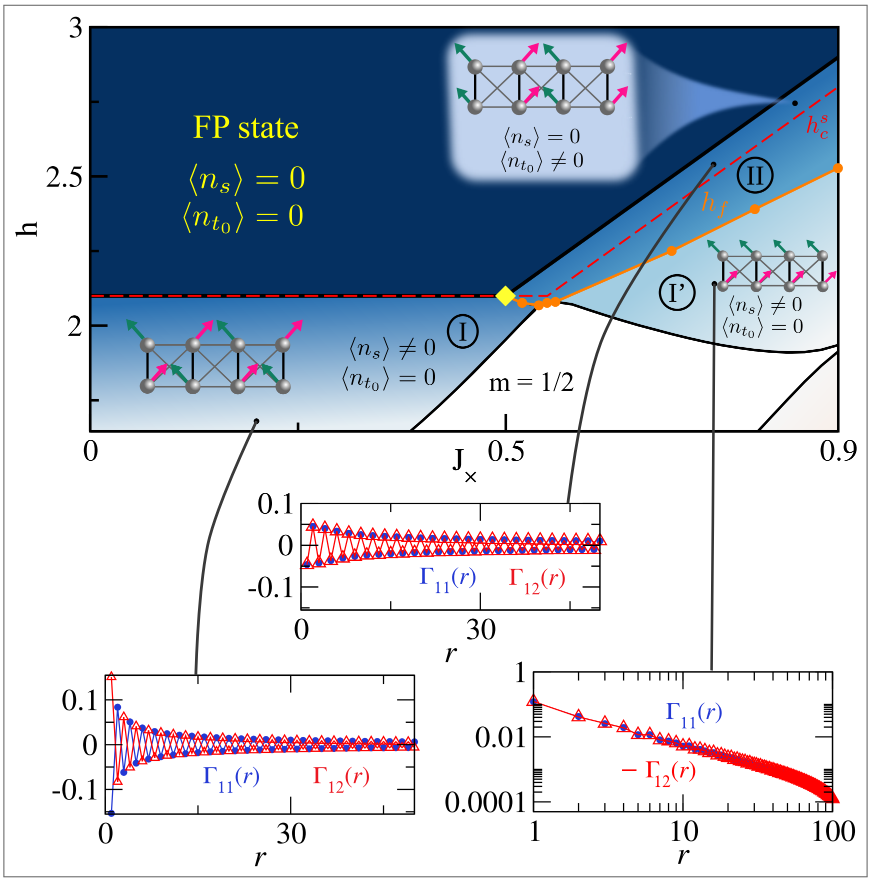

Source: Reference [47]

At the bicritical point ($J_\times = 0.5$, $h = 2.1$) [209–211], the critical phases I and II merge into the FP phase, where both $\langle \hat{n}_s \rangle$ and $\langle \hat{n}_{t_0} \rangle$ vanish and the excitation gap remains finite. For $J_\times < 0.5$, decreasing h drives a condensation of singlets, yielding $\langle \hat{n}_s \rangle \neq 0$ and $\langle \hat{n}_{t_0} \rangle = 0$ in phase I. For $J_\times > 0.5$, triplet $|t_0\rangle$ condensation occurs, with $\langle \hat{n}_s \rangle = 0$ and $\langle \hat{n}_{t_0} \rangle \neq 0$ in phase II, which maps onto a spin–1 chain in a magnetic field [49, 52, 53].

The transition from phase II to phase I or I′ along the line $h_f(J_\times)$ is of first order, as is the transition from the $m = 1/2$ plateau to phase II at $J_\times \approx J_\parallel$. All three phases— I, I′, and II—are gapless and characterized by distinct local configurations: rungs in phases I and I′ are in superpositions of singlets and $|t_1\rangle$ triplets, while in phase II, they are in $|t_0\rangle$ triplets. At $h = h_f$, the energy becomes flat as a function of magnetization in the thermodynamic limit, indicating a degenerate ground state for $m_i^{(\text{jump})} < m < m_f^{(\text{jump})}$ and macroscopic phase separation between singlet-rich (I or I′) and triplet-rich (II) domains.

Figure 37 presents the phase diagram for $0.5 \leq m \leq 1$, $0.5 \leq J_\times \leq 1.12$, and $L = 128$.

Figure 37 – DMRG results for the magnetization jump boundaries $m_i^{(\text{jump})}$ (lower) and $m_f^{(\text{jump})}$ (upper) versus $J_\times$ at $J_\parallel = 0.55$. Data are shown for $L = 128$ (•) and the thermodynamic limit $L \to \infty$ ($*$), with error bars $\Delta m = 1/128$. Phases I, I′, and II correspond to Fig.36. The bicritical point at $J_\times = 0.5$, $m = 1$ ($h = 2.1$) and the Kosterlitz-Thouless (KT) point are marked. Inset: singlet ($\langle \hat{n}_s \rangle$) and triplet $|t_0\rangle$ ($\langle \hat{n}_{t_0} \rangle$) probability densities along the chain for $J_\times = 0.52$, $m = 102/128$ and $J_\times = 0.55$, $m = 90/128$.

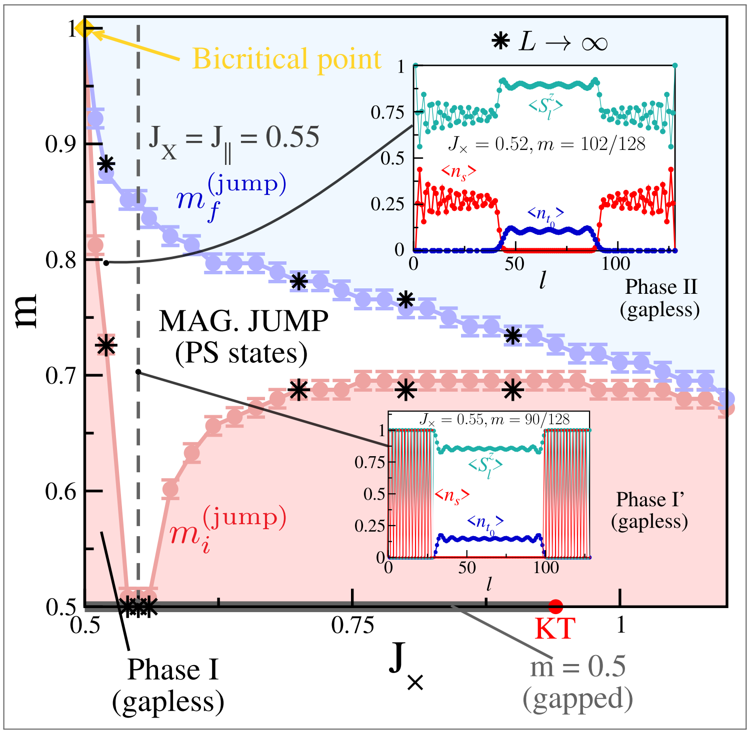

Source: Reference [47]

The phase separation region spans from the bicritical point at ($J_\times = 0.5$, $m = 1$) to the termination point of the magnetization jump at $J_\times \gtrsim 1.1$. Within the coexistence region $m_i^{(\text{jump})} < m < m_f^{(\text{jump})}$, phase II coexists with phase I for $0.5 < J_\times < 0.55$, and with phase I′ for $J_\times > 0.55$. At $J_\times = J_\parallel$, phase II also coexists with the $m = 1/2$ plateau.

4.3.2 Kosterlitz-Thouless Transition Points

At the KT transitions, the magnetization remains fixed at $m = 1/2$, and the excitation gap Δh closes with an essential singularity. On the gapless side, the transverse spin correlations $\Gamma_{ij}(r)$ (Eq. (4.51)) follow the asymptotic behavior of Eq. (4.21) with Luttinger parameter $K = 1/2$, indicating broken translational symmetry and one boson per two rungs [135].

To estimate the critical coupling J_c in finite systems with open boundaries, we extrapolate the thermodynamic-limit value of K based on the known critical condition $K = 1/2$ at $J = J_c$ [87, 212]. Figures 38(a) and (b) display $\Gamma_{11}(r)$ for two representative values of $J_\times$ at $m = 1/2$. Fits to Eq. (4.21) yield estimates for K. Because K depends on the fitting range r in systems with open boundaries [212], we perform fits over multiple intervals and extrapolate the resulting K values, as shown in Figs. 38(c) and (d).

Figure 38 – Transverse spin correlations $\Gamma_{11}(r)$ and Luttinger parameter K at $m = 1/2$, $J_\parallel = 0.55$. (a) $(-1)^r\Gamma_{11}(r)$ for $J_\times = 0.25$; (b) $\Gamma_{11}(r)$ for $J_\times = 0.95$; both for $L = 128, 192, 256$. (c,d) K vs $1/L$ for $J_\times = 0.25$ and 0.95, respectively, from fits to $1/r^{1/2K}$ over $r \in [8, 16], [16, 32], [32, 48]$. Extrapolated $K = (K_{\min} + K_{\max})/2$ with error $\delta K = (K_{\max} - K_{\min})/2$.

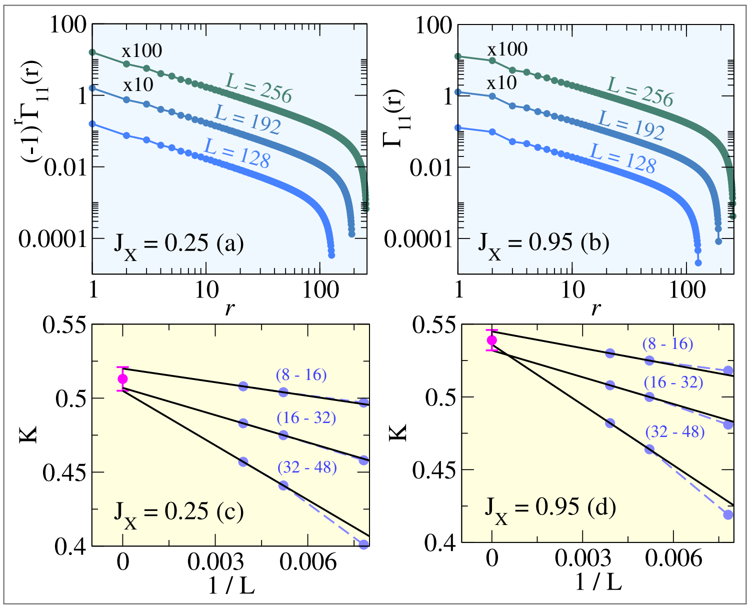

Source: Reference [47]

The extrapolated thermodynamic-limit value of K is estimated as the midpoint of its range over the two largest system sizes:

$$K = \frac{K_{\max} + K_{\min}}{2}, \quad \delta K = \frac{K_{\max} - K_{\min}}{2} \tag{4.52}$$

Figures 39(a) and (b) present K versus $J_\times$ near the two KT transitions, for $J_\times < J_\parallel$ and $J_\times > J_\parallel$, respectively. The critical couplings are identified as:

$$J_{\times,\,\mathrm{KT}_1} = 0.255 \pm 0.005, \quad J_{\times,\,\mathrm{KT}_2} = 0.935 \pm 0.005. \tag{4.53}$$

The corresponding critical fields h_{KT_1} and h_{KT_2} are determined by extrapolating the plateau boundaries h_- and h_+ at $m = 1/2$, for $J_\times$ values close to the critical points (Figs. 39(c,d)):

$$h_{\mathrm{KT}_1} = 1.467 \pm 0.002, \quad h_{\mathrm{KT}_2} = 1.98 \pm 0.01. \tag{4.54}$$

Figure 39 – (a, b) Thermodynamic-limit Luttinger parameter K versus $J_\times$ near Kosterlitz-Thouless transitions, with critical points $J_{\times,\,\mathrm{KT}_1} = 0.255 \pm 0.005$ and $J_{\times,\,\mathrm{KT}_2} = 0.935 \pm 0.005$. (c, d) Extrapolation of critical fields h_-, h_+ at $m = 1/2$ to the thermodynamic limit, yielding $h_{\mathrm{KT}_1} = 1.467 \pm 0.002$ and $h_{\mathrm{KT}_2} = 1.98 \pm 0.01$.

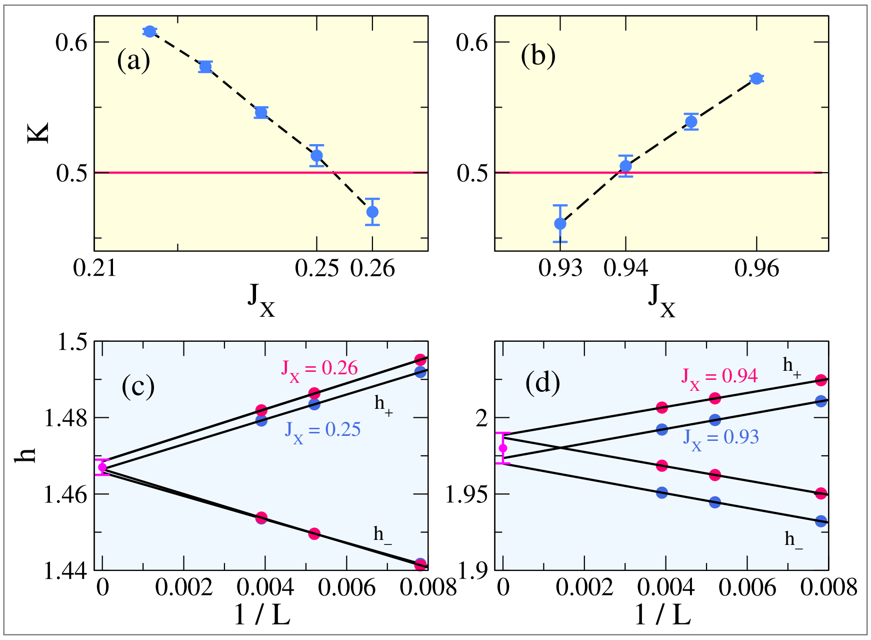

Source: Reference [47]

In the regime described by Eq. (4.22), the system maps onto an spin$-\frac{1}{2}$ XXZ chain, for which the Bethe ansatz predicts a KT transition at $J_\times = J_\parallel/3$ for $J_\times < J_\parallel$. For $J_\parallel = 0.55$, this yields $J_\times = 0.18$, which deviates from the numerical result $J_{\times,\,\mathrm{KT}_1} = 0.255 \pm 0.005$ by a correction of order $\sim J^2_{\times,\,\mathrm{KT}_1}$. For $J_{\times,\,\mathrm{KT}_2} = 0.935 \pm 0.005$, the mapping becomes unreliable as $J_\times \approx J_\parallel$.

Exploiting symmetry under leg exchange, we generalize the KT transition curves for $J_{\parallel} = 0.2$, 0.55, and 0.8, and include the corresponding symmetric points, as shown in Fig. 40. The critical lines are well described by perturbative fits:

$$\mathrm{KT}_1: \quad J_{\times} = \frac{J_{\parallel}}{3} + 0.16J_{\parallel}^2 + 0.12J_{\parallel}^3, \tag{4.55}$$

$$\mathrm{KT}_2: \quad J_{\times} = 3J_{\parallel} - 3.77J_{\parallel}^2 + 2.60J_{\parallel}^3. \tag{4.56}$$

Figure 40 – KT transitions in the $J_{\times}$ versus $J_{\parallel}$ plane. Calculated points (●) and symmetric points (●) are shown, with error bars smaller than or equal to symbol size. Solid lines $J_{\times} = J_{\parallel}/3$ and $J_{\times} = 3J_{\parallel}$ represent perturbation theory results. Dashed lines are fits to KT_1 ($J_{\parallel}/3 + 0.16J_{\parallel}^2 + 0.12J_{\parallel}^3$) and KT_2 ($3J_{\parallel} - 3.77J_{\parallel}^2 + 2.60J_{\parallel}^3$).

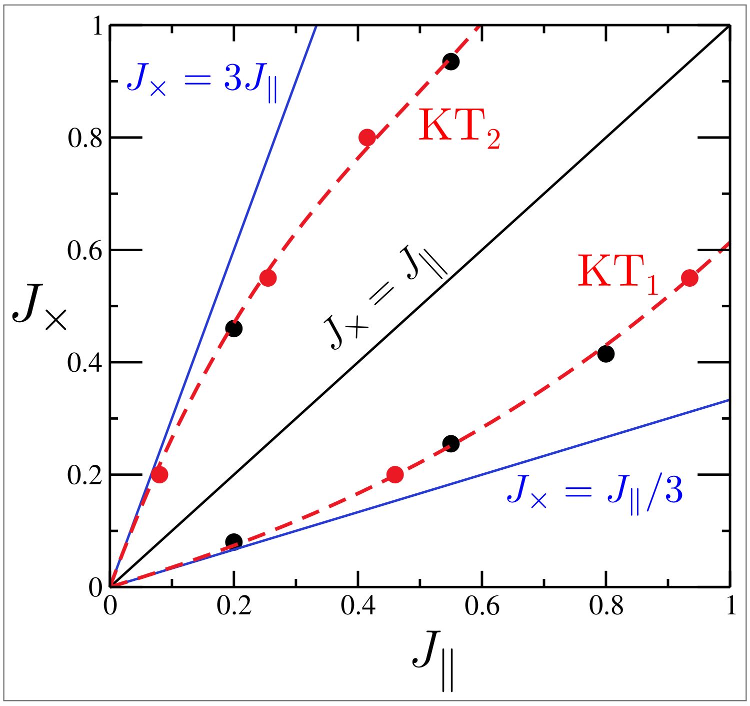

Source: Reference [47]

4.3.3 Other Phase Diagrams

We now examine the phase diagrams for $J_{\parallel} = 0.2$ and $J_{\parallel} = 0.8$, shown in Figs. 41(a) and 41(b), respectively. For $J_{\parallel} = 0.2$, no bicritical point or first-order transition line is observed, as the minima of the singlet and triplet bands do not cross for $J_{\parallel} < 0.5$ (see Fig. 33). In contrast, for $J_{\parallel} = 0.8$, a bicritical point emerges at $J_{\times} = 0.5$, $h = 1 + 2J_{\parallel}$, consistent with the expected behavior for $J_{\parallel} > 0.5$.

Figure 41 – (b) DMRG phase diagram of magnetic field h versus frustration $J_\times$ for $J_\parallel = 0.8$. Thermodynamic-limit transition lines are derived from finite-size scaling of magnetization m versus h, with m color-coded for $L = 128$. The diagram highlights fully polarized (FP), gapped paramagnetic (PM), gapless Luttinger liquid (LL), and singlet Haldane phases, with Luttinger parameter K at incommensurate transitions, Kosterlitz-Thouless (KT) points, a first-order transition line (dashed), and a bicritical point (♦). (c) Intradimer correlation $\langle \mathbf{S}_{l,1} \cdot \mathbf{S}_{l,2} \rangle$ versus $J_\times$ for fixed h, with first-order transitions marked (orange lines) as in (b).

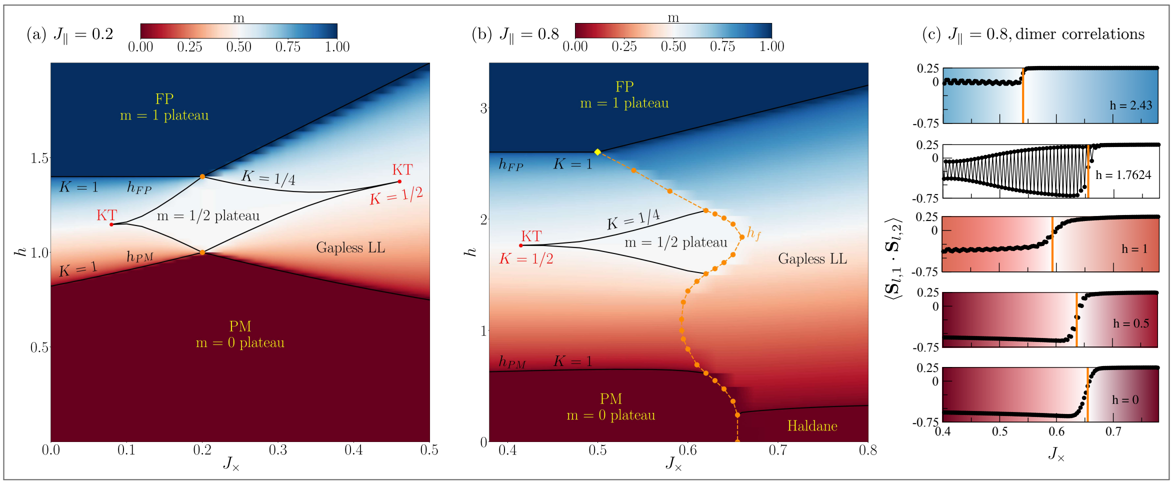

Source: Reference [47]

4.3.3.1 *Case:* $J_\parallel = 0.2$

At $J_\parallel = 0.2$, two first-order transitions occur at $J_\times = J_\parallel = 0.2$: one between the $m = 0$ and $m = 1/2$ plateaus at $h = 1$, and another between the $m = 1/2$ and $m = 1$ plateaus at $h = h_{\mathrm{FP}}$. Each transition point lies at the junction of four second-order lines, delineating coexistence regions between disordered phases: $m = 0$ with $m = 1/2$, and $m = 1/2$ with $m = 1$. The surrounding Luttinger liquid phases ($0 < m < 1/2$ at $h = 1$ and $1/2 < m < 1$ at $h = h_{\mathrm{FP}}$) merge with these disordered phases, analogously to the scenario at $J_\times = J_\parallel = 0.55$, $h = 1$ (Fig. 34).

The $m = 1/2$ plateau closes via KT transitions for both $J_\times < J_\parallel$ and $J_\times > J_\parallel$. DMRG simulations show that the ground state is a coherent superposition of $|t_1\rangle$ triplets and $|s\rangle$ singlets, similar to the case $J_\parallel = 0.55$, $J_\times = 0.4$ (Fig. 35).

According to Landau theory, a tetracritical point arises at the intersection of four second-order lines separating three ordered phases [209, 210]. However, at $J_\times = J_\parallel = 0.2$, both $h = 1$ and $h = h_{\mathrm{FP}}$ involve disordered phases ($m = 0$, $1/2$, or 1), thus precluding classification as a tetracritical point.

4.3.3.2 Case $J_{\parallel} = 0.8$

The phase diagram for $J_{\parallel} = 0.8$ features both a bicritical point and a first-order transition line. In contrast to the $J_{\parallel} = 0.2$ and 0.55 cases, the $m = 1/2$ plateau closes via a KT transition only for $J_{\times} < J_{\parallel}$. For $J_{\times} > J_{\parallel}$, no KT transition occurs due to the steeper decline of the singlet condensation field, driven by interactions that go beyond the free hard-core boson picture.

While finite-size scaling identifies the phase boundaries, additional insight is gained from dimer correlations $\langle \mathbf{S}_{l,1} \cdot \mathbf{S}_{l,2} \rangle$. In simulations with a spatially varying $J_{\times}$ at fixed h [213], a linear gradient of $J_{\times}$ is applied along the ladder (Fig. 41(c)). Across the first-order transition (orange line), the correlation takes $\langle \mathbf{S}_{l,1} \cdot \mathbf{S}_{l,2} \rangle = 0.25$ in phase II (right side), resembling a spin–1 chain, and varies from approximately -0.75 to 0 on the left side as h increases from 0 to 2.43.

At $m = 0$, the right side of the first-order line (phase II) realizes a gapped Haldane phase with nontrivial topology, in contrast to the trivial gapped PM ($m = 0$) state on the left.

5 MIXED-SPIN LADDER

One-dimensional spin–$\frac{1}{2}$ ladder models constitute a fundamental framework for investigating interacting quantum systems in reduced dimensions. The prototypical spin–$\frac{1}{2}$ two-leg ladder is known to possess a gapped singlet ground state accompanied by short-range spin correlations. In contrast, mixed-spin ladders—where the spin magnitudes and exchange couplings alternate along the rungs or legs—can give rise to ferrimagnetic ground states, as anticipated by the Lieb–Mattis theorem [75]. A substantial body of work [64–66, 68, 69, 71–74] has been devoted to exploring these systems, revealing a rich variety of ground-state phases and quantum phenomena. Notably, ferrimagnetic order is not exclusive to mixed-spin ladders but also emerges in other one-dimensional quantum spin models, where it exhibits remarkable and often unconventional features [77, 78].

Alternating spin chains composed of spin–$(\frac{1}{2}, 1)$ and spin–$(\frac{1}{2}, \frac{5}{2})$ units exhibit ferrimagnetic ground states characterized by quantized magnetization plateaus. In particular, the former system displays a $1/3$ magnetization plateau [79–84], while the latter supports both $1/3$ and $2/3$ plateaus [85]. Recent studies employing the DMRG method have investigated various aspects of these systems, including density-dependent magnon hopping, magnon-magnon interactions within the spin–wave framework, and the presence of edge states [86].

In certain anisotropic spin models, the $1/3$ plateau vanishes via a KT-type transition [87], a phenomenon also observed in anisotropic ferrimagnetic chains [88–90]. By contrast, isotropic spin–$\frac{1}{2}$ trimer systems exhibit a robust $1/3$ plateau without undergoing a KT transition [91].

The Hamiltonian describing the alternating spin–(s, S) ladder in the presence of an external magnetic field h is given by

$$\begin{aligned}\hat{\mathcal{H}} = J \sum_{j} \left[\hat{\mathbf{s}}_j^{(1)} \cdot \hat{\mathbf{S}}_j^{(1)} + \hat{\mathbf{s}}_j^{(2)} \cdot \hat{\mathbf{S}}_j^{(2)} + \hat{\mathbf{S}}_j^{(1)} \cdot \hat{\mathbf{s}}_{j+1}^{(1)} + \hat{\mathbf{s}}_j^{(2)} \cdot \hat{\mathbf{S}}_{j+1}^{(2)} \right] \\ + J_{\perp} \sum_{j} \left[\hat{\mathbf{s}}_j^{(1)} \cdot \hat{\mathbf{S}}_j^{(2)} + \hat{\mathbf{S}}_j^{(1)} \cdot \hat{\mathbf{s}}_j^{(2)} \right] - h\hat{S}^z, \qquad (5.1)\end{aligned}$$

where $\hat{\mathbf{s}}_j^{\alpha}$ and $\hat{\mathbf{S}}_j^{\alpha}$ are spin operators located at unit cell j and leg $\alpha = 1, 2$, with quantum numbers s and S, respectively. These satisfy $(\hat{\mathbf{s}}_j^{\alpha})^2 = s(s+1)$ and $(\hat{\mathbf{S}}_j^{\alpha})^2 = S(S+1)$. The exchange coupling along the legs is denoted by $J = 1$, which sets the energy scale. The parameter $J_\perp$ represents the rung coupling, and $\hat{S}^z$ is the total spin z-component, with $g\mu_B \equiv 1$.

Figure 42 – (a) Spin-(s, S) ladder with a four-spin unit cell (two spins of each type) and periodicity $2u$, where u is the rung spacing. The leg coupling J sets the scale; phases are tuned via $J_\perp$. (b) Swapping spins on alternate rungs reduces the periodicity to u. (c) Folded and unfolded Brillouin zones for $J_\perp = -0.5$ in a system with $L = 20$ rungs.

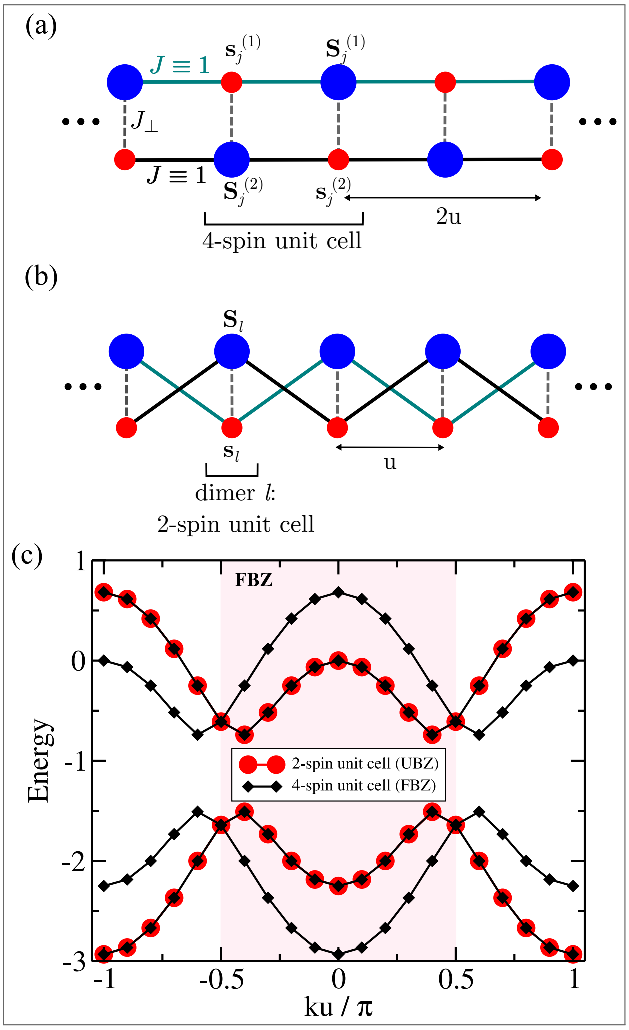

Source: Reference [74]

For analytical approaches such as spin–wave theory, it is convenient to consider a unit cell of size $2u$, where u denotes the spacing between neighboring rungs (see Fig. 42(a)). This unit cell contains four spins—two of magnitude s and two of magnitude S—resulting in four magnon bands and a first Brillouin zone (*Folded Brillouin Zone* (FBZ)) of size $k = 2\pi/2u$. The Hamiltonian is invariant under a glide reflection symmetry [214, 215], which combines a translation by u with leg exchange $(1 \leftrightarrow 2)$. This symmetry permits the use of a reduced unit cell containing only one rung (two spins: s and S), leading to two magnon bands and an *Unfolded Brillouin Zone* (UBZ) of size $k = 2\pi/u$. Upon reindexing the spins accordingly (see Fig. 42(b)), the Hamiltonian takes the simplified form:

$$\hat{\mathcal{H}} = J_\perp \sum_j \hat{\mathbf{s}}_j \cdot \hat{\mathbf{S}}_j + \sum_j \left(\hat{\mathbf{s}}_j \cdot \hat{\mathbf{S}}_{j+1} + \hat{\mathbf{S}}_j \cdot \hat{\mathbf{s}}_{j+1} \right) - h\hat{S}^z, \tag{5.2}$$

where j indexes the rungs.

In the presence of a magnetic field, these systems develop a quantized magnetization plateau at $s^z = S - s = 1/2$ per unit cell. For the decoupled case $J_\perp = 0$, the critical fields are given by $h_- = 0$ and $h_+ = \Delta$, where Δ denotes the gap to the next magnetization sector. More generally, the critical fields can be computed as

$$h_\pm = \left| E[s^z = (S - s) \pm 1, h = 0] - E[s^z = (S - s), h = 0] \right|, \tag{5.3}$$

where $E[s^z, h = 0]$ denotes the ground state energy in the sector with total magnetization s^z at zero field.

5.1 THE ALTERNATING SPIN–$(\frac{1}{2}, 1)$ LADDER

For $s = 1/2$ and $S = 1$, Eq. (5.3) predicts a magnetization plateau at one third of the fully polarized value. The critical fields in the thermodynamic limit, $h_-(J_\perp)$ and $h_+(J_\perp)$, were determined via DMRG simulations combined with finite-size scaling [74]. The resulting phase diagram is shown in Fig. 43.

At $J_\perp = 0$, the system consists of two decoupled alternating spin chains with $(1/2, 1)$ rungs, each with a unit cell of length $2u$ (see Fig. 42(a)). The ground state carries a total spin $1/2$ per unit cell, corresponding to $1/3$ of the fully polarized magnetization, in agreement with the Lieb-Mattis theorem. The system displays long-range ferrimagnetic order with a spin gap $\Delta \approx 1.76$ [80–84] for spin-raising excitations, while spin-lowering excitations remain gapless due to spontaneous breaking of spin-rotational symmetry.

For $J_\perp < 0$, the conditions of the Lieb-Mattis theorem no longer apply, and the ground state becomes a singlet ($S_{\text{GS}} = 0$) at $h = 0$. Nonetheless, the $1/3$ magnetization plateau remains stable for $J_\perp < 0$, with a finite lower critical field ($h_- > 0$). As $J_\perp$ increases, the plateau terminates at a KT transition where $h_- = h_+$ in the thermodynamic limit, with surrounding gapless regions in the LL universality class.

Figure 43 – DMRG-derived phase diagram of magnetic field h versus rung coupling $J_\perp$ for the $(1/2, 1)$ alternating spin ladder. Thermodynamic-limit transition lines are obtained via finite-size scaling of the per-rung magnetization m as a function of h. The color scale indicates m for a system with $L = 100$ rungs.

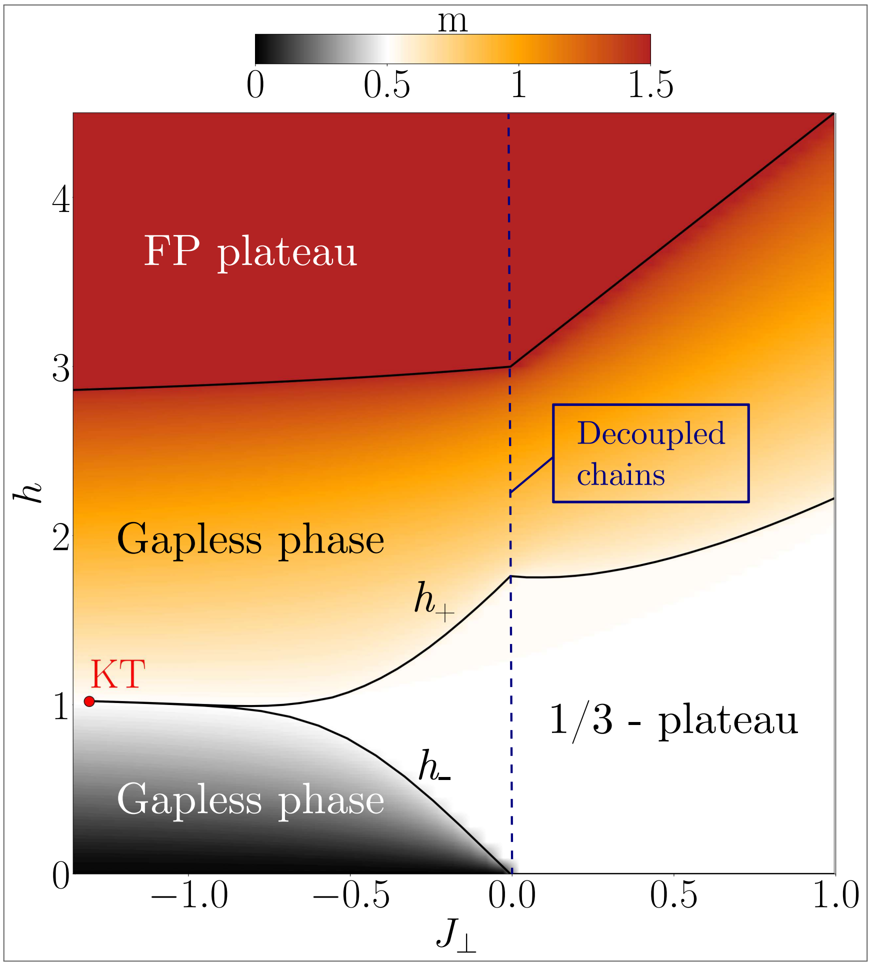

Source: Reference [74]

5.1.1 Spin-Wave Theory

Spin-wave theory provides a useful framework for analyzing the critical field of the FP plateau and other regions of the phase diagram for general s and S. Using the Holstein-Primakoff transformation, spin operators are mapped to bosonic variables:

$$\hat{s}^z = s - \hat{n}, \tag{5.4}$$

$$\hat{s}^+ = \sqrt{2s - \hat{n}}\hat{a}, \tag{5.5}$$

$$\hat{s}^- = \hat{a}^\dagger\sqrt{2s - \hat{n}}, \tag{5.6}$$

where $\hat{a}^\dagger$ and $\hat{a}$ are bosonic creation and annihilation operators, and $\hat{n} = \hat{a}^\dagger\hat{a}$. For large-$S$ expansions, a leading-order approximation is used:

$$\hat{s}^+ = \sqrt{2s}\left(1 - \frac{\hat{n}}{4s} + \mathcal{O}(s^2)\right)\hat{a} \approx \sqrt{2s}\hat{a}, \tag{5.7}$$

$$\hat{s}^- = \hat{a}^\dagger\sqrt{2s}\left(1 - \frac{\hat{n}}{4s} + \mathcal{O}(s^2)\right) \approx \sqrt{2s}\hat{a}^\dagger. \tag{5.8}$$

This is valid in the low-density regime.

Applying this to Eq. (5.2) for rung j yields:

$$\hat{s}_j^z = \frac{1}{2} - \hat{n}_{aj}, \qquad \hat{S}_j^z = 1 - \hat{n}_{bj}, \tag{5.9}$$

$$\hat{s}_j^+ = \hat{a}_j, \qquad \hat{S}_j^+ = \sqrt{2}\hat{b}_j, \tag{5.10}$$

$$\hat{s}_j^- = \hat{a}_j^\dagger, \qquad \hat{S}_j^- = \sqrt{2}\hat{b}_j^\dagger. \tag{5.11}$$

The interaction term $\hat{\mathbf{s}}_i \cdot \hat{\mathbf{S}}_j$ becomes:

$$\begin{aligned}\hat{\mathbf{s}}_i \cdot \hat{\mathbf{S}}_j &= \hat{s}_i^z\hat{S}_j^z + \frac{\hat{s}_i^+\hat{S}_j^- + \hat{S}_j^+\hat{s}_i^-}{2} \\ &= \hat{n}_{ai}(\hat{n}_{bj} - 1) - \frac{1 - \hat{n}_{bj}}{2} + \frac{\hat{a}_i\hat{b}_j^\dagger + \hat{b}_j\hat{a}_i^\dagger}{\sqrt{2}}.\end{aligned} \tag{5.12}$$

Substituting into Eq. (5.2), neglecting constants, and applying a Fourier transform gives:

$$\hat{\mathcal{H}} = \sum_k \left[t_{kk}(\hat{a}_k^\dagger\hat{b}_k + \hat{b}_k^\dagger\hat{a}_k) + (\varepsilon_a + h)\hat{n}_{ak} + (\varepsilon_b + h)\hat{n}_{bk}\right], \tag{5.13}$$

where $t_{kk} = (J_\perp + 2\cos ku)/\sqrt{2}$, $\varepsilon_a = -(J_\perp + 2)$, and $\varepsilon_b = -(J_\perp + 2)/2$.

Diagonalizing this Hamiltonian yields the dispersions:

$$\begin{aligned}\omega_h^{(\pm)}(k) &= \frac{\varepsilon_a + \varepsilon_b}{2} \pm \frac{1}{2}\sqrt{(\varepsilon_a - \varepsilon_b)^2 + 4t_{kk}^2} + h \\ &= -\frac{3}{4}(J_\perp + 2) \pm \frac{1}{4}\sqrt{(J_\perp + 2)^2 + 8(J_\perp + 2\cos ku)^2} + h.\end{aligned} \tag{5.14}$$

The FP state remains stable for h larger than the minimum of the lower band $\omega_h^{(-)}(k)$, which occurs at $k = 0$ for $J_\perp > 0$ and at $k = \pi/u$ for $J_\perp < 0$. Thus, the critical field for the onset of the FP plateau is:

$$h_{\mathrm{FP}}(J_\perp > 0) = -\omega_{h=0}^{(-)}(0) = \frac{3}{2}(J_\perp + 2), \tag{5.15}$$

$$h_{\mathrm{FP}}(J_\perp < 0) = -\omega_{h=0}^{(-)}\left(\frac{\pi}{u}\right) = \frac{3}{4}(J_\perp + 2) + \frac{1}{4}\sqrt{(J_\perp + 2)^2 + 8(J_\perp - 2)^2}. \tag{5.16}$$

The two bands for $h = 0$ are shown in Fig. 44.

Figure 44 – Lower $\omega^{(-)}(k)$ and upper $\omega^{(+)}(k)$ free spin-wave magnon bands, calculated from the classical ferromagnetic vacuum at zero magnetic field ($h = 0$). The bands are shown for $J_\perp$ ranging from -1 to 1 in steps of 0.2.

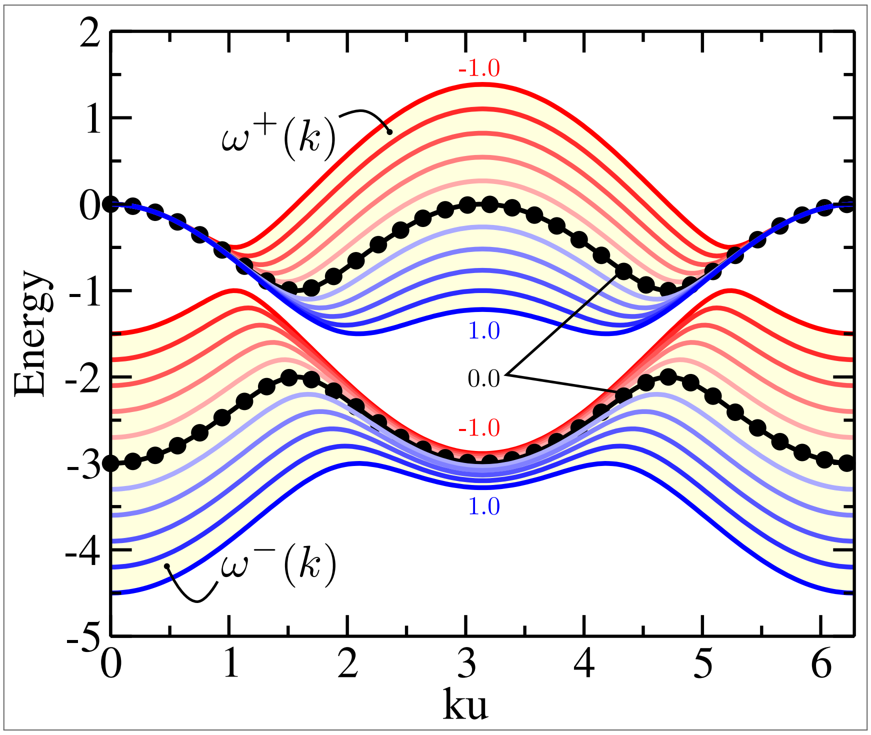

Source: Reference [74]

Interpreting magnons as hard-core bosons (equivalent to spinless fermions), the 1/3 magnetization plateau corresponds to full occupancy of the lower band, whose number of states matches the number of rungs. The plateau width is given by the band gap, as shown in Fig. 43. However, spin-wave theory predicts a gap closure ($h_- = h_+$) at $J_\perp = -2$, $h = 0$, which deviates from DMRG results [74]:

$$J_{\perp,\mathrm{KT}} = -1.32 \tag{5.17}$$

$$h_{\mathrm{KT}} = 1.02 \tag{5.18}$$

5.1.2 Magnetization

The magnetization on spin–$\frac{1}{2}$, spin–1, and full $(\frac{1}{2}, 1)$ rungs for $J_\perp = -0.25$ and 0.25 is shown in Fig. 45(a), obtained via DMRG simulations with an h-scan from $h = 0$ to $h \approx 3.39$. The FP critical fields match Eqs. (5.15) and (5.16):

$$h_{\mathrm{FP}}(J_\perp = -0.25) = 2.96, \tag{5.19}$$

$$h_{\mathrm{FP}}(J_\perp = 0.25) = 3.38. \tag{5.20}$$

Figure 45 – DMRG results showing average magnetizations of spin-$\frac{1}{2}$ and spin-1 sites, and the average rung magnetization, from h-scan calculations for (a) $J_\perp = 0.25$ and (b) $J_\perp = -0.25$. (c) Comparison of critical fields estimated from h-scans with those obtained via finite-size scaling of per-rung magnetization curves.

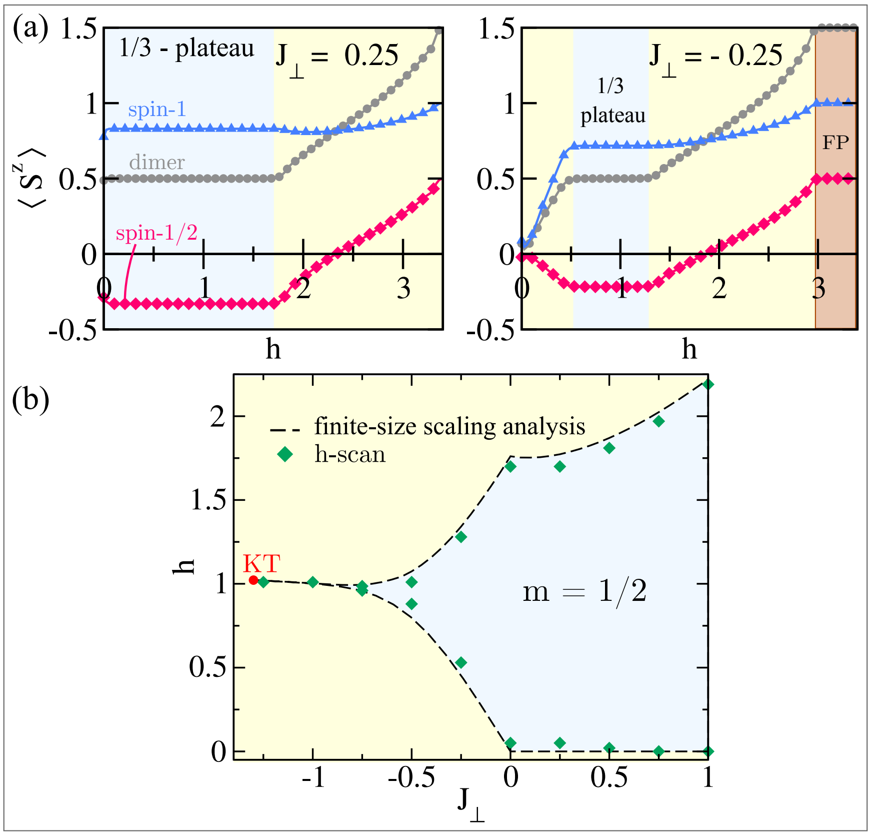

Source: Reference [74]

Ferrimagnetic order is visible in the 1/3 plateau for both values of $J_\perp$. Magnon occupancy at spin–1/2 sites, $\langle \hat{n}_a \rangle = 1/2 - \langle \hat{S}^z_a \rangle$, exceeds that at spin–1 sites, $\langle \hat{n}_b \rangle = 1 - \langle \hat{S}^z_b \rangle$, for rung magnetizations between $m = 0.5$ and full polarization. This asymmetry originates from the local potential difference:

$$\Delta\varepsilon = \varepsilon_a - \varepsilon_b = -\frac{1}{2}(J_\perp + 2). \tag{5.21}$$

For $J_\perp = -0.25$, the reduced $\Delta\varepsilon$ diminishes the imbalance. In the range $0 < m < 0.5$, magnon occupancy at spin–1 sites rises steeply while it decreases at spin–1/2 sites, as the total rung magnon density $\langle \hat{n}_{\text{rung}} \rangle = 1.5 - m$ exceeds 1, highlighting the role of interaction effects.

Critical fields h_- and h_+ extracted from finite-size scaling and h-scans show excellent agreement. For $J_\perp < 0$, the gap becomes small, making h_- and h_+ harder to resolve. Centering h-scans around the expected critical fields improves accuracy in these regimes.

Rung magnetization from $J_\perp$-scans—where $J_\perp$ varies linearly across the system under fixed h—is shown in Fig. 46. Results from uniform systems with $J_\perp = -0.4$ and -0.25 closely match the $J_\perp$-scan data at $h = 0.45$, except for minor boundary effects near the plateau's critical point.

Figure 46 – The average rung magnetization, computed using DMRG for a $J_\perp$-scan at $h = 0.45$, is shown in the main plot. The inset displays results for $h = 0.45$, 1.35, and 2.5. Critical transition points J_c to the 1/3-plateau are marked for $h = 0.45$ and 1.35.

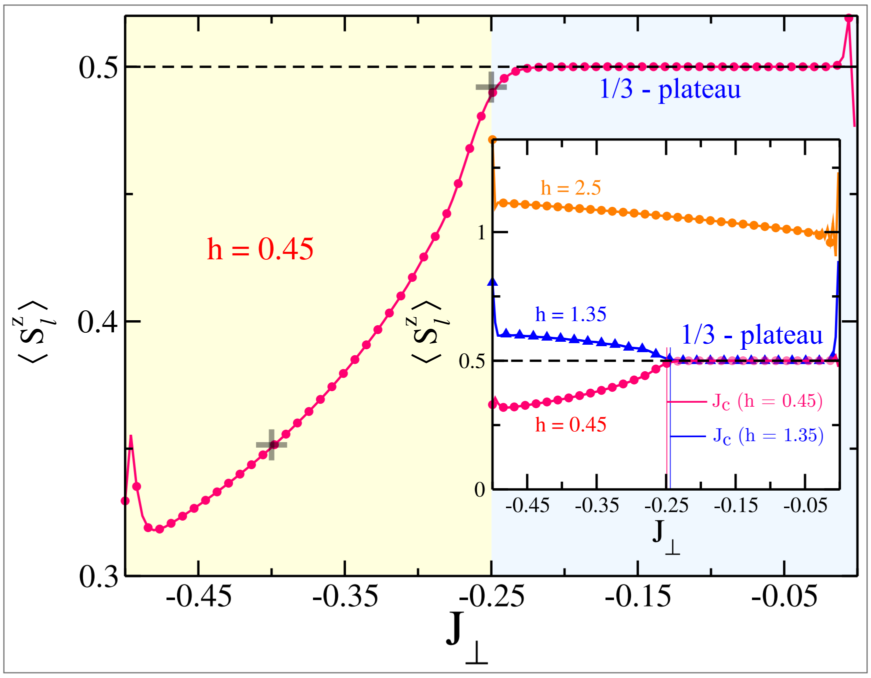

Source: Reference [74]

The inset of Fig. 46 displays rung magnetization for $J_\perp$-scans at $h = 2.5$, 1.35, and 0.45. At $h = 2.5$, the system never reaches the 1/3 plateau ($m = 0.5$), while at $h = 1.35$ and 0.45, the plateau becomes visible. The corresponding critical values of $J_\perp$ match those in Fig. 43. For $h = 0.45$, the plateau is approached from below, while for $h = 1.35$, magnetization remains above $m = 0.5$ as $J_\perp$ decreases past the critical point.

5.2 KOSTERLITZ-THOULESS TRANSITION

In gapless phases, the transverse spin correlation function exhibits a power-law decay at long distances:

$$\Gamma(r) \sim r^{-1/2K}, \tag{5.22}$$

where K is the Luttinger parameter. At the 1/3 magnetization plateau, the system hosts two bosons per unit cell, corresponding to integer filling. The KT transition occurs when $K = 2$ [135]. To locate this transition, the magnetization is fixed at the 1/3-plateau value ($m = 1/2$), and $J_\perp$ is varied to identify the point where $K = 2$. In practice, finite-size effects and the exponentially small energy gap near the KT transition render this determination nontrivial.

5.2.1 Transverse Spin Correlations

Figure 47 presents transverse spin correlation functions between spin–$\frac{1}{2}$ and spin–1 sites within the same rung and along the ladder for representative values of $J_\perp$ in both the $J_\perp < 0$ and $J_\perp > 0$ regimes.

Figure 47 – (a) Transverse spin correlation function between spin-1/2 and spin-1 sites on the same rung, computed using DMRG for $J_\perp = -0.25$ and $J_\perp = 0.25$ in an h-scan, for a system size $L = 128$. Local extrema are indicated by triangles. (b) Transverse spin correlation function $\Gamma(r)$ for specified magnetization per rung m and $J_\perp$ values, calculated for $L = 128$. (c) Schematic of short-range magnetic order for the indicated m and $J_\perp$ values.

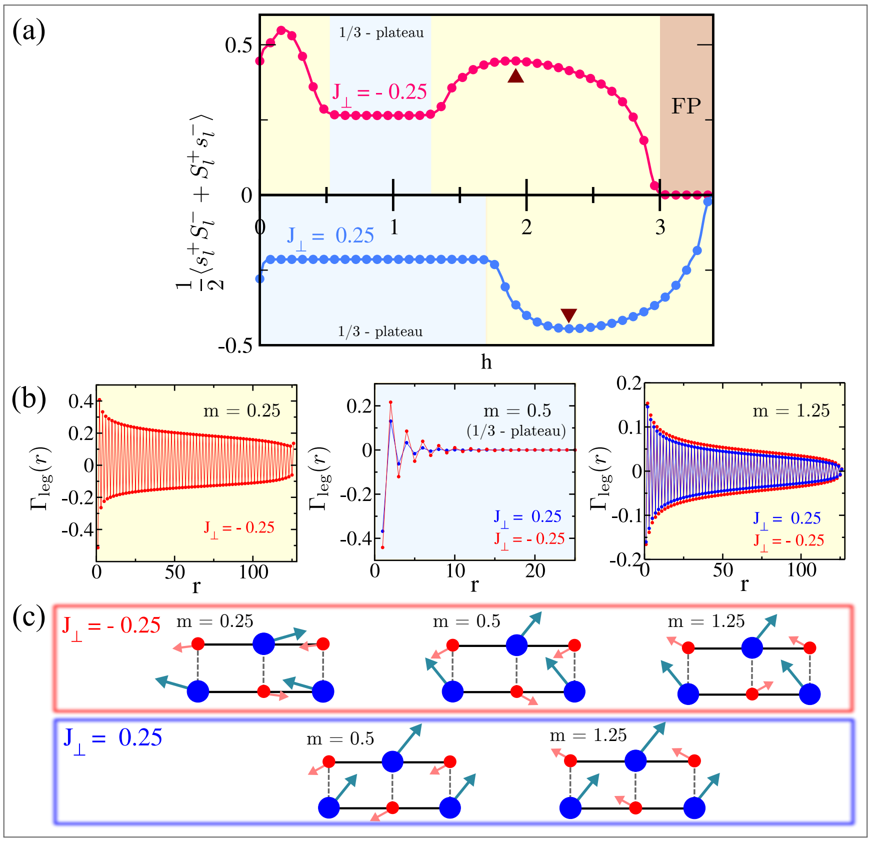

Source: Reference [74]

The transverse spin correlation function is defined as:

$$C_{ij} = \frac{1}{2}\langle \hat{S}_i^+ \hat{S}_j^- + \hat{S}_j^+ \hat{S}_i^- \rangle, \tag{5.23}$$

where i and j denote ladder sites. In Fig. 47(a), for $J_\perp < 0$, the transverse correlation remains positive from $h = 0$ up to the saturation field. Semiclassically, spin–$\frac{1}{2}$ and spin–1 projections in the xy-plane align in the same direction, as illustrated in Fig. 47(c). For $J_\perp > 0$, the spin projections on each rung point in opposite directions, also depicted in Fig. 47(c). In both cases, correlations remain stable within the plateau regions. Local extrema, marked by triangles, appear near the field where the spin–$\frac{1}{2}$ magnetization vanishes, as observed in Fig. 45(a).

The transverse spin correlation along a ladder leg is shown in Fig. 47(b) and defined as:

$$\Gamma_{\text{leg}}(r)_L = \langle C_{ij} \rangle_{|l(i)-l(j)|=r}, \tag{5.24}$$

for a system of size L, where $l(i)$ denotes the rung index of site i. A spatial average over all site pairs on the same leg separated by distance r mitigates boundary effects. In the gapless phases ($m = 0.25$ and $m = 1.25$), correlations follow the power-law behavior characteristic of the LL phase, except at large distances due to open boundary conditions. In contrast, for the $m = 0.5$ plateau, the correlation decays exponentially, indicating a gapped phase. For both signs of $J_\perp$, leg correlations alternate in sign, consistent with the semiclassical configurations shown in Fig. 47(c). Magnetization profiles of spin–$\frac{1}{2}$ and spin–1 sites, displayed in Fig. 46, further corroborate this picture.

5.2.2 Identifying KT Transition Points

The correlation function in Eq. (5.22) is evaluated for system sizes $L = 128$, 192, and 256 over a range of $J_\perp$ values near the anticipated transition. Figures 48(a) and 48(b) show representative cases for $J_\perp = -1.4$ and $J_\perp = -1.2$, respectively.

To estimate the Luttinger parameter K in the thermodynamic limit, the correlation data are fitted to Eq.(5.22) over the distance intervals (8,16), (16,32), and (32,48) for each system size. The resulting K values are extrapolated to the infinite-size limit, as illustrated in Figs. 48(c) and 48(d). The extrapolated K and its uncertainty are estimated from the variation across system sizes as $L \to \infty$.

Finally, Fig. 48(e) plots K as a function of $J_\perp$ near the transition. The crossing point with $K = 2$ yields an estimate for the KT transition:

$$J_{\perp,\text{KT}} = -1.32 \pm 0.02, \tag{5.25}$$

This estimate is supported by the error behavior: errors are larger in the gapped region, where finite-size effects dominate, and become negligible in the gapless phase, where the correlation length diverges.

Figure 48 – DMRG results for the transverse spin correlation function $(-1)^r\Gamma(r)$, with r as the distance along a ladder leg, at $m = 1/3$ for (a) $J_\perp = -1.4$ and (b) $J_\perp = -1.2$, shown for system sizes L as indicated. The Luttinger parameter K is computed for (c) $J_\perp = -1.4$ and (d) $J_\perp = -1.2$ by fitting the correlation data to $r^{-1/(2K)}$ over distance intervals $8 \leq r \leq 16$, $16 \leq r \leq 32$, and $32 \leq r \leq 48$. (e) Thermodynamic-limit K versus $J_\perp$ near the Kosterlitz-Thouless (KT) transition, with the critical point estimated at $J_{\perp,\mathrm{KT}} = -1.32 \pm 0.02$.

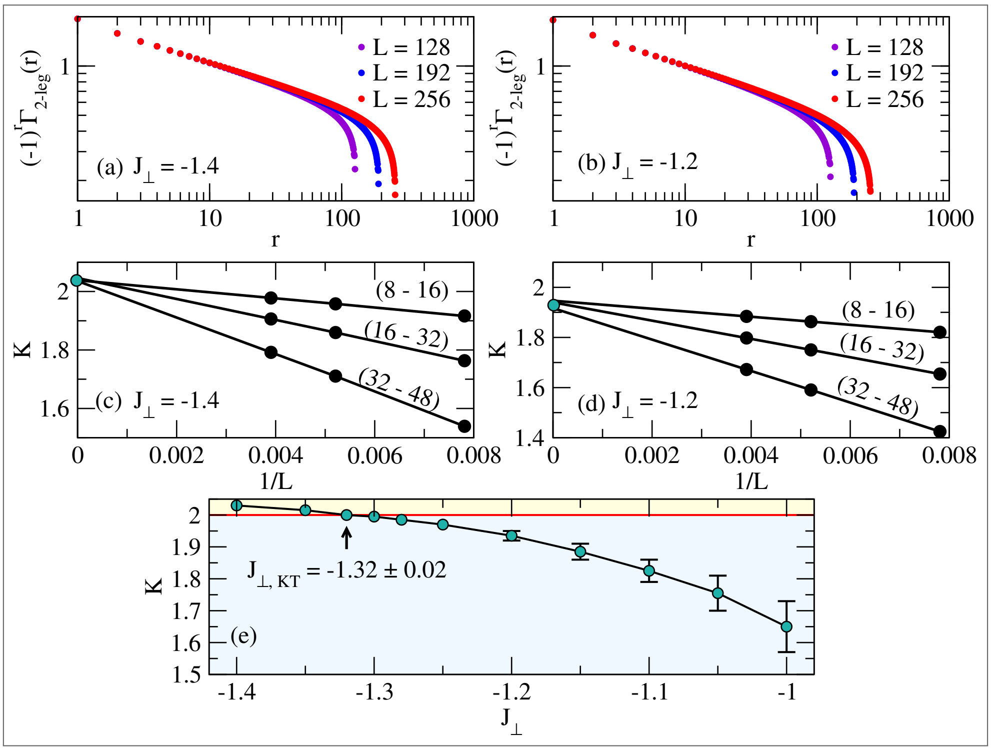

Source: Reference [74]

6 COUPLED TWO-LEG LADDERS

The preceding chapters focused on isolated two-leg ladders, including both frustrated and mixed-spin variants. In this chapter, we turn our attention to coupled spin-$\frac{1}{2}$ two-leg ladders with both nearest-neighbor and diagonal exchange interactions. While two-leg ladders have been extensively investigated through analytical and numerical techniques—leading to a nearly complete characterization of their phase diagrams—the determination of precise phase boundaries remains an open problem. In contrast, fully 2D quantum spin systems, despite substantial research over the past decades, are far less understood. Their increased complexity and the significantly higher computational demands pose formidable challenges relative to their 1D and quasi-1D counterparts.

Low-dimensional quantum systems host a variety of emergent phenomena, including the LL phase, which is restricted to 1D. Coupled spin ladders thus offer an appealing theoretical framework for probing emergent 2D physics while retaining the analytical tractability and numerical accessibility of quasi-1D models. However, the phase diagram of 2D coupled ladders remains largely unexplored, particularly in the presence of frustration, making it a fertile ground for further investigation. Most prior studies have focused on unfrustrated coupled ladders, since standard techniques for studying frustrated 2D quantum magnets—such as Quantum Monte Carlo—are hindered by the *minus-sign problem*.

Experimentally, several materials have been identified as realizations of coupled spin ladder systems [98, 99, 102, 216]. These compounds provide valuable platforms to test theoretical predictions and to explore exotic quantum phases. Advances in experimental techniques such as inelastic neutron scattering, nuclear magnetic resonance, and other spectroscopic probes have revealed signatures of spin gap formation, quantum criticality, and phases stabilized by frustration and interladder coupling. Further experimental efforts—particularly under extreme conditions such as high magnetic fields or ultra-low temperatures—hold the potential to unveil novel aspects of the intricate interplay between dimensionality, frustration, and quantum correlations in these systems.

6.1 N COUPLED LADDERS

A system of N coupled spin$-\frac{1}{2}$ two-leg ladders can be represented as a single $2N$-leg ladder with alternating rung couplings, as illustrated in Figure 49. The corresponding Hamiltonian is given by

$$\hat{\mathcal{H}} = \sum_{i=1}^{L}\left[J_\perp \sum_{\substack{k=1\\ \text{odd}}}^{2N-1} \hat{\mathbf{S}}_{i,k}\cdot\hat{\mathbf{S}}_{i,k+1} + J'_\perp \sum_{\substack{k=2\\ \text{even}}}^{2N-1} \hat{\mathbf{S}}_{i,k}\cdot\hat{\mathbf{S}}_{i,k+1}\right] + J_\parallel \sum_{i=1}^{L-1}\sum_{k=1}^{2N} \hat{\mathbf{S}}_{i,k}\cdot\hat{\mathbf{S}}_{i+1,k}, \tag{6.1}$$

where $\hat{\mathbf{S}}_{i,k}$ denotes the spin$-\frac{1}{2}$ operator at rung position i and leg k, and $0 \leq J'_\perp \leq J_\perp$. The limits $J'_\perp = 0$ and $J'_\perp = J_\perp$ correspond, respectively, to decoupled two-leg ladders and a uniform $2N$-leg ladder. The former exhibits independent RS states on each ladder with a finite gap for $J_\perp > 0$ and a critical point at $J_{\perp,\,\mathrm{c}} = 0$. In contrast, the latter is characterized by an extended, uniform geometry. These limiting cases provide useful benchmarks for understanding the behavior of the intermediate regime.

Figure 49 – Schematic of coupled two-leg ladders. Thick lines denote antiferromagnetic exchange couplings within each ladder ($J_\perp$, $J_\parallel$), and dashed lines indicate interladder couplings ($J'_\perp$). All couplings are positive.

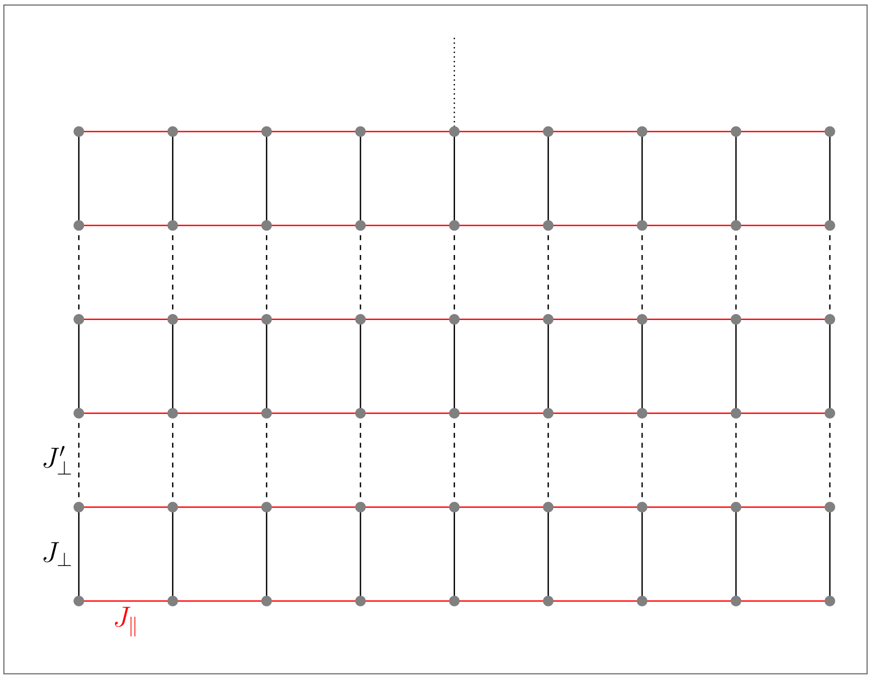

Source: The author (2025).

When $J_\perp = J'_\perp$, the model describes a uniform $2N$-leg ladder, an even-leg quasi-2D system. As discussed in Section 3.4, such systems exhibit a finite spin gap at the isotropic point $J_\perp = J_\parallel$. Fixing $J_\parallel > 0$ as the energy scale, the phase diagram can be explored by tuning $J_\perp$. In the strong-rung limit $J_\perp \gg J_\parallel$, the system effectively consists of decoupled $2N$-spin rungs, forming a product of singlet states with an energy gap that scales as $\Delta \sim J_\perp$ [176]. Numerical estimates at the isotropic point $J_\perp = J_\parallel = J$ yield $\Delta_2 = 0.5J$ ($N = 1$), $\Delta_4 = (0.16 \pm 0.01)J$ ($N = 2$), and $\Delta_6 = 0.05J$ ($N = 3$) [168, 171].

Nishiyama *et al.* [217] demonstrated that the four-leg ladder exhibits a RVB structure (see Figure 50), with a phase diagram qualitatively similar to the two-leg case. They identified two distinct disordered phases, one for $J_\perp > 0$ and another for $J_\perp < 0$, separated by a critical point at $J_{\perp,\,\mathrm{c}} = 0$. Their findings suggest that the RVB character is a generic feature of even-leg ladders.

Figure 50 – Schematic of the expected resonating valence bond (RVB) state in a four-leg ladder. The RVB pattern (a) dominates for $J_\perp > 0$, and pattern (b) dominates for $J_\perp < 0$.

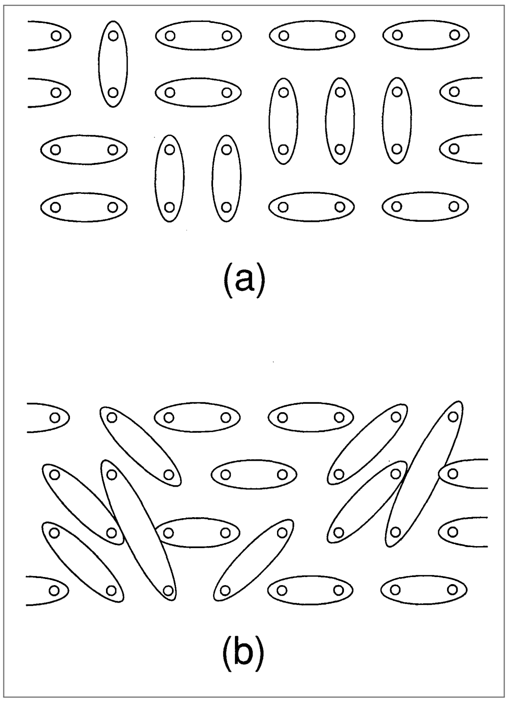

Source: Reference [217]

Figure 51 shows the ground state configuration for a four-leg ladder at $J_\perp = 1$. In the strong-rung regime ($J_\parallel = 0.2$), the ground state is predominantly composed of singlets on each rung. As $J_\parallel$ increases, these singlets resonate and delocalize along the leg direction, reducing local rung-singlet correlations. As the number of legs $2N$ increases, the gap decreases due to enhanced singlet delocalization. This behavior follows an exponential decay [170]:

$$\Delta_{\mathcal{N}} \sim \mathcal{N} S^2 \exp\left(-S\mathcal{N}a\right), \tag{6.2}$$

where a is a constant, S is the spin magnitude, and $\mathcal{N}$ is the even number of legs.

Figure 51 – DMRG results for the ground state of a spin-$\frac{1}{2}$ four-leg ladder with $L = 32$ rungs, open boundary conditions, and couplings $J_\perp = J'_\perp = 1$. Panels show $J_\parallel = 0.2$ (a), $J_\parallel = 0.6$ (b), and $J_\parallel = 1$ (c). In (a), rung singlets are prominent. As $J_\parallel$ increases, singlets delocalize along the legs, weakening rung-singlet correlations. Calculations used a bond dimension of 3000 and a truncation error of 10^{-7}.

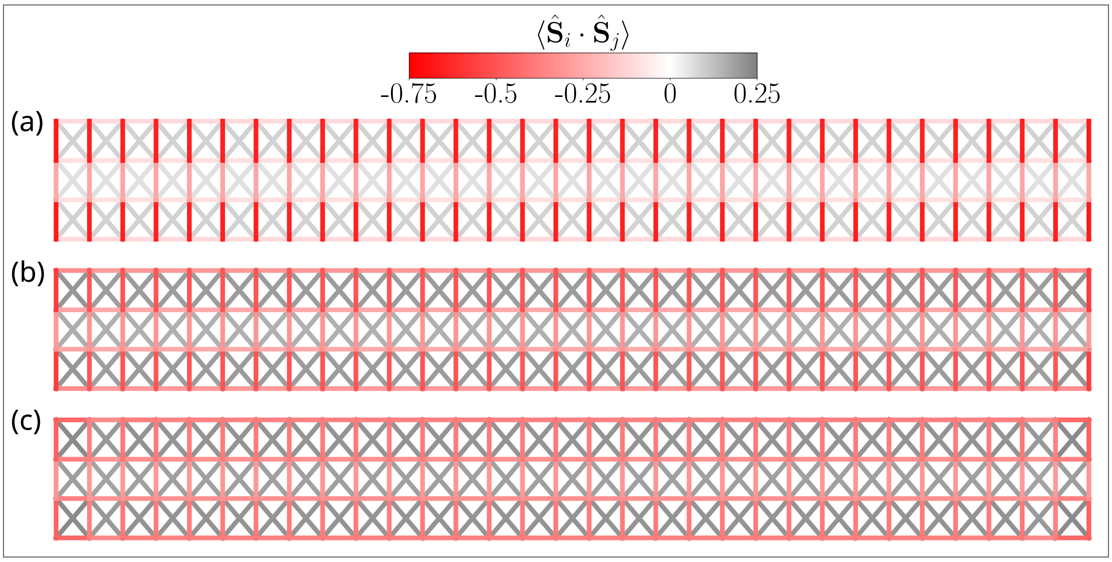

Source: The author (2025).

For the case $N = 2$, we investigate the spin gap and dimerization order parameters. The latter are defined as

$$D_\alpha = \frac{1}{N_\alpha} \sum_{\mathbf{i}} (-1)^{\mathbf{i}_\alpha} \langle \hat{\mathbf{S}}_{\mathbf{i}} \cdot \hat{\mathbf{S}}_{\mathbf{i}+\mathbf{e}_\alpha} \rangle, \tag{6.3}$$

where $\alpha \in \{x, y\}$ denotes the spatial direction, $\mathbf{i} = (i_x, i_y)$ specifies the lattice site, and N_α is the total number of bonds in direction α. For a four-leg ladder of length L, we have $N_x = 4(L-1)$ and $N_y = 3L$. This quantity serves as an order parameter for detecting dimerized phases, such as a VBS. In contrast, an RVB state corresponds to a quantum superposition of multiple singlet coverings and does not exhibit fixed dimerization patterns. Accordingly, we expect $D_\alpha = 0$ in the RVB phase.

If even-leg ladders generically host RVB-type ground states with finite gaps, their phase diagram is expected to consist exclusively of disordered phases. As $J'_\perp$ is increased from zero, the system smoothly interpolates between decoupled two-leg ladders and a uniform $2N$-leg ladder, remaining within the same gapped phase for finite N. Therefore, no quantum phase transition is expected as long as $N \ll L/2$ remains, since the limiting states at $J'_\perp = 0$ and $J'_\perp = J_\perp$ are adiabatically connected. Numerical results for $N = 2$, shown in Figure 52, are consistent with this expectation.

Figure 52 – DMRG results for a spin-$\frac{1}{2}$ $2N$-leg ladder with $J_\perp = 1$. (a) Spin gap extrapolated to the thermodynamic limit for $N = 2$ and $N = 3$ at the isotropic point ($J_\perp = J_\parallel$). (b) Spin gap extrapolated for $N = 2$ at the non-isotropic point ($J_\parallel = J_\perp/2$). (c, d) Linear extrapolations of dimerization order parameters D_x and D_y, respectively, for $N = 2$ and $J_\parallel = J_\perp$. Calculations used a bond dimension of 3000 and a truncation error of 10^{-7}.

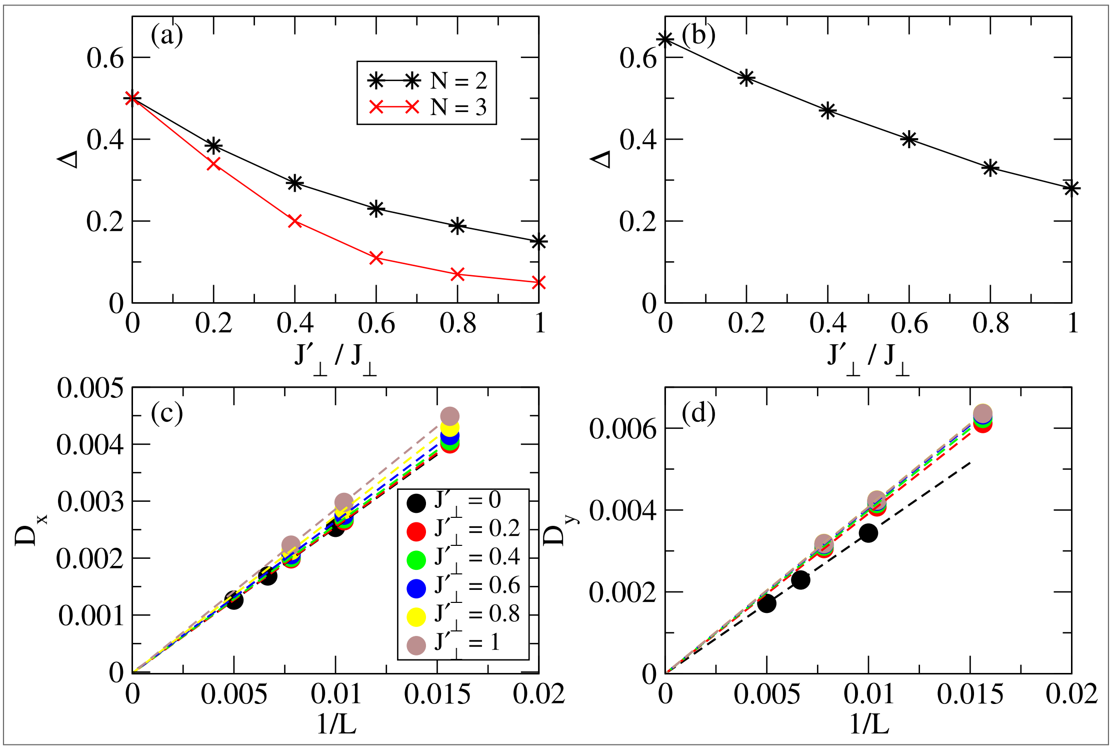

Source: The author (2025).

6.1.1 The Square Lattice Limit

For $N \ll L/2$, the system exhibits no phase transition. However, as N approaches $L/2$, the $2N$-leg ladder gradually approximates a 2D square lattice. Unlike finite even-leg ladders, which are gapped and exhibit short-range RVB correlations, the square lattice displays long-range Néel order. Despite their similar short-distance physics, the qualitative difference in long-range behavior implies the emergence of a quantum phase transition in the thermodynamic limit—from a disordered phase to one with long-range magnetic order.

Consider the case of isotropic couplings ($J_\perp = J_\parallel \equiv J$) in the limit $N \to L/2$. For $J'_\perp = 0$, the system consists of decoupled two-leg ladders in the gapped RVB phase. At the other extreme, $J'_\perp = J$ corresponds to a spin–$\frac{1}{2}$ AFM square lattice, characterized by Néel order and gapless excitations [218]. A quantum critical point emerges at a finite interladder coupling $J'_{\perp,\,\mathrm{c}} \approx 0.31J$, as reported by mean-field theory [33], quantum Monte Carlo simulations [92, 96], iPEPS calculations [219], and the coupled cluster method [105]. Experimental realizations of this transition are observed in materials such as $\mathrm{Ba_2CuTeO_6}$ [98, 99] and $\mathrm{C_9H_{18}N_2CuBr_4}$ [102].

For small N, tuning $J'_\perp$ interpolates smoothly between the disordered RVB phases of two-leg and even-leg ladders, with no indication of a phase transition. As N increases, however, the energy gap decreases exponentially, as described by Eq. (6.2), and square-lattice effects begin to dominate. This ultimately leads to the development of long-range order. Therefore, a genuine quantum phase transition arises between the disordered phase characteristic of finite-width ladders and the ordered phase of the square lattice in the 2D limit.

6.2 N COUPLED FRUSTRATED TWO-LEG LADDERS

Introducing diagonal exchange couplings $J_\times$ and $J'_\times$ into the system shown in Figure 49 results in a model of N coupled spin$-\frac{1}{2}$ frustrated two-leg ladders, illustrated in Figure 53.

Figure 53 – Schematic of coupled frustrated two-leg ladders. Thick lines denote antiferromagnetic couplings within each ladder ($J_\perp$, $J_\parallel$, $J_\times$), and dashed lines indicate interladder couplings ($J'_\perp$, $J'_\times$). All couplings are positive.

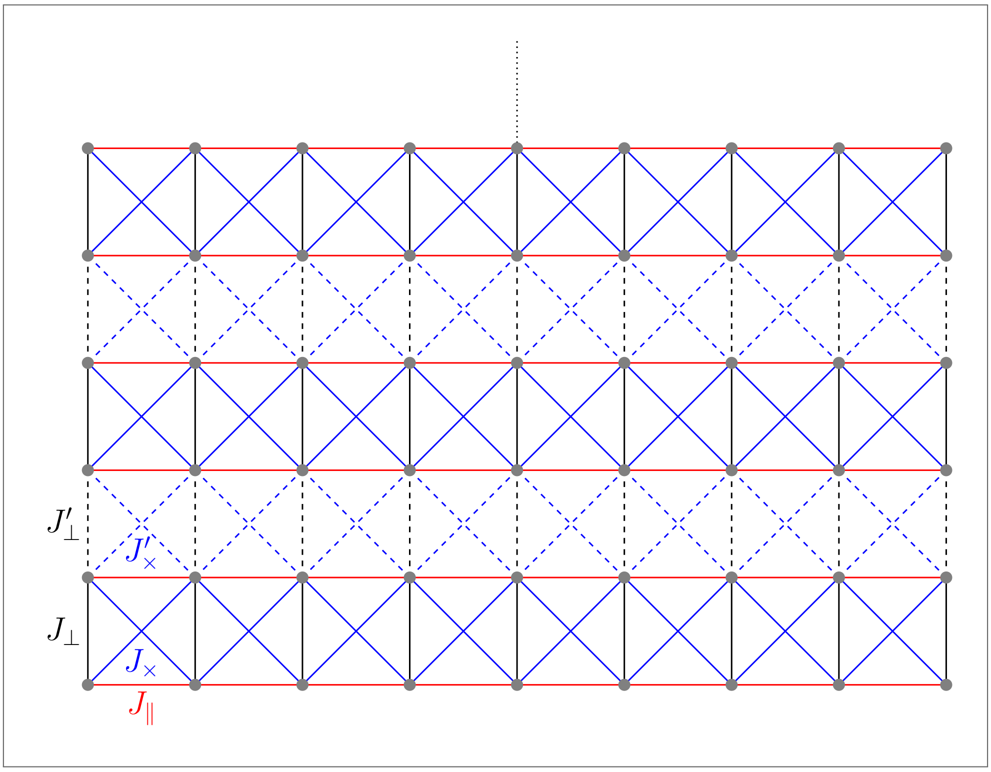

Source: The author (2025).

The corresponding Hamiltonian extends Eq. (6.1) and is given by:

$$\hat{\mathcal{H}} = \sum_{k=1}^{2N-1} \Big[\sum_{i=1}^{L} J_k^{(\text{rung})} \hat{\mathbf{S}}_{i,k} \cdot \hat{\mathbf{S}}_{i,k+1} + \sum_{i=1}^{L-1} J_k^{(\text{diag})} (\hat{\mathbf{S}}_{i,k} \cdot \hat{\mathbf{S}}_{i+1,k+1} + \hat{\mathbf{S}}_{i,k+1} \cdot \hat{\mathbf{S}}_{i+1,k}) \Big] + J_\parallel \sum_{k=1}^{2N} \sum_{i=1}^{L-1} \hat{\mathbf{S}}_{i,k} \cdot \hat{\mathbf{S}}_{i+1,k}. \tag{6.4}$$

Here, the rung and diagonal couplings alternate: $J_k^{(\text{rung})} = J_\perp$ for odd k and $J'_\perp$ for even k, while $J_k^{(\text{diag})} = J_\times$ (odd k) or $J'_\times$ (even k). We consider the parameter ranges $0 \le J'_\perp \le J_\perp$ and $0 \le J'_\times \le J_\times$. When $J'_\perp = J'_\times = 0$, the system consists of N decoupled frustrated two-leg ladders, which exhibit RS and Haldane ground states. On the other hand, setting $J'_\perp = J_\perp$ and $J'_\times = J_\times$ yields a uniform $2N$-leg frustrated ladder.

To facilitate the analysis, we define rung operators:

$$\hat{\mathbf{R}}_{i,k} = \hat{\mathbf{S}}_{i,k} + \hat{\mathbf{S}}_{i,k+1}, \quad \hat{\mathbf{D}}_{i,k} = \hat{\mathbf{S}}_{i,k} - \hat{\mathbf{S}}_{i,k+1}. \tag{6.5}$$

Using these definitions, the Hamiltonian becomes:

$$\begin{aligned} \hat{\mathcal{H}} &= \sum_{\substack{k=1 \\ \text{odd}}}^{2N-1} \left[\frac{J_\perp}{2} \sum_{i=1}^{L} \hat{\mathbf{R}}_{i,k}^2 + \frac{J_\parallel + J_\times}{2} \sum_{i=1}^{L-1} \hat{\mathbf{R}}_{i,k} \cdot \hat{\mathbf{R}}_{i+1,k} + \frac{J_\parallel - J_\times}{2} \sum_{i=1}^{L-1} \hat{\mathbf{D}}_{i,k} \cdot \hat{\mathbf{D}}_{i+1,k} \right] \\ &\quad + \sum_{\substack{k=2 \\ \text{even}}}^{2N-1} \left[\frac{J'_\perp}{2} \sum_{i=1}^{L} \hat{\mathbf{R}}_{i,k}^2 + \frac{J'_\times}{2} \sum_{i=1}^{L-1} (\hat{\mathbf{R}}_{i,k} \cdot \hat{\mathbf{R}}_{i+1,k} - \hat{\mathbf{D}}_{i,k} \cdot \hat{\mathbf{D}}_{i+1,k}) \right], & (6.6) \\ &= \sum_{\substack{k=1 \\ \text{odd}}}^{2N-1} \hat{\mathcal{H}}_k(J_\perp, J_\parallel, J_\times) + \sum_{\substack{k=2 \\ \text{even}}}^{2N-1} \hat{\mathcal{H}}'_k(J'_\perp, J'_\times). & (6.7) \end{aligned}$$

In this form, $\hat{\mathcal{H}}_k$ corresponds to the Hamiltonian of a single frustrated two-leg ladder, while $\hat{\mathcal{H}}'_k$ represents a two-leg ladder with rung coupling $J'_\perp$ and leg coupling $J'_\times$. The full Hamiltonian thus describes a system composed of N frustrated two-leg ladders and $N-1$ interleaved unfrustrated ladders.

The structure of the Hamiltonian leads to the following commutation relations:

$$[\hat{\mathcal{H}}_n, \hat{\mathcal{H}}_m] = [\hat{\mathcal{H}}'_n, \hat{\mathcal{H}}'_m] = 0 \quad \text{for all} \quad n, m, \tag{6.8}$$

since frustrated and unfrustrated ladders do not share sites among themselves. However, frustrated and unfrustrated ladders do share sites when adjacent, which leads to:

$$[\hat{\mathcal{H}}_n, \hat{\mathcal{H}}'_m] \neq 0 \quad \text{for} \quad m = n \pm 1, \tag{6.9}$$

$$[\hat{\mathcal{H}}_n, \hat{\mathcal{H}}'_m] = 0 \quad \text{for} \quad m \neq n \pm 1. \tag{6.10}$$

As discussed in Chapter 4, a single frustrated two-leg ladder is invariant under the exchange $J_\parallel \leftrightarrow J_\times$. In the coupled system, this symmetry remains valid only if $J'_\times \neq J_\times$; it is explicitly broken when $J'_\times = J_\times$ due to the presence of cross-coupling terms in Eq. (6.6).

To characterize different phases, we compute the average effective rung spin S, defined through the total rung spin operator:

$$\hat{S}_i = \sum_{k=1}^{2N} \hat{S}_{i,k}, \tag{6.11}$$

which leads to:

$$\hat{S}_i^2 = \sum_{k=1}^{2N} \hat{S}_{i,k}^2 + 2 \sum_{\alpha=1}^{2N-1} \sum_{\beta=\alpha+1}^{2N} \hat{S}_{i,\alpha} \cdot \hat{S}_{i,\beta}, \tag{6.12}$$

$$\langle \hat{S}_i^2 \rangle = \sum_{k=1}^{2N} \langle \hat{S}_{i,k}^2 \rangle + 2 \sum_{\alpha=1}^{2N-1} \sum_{\beta=\alpha+1}^{2N} \langle \hat{S}_{i,\alpha} \cdot \hat{S}_{i,\beta} \rangle, \tag{6.13}$$

$$S_i(S_i+1) = \frac{3N}{2} + 2 \sum_{\alpha=1}^{2N-1} \sum_{\beta=\alpha+1}^{2N} \langle \hat{S}_{i,\alpha} \cdot \hat{S}_{i,\beta} \rangle. \tag{6.14}$$

Here, S_i denotes the total spin on rung i, and $2N$ is the number of legs. The average effective rung spin is then computed as:

$$S = \frac{1}{L} \sum_{i=1}^{L} S_i, \tag{6.15}$$

with each S_i extracted from Eq. (6.14).

6.2.1 Square Lattice Models

When $J'_\perp = J_\perp$ and $J'_\times = J_\times$, the system becomes a uniform even-leg frustrated ladder, which can be viewed as a quasi-2D analogue of the square lattice with nearest-neighbor ($J_1 = J_\perp = J_\parallel$) and next-nearest-neighbor ($J_2 = J_\times$) interactions. This configuration corresponds to the well-known J_1–J_2 Heisenberg model.

6.2.1.1 The J_1–J_2 Model

The spin$\frac{1}{2}$ HAF J_1–J_2 model on the square lattice has long been conjectured to host a *Quantum Spin Liquid* (QSL) phase and is often discussed in connection with high-T_c superconductivity [220–224]. Despite extensive investigation over the past decades, the zero-temperature phase diagram of this model remains under debate. For $J_2/J_1 \lesssim 0.41$, the ground state exhibits Néel AFM order. For $J_2/J_1 \gtrsim 0.62$, the system enters a collinear AFM phase. The nature of the intermediate region $(0.41 \lesssim J_2/J_1 \lesssim 0.62)$ remains controversial, with quantum fluctuations possibly destabilizing magnetic order and giving rise to a magnetically disordered PM phase.

Several competing scenarios have been proposed for this intermediate regime. These include columnar [225–229] or plaquette [230–237] VBS states, as well as gapless [238–249] or gapped [123] QSL phases.

A 2012 DMRG study suggested the presence of a gapped $\mathbb{Z}_2$ QSL in the range $0.41 \lesssim J_2/J_1 \lesssim 0.62$ [123]. In contrast, a 2014 SU(2)-symmetric DMRG study identified a plaquette VBS phase for $0.5 \lesssim J_2/J_1 \lesssim 0.61$, and a near-critical region between $0.44 \lesssim J_2/J_1 \lesssim 0.5$ [233]. More recently, a 2018 DMRG analysis proposed a gapless QSL phase for $0.46 \lesssim J_2/J_1 \lesssim 0.52$, and a VBS phase for $0.52 \lesssim J_2/J_1 \lesssim 0.62$ [247]. A 2022 PEPS study on 24×24 lattices found a gapless QSL for $0.45 \lesssim J_2/J_1 \lesssim 0.56$, followed by a VBS for $0.56 \lesssim J_2/J_1 \lesssim 0.61$ [250], as shown in Figure 54. However, a 2024 study challenged these results, favoring a direct transition from Néel to collinear order via an intermediate plaquette VBS phase and reporting no evidence of a QSL [124, 251].

Figure 54 – Proposed phase diagram of the spin-$\frac{1}{2}$ antiferromagnetic J_1–J_2 square-lattice model, as presented in the work referenced by the figure. The nonmagnetic region is $0.45 \lesssim J_2/J_1 \lesssim 0.61$, and it is a gapless spin liquid phase for $0.45 \lesssim J_2/J_1 \lesssim 0.56$ and a VBS phase for $0.56 \lesssim J_2/J_1 \lesssim 0.61$.

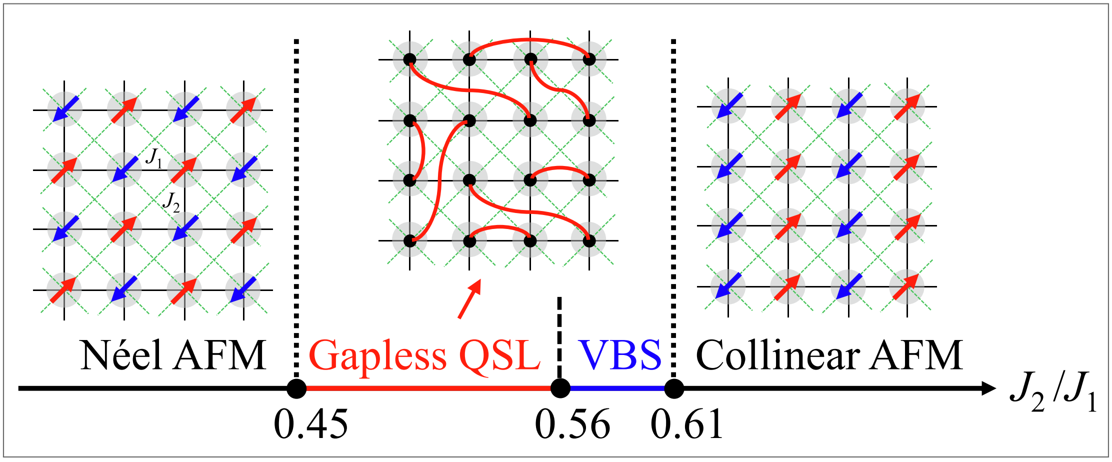

Source: Reference [250]

6.2.1.2 The J_{1x}–J_{1y}–J_2 Model

The J_{1x}–J_{1y}–J_2 model generalizes the J_1–J_2 model by introducing anisotropic nearest-neighbor couplings J_{1x} and J_{1y} along the x- and y-directions, respectively [194, 252–254]. This additional degree of freedom enriches the phase diagram and may stabilize novel quantum phases.

Using tensor network techniques, Liu *et al.* [252] mapped out the phase diagram of this model (Figure 55). In the strongly anisotropic regime, a continuous transition is observed between Néel AFM and columnar VBS phases, characterized by emergent O(4) symmetry. As the anisotropy is reduced, this transition line terminates at a tricritical point, beyond which a gapless QSL phase appears between the AFM and VBS phases.

Figure 55 – Ground-state phase diagram of the J_{1x}-J_{1y}-J_2 model, including four phases: the Néel (AFM), VBS, gapless QSL, and a collinear (stripe) phase. The dashed blue lines denote the hypothetical shape of the VBS phase close to the origin. Solid blue lines in the middle region denote the unknown QSL shape close to the tricritical point (filled blue circle). Open blue circles have emergent O(4) symmetry.

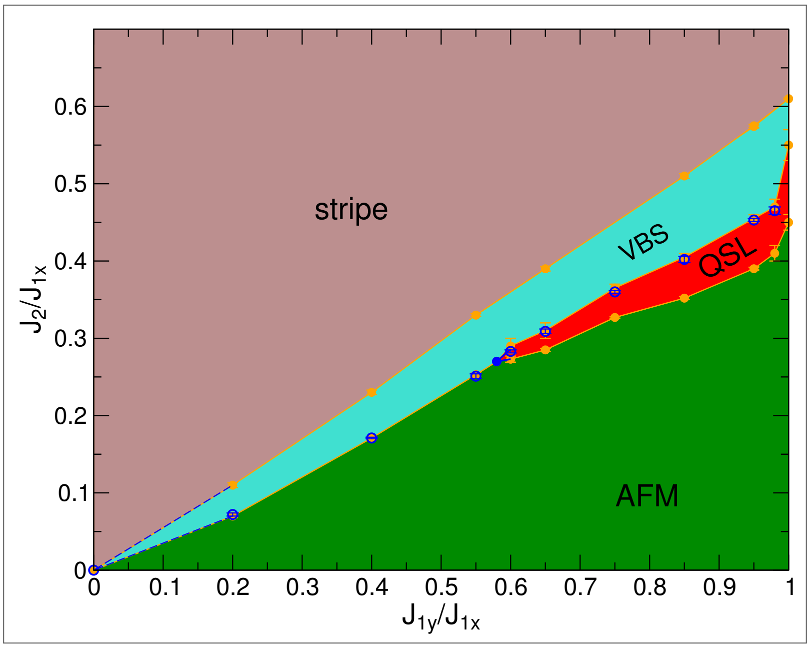

Source: Reference [252]

6.2.2 Numerical Results for the Frustrated Four-Leg Ladder

As the ladder width increases, square lattice models become increasingly relevant. However, narrow ladders retain quasi-1D behavior. As discussed in Section 4.1, a frustrated two-leg ladder in the RT phase maps onto a spin–1 chain exhibiting a Haldane phase. For a four-leg ladder, one might expect spin–2 chain behavior, although spin–1 rung states are also possible due to the presence of four spin–$\frac{1}{2}$ sites per rung.

Figure 56 presents the finite-size phase diagram of a frustrated four-leg ladder with fixed perpendicular coupling $J_\perp = 1$. The diagram identifies distinct regions based on the average rung spin S, notably $0 < S < 1$ and $1.5 < S < 1.9$. The $S = 0$ region corresponds to the gapped RS phase, characterized by a fully gapped configuration. In contrast, the $S = 1$ and $S = 2$ regions suggest analogies with spin–1 and spin–2 chains, respectively, implying distinct magnetic behaviors. To characterize these phases, we analyze key physical quantities such as local magnetization, spin gaps, and order parameters, offering insights into the nature of the underlying quantum states and their transitions.

Figure 56 – DMRG results for the ground-state phase diagram of a spin-$\frac{1}{2}$ frustrated four-leg ladder with $L = 32$ rungs. The color scale represents the average total rung spin, excluding four rungs from each edge to minimize finite-size effects. Calculations used a bond dimension of 3000 and a truncation error of 10^{-7}.

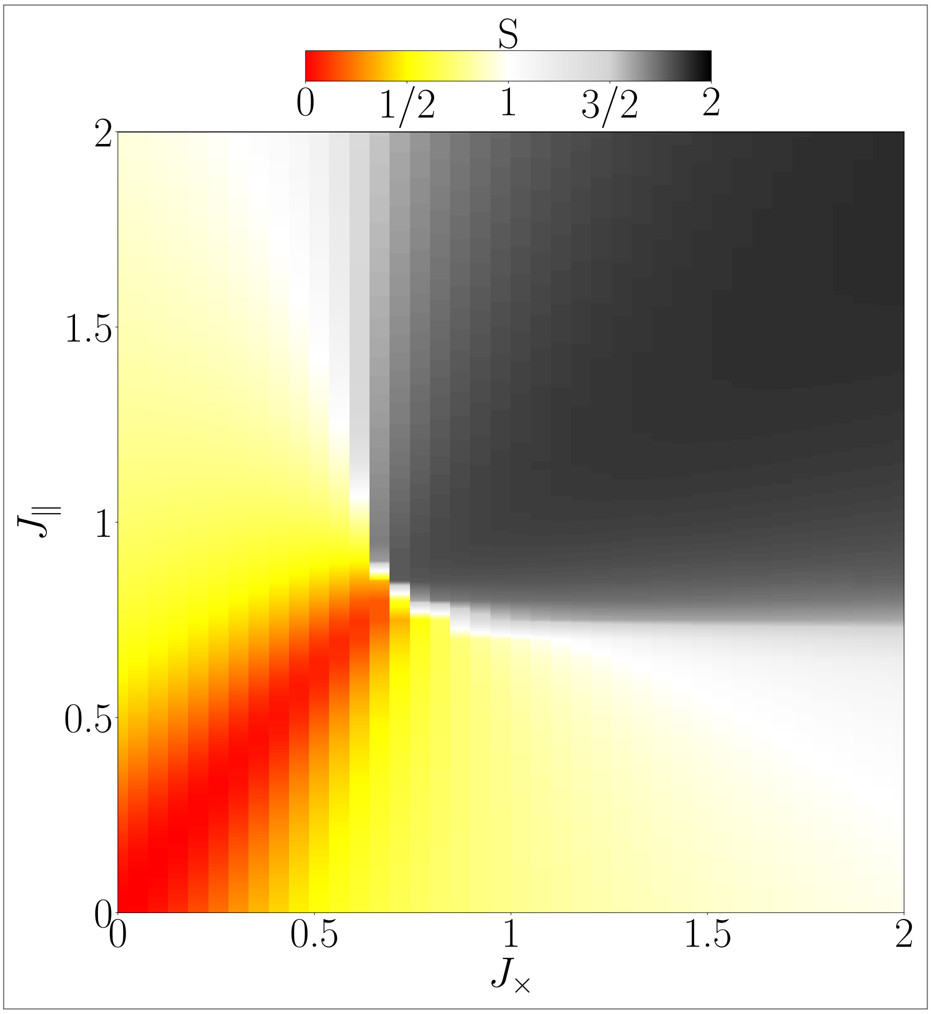

Source: The author (2025).

Figure 57 displays the local rung spin S_i and magnetization profiles for the ground and first excited states. In the ground state, $\langle \hat{S}_i^z \rangle = 0$, consistent with both spin–$\frac{1}{2}$ and spin–2 chains. In the first excited state, behavior varies across regions: the $S = 1/2$ region exhibits a localized magnon, while the $S \approx 1$ region shows a magnon-like excitation without edge states. The $S \approx 1.9$ region displays a magnetization profile closely resembling that of a spin–2 chain, indicating that the system effectively mimics a spin–S chain when $S \approx 2$.

Figure 57 – DMRG results for a spin-$\frac{1}{2}$ frustrated four-leg ladder with $L = 96$ rungs and open boundary conditions. Shown are the local rung spin S_i, ground-state magnetization $\langle \hat{S}_i^z \rangle$, and first excited-state magnetization $\langle \Delta \hat{S}_i^z \rangle$ at selected phase diagram points. Calculations used a bond dimension of 3000 and a truncation error of 10^{-7}.

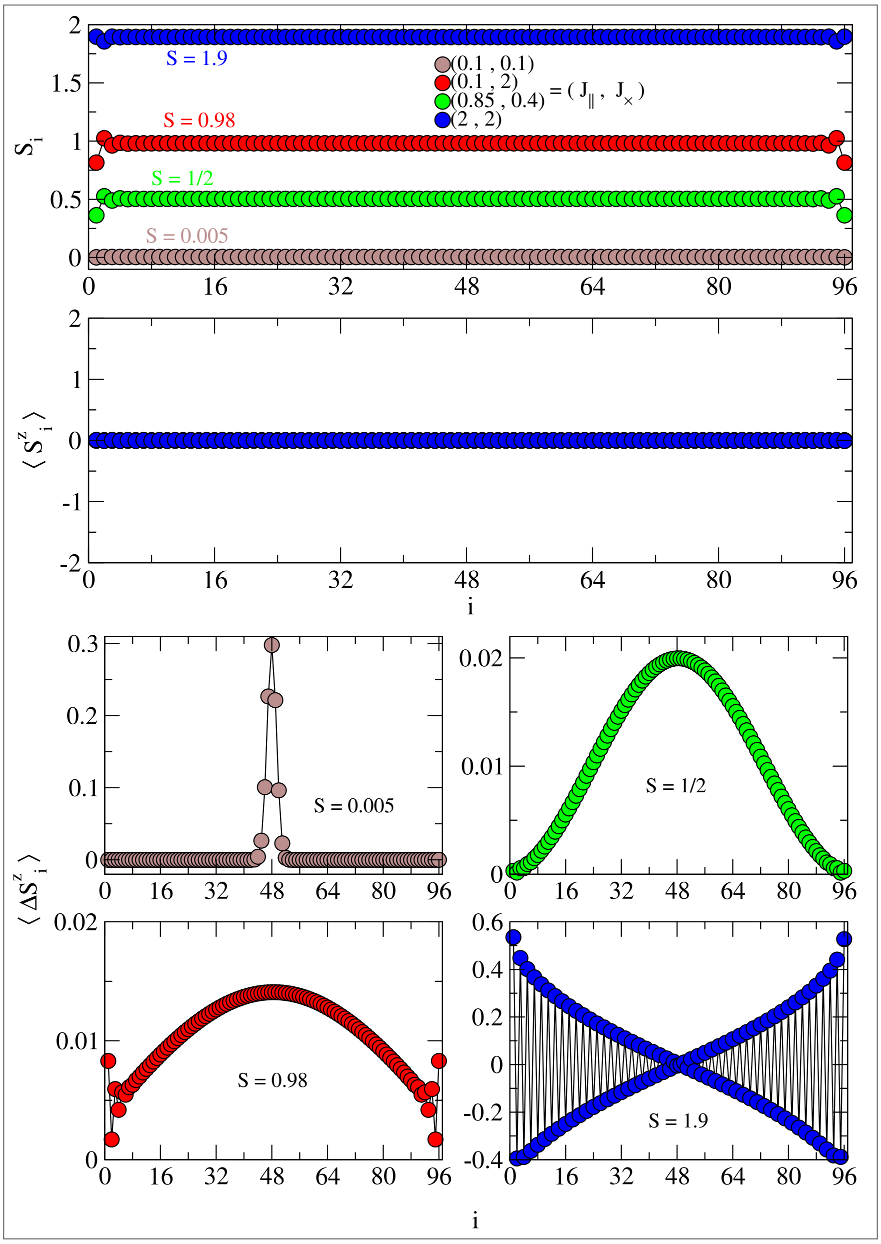

Source: The author (2025)

Unlike the two-leg ladder, the four-leg ladder does not exhibit spin–1 chain behavior or the associated SPT Haldane phase. The string order parameter is defined as:

$$\mathcal{O}^z_{\text{str}} = \lim_{|j-i|\to\infty} \left\langle \hat{S}^z_i \exp\left[\frac{i\pi}{S}\sum_{k=i+1}^{j-i} \hat{S}^z_k\right] \hat{S}^z_j \right\rangle, \quad \hat{S}^z_n = \hat{S}^z_{n,1} + \hat{S}^z_{n,2} + \hat{S}^z_{n,3} + \hat{S}^z_{n,4} \tag{6.16}$$

DMRG calculations yield $\mathcal{O}^z_{\text{str}} = 0$ for $S = 0.98$ and $\mathcal{O}^z_{\text{str}} \approx -0.58$ for $S = 1.9$, after linear extrapolation. These results are shown in Figure 58, alongside spin gap extrapolations.

Figure 58 – DMRG results for a spin-$\frac{1}{2}$ frustrated four-leg ladder with $L = 48$, 72, and 96 rungs under open boundary conditions. Shown are linear extrapolations of the spin gap Δ and string order parameter $\mathcal{O}^z_{\text{str}}$. Calculations used a bond dimension of 3000 and a truncation error of 10^{-7}.

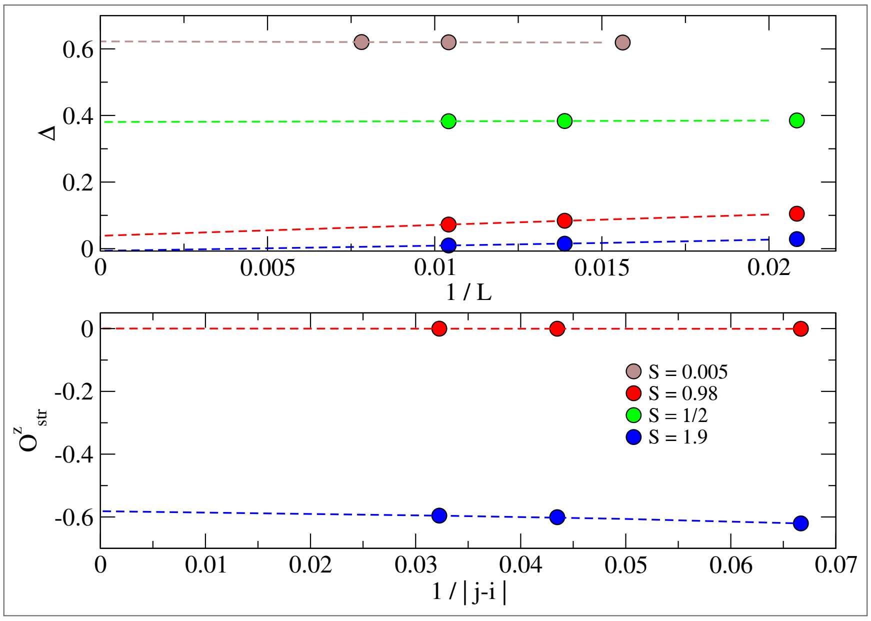

Source: The author (2025)

For $S = 1.9$, the four-leg ladder mimics a spin–2 chain, with a nonzero string order parameter and spin–2-like magnetization profile. The nearly vanishing spin gap may reflect numerical limitations, as the spin–2 chain gap is known to be small ($\Delta \approx 0.09$ [156]). The exponential decay of the spin gap with increasing leg number likely renders linear extrapolation unreliable.

The RT phase observed here is distinct from the SPT Haldane phase and is adiabatically connected to the RS phase. For $S < 1$, Figure 57 reveals a localized magnon in the RS phase at $S = 0$, which progressively delocalizes as S increases, reducing the spin gap. Both phases are gapped and exhibit trivial ground states. This adiabatic connection explains the absence of spin–1 chain behavior in the four-leg ladder: unlike the two-leg ladder, which undergoes a first-order RS–RT transition, the four-leg system smoothly interpolates between RS and RT phases, bypassing the topologically nontrivial Haldane phase.

6.3 NUMERICAL RESULTS FOR TWO COUPLED FRUSTRATED LADDERS

We consider a system of two coupled frustrated ladders, with interladder couplings satisfying $0 \leq J'_\perp \leq J_\perp$ and $0 \leq J'_\times \leq J_\times$. The Hamiltonian is given by

$$\begin{aligned}\hat{\mathcal{H}} = J_\perp \sum_{\alpha\in\{1,3\}} \sum_{i=1}^{L} \hat{\mathbf{S}}_{i,\alpha} \cdot \hat{\mathbf{S}}_{i,\alpha+1} + J_\times \sum_{\alpha\in\{1,3\}} \sum_{i=1}^{L-1} \left(\hat{\mathbf{S}}_{i,\alpha} \cdot \hat{\mathbf{S}}_{i+1,\alpha+1} + \hat{\mathbf{S}}_{i+1,\alpha} \cdot \hat{\mathbf{S}}_{i,\alpha+1}\right) \\ + J'_\perp \sum_{i=1}^{L} \hat{\mathbf{S}}_{i,2} \cdot \hat{\mathbf{S}}_{i,3} + J'_\times \sum_{i=1}^{L-1} \left(\hat{\mathbf{S}}_{i,2} \cdot \hat{\mathbf{S}}_{i+1,3} + \hat{\mathbf{S}}_{i+1,2} \cdot \hat{\mathbf{S}}_{i,3}\right) \\ + J_\parallel \sum_{\alpha=1}^{4} \sum_{i=1}^{L-1} \hat{\mathbf{S}}_{i,\alpha} \cdot \hat{\mathbf{S}}_{i+1,\alpha}. \end{aligned} \tag{6.17}$$

The couplings $J_\perp$, $J_\parallel$, and $J_\times$ define two identical, individually frustrated spin ladders, while the interladder interactions $J'_\perp$ and $J'_\times$ form an effective ladder structure, with $J'_\perp$ acting as a rung coupling and $J'_\times$ as a leg coupling. Throughout this section, we fix $J_\perp = 1$ and $J_\parallel = 0.8$. For these values, an isolated frustrated ladder hosts both the RS and Haldane phases, separated by a first-order quantum phase transition occurring at $J_{\times,\,\mathrm{c}} \approx 0.67 \pm 0.01$ [47]. We investigate the effects of interladder coupling by focusing on the lower ladder, taking advantage of the system's reflection symmetry.

For $J_\times = 0.64$, the isolated frustrated ladder resides in the RS phase. Figure 59(a) presents the phase diagram of the lower frustrated ladder when it is coupled to an identical upper ladder. The interladder couplings $J'_\perp$ and $J'_\times$ can drive a phase transition from the RS phase to a RT phase within specific regions of parameter space. This transition emerges due to the structure of the Hamiltonian, which consists of two decoupled frustrated ladders and an additional effective ladder. While the two frustrated ladders do not share any sites, the effective ladder overlaps with both, mediating indirect interactions between them.

The effective ladder, characterized by AFM couplings ($J'_\perp, J'_\times > 0$), favors the formation of an RS phase. In contrast, the frustration within the individual ladders tends to destabilize this RS phase, promoting an RT phase instead. The competition between the effective ladder and the frustrated ladders thus underlies the phase transitions observed in the system.

Consider two limiting cases. First, when $J_\times = 0$, the effective ladder reduces to a set of decoupled rungs. For $J'_\perp > 0$, these rungs form local singlets, thereby stabilizing the RS phase. At $J_\times = 0.64$, the isolated frustrated ladder is also in the RS phase. However, as $J'_\perp$ increases, the effective ladder increasingly favors singlet formation on its rungs. For sufficiently large $J'_\perp$, this singlet formation competes with that of the frustrated ladder, effectively capturing singlets and destabilizing its RS phase, thereby inducing a transition to the RT phase.

Second, in the limit $J'_\perp = 0$, singlets preferentially form along the legs of the effective ladder rather than on its rungs. This accounts for the extended region in Figure 59(a) where the frustrated ladder remains in the RS phase. When $J'_\perp \approx J'_\times$, the competition between rung and leg singlet formation within the effective ladder reduces its ability to disrupt the singlet structure of the frustrated ladder, thereby allowing it to retain its rung-singlet character. As $J'_\perp \to J_\perp$, the phase transition becomes increasingly smooth, and the system begins to resemble a four-leg frustrated ladder.

Figure 59 – Ground-state phase diagram obtained via DMRG for (a) the lower ladder and (b) the effective ladder of two coupled frustrated ladders with $L = 32$ rungs and $J_\times = 0.64$. To mitigate finite-size effects, four rungs at each edge were excluded during averaging. The coupling $J'_\perp$ promotes rung-singlet formation in the effective ladder, whereas $J'_\times$ encourages singlets along the legs. The effective ladder captures rung-singlets from the frustrated ladder, causing the frustrated ladder to transition from a rung-singlet to a rung-triplet phase.

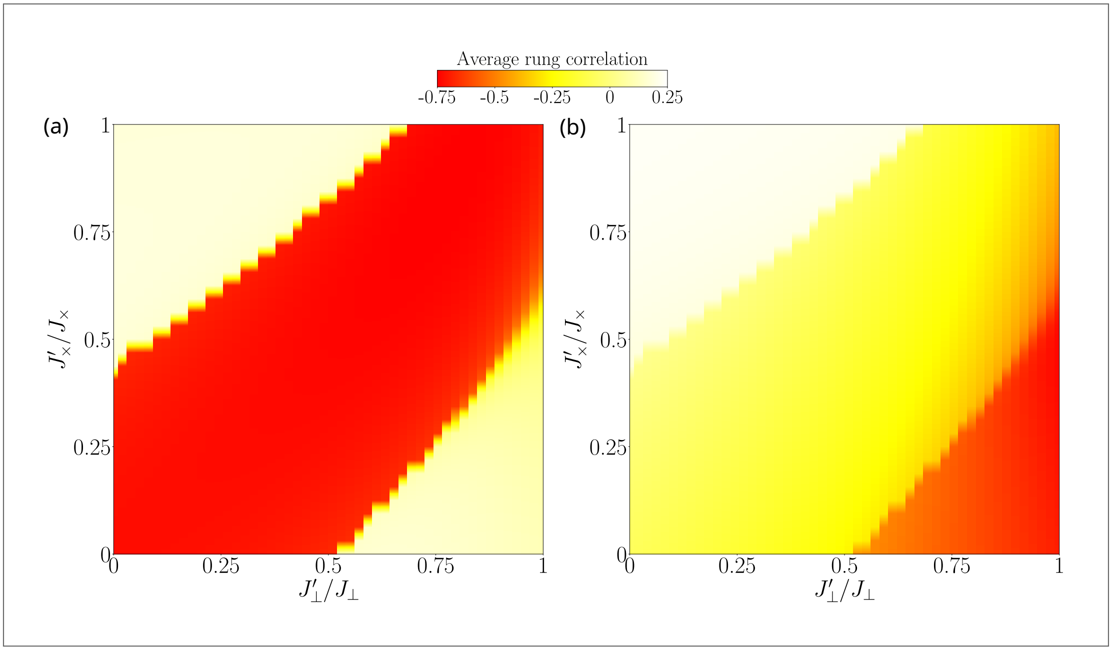

Source: The author (2025).

Figure 59(b) presents the phase diagram of the effective ladder. In the regime $J'_\perp \gg J'_\times$, singlet formation is predominantly localized on the rungs, whereas for $J'_\perp \ll J'_\times$, singlets form primarily along the legs, giving rise to the RT phase. In both limits, the effective ladder competes with the frustrated ladder for singlet correlations, driving the latter's transition from the RS phase to the RT phase. Conversely, when $J'_\perp \approx J'_\times$, the effective ladder lacks a dominant singlet configuration, allowing the frustrated ladder to preserve its rung-singlet order.

For $J_\times = 0.7$, the isolated frustrated ladder is in the Haldane phase, characterized by a rung-triplet formation rather than rung singlets. Figure 60 shows the phase diagram for the lower frustrated ladder (a) and the effective ladder (b) in this regime. Since the frustrated ladder no longer hosts rung singlets, the effective ladder cannot compete for them and consequently remains in the RS phase. However, near the four-leg ladder limit ($J'_\perp \approx J_\perp, J'_\times \approx J_\times$), the system gradually loses its quasi-1D character.

Figure 60 – Ground-state phase diagram obtained via DMRG for (a) the lower ladder and (b) the effective ladder of two coupled frustrated ladders with $L = 32$ rungs and $J_\times = 0.7$. To mitigate finite-size effects, four rungs at each edge were excluded during averaging. The lower ladder predominantly remains in the rung-triplet phase but transitions to a rung-singlet phase near the four-leg regime, losing its quasi-one-dimensional behavior.

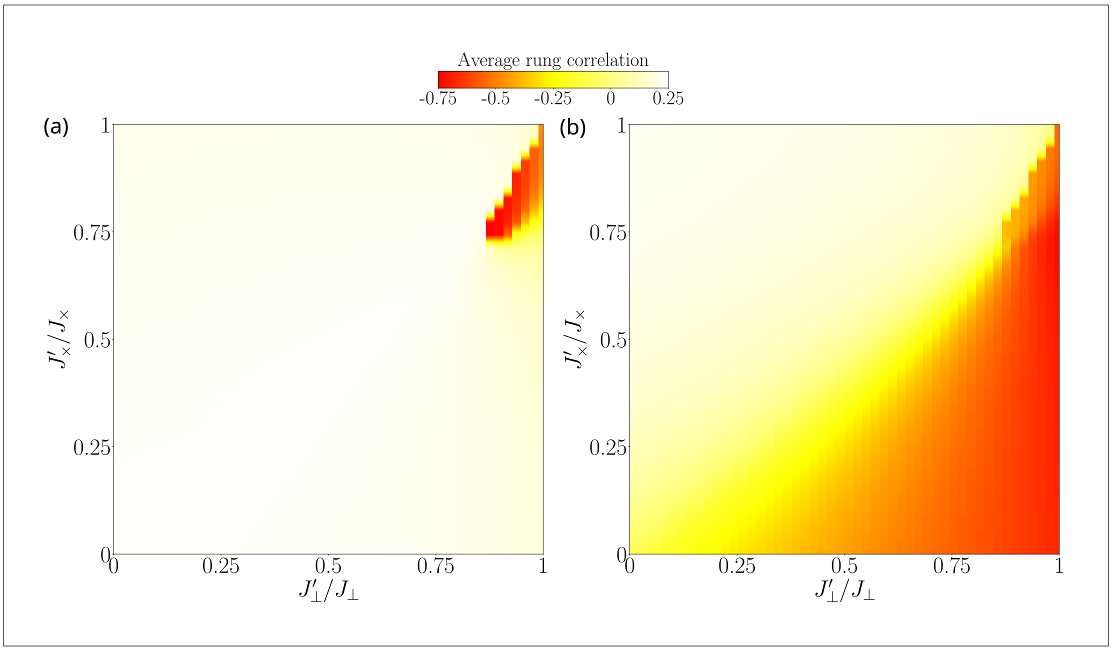

Source: The author (2025).

To quantify this transition, we compute the string order parameter for the lower ladder at $J_\times = 0.7$, performing a linear extrapolation to the thermodynamic limit in two representative cases: $J'_\perp = 0$, and $J'_\times = 0$. As shown in Figure 61, both types of coupling suppress the nontrivial Haldane order, reducing it to the trivial $S = 1$ phase previously observed in the four-leg ladder.

Figure 61 – DMRG-based linear extrapolation of the string order parameter $\mathcal{O}^z_{\mathrm{str}}$ for the lower frustrated ladder with $J_\times = 0.7$. Two paths were analyzed: (1) fixing $J'_\perp = 0$ while varying $J'_\times$, and (2) fixing $J'_\times = 0$ while varying $J'_\perp$. In both cases, the couplings destabilize the SPT Haldane $S = 1$ phase.

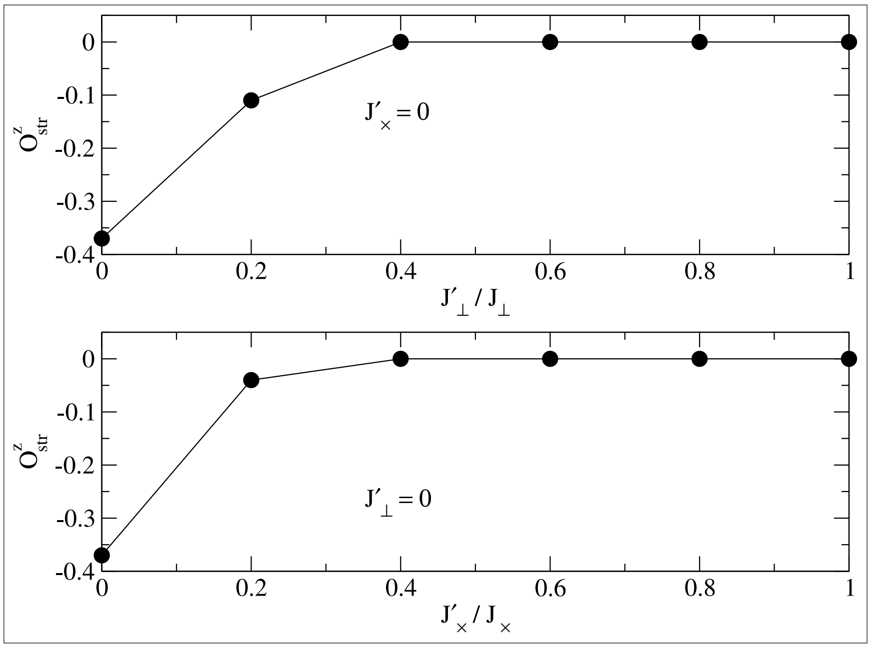

Source: The author (2025).

Considering the full system, Figure 62 displays phase diagrams of the effective rung spin for various values of $J_\times$. These diagrams closely follow the structure seen in the lower ladder, but account for the contributions of both ladders. As $J_\times$ approaches the transition point ($J_{\times,\,\mathrm{c}} \approx 0.67$), the RS phase region narrows considerably. Notably, even at $J_\times = 0.7$, a small RS phase region survives near the four-leg limit ($J'_\perp \approx J_\perp$, $J'_\times \approx J_\times$).

In contrast to unfrustrated systems, frustration induces quantum phase transitions even for a small number of coupled ladders. However, interladder coupling ultimately diminishes the quasi-1D character of the original frustrated two-leg ladder, particularly through the emergence of the RT phase, which lacks topological order.

Figure 62 – Ground-state phase diagrams of the entire system with $L = 32$ rungs, obtained via DMRG. To mitigate finite-size effects, four rungs at each edge were excluded when calculating the average rung total spin S. The phase diagrams reveal three primary regions: $S = 0$, $S = 1$, and $S \approx 2$. These transitions are driven by the shifts in the upper and lower frustrated ladders from rung-singlet to rung-triplet phases.

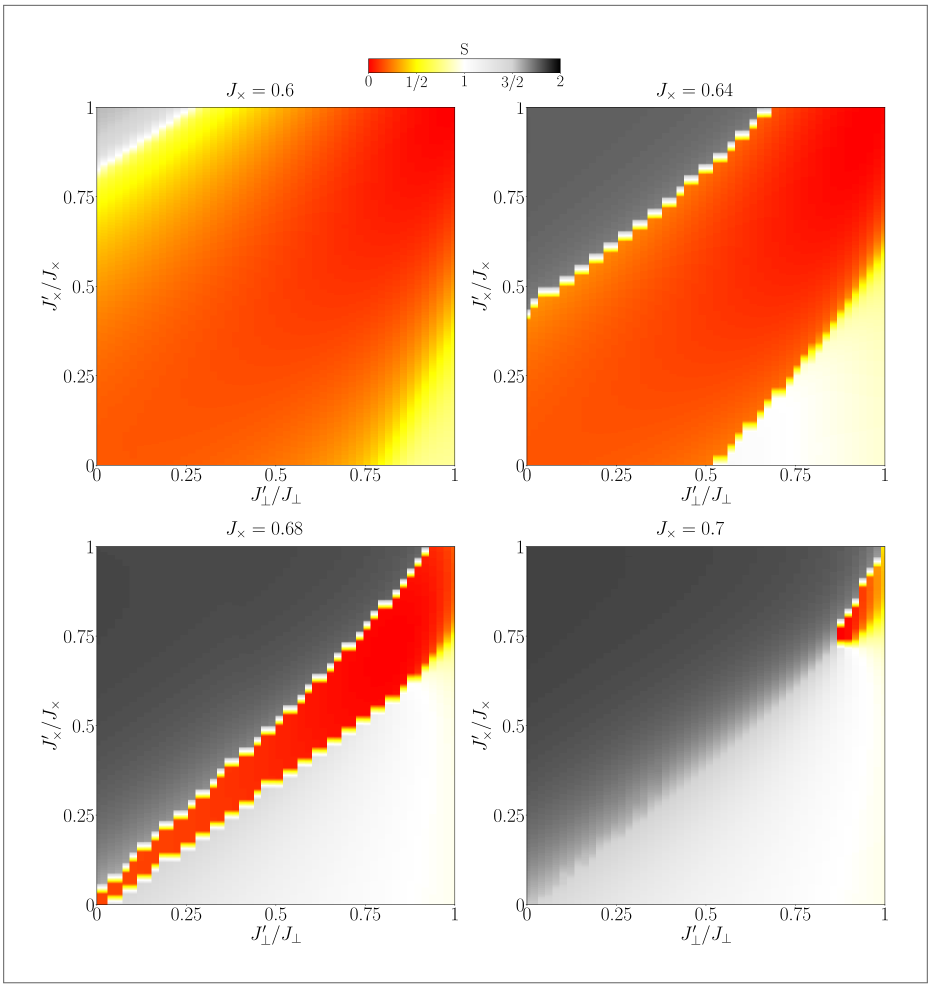

Source: The author (2025).

7 CONCLUSION

This thesis has explored the intricate quantum phase diagrams of low-dimensional quantum systems, with particular emphasis on spin–$\frac{1}{2}$ ladder chains and their variants. By combining advanced numerical techniques—chiefly the DMRG method—with analytical approaches, we have investigated the emergence of distinct quantum phases, topological properties, and critical phenomena in these systems. Our contributions advance the field of quantum magnetism by elucidating how frustration, topology, and external magnetic fields govern the ground-state behavior of spin ladders. The results, published in [47, 74], offer a solid foundation for both theoretical development and experimental exploration in condensed matter physics.

A central achievement of this thesis is the comprehensive analysis of the spin–$\frac{1}{2}$ frustrated two-leg ladder in an external magnetic field. By computing transverse spin correlation functions, we accurately estimated the KT transition points associated with the closure of the fractional $m = 1/2$ magnetization plateau for intra-ladder couplings $J_{\parallel} = 0.2$, 0.55, and 0.8. For $J_{\parallel} = 0.2$ and 0.55, two KT transitions were identified: one in the regime $J_{\times} < J_{\parallel}$ and another in $J_{\times} > J_{\parallel}$. In contrast, the case $J_{\parallel} = 0.8$ exhibits only a single KT transition in the $J_{\times} < J_{\parallel}$ region, followed by a first-order transition into a spin–1 phase. Exploiting the symmetry of the ladder, we mapped out the full curve of KT points in the $J_{\times}$ vs. $J_{\parallel}$ plane, thus delineating the phase boundaries of the $m = 1/2$ plateau. These findings, detailed in [47], reveal the delicate competition between frustration and rung coupling in stabilizing fractional magnetization plateaus. We expect these results to motivate experimental studies in candidate materials or optical lattice platforms, particularly those probing dynamical and finite-temperature effects in non-equilibrium regimes.

Another significant contribution lies in the study of the mixed spin–$(\frac{1}{2}, 1)$ alternating ladder under an external field. We constructed its phase diagram as a function of the magnetic field h and the interdimer coupling $J_{\perp}$, identifying two distinct magnetization plateaus: one at full polarization and another at 1/3 of the saturation magnetization. The 1/3 plateau, occurring for negative $J_{\perp}$, vanishes at $J_{\perp} = -1.32$ via a KT-type transition, which we characterized using transverse spin correlations and the Luttinger parameter $K = 2$. The critical fields delimiting the fully polarized phase were obtained exactly from magnon dispersion relations, treating the polarized state as the vacuum. While a hard-core boson approximation combined with a free-spin-wave treatment qualitatively reproduces the 1/3 plateau, it significantly overestimates the width and fails to capture the precise critical points determined by DMRG. This highlights the importance of numerical accuracy in analyzing mixed-spin systems. These results, presented in [74], suggest promising directions for future studies, including the effects of disorder on magnetization plateaus [255], edge-state coupling in mixed-spin chains [86], and ferrimagnetic coupled ladders [256].

The thesis also advances our understanding of coupled ladder systems, both unfrustrated and frustrated. In the unfrustrated case, our DMRG results for two and three coupled ladders indicate the absence of sharp quantum phase transitions: increasing the interladder coupling $J'_\perp$ leads to an adiabatic evolution of the RVB state from two-leg to multi-leg systems. This continuity underscores the robustness of RVB physics in such systems. In contrast, the frustrated case exhibits a rich variety of phase transitions. For two coupled ladders, we constructed phase diagrams near the first-order transition between the RS and Haldane phases observed in a single frustrated ladder. We showed that interladder coupling drives a transition from the RS phase to a trivial RT phase, while stronger intra-ladder coupling destabilizes the SPT Haldane phase. Furthermore, for the four-leg frustrated ladder, our results demonstrate that the system behaves effectively as a spin–2 chain, distinct from spin–$\frac{1}{2}$ or spin–1 chains. These findings open a promising route for exploring phase transitions in coupled spin ladders—an area still under active investigation.

Altogether, the results presented in this thesis deepen the theoretical framework for understanding low-dimensional quantum systems. The precise determination of phase boundaries, the identification of fractional and topological phases, and the treatment of coupled systems all highlight the synergy between advanced numerical tools like DMRG and physical intuition. Our results help bridge the gap between theoretical models and realizable experimental platforms such as solid-state compounds or cold atoms in optical lattices. Moreover, the failure of certain approximate methods, such as the hard-core boson approach, to capture critical phenomena underscores the need for further refinement of both numerical and analytical methods.

Several avenues remain open for future work. The role of disorder in stabilizing or destroying magnetization plateaus, especially in mixed-spin chains, is still not fully understood. Finite-size scaling of phase boundaries in coupled ladders could clarify the thermodynamic behavior and reveal emergent criticality. The extension to three or six coupled frustrated ladders may uncover novel phases and transitions. Exploring the out-of-equilibrium dynamics under quantum quenches or thermal driving could shed light on non-equilibrium physics in these systems. Further studies on edge-state coupling and frustration in ferrimagnetic ladders may also reveal new topological or symmetry-protected phases.

REFERENCES

[1] Andrew D. Jackson and Ole Knudsen., editors. *39a Experiments on the Effect of a Current of Electricity on the Magnetic Needle (1820)*, pages 417–420. Princeton University Press, Princeton, 1998. ISBN 9781400864850. doi: doi: 10.1515/9781400864850.417. URL `https://doi.org/10.1515/9781400864850.417`.

[2] James Clerk Maxwell. A dynamical theory of the electromagnetic field. *Philosophical Transactions of the Royal Society of London*, 155:459–512, 1865. doi: 10.1098/rstl.1865.0008. URL `https://doi.org/10.1098/rstl.1865.0008`.

[3] J. J. Thomson. Xl. cathode rays. *The London, Edinburgh, and Dublin Philosophical Magazine and Journal of Science*, 44(269):293–316, 1897. doi: 10.1080/14786449708621070. URL `https://doi.org/10.1080/14786449708621070`.

[4] N. Bohr. I. on the constitution of atoms and molecules. *The London, Edinburgh, and Dublin Philosophical Magazine and Journal of Science*, 26(151):1–25, 1913. doi: 10.1080/14786441308634955. URL `https://doi.org/10.1080/14786441308634955`.

[5] Walther Gerlach and Otto Stern. Der experimentelle nachweis der richtungsquantelung im magnetfeld. *Zeitschrift für Physik*, 9(1):349–352, December 1922. ISSN 1434-601X. doi: 10.1007/bf01326983. URL `http://dx.doi.org/10.1007/BF01326983`.

[6] Pierre Curie. Propriétés magnétiques des corps à diverses températures. *Annales de Chimie et de Physique*, 7:289–405, 1895.

[7] W Lenz. Beitrag zum Verständnis der magnetischen Erscheinungen in festen Körpern. *Z. Phys.*, 21:613–615, 1920. URL `http://cds.cern.ch/record/460663`.

[8] Ernst Ising. Beitrag zur theorie des ferromagnetismus. *Zeitschrift für Physik*, 31(1):253–258, February 1925. ISSN 0044-3328. doi: 10.1007/bf02980577. URL `http://dx.doi.org/10.1007/BF02980577`.

[9] Lars Onsager. Crystal statistics. i. a two-dimensional model with an order-disorder transition. *Phys. Rev.*, 65:117–149, Feb 1944. doi: 10.1103/PhysRev.65.117. URL `https://link.aps.org/doi/10.1103/PhysRev.65.117`.

[10] Kurt Binder and Dieter W. Heermann. *Monte Carlo Simulation in Statistical Physics: An Introduction.* Springer Berlin Heidelberg, 2010. ISBN 9783642031632. doi: 10.1007/978-3-642-03163-2. URL `http://dx.doi.org/10.1007/978-3-642-03163-2`.

[11] Anders W. Sandvik. Computational studies of quantum spin systems. *AIP Conference Proceedings*, 1297(1):135–338, 11 2010. ISSN 0094-243X. doi: 10.1063/1.3518900. URL `https://doi.org/10.1063/1.3518900`.

[12] N. D. Mermin and H. Wagner. Absence of ferromagnetism or antiferromagnetism in one- or two-dimensional isotropic heisenberg models. *Phys. Rev. Lett.*, 17:1133–1136, Nov 1966. doi: 10.1103/PhysRevLett.17.1133. URL `https://link.aps.org/doi/10.1103/PhysRevLett.17.1133`.

[13] J M Kosterlitz and D J Thouless. Ordering, metastability and phase transitions in two-dimensional systems. *Journal of Physics C: Solid State Physics*, 6(7):1181, apr 1973. doi: 10.1088/0022-3719/6/7/010. URL `https://dx.doi.org/10.1088/0022-3719/6/7/010`.

[14] Ch. Rüegg, K. Kiefer, B. Thielemann, D. F. McMorrow, V. Zapf, B. Normand, M. B. Zvonarev, P. Bouillot, C. Kollath, T. Giamarchi, S. Capponi, D. Poilblanc, D. Biner, and K. W. Krämer. Thermodynamics of the spin luttinger liquid in a model ladder material. *Phys. Rev. Lett.*, 101:247202, Dec 2008. doi: 10.1103/PhysRevLett.101.247202. URL `https://link.aps.org/doi/10.1103/PhysRevLett.101.247202`.

[15] U. Schollwöck. The density-matrix renormalization group. *Rev. Mod. Phys.*, 77:259–315, Apr 2005. doi: 10.1103/RevModPhys.77.259. URL `https://link.aps.org/doi/10.1103/RevModPhys.77.259`.

[16] Steven R. White. Density matrix formulation for quantum renormalization groups. *Phys. Rev. Lett.*, 69:2863–2866, Nov 1992. doi: 10.1103/PhysRevLett.69.2863. URL `https://link.aps.org/doi/10.1103/PhysRevLett.69.2863`.

[17] Steven R. White. Density-matrix algorithms for quantum renormalization groups. *Phys. Rev. B*, 48:10345–10356, Oct 1993. doi: 10.1103/PhysRevB.48.10345. URL `https://link.aps.org/doi/10.1103/PhysRevB.48.10345`.

[18] Dian Wu, Riccardo Rossi, Filippo Vicentini, Nikita Astrakhantsev, Federico Becca, Xiaodong Cao, Juan Carrasquilla, Francesco Ferrari, Antoine Georges, Mohamed Hibat-Allah, Masatoshi Imada, Andreas M. Läuchli, Guglielmo Mazzola, Antonio Mezzacapo, Andrew Millis, Javier Robledo Moreno, Titus Neupert, Yusuke Nomura, Jannes Nys, Olivier Parcollet, Rico Pohle, Imelda Romero, Michael Schmid, J. Maxwell Silvester, Sandro Sorella, Luca F. Tocchio, Lei Wang, Steven R. White, Alexander Wietek, Qi Yang, Yiqi Yang, Shiwei Zhang, and Giuseppe Carleo. Variational benchmarks for quantum many-body problems. *Science*, 386(6719):296–301, 2024. doi: 10.1126/science.adg9774. URL https://www.science.org/doi/abs/10.1126/science.adg9774.

[19] F. D. M. Haldane. Nonlinear field theory of large-spin heisenberg antiferromagnets: Semiclassically quantized solitons of the one-dimensional easy-axis néel state. *Phys. Rev. Lett.*, 50:1153–1156, Apr 1983. doi: 10.1103/PhysRevLett.50.1153. URL https://link.aps.org/doi/10.1103/PhysRevLett.50.1153.

[20] F.D.M. Haldane. Continuum dynamics of the 1-d heisenberg antiferromagnet: Identification with the O(3) nonlinear sigma model. *Physics Letters A*, 93(9):464–468, 1983. ISSN 0375-9601. doi: https://doi.org/10.1016/0375-9601(83)90631-X. URL https://www.sciencedirect.com/science/article/pii/037596018390631X.

[21] Frank Pollmann, Erez Berg, Ari M. Turner, and Masaki Oshikawa. Symmetry protection of topological phases in one-dimensional quantum spin systems. *Phys. Rev. B*, 85:075125, Feb 2012. doi: 10.1103/PhysRevB.85.075125. URL https://link.aps.org/doi/10.1103/PhysRevB.85.075125.

[22] Xiao-Gang Wen. Choreographed entanglement dances: Topological states of quantum matter. *Science*, 363(6429):eaal3099, 2019. doi: 10.1126/science.aal3099. URL https://www.science.org/doi/abs/10.1126/science.aal3099.

[23] J. P. Renard, M. Verdaguer, L. P. Regnault, W. A. C. Erkelens, J. Rossat-Mignod, and W. G. Stirling. Presumption for a quantum energy gap in the quasi-one-dimensional $S = 1$ heisenberg antiferromagnet $\mathrm{Ni(C_2H_8N_2)_2NO_2(ClO_4)}$. *Europhysics Letters*, 3(8):945, apr 1987. doi: 10.1209/0295-5075/3/8/013. URL https://dx.doi.org/10.1209/0295-5075/3/8/013.

[24] M. Hagiwara, K. Katsumata, Ian Affleck, B. I. Halperin, and J. P. Renard. Observation of s=1/2 degrees of freedom in an s=1 linear-chain heisenberg antiferromagnet. *Phys. Rev. Lett.*, 65:3181–3184, Dec 1990. doi: 10.1103/PhysRevLett.65.3181. URL `https://link.aps.org/doi/10.1103/PhysRevLett.65.3181`.

[25] J. Mögerle, K. Brechtelsbauer, A.T. Gea-Caballero, J. Prior, G. Emperauger, G. Bornet, C. Chen, T. Lahaye, A. Browaeys, and H.P. Büchler. Spin-1 haldane phase in a chain of rydberg atoms. *PRX Quantum*, 6:020332, May 2025. doi: 10.1103/PRXQuantum.6.020332. URL `https://link.aps.org/doi/10.1103/PRXQuantum.6.020332`.

[26] F. Duncan M. Haldane. Nobel lecture: Topological quantum matter. *Rev. Mod. Phys.*, 89:040502, Oct 2017. doi: 10.1103/RevModPhys.89.040502. URL `https://link.aps.org/doi/10.1103/RevModPhys.89.040502`.

[27] T. Jolicoeur and Olivier Golinelli. Physics of integer-spin antiferromagnetic chains: Haldane gaps and edge states. *Comptes Rendus Chimie*, 22(6):445–451, 2019. ISSN 1631-0748. doi: https://doi.org/10.1016/j.crci.2019.05.005. URL `https://www.sciencedirect.com/science/article/pii/S1631074819300943`. Forty years of exchange interactions on the occasion of the 75th birthday of Michel Verdaguer.

[28] Pimonpan Sompet, Sarah Hirthe, Dominik Bourgund, Thomas Chalopin, Julian Bibo, Joannis Koepsell, Petar Bojović', Ruben Verresen, Frank Pollmann, Guillaume Salomon, Christian Gross, Timon A. Hilker, and Immanuel Bloch. Realizing the symmetry-protected haldane phase in fermi–hubbard ladders. *Nature*, 606(7914): 484–488, June 2022. ISSN 1476-4687. doi: 10.1038/s41586-022-04688-z. URL `http://dx.doi.org/10.1038/s41586-022-04688-z`.

[29] Keola Wierschem and Pinaki Sengupta. Characterizing the haldane phase in quasi-one-dimensional spin-1 heisenberg antiferromagnets. *Modern Physics Letters B*, 28 (32):1430017, 2014. doi: 10.1142/S0217984914300178. URL `https://doi.org/10.1142/S0217984914300178`.

[30] M. Z. Hasan and C. L. Kane. Colloquium: Topological insulators. *Rev. Mod. Phys.*, 82:3045–3067, Nov 2010. doi: 10.1103/RevModPhys.82.3045. URL `https://link.aps.org/doi/10.1103/RevModPhys.82.3045`.

[31] Mithilesh Nayak, Dominic Blosser, Andrey Zheludev, and Frédéric Mila. Magnetic-field-induced bound states in spin-$\frac{1}{2}$ ladders. *Phys. Rev. Lett.*, 124:087203, Feb 2020. doi: 10.1103/PhysRevLett.124.087203. URL `https://link.aps.org/doi/10.1103/PhysRevLett.124.087203`.

[32] Elbio Dagotto and T. M. Rice. Surprises on the way from one- to two-dimensional quantum magnets: The ladder materials. *Science*, 271(5249):618–623, 1996. doi: 10.1126/science.271.5249.618. URL `https://www.science.org/doi/abs/10.1126/science.271.5249.618`.

[33] Sudha Gopalan, T. M. Rice, and M. Sigrist. Spin ladders with spin gaps: A description of a class of cuprates. *Phys. Rev. B*, 49:8901–8910, Apr 1994. doi: 10.1103/PhysRevB.49.8901. URL `https://link.aps.org/doi/10.1103/PhysRevB.49.8901`.

[34] T. M. Rice, S. Gopalan, and M. Sigrist. Superconductivity, spin gaps and luttinger liquids in a class of cuprates. *Europhysics Letters*, 23(6):445, aug 1993. doi: 10.1209/0295-5075/23/6/011. URL `https://dx.doi.org/10.1209/0295-5075/23/6/011`.

[35] M. Sigrist, T. M. Rice, and F. C. Zhang. Superconductivity in a quasi-one-dimensional spin liquid. *Phys. Rev. B*, 49:12058–12061, May 1994. doi: 10.1103/PhysRevB.49.12058. URL `https://link.aps.org/doi/10.1103/PhysRevB.49.12058`.

[36] Ian Affleck. Spin gap and symmetry breaking in CuO_2 layers and other antiferromagnets. *Phys. Rev. B*, 37:5186–5192, Apr 1988. doi: 10.1103/PhysRevB.37.5186. URL `https://link.aps.org/doi/10.1103/PhysRevB.37.5186`.

[37] E. Dagotto, J. Riera, and D. Scalapino. Superconductivity in ladders and coupled planes. *Phys. Rev. B*, 45:5744–5747, Mar 1992. doi: 10.1103/PhysRevB.45.5744. URL `https://link.aps.org/doi/10.1103/PhysRevB.45.5744`.

[38] A. Parola, S. Sorella, and Q. F. Zhong. Realization of a spin liquid in a two dimensional quantum antiferromagnet. *Phys. Rev. Lett.*, 71:4393–4396, Dec 1993. doi: 10.1103/PhysRevLett.71.4393. URL `https://link.aps.org/doi/10.1103/PhysRevLett.71.4393`.

[39] S. R. White, R. M. Noack, and D. J. Scalapino. Resonating valence bond theory of coupled heisenberg chains. *Phys. Rev. Lett.*, 73:886–889, Aug 1994. doi: 10.1103/PhysRevLett.73.886. URL https://link.aps.org/doi/10.1103/PhysRevLett.73.886.

[40] N Hatano and Y Nishiyama. Scaling theory of antiferromagnetic heisenberg ladder models. *Journal of Physics A: Mathematical and General*, 28(14):3911, jul 1995. doi: 10.1088/0305-4470/28/14/012. URL https://dx.doi.org/10.1088/0305-4470/28/14/012.

[41] M. Azuma, Z. Hiroi, M. Takano, K. Ishida, and Y. Kitaoka. Observation of a spin gap in $srcu_2o_3$ comprising spin-$\frac{1}{2}$ quasi-1d two-leg ladders. *Phys. Rev. Lett.*, 73:3463–3466, Dec 1994. doi: 10.1103/PhysRevLett.73.3463. URL https://link.aps.org/doi/10.1103/PhysRevLett.73.3463.

[42] R. S. Eccleston, T. Barnes, J. Brody, and J. W. Johnson. Inelastic neutron scattering from the spin ladder compound $(VO)_2P_2O_7$. *Phys. Rev. Lett.*, 73:2626–2629, Nov 1994. doi: 10.1103/PhysRevLett.73.2626. URL https://link.aps.org/doi/10.1103/PhysRevLett.73.2626.

[43] K. Kojima, A. Keren, G. M. Luke, B. Nachumi, W. D. Wu, Y. J. Uemura, M. Azuma, and M. Takano. Magnetic behavior of the 2-leg and 3-leg spin ladder cuprates $Sr_{n-1}Cu_{n+1}O_{2n}$. *Phys. Rev. Lett.*, 74:2812–2815, Apr 1995. doi: 10.1103/PhysRevLett.74.2812. URL https://link.aps.org/doi/10.1103/PhysRevLett.74.2812.

[44] C. Mennerich, H.-H. Klauss, M. Broekelmann, F. J. Litterst, C. Golze, R. Klingeler, V. Kataev, B. Büchner, S.-N. Grossjohann, W. Brenig, M. Goiran, H. Rakoto, J.-M. Broto, O. Kataeva, and D. J. Price. Antiferromagnetic dimers of ni(ii) in the $s = 1$ spin-ladder $na_2ni_2(C_2O_4)_3(H_2O)_2$. *Phys. Rev. B*, 73:174415, May 2006. doi: 10.1103/PhysRevB.73.174415. URL https://link.aps.org/doi/10.1103/PhysRevB.73.174415.

[45] F. Damay, C. Martin, V. Hardy, A. Maignan, C. Stock, and S. Petit. Quantum gapped spin excitations in the $s = \frac{3}{2}$ zigzag ladder compound β-$cacr_2o_4$. *Phys. Rev.*

B, 84:020402, Jul 2011. doi: 10.1103/PhysRevB.84.020402. URL https://link.aps.org/doi/10.1103/PhysRevB.84.020402.

[46] Fran çoise Damay, Christine Martin, Vincent Hardy, Antoine Maignan, Gilles André, Kevin Knight, Sean R. Giblin, and Laurent C. Chapon. Zigzag ladders with staggered magnetic chirality in the $s = \frac{3}{2}$ compound β-cacr$_2$o$_4$. *Phys. Rev. B*, 81:214405, Jun 2010. doi: 10.1103/PhysRevB.81.214405. URL https://link.aps.org/doi/10.1103/PhysRevB.81.214405.

[47] D. S. Almeida and R. R. Montenegro-Filho. Quantum bicritical point and phase separation in a frustrated heisenberg ladder. *Phys. Rev. B*, 108:224433, Dec 2023. doi: 10.1103/PhysRevB.108.224433. URL https://link.aps.org/doi/10.1103/PhysRevB.108.224433.

[48] J.-B. Fouet, F. Mila, D. Clarke, H. Youk, O. Tchernyshyov, P. Fendley, and R. M. Noack. Condensation of magnons and spinons in a frustrated ladder. *Phys. Rev. B*, 73:214405, Jun 2006. doi: 10.1103/PhysRevB.73.214405. URL https://link.aps.org/doi/10.1103/PhysRevB.73.214405.

[49] A. Honecker, F. Mila, and M. Troyer. Magnetization plateaux and jumps in a class of frustrated ladders: A simple route to a complex behaviour. *The European Physical Journal B*, 15(2):227–233, May 2000. ISSN 1434-6028. doi: 10.1007/s100510051120. URL http://dx.doi.org/10.1007/s100510051120.

[50] Guang-Hua Liu, Xiao-Yan Deng, and Rui Wen. Phase diagram of the frustrated spin ladder with the next nearest intrachain couplings. *Physica B: Condensed Matter*, 407(12):2068–2071, 2012. ISSN 0921-4526. doi: https://doi.org/10.1016/j.physb.2012.02.006. URL https://www.sciencedirect.com/science/article/pii/S0921452612001743.

[51] Stefan Wessel, B. Normand, Frédéric Mila, and Andreas Honecker. Efficient Quantum Monte Carlo simulations of highly frustrated magnets: the frustrated spin-1/2 ladder. *SciPost Phys.*, 3:005, 2017. doi: 10.21468/SciPostPhys.3.1.005. URL https://scipost.org/10.21468/SciPostPhys.3.1.005.

[52] Martin P. Gelfand. Linked-tetrahedra spin chain: Exact ground state and excitations. *Phys. Rev. B*, 43:8644–8645, Apr 1991. doi: 10.1103/PhysRevB.43.8644. URL https://link.aps.org/doi/10.1103/PhysRevB.43.8644.

[53] Steven R. White. Equivalence of the antiferromagnetic heisenberg ladder to a single s=1 chain. *Phys. Rev. B*, 53:52–55, Jan 1996. doi: 10.1103/PhysRevB.53.52. URL https://link.aps.org/doi/10.1103/PhysRevB.53.52.

[54] Frédéric Michaud, Tommaso Coletta, Salvatore R. Manmana, Jean-David Picon, and Frédéric Mila. Frustration-induced plateaus in $s \geq \frac{1}{2}$ heisenberg spin ladders. *Phys. Rev. B*, 81:014407, Jan 2010. doi: 10.1103/PhysRevB.81.014407. URL https://link.aps.org/doi/10.1103/PhysRevB.81.014407.

[55] F. Mila. Ladders in a magnetic field: a strong coupling approach. *The European Physical Journal B*, 6(2):201–205, November 1998. ISSN 1434-6028. doi: 10.1007/s100510050542. URL http://dx.doi.org/10.1007/s100510050542.

[56] Keisuke Totsuka. Magnetization plateau in the $s = \frac{1}{2}$ heinsenberg spin chain with next-nearest-neighbor and alternating nearest-neighbor interactions. *Phys. Rev. B*, 57:3454–3465, Feb 1998. doi: 10.1103/PhysRevB.57.3454. URL https://link.aps.org/doi/10.1103/PhysRevB.57.3454.

[57] Takashi Tonegawa, Takeshi Nishida, and Makoto Kaburagi. Ground-state magnetization curve of a generalized spin-1/2 ladder. *Physica B: Condensed Matter*, 246-247:368–371, 1998. ISSN 0921-4526. doi: https://doi.org/10.1016/S0921-4526(97)00937-X. URL https://www.sciencedirect.com/science/article/pii/S092145269700937X.

[58] B. Koteswararao, S. Salunke, A. V. Mahajan, I. Dasgupta, and J. Bobroff. Spin-gap behavior in the two-leg spin-ladder Bicu$_2$Po$_6$. *Phys. Rev. B*, 76:052402, Aug 2007. doi: 10.1103/PhysRevB.76.052402. URL https://link.aps.org/doi/10.1103/PhysRevB.76.052402.

[59] Alexander A. Tsirlin, Ioannis Rousochatzakis, Deepa Kasinathan, Oleg Janson, Ramesh Nath, Franziska Weickert, Christoph Geibel, Andreas M. Läuchli, and Helge Rosner. Bridging frustrated-spin-chain and spin-ladder physics: Quasi-one-dimensional magnetism of bicu$_2$po$_6$. *Phys. Rev. B*, 82:144426, Oct 2010. doi: 10.

1103/PhysRevB.82.144426. URL https://link.aps.org/doi/10.1103/PhysRevB.82.144426.

[60] G. Rousse, J. Rodríguez-Carvajal, C. Giacobbe, M. Sun, O. Vaccarelli, and G. Radtke. Low-temperature structural transition in the quasi-one-dimensional spin-$\frac{1}{2}$ compound $Li_2Cu_2O(SO_4)_2$. *Phys. Rev. B*, 95:144103, Apr 2017. doi: 10.1103/PhysRevB.95.144103. URL https://link.aps.org/doi/10.1103/PhysRevB.95.144103.

[61] Meiling Sun, Gwenaëlle Rousse, Artem M. Abakumov, Matthieu Saubanère, Marie-Liesse Doublet, Juan Rodríguez-Carvajal, Gustaaf Van Tendeloo, and Jean-Marie Tarascon. Li2cu2o(so4)2: a possible electrode for sustainable li-based batteries showing a 4.7 v redox activity vs li+/li0. *Chemistry of Materials*, 27(8):3077–3087, 2015. doi: 10.1021/acs.chemmater.5b00588. URL https://doi.org/10.1021/acs.chemmater.5b00588.

[62] O. Vaccarelli, G. Rousse, A. Saúl, and G. Radtke. Magnetic dimerization in the frustrated spin ladder $li_2cu_2O(SO_4)_2$. *Phys. Rev. B*, 96:180406, Nov 2017. doi: 10.1103/PhysRevB.96.180406. URL https://link.aps.org/doi/10.1103/PhysRevB.96.180406.

[63] O. Vaccarelli, A. Honecker, P. Giura, K. Béneut, B. Fåk, G. Rousse, and G. Radtke. Triplet excitations in the frustrated spin ladder $li_2cu_2O(SO_4)_2$. *Phys. Rev. B*, 99:064416, Feb 2019. doi: 10.1103/PhysRevB.99.064416. URL https://link.aps.org/doi/10.1103/PhysRevB.99.064416.

[64] Takahiro Fukui and Norio Kawakami. Alternating-spin ladders. *Phys. Rev. B*, 57:398–402, Jan 1998. doi: 10.1103/PhysRevB.57.398. URL https://link.aps.org/doi/10.1103/PhysRevB.57.398.

[65] A. Langari and M. A. Martín-Delgado. Alternating-spin ladders in a magnetic field: Formation of magnetization plateaux. *Phys. Rev. B*, 62:11725–11730, Nov 2000. doi: 10.1103/PhysRevB.62.11725. URL https://link.aps.org/doi/10.1103/PhysRevB.62.11725.

[66] A. Langari and M. A. Martín-Delgado. Low-energy properties of ferrimagnetic two-leg ladders: A lanczos study. *Phys. Rev. B*, 63:054432, Jan 2001. doi: 10.

1103/PhysRevB.63.054432. URL https://link.aps.org/doi/10.1103/PhysRevB.63.054432.

[67] N. B. Ivanov and J. Richter. Collective excitations in ferrimagnetic heisenberg ladders. *Phys. Rev. B*, 63:144429, Mar 2001. doi: 10.1103/PhysRevB.63.144429. URL https://link.aps.org/doi/10.1103/PhysRevB.63.144429.

[68] D. N. Aristov and M. N. Kiselev. Ferrimagnetic mixed-spin ladders in weak- and strong-coupling limits. *Phys. Rev. B*, 70:224402, Dec 2004. doi: 10.1103/PhysRevB.70.224402. URL https://link.aps.org/doi/10.1103/PhysRevB.70.224402.

[69] S. Chen, L. Wang, and Y. P. Wang. Phase diagram of frustrated mixed-spin ladders in the strong-coupling limit. *The European Physical Journal B*, 57(3):265–270, June 2007. ISSN 1434-6036. doi: 10.1140/epjb/e2007-00180-9. URL http://dx.doi.org/10.1140/epjb/e2007-00180-9.

[70] G I Japaridze, A Langari, and S Mahdavifar. Spin ladder with anisotropic ferromagnetic legs in a transverse magnetic field. *Journal of Physics: Condensed Matter*, 19(7):076201, jan 2007. doi: 10.1088/0953-8984/19/7/076201. URL https://dx.doi.org/10.1088/0953-8984/19/7/076201.

[71] V. Ravi Chandra, N. B. Ivanov, and J. Richter. Frustrated spin ladder with alternating spin-1 and spin-$\frac{1}{2}$ rungs. *Phys. Rev. B*, 81:024409, Jan 2010. doi: 10.1103/PhysRevB.81.024409. URL https://link.aps.org/doi/10.1103/PhysRevB.81.024409.

[72] Yan Qi, Song-Wei Lv, An Du, and Nai-sen Yu. Interplay between spin frustration and magnetism in the exactly solved two-leg mixed spin ladder*. *Chinese Physics B*, 25(11):117501, sep 2016. doi: 10.1088/1674-1056/25/11/117501. URL https://dx.doi.org/10.1088/1674-1056/25/11/117501.

[73] N. Ahmadi, J. Abouie, R. Haghshenas, and D. Baeriswyl. Frustrated mixed-spin ladders: Evidence for a bond-order wave phase between rung-singlet and haldane phases. *Phys. Rev. B*, 106:174419, Nov 2022. doi: 10.1103/PhysRevB.106.174419. URL https://link.aps.org/doi/10.1103/PhysRevB.106.174419.

[74] D. S. Almeida, A. S. Bibiano-Filho, W. M. da Silva, and R. R. Montenegro-Filho. Mixed-spin heisenberg ladders in a magnetic field. *Phys. Rev. E*, 111:014149, Jan

2025. doi: 10.1103/PhysRevE.111.014149. URL https://link.aps.org/doi/10.1103/PhysRevE.111.014149.

[75] Elliott Lieb and Daniel Mattis. Ordering energy levels of interacting spin systems. *Journal of Mathematical Physics*, 3(4):749–751, 07 1962. ISSN 0022-2488. doi: 10.1063/1.1724276. URL https://doi.org/10.1063/1.1724276.

[76] Guang-Shan Tian. Coexistence of the ferromagnetic and antiferromagnetic long-range orders in the generalized antiferromagnetic heisenberg model on a bipartite lattice. *Journal of Physics A: Mathematical and General*, 27(7):2305, apr 1994. doi: 10.1088/0305-4470/27/7/012. URL https://dx.doi.org/10.1088/0305-4470/27/7/012.

[77] Yusaku Noriki and Shoji Yamamoto. Modified spin-wave theory on low-dimensional heisenberg ferrimagnets: A new robust formulation. *Journal of the Physical Society of Japan*, 86(3):034714, 2017. doi: 10.7566/JPSJ.86.034714. URL https://doi.org/10.7566/JPSJ.86.034714.

[78] Luan M. Veríssimo, Maria S.S. Pereira, Jozef Strečka, and Marcelo L. Lyra. Topological quantum phase transition in a mixed-spin heisenberg tetramer chain with alternating spin-1/2 and spin-5/2 dimers. *Journal of Magnetism and Magnetic Materials*, 571:170595, 2023. ISSN 0304-8853. doi: https://doi.org/10.1016/j.jmmm.2023.170595. URL https://www.sciencedirect.com/science/article/pii/S0304885323002445.

[79] F C Alcaraz and A L Malvezzi. Critical behaviour of mixed heisenberg chains. *Journal of Physics A: Mathematical and General*, 30(3):767, feb 1997. doi: 10.1088/0305-4470/30/3/003. URL https://dx.doi.org/10.1088/0305-4470/30/3/003.

[80] S Brehmer, H-J Mikeska, and Shoji Yamamoto. Low-temperature properties of quantum antiferromagnetic chains with alternating spins and. *Journal of Physics: Condensed Matter*, 9(19):3921, may 1997. doi: 10.1088/0953-8984/9/19/012. URL https://dx.doi.org/10.1088/0953-8984/9/19/012.

[81] Swapan K Pati, S Ramasesha, and Diptiman Sen. A density matrix renormalization group study of low-energy excitations and low-temperature properties of alternating spin systems. *Journal of Physics: Condensed Matter*, 9(41):8707, oct 1997. doi:

10.1088/0953-8984/9/41/016. URL `https://dx.doi.org/10.1088/0953-8984/9/41/016`.

[82] Swapan K. Pati, S. Ramasesha, and Diptiman Sen. Low-lying excited states and low-temperature properties of an alternating spin-1–spin-1/2 chain: A density-matrix renormalization-group study. *Phys. Rev. B*, 55:8894–8904, Apr 1997. doi: 10.1103/PhysRevB.55.8894. URL `https://link.aps.org/doi/10.1103/PhysRevB.55.8894`.

[83] Shoji Yamamoto, S. Brehmer, and H.-J. Mikeska. Elementary excitations of heisenberg ferrimagnetic spin chains. *Phys. Rev. B*, 57:13610–13616, Jun 1998. doi: 10.1103/PhysRevB.57.13610. URL `https://link.aps.org/doi/10.1103/PhysRevB.57.13610`.

[84] K. Maisinger, U. Schollwöck, S. Brehmer, H. J. Mikeska, and Shoji Yamamoto. Thermodynamics of the $(1, \frac{1}{2})$ ferrimagnet in finite magnetic fields. *Phys. Rev. B*, 58:R5908–R5911, Sep 1998. doi: 10.1103/PhysRevB.58.R5908. URL `https://link.aps.org/doi/10.1103/PhysRevB.58.R5908`.

[85] Antônio S F Tenório, R R Montenegro-Filho, and M D Coutinho-Filho. Quantum phase transitions in alternating spin-$(\frac{1}{2}, \frac{5}{2})$ heisenberg chains. *Journal of Physics: Condensed Matter*, 23(50):506003, dec 2011. doi: 10.1088/0953-8984/23/50/506003. URL `https://dx.doi.org/10.1088/0953-8984/23/50/506003`.

[86] W. M. da Silva and R. R. Montenegro-Filho. Role of density-dependent magnon hopping and magnon-magnon repulsion in ferrimagnetic spin-$(1/2, s)$ chains in a magnetic field. *Phys. Rev. B*, 103:054432, Feb 2021. doi: 10.1103/PhysRevB.103.054432. URL `https://link.aps.org/doi/10.1103/PhysRevB.103.054432`.

[87] R. R. Montenegro-Filho, F. S. Matias, and M. D. Coutinho-Filho. Topology of many-body edge and extended quantum states in an open spin chain: 1/3 plateau, kosterlitz-thouless transition, and luttinger liquid. *Phys. Rev. B*, 102:035137, Jul 2020. doi: 10.1103/PhysRevB.102.035137. URL `https://link.aps.org/doi/10.1103/PhysRevB.102.035137`.

[88] Karlová Katarína, Jozef Strečka, and Marcelo L. Lyra. Breakdown of intermediate one-half magnetization plateau of spin-1/2 ising-heisenberg and heisenberg branched

chains at triple and kosterlitz-thouless critical points. *Phys. Rev. E*, 100:042127, Oct 2019. doi: 10.1103/PhysRevE.100.042127. URL https://link.aps.org/doi/10.1103/PhysRevE.100.042127.

[89] Luan M. Veríssimo, Maria S. S. Pereira, Jozef Strečka, and Marcelo L. Lyra. Kosterlitz-thouless and gaussian criticalities in a mixed spin-($\frac{1}{2}, \frac{5}{2}, \frac{1}{2}$) heisenberg branched chain with exchange anisotropy. *Phys. Rev. B*, 99:134408, Apr 2019. doi: 10.1103/PhysRevB.99.134408. URL https://link.aps.org/doi/10.1103/PhysRevB.99.134408.

[90] Luan M Veríssimo, Maria S S Pereira, Jozef Strečka, and Marcelo L Lyra. Ground-state phase diagram and universality of sequential topological valence-bond-solid quantum transitions in a mixed tetramer chain. *Journal of Physics: Condensed Matter*, 36(16):165802, jan 2024. doi: 10.1088/1361-648X/ad1ca4. URL https://dx.doi.org/10.1088/1361-648X/ad1ca4.

[91] R. R. Montenegro-Filho, E. J. P. Silva-Júnior, and M. D. Coutinho-Filho. Ground-state phase diagram and thermodynamics of coupled trimer chains. *Phys. Rev. B*, 105:134423, Apr 2022. doi: 10.1103/PhysRevB.105.134423. URL https://link.aps.org/doi/10.1103/PhysRevB.105.134423.

[92] Luca Capriotti and Federico Becca. Quantum phase transition in coupled spin ladders. *Phys. Rev. B*, 65:092406, Feb 2002. doi: 10.1103/PhysRevB.65.092406. URL https://link.aps.org/doi/10.1103/PhysRevB.65.092406.

[93] S. Dalosto and J. Riera. Magnetic order in ferromagnetically coupled spin ladders. *Physical Review B - Condensed Matter and Materials Physics*, 62(2):928 – 933, 2000. doi: 10.1103/physrevb.62.928. URL https://www.scopus.com/inward/record.uri?eid=2-s2.0-4244142861&doi=10.1103%2fphysrevb.62.928&partnerID=40&md5=c0fb1ffb89a0d7b0aef3aa502a24b4e8. Cited by: 15; All Open Access, Green Open Access.

[94] M. Jeong, H. Mayaffre, C. Berthier, D. Schmidiger, A. Zheludev, and M. Horvatić. Magnetic-order crossover in coupled spin ladders. *Phys. Rev. Lett.*, 118:167206, Apr 2017. doi: 10.1103/PhysRevLett.118.167206. URL https://link.aps.org/doi/10.1103/PhysRevLett.118.167206.

[95] Y.J. Kim, R.J. Birgeneau, M.A. Kastner, Y.S. Lee, Y. Endoh, G. Shirane, and K. Yamada. Quantum monte carlo study of weakly coupled spin ladders. *Physical Review B - Condensed Matter and Materials Physics*, 60 (5):3294 – 3304, 1999. doi: 10.1103/PhysRevB.60.3294. URL `https://www.scopus.com/inward/record.uri?eid=2-s2.0-0000630545&doi=10.1103%2fPhysRevB.60.3294&partnerID=40&md5=fb1c81b6b5f48271707aae98edd2f8fa`. Cited by: 20; All Open Access, Green Open Access.

[96] Munehisa Matsumoto, Chitoshi Yasuda, Synge Todo, and Hajime Takayama. Ground-state phase diagram of quantum heisenberg antiferromagnets on the anisotropic dimerized square lattice. *Phys. Rev. B*, 65:014407, Nov 2001. doi: 10.1103/PhysRevB.65.014407. URL `https://link.aps.org/doi/10.1103/PhysRevB.65.014407`.

[97] Jakub Tworzydło, O. Osman, C.A. van Duin, and Jan Zaanen. Quantum magnetism in the stripe phase: Bond versus site order. *Physical Review B - Condensed Matter and Materials Physics*, 59(1):115 – 118, 1999. doi: 10.1103/PhysRevB.59.115. URL `https://www.scopus.com/inward/record.uri?eid=2-s2.0-0001194773&doi=10.1103%2fPhysRevB.59.115&partnerID=40&md5=2f28edbfd251a2989ba263c7152f64e8`. Cited by: 43; All Open Access, Green Open Access.

[98] A. S. Gibbs, A. Yamamoto, A. N. Yaresko, K. S. Knight, H. Yasuoka, M. Majumder, M. Baenitz, P. J. Saines, J. R. Hester, D. Hashizume, A. Kondo, K. Kindo, and H. Takagi. $s = \frac{1}{2}$ quantum critical spin ladders produced by orbital ordering in ba_2cuteo_6. *Phys. Rev. B*, 95:104428, Mar 2017. doi: 10.1103/PhysRevB.95.104428. URL `https://link.aps.org/doi/10.1103/PhysRevB.95.104428`.

[99] David Macdougal, Alexandra S. Gibbs, Tao Ying, Stefan Wessel, Helen C. Walker, David Voneshen, Frédéric Mila, Hidenori Takagi, and Radu Coldea. Spin dynamics of coupled spin ladders near quantum criticality in ba_2cuteo_6. *Phys. Rev. B*, 98:174410, Nov 2018. doi: 10.1103/PhysRevB.98.174410. URL `https://link.aps.org/doi/10.1103/PhysRevB.98.174410`.

[100] Charlotte Pughe, Otto H. J. Mustonen, Alexandra S. Gibbs, Stephen Lee, Rhea Stewart, Ben Gade, Chennan Wang, Hubertus Luetkens, Anna Foster, Fiona C.

Coomer, Hidenori Takagi, and Edmund J. Cussen. Partitioning the two-leg spin ladder in $ba_2cu_{1-x}zn_xteo_6$: From magnetic order through spin-freezing to paramagnetism. *Chemistry of Materials*, 35(7):2752–2761, 2023. doi: 10.1021/acs.chemmater.2c02939. URL https://doi.org/10.1021/acs.chemmater.2c02939.

[101] Firas Awwadi, Roger D. Willett, Brendan Twamley, Ryan Schneider, and Christopher P. Landee. Strong rail spin 1/2 antiferromagnetic ladder systems: (dimethylammonium)(3,5-dimethylpyridinium)cux4, x = cl, br. *Inorganic Chemistry*, 47(20):9327–9332, 2008. doi: 10.1021/ic800905e. URL https://doi.org/10.1021/ic800905e. PMID: 18816048.

[102] Tao Hong, K. P. Schmidt, K. Coester, F. F. Awwadi, M. M. Turnbull, Y. Qiu, J. A. Rodriguez-Rivera, M. Zhu, X. Ke, C. P. Aoyama, Y. Takano, Huibo Cao, W. Tian, J. Ma, R. Custelcean, H. D. Zhou, and M. Matsuda. Magnetic ordering induced by interladder coupling in the spin-$\frac{1}{2}$ heisenberg two-leg ladder antiferromagnet $c_9h_{18}n_2cubr_4$. *Phys. Rev. B*, 89:174432, May 2014. doi: 10.1103/PhysRevB.89.174432. URL https://link.aps.org/doi/10.1103/PhysRevB.89.174432.

[103] T. Ying, K. P. Schmidt, and S. Wessel. Higgs mode of planar coupled spin ladders and its observation in $c_9h_{18}n_2cubr_4$. *Phys. Rev. Lett.*, 122:127201, Mar 2019. doi: 10.1103/PhysRevLett.122.127201. URL https://link.aps.org/doi/10.1103/PhysRevLett.122.127201.

[104] Tao Hong, Masashige Matsumoto, Yiming Qiu, Wangchun Chen, Thomas R. Gentile, Shannon Watson, Firas F. Awwadi, Mark M. Turnbull, Sachith E. Dissanayake, Harish Agrawal, Rasmus Toft-Petersen, Bastian Klemke, Kris Coester, Kai P. Schmidt, and David A. Tennant. Higgs amplitude mode in a two-dimensional quantum antiferromagnet near the quantum critical point. *Nature Physics*, 13 (7):638–642, July 2017. ISSN 1745-2481. doi: 10.1038/nphys4182. URL http://dx.doi.org/10.1038/nphys4182.

[105] Jian-Jun Jiang. Coupled cluster study of the coupled spin ladders with frustration. *Physica A: Statistical Mechanics and its Applications*, 540:123131, 2020. ISSN 0378-4371. doi: https://doi.org/10.1016/j.physa.2019.123131. URL https://www.sciencedirect.com/science/article/pii/S0378437119317650.

[106] Kenneth G. Wilson. The renormalization group: Critical phenomena and the kondo problem. *Rev. Mod. Phys.*, 47:773–840, Oct 1975. doi: 10.1103/RevModPhys.47.773. URL https://link.aps.org/doi/10.1103/RevModPhys.47.773.

[107] S. R. White and R. M. Noack. Real-space quantum renormalization groups. *Phys. Rev. Lett.*, 68:3487–3490, Jun 1992. doi: 10.1103/PhysRevLett.68.3487. URL https://link.aps.org/doi/10.1103/PhysRevLett.68.3487.

[108] Adrian E. Feiguin. The density matrix renormalization group and its time-dependent variants. *AIP Conference Proceedings*, 1419(1):5–92, 12 2011. ISSN 0094-243X. doi: 10.1063/1.3667323. URL https://doi.org/10.1063/1.3667323.

[109] Ulrich Schollwöck. The density-matrix renormalization group in the age of matrix product states. *Annals of Physics*, 326(1):96–192, 2011. ISSN 0003-4916. doi: https://doi.org/10.1016/j.aop.2010.09.012. URL https://www.sciencedirect.com/science/article/pii/S0003491610001752. January 2011 Special Issue.

[110] C. Lanczos. An iteration method for the solution of the eigenvalue problem of linear differential and integral operators. *Journal of Research of the National Bureau of Standards*, 45(4):255, October 1950. doi: 10.6028/jres.045.026. URL https://doi.org/10.6028/jres.045.026.

[111] André Luiz Malvezzi. An introduction to numerical methods in low-dimensional quantum systems. *Brazilian Journal of Physics*, 33(1), March 2003. ISSN 0103-9733. doi: 10.1590/s0103-97332003000100004. URL http://dx.doi.org/10.1590/S0103-97332003000100004.

[112] Guifré Vidal. Efficient classical simulation of slightly entangled quantum computations. *Phys. Rev. Lett.*, 91:147902, Oct 2003. doi: 10.1103/PhysRevLett.91.147902. URL https://link.aps.org/doi/10.1103/PhysRevLett.91.147902.

[113] Matthew Fishman, Steven R. White, and E. Miles Stoudenmire. The ITensor Software Library for Tensor Network Calculations. *SciPost Phys. Codebases*, page 4, 2022. doi: 10.21468/SciPostPhysCodeb.4. URL https://scipost.org/10.21468/SciPostPhysCodeb.4.

[114] Martin Ganahl, Jackson Beall, Markus Hauru, Adam G.M. Lewis, Tomasz Wojno, Jae Hyeon Yoo, Yijian Zou, and Guifre Vidal. Density matrix renormalization group

with tensor processing units. *PRX Quantum*, 4:010317, Feb 2023. doi: 10.1103/PRXQuantum.4.010317. URL https://link.aps.org/doi/10.1103/PRXQuantum.4.010317.

[115] C. Hubig, I. P. McCulloch, U. Schollwöck, and F. A. Wolf. Strictly single-site dmrg algorithm with subspace expansion. *Phys. Rev. B*, 91:155115, Apr 2015. doi: 10.1103/PhysRevB.91.155115. URL https://link.aps.org/doi/10.1103/PhysRevB.91.155115.

[116] Ryan Levy, Edgar Solomonik, and Bryan K. Clark. Distributed-memory dmrg via sparse and dense parallel tensor contractions. *SC20: International Conference for High Performance Computing, Networking, Storage and Analysis*, pages 1–14, 2020. URL https://api.semanticscholar.org/CorpusID:220496045.

[117] Ernest R. Davidson. The iterative calculation of a few of the lowest eigenvalues and corresponding eigenvectors of large real-symmetric matrices. *Journal of Computational Physics*, 17(1):87–94, 1975. ISSN 0021-9991. doi: https://doi.org/10.1016/0021-9991(75)90065-0. URL https://www.sciencedirect.com/science/article/pii/0021999175900650.

[118] Steven R. White and A. L. Chernyshev. Neél order in square and triangular lattice heisenberg models. *Phys. Rev. Lett.*, 99:127004, Sep 2007. doi: 10.1103/PhysRevLett.99.127004. URL https://link.aps.org/doi/10.1103/PhysRevLett.99.127004.

[119] M. Q. Weng, D. N. Sheng, Z. Y. Weng, and Robert J. Bursill. Spin-liquid phase in an anisotropic triangular-lattice heisenberg model: Exact diagonalization and density-matrix renormalization group calculations. *Phys. Rev. B*, 74:012407, Jul 2006. doi: 10.1103/PhysRevB.74.012407. URL https://link.aps.org/doi/10.1103/PhysRevB.74.012407.

[120] Shin-ichiro Yoshikawa, Kouichi Okunishi, Makoto Senda, and Seiji Miyashita. Quantum fluctuation-induced phase transition in s=1/2 xy-like heisenberg antiferromagnets on the triangular lattice. *Journal of the Physical Society of Japan*, 73(7):1798–1804, 2004. doi: 10.1143/JPSJ.73.1798. URL https://doi.org/10.1143/JPSJ.73.1798.

[121] H. C. Jiang, Z. Y. Weng, and D. N. Sheng. Density matrix renormalization group numerical study of the kagome antiferromagnet. *Phys. Rev. Lett.*, 101:117203, Sep 2008. doi: 10.1103/PhysRevLett.101.117203. URL https://link.aps.org/doi/10.1103/PhysRevLett.101.117203.

[122] Simeng Yan, David A. Huse, and Steven R. White. Spin-liquid ground state of the $S = 1/2$ kagome heisenberg antiferromagnet. *Science*, 332(6034):1173–1176, 2011. doi: 10.1126/science.1201080. URL https://www.science.org/doi/abs/10.1126/science.1201080.

[123] Hong-Chen Jiang, Hong Yao, and Leon Balents. Spin liquid ground state of the spin-$\frac{1}{2}$ square J_1-J_2 heisenberg model. *Phys. Rev. B*, 86:024424, Jul 2012. doi: 10.1103/PhysRevB.86.024424. URL https://link.aps.org/doi/10.1103/PhysRevB.86.024424.

[124] Xiangjian Qian and Mingpu Qin. Absence of spin liquid phase in the $J_1 - J_2$ heisenberg model on the square lattice. *Phys. Rev. B*, 109:L161103, Apr 2024. doi: 10.1103/PhysRevB.109.L161103. URL https://link.aps.org/doi/10.1103/PhysRevB.109.L161103.

[125] J. C. Xavier. A simple way to avoid metastable configurations in the density-matrix renormalization-group algorithms. *Brazilian Journal of Physics*, 39(3):596–599, September 2009. ISSN 0103-9733. doi: 10.1590/s0103-97332009000500016. URL http://dx.doi.org/10.1590/S0103-97332009000500016.

[126] E.M. Stoudenmire and Steven R. White. Studying two-dimensional systems with the density matrix renormalization group. *Annual Review of Condensed Matter Physics*, 3(Volume 3, 2012):111–128, 2012. ISSN 1947-5462. doi: https://doi.org/10.1146/annurev-conmatphys-020911-125018. URL https://www.annualreviews.org/content/journals/10.1146/annurev-conmatphys-020911-125018.

[127] F. Verstraete, D. Porras, and J. I. Cirac. Density matrix renormalization group and periodic boundary conditions: A quantum information perspective. *Phys. Rev. Lett.*, 93:227205, Nov 2004. doi: 10.1103/PhysRevLett.93.227205. URL https://link.aps.org/doi/10.1103/PhysRevLett.93.227205.

[128] A.F. Albuquerque, F. Alet, P. Corboz, P. Dayal, A. Feiguin, S. Fuchs, L. Gamper, E. Gull, S. Gürtler, A. Honecker, R. Igarashi, M. Körner, A. Kozhevnikov, A. Läuchli, S.R. Manmana, M. Matsumoto, I.P. McCulloch, F. Michel, R.M. Noack, G. Pawłowski, L. Pollet, T. Pruschke, U. Schollwöck, S. Todo, S. Trebst, M. Troyer, P. Werner, and S. Wessel. The alps project release 1.3: Open-source software for strongly correlated systems. *Journal of Magnetism and Magnetic Materials*, 310(2, Part 2):1187–1193, 2007. ISSN 0304-8853. doi: https://doi.org/10.1016/j.jmmm.2006.10.304. URL https://www.sciencedirect.com/science/article/pii/S0304885306014983. Proceedings of the 17th International Conference on Magnetism.

[129] F. Alet, P. Dayal, A. Grzesik, A. Honecker, M. Körner, A. Läuchli, S. R. Manmana, I. P. McCulloch, F. Michel, R. M. Noack, G. Schmid, U. Schollwöck, F. Stöckli, S. Todo, S. Trebst, M. Troyer, P. Werner, and S. Wessel. The alps project: Open source software for strongly correlated systems. *Journal of the Physical Society of Japan*, 74(Suppl):30–35, 2005. doi: 10.1143/JPSJS.74S.30. URL https://doi.org/10.1143/JPSJS.74S.30.

[130] B Bauer, L D Carr, H G Evertz, A Feiguin, J Freire, S Fuchs, L Gamper, J Gukelberger, E Gull, S Guertler, A Hehn, R Igarashi, S V Isakov, D Koop, P N Ma, P Mates, H Matsuo, O Parcollet, G Pawłowski, J D Picon, L Pollet, E Santos, V W Scarola, U Schollwöck, C Silva, B Surer, S Todo, S Trebst, M Troyer, M L Wall, P Werner, and S Wessel. The alps project release 2.0: open source software for strongly correlated systems. *Journal of Statistical Mechanics: Theory and Experiment*, 2011(05):P05001, may 2011. doi: 10.1088/1742-5468/2011/05/P05001. URL https://dx.doi.org/10.1088/1742-5468/2011/05/P05001.

[131] L.D. Faddeev and L.A. Takhtajan. What is the spin of a spin wave? *Physics Letters A*, 85(6):375–377, 1981. ISSN 0375-9601. doi: https://doi.org/10.1016/0375-9601(81)90335-2. URL https://www.sciencedirect.com/science/article/pii/0375960181903352.

[132] J. M. Luttinger. An exactly soluble model of a many-fermion system. *Journal of Mathematical Physics*, 4(9):1154–1162, 09 1963. ISSN 0022-2488. doi: 10.1063/1.1704046. URL https://doi.org/10.1063/1.1704046.

[133] Sin-itiro Tomonaga. Remarks on bloch's method of sound waves applied to many-fermion problems. *Progress of Theoretical Physics*, 5(4):544–569, 07 1950. ISSN 0033-068X. doi: 10.1143/ptp/5.4.544. URL https://doi.org/10.1143/ptp/5.4.544.

[134] Thierry Giamarchi. *Quantum Physics in One Dimension*. Oxford University Press, 12 2003. ISBN 9780198525004. doi: 10.1093/acprof:oso/9780198525004.001.0001. URL https://doi.org/10.1093/acprof:oso/9780198525004.001.0001.

[135] M. A. Cazalilla, R. Citro, T. Giamarchi, E. Orignac, and M. Rigol. One dimensional bosons: From condensed matter systems to ultracold gases. *Rev. Mod. Phys.*, 83: 1405–1466, Dec 2011. doi: 10.1103/RevModPhys.83.1405. URL https://link.aps.org/doi/10.1103/RevModPhys.83.1405.

[136] A. O. Gogolin, A. A. Nersesyan, and A. M. Tsvelik. Bosonization and strongly correlated systems, 1999. URL https://arxiv.org/abs/cond-mat/9909069.

[137] F. D. M. Haldane. Luttinger liquid theory of one-dimensional quantum fluids. I. Properties of the Luttinger model and their extension to the general 1D interacting spinless Fermi gas. *J. Phys. C*, 14:2585–2609, 1981. doi: 10.1088/0022-3719/14/19/010.

[138] T. GIAMARCHI. Some experimental tests of tomonaga–luttinger liquids. *International Journal of Modern Physics B*, 26(22):1244004, 2012. doi: 10.1142/S0217979212440043. URL https://doi.org/10.1142/S0217979212440043.

[139] H. Bethe. Zur theorie der metalle: I. eigenwerte und eigenfunktionen der linearen atomkette. *Zeitschrift für Physik*, 71(3–4):205–226, March 1931. ISSN 1434-601X. doi: 10.1007/bf01341708. URL http://dx.doi.org/10.1007/BF01341708.

[140] Thao T. Tran, Chris A. Pocs, Yubo Zhang, Michal J. Winiarski, Jianwei Sun, Minhyea Lee, and Tyrel M. McQueen. Spinon excitations in the quasi-one-dimensional $s = \frac{1}{2}$ chain compound $Cs_4CuSb_2Cl_{12}$. *Phys. Rev. B*, 101:235107, Jun 2020. doi: 10.1103/PhysRevB.101.235107. URL https://link.aps.org/doi/10.1103/PhysRevB.101.235107.

[141] Oliver Breunig, Markus Garst, Andreas Klümper, Jens Rohrkamp, Mark M. Turnbull, and Thomas Lorenz. Quantum criticality in the spin-1/2 heisenberg

chain system copper pyrazine dinitrate. *Science Advances*, 3(12):eaao3773, 2017. doi: 10.1126/sciadv.aao3773. URL `https://www.science.org/doi/abs/10.1126/sciadv.aao3773`.

[142] Bella Lake, D. Alan Tennant, Chris D. Frost, and Stephen E. Nagler. Quantum criticality and universal scaling of a quantum antiferromagnet. *Nature Materials*, 4(4):329–334, March 2005. ISSN 1476-4660. doi: 10.1038/nmat1327. URL `http://dx.doi.org/10.1038/nmat1327`.

[143] H. Mutka, C. Payen, and P. Molinié. One-dimensional heisenberg antiferromagnet with spin s = 3/2. experiments on agcrp2s6. *Europhysics Letters*, 21(5):623, feb 1993. doi: 10.1209/0295-5075/21/5/020. URL `https://dx.doi.org/10.1209/0295-5075/21/5/020`.

[144] Shinichi Itoh, Yasuo Endoh, Kazuhisa Kakurai, and Hidekazu Tanaka. Quantum spin dynamics of an $S = 3/2$ heisenberg antiferromagnetic chain: Inelastic pulsed neutron scattering from csvcl$_3$. *Phys. Rev. Lett.*, 74:2375–2378, Mar 1995. doi: 10.1103/PhysRevLett.74.2375. URL `https://link.aps.org/doi/10.1103/PhysRevLett.74.2375`.

[145] K. Hallberg, X. Q. G. Wang, P. Horsch, and A. Moreo. Critical behavior of the $S = 3/2$ antiferromagnetic heisenberg chain. *Phys. Rev. Lett.*, 76:4955–4958, Jun 1996. doi: 10.1103/PhysRevLett.76.4955. URL `https://link.aps.org/doi/10.1103/PhysRevLett.76.4955`.

[146] Martin Mourigal, Mechthild Enderle, Axel Klöpperpieper, Jean-Sébastien Caux, Anne Stunault, and Henrik M. Rønnow. Fractional spinon excitations in the quantum heisenberg antiferromagnetic chain. *Nature Physics*, 9(7):435–441, June 2013. ISSN 1745-2481. doi: 10.1038/nphys2652. URL `http://dx.doi.org/10.1038/nphys2652`.

[147] I Affleck, D Gepner, H J Schulz, and T Ziman. Critical behaviour of spin-s heisenberg antiferromagnetic chains: analytic and numerical results. *Journal of Physics A: Mathematical and General*, 22(5):511, mar 1989. doi: 10.1088/0305-4470/22/5/015. URL `https://dx.doi.org/10.1088/0305-4470/22/5/015`.

[148] I Affleck. Quantum spin chains and the haldane gap. *Journal of Physics: Condensed Matter*, 1(19):3047, may 1989. doi: 10.1088/0953-8984/1/19/001. URL `https://dx.doi.org/10.1088/0953-8984/1/19/001`.

[149] O. Golinelli, Th. Jolicoeur, and R. Lacaze. Finite-lattice extrapolations for a haldane-gap antiferromagnet. *Phys. Rev. B*, 50:3037–3044, Aug 1994. doi: 10.1103/PhysRevB.50.3037. URL `https://link.aps.org/doi/10.1103/PhysRevB.50.3037`.

[150] Steven R. White and David A. Huse. Numerical renormalization-group study of low-lying eigenstates of the antiferromagnetic s=1 heisenberg chain. *Phys. Rev. B*, 48:3844–3852, Aug 1993. doi: 10.1103/PhysRevB.48.3844. URL `https://link.aps.org/doi/10.1103/PhysRevB.48.3844`.

[151] L.P. Regnault, J. Rossat-Mignod, and J.P. Renard. Wave vector dependences of magnetic excitations in the s= 1 one-dimensional antiferromagnet nenp. *Journal of Magnetism and Magnetic Materials*, 104-107:869–870, 1992. ISSN 0304-8853. doi: https://doi.org/10.1016/0304-8853(92)90400-I. URL `https://www.sciencedirect.com/science/article/pii/030488539290400I`. Proceedings of the International Conference on Magnetism, Part II.

[152] J. P. Renard, M. Verdaguer, L. P. Regnault, W. A. C. Erkelens, J. Rossat-Mignod, J. Ribas, W. G. Stirling, and C. Vettier. Quantum energy gap in two quasi-one-dimensional s=1 heisenberg antiferromagnets (invited). *Journal of Applied Physics*, 63(8):3538–3542, 04 1988. ISSN 0021-8979. doi: 10.1063/1.340736. URL `https://doi.org/10.1063/1.340736`.

[153] U. Schollwöck and T. Jolicoeur. Haldane gap and hidden order in the s = 2 antiferromagnetic quantum spin chain. *Europhysics Letters*, 30(8):493, jun 1995. doi: 10.1209/0295-5075/30/8/009. URL `https://dx.doi.org/10.1209/0295-5075/30/8/009`.

[154] Synge Todo and Kiyoshi Kato. Cluster algorithms for general- S quantum spin systems. *Phys. Rev. Lett.*, 87:047203, Jul 2001. doi: 10.1103/PhysRevLett.87.047203. URL `https://link.aps.org/doi/10.1103/PhysRevLett.87.047203`.

[155] Xiaoqun Wang, Shaojing Qin, and Lu Yu. Haldane gap for the $s = 2$ antiferromagnetic heisenberg chain revisited. *Phys. Rev. B*, 60:14529–14532, Dec 1999. doi: 10.1103/PhysRevB.60.14529. URL `https://link.aps.org/doi/10.1103/PhysRevB.60.14529`.

[156] Hiroki Nakano and Toru Sakai. Precise estimation of the s = 2 haldane gap by numerical diagonalization. *Journal of the Physical Society of Japan*, 87(10):105002, 2018. doi: 10.7566/JPSJ.87.105002. URL `https://doi.org/10.7566/JPSJ.87.105002`.

[157] G. E. Granroth, M. W. Meisel, M. Chaparala, Th. Jolicœur, B. H. Ward, and D. R. Talham. Experimental evidence of a haldane gap in an $S = 2$ quasi-linear-chain antiferromagnet. *Phys. Rev. Lett.*, 77:1616–1619, Aug 1996. doi: 10.1103/PhysRevLett.77.1616. URL `https://link.aps.org/doi/10.1103/PhysRevLett.77.1616`.

[158] M Hagiwara, Y Idutsu, Z Honda, and S Yamamoto. Magnetic properties of the s=2 heisenberg antiferromagnetic chain compound mncl3(bpy). *Journal of Physics: Conference Series*, 400(3):032014, dec 2012. doi: 10.1088/1742-6596/400/3/032014. URL `https://dx.doi.org/10.1088/1742-6596/400/3/032014`.

[159] Ian Affleck, Tom Kennedy, Elliott H. Lieb, and Hal Tasaki. Rigorous results on valence-bond ground states in antiferromagnets. *Phys. Rev. Lett.*, 59:799–802, Aug 1987. doi: 10.1103/PhysRevLett.59.799. URL `https://link.aps.org/doi/10.1103/PhysRevLett.59.799`.

[160] F. D. M. Haldane. Ground state properties of antiferromagnetic chains with unrestricted spin: Integer spin chains as realisations of the O(3) non-linear sigma model, 2016. URL `https://arxiv.org/abs/1612.00076`.

[161] K. v. Klitzing, G. Dorda, and M. Pepper. New method for high-accuracy determination of the fine-structure constant based on quantized hall resistance. *Phys. Rev. Lett.*, 45:494–497, Aug 1980. doi: 10.1103/PhysRevLett.45.494. URL `https://link.aps.org/doi/10.1103/PhysRevLett.45.494`.

[162] D. C. Tsui, H. L. Stormer, and A. C. Gossard. Two-dimensional magnetotransport in the extreme quantum limit. *Phys. Rev. Lett.*, 48:1559–1562, May 1982.

doi: 10.1103/PhysRevLett.48.1559. URL https://link.aps.org/doi/10.1103/PhysRevLett.48.1559.

[163] Zheng-Cheng Gu and Xiao-Gang Wen. Tensor-entanglement-filtering renormalization approach and symmetry-protected topological order. *Phys. Rev. B*, 80:155131, Oct 2009. doi: 10.1103/PhysRevB.80.155131. URL https://link.aps.org/doi/10.1103/PhysRevB.80.155131.

[164] Koos Rommelse and Marcel den Nijs. Preroughening transitions in surfaces. *Phys. Rev. Lett.*, 59:2578–2581, Nov 1987. doi: 10.1103/PhysRevLett.59.2578. URL https://link.aps.org/doi/10.1103/PhysRevLett.59.2578.

[165] Tom Kennedy and Hal Tasaki. Hidden $z_2 \times z_2$ symmetry breaking in haldane-gap antiferromagnets. *Phys. Rev. B*, 45:304–307, Jan 1992. doi: 10.1103/PhysRevB.45.304. URL https://link.aps.org/doi/10.1103/PhysRevB.45.304.

[166] M Oshikawa. Hidden $Z_2 \times Z_2$ symmetry in quantum spin chains with arbitrary integer spin. *Journal of Physics: Condensed Matter*, 4(36):7469, sep 1992. doi: 10.1088/0953-8984/4/36/019. URL https://dx.doi.org/10.1088/0953-8984/4/36/019.

[167] Hiroshi Ueda, Hiroki Nakano, and Koichi Kusakabe. Finite-size scaling of string order parameters characterizing the haldane phase. *Phys. Rev. B*, 78:224402, Dec 2008. doi: 10.1103/PhysRevB.78.224402. URL https://link.aps.org/doi/10.1103/PhysRevB.78.224402.

[168] F. B. Ramos and J. C. Xavier. n-leg spin-s heisenberg ladders: A density-matrix renormalization group study. *Phys. Rev. B*, 89:094424, Mar 2014. doi: 10.1103/PhysRevB.89.094424. URL https://link.aps.org/doi/10.1103/PhysRevB.89.094424.

[169] D. Sénéchal. Semiclassical description of spin ladders. *Phys. Rev. B*, 52:15319–15326, Dec 1995. doi: 10.1103/PhysRevB.52.15319. URL https://link.aps.org/doi/10.1103/PhysRevB.52.15319.

[170] Germán Sierra. The nonlinear sigma model and spin ladders. *Journal of Physics A: Mathematical and General*, 29(12):3299, jun 1996. doi: 10.1088/0305-4470/29/12/032. URL https://dx.doi.org/10.1088/0305-4470/29/12/032.

[171] Beat Frischmuth, Beat Ammon, and Matthias Troyer. Susceptibility and low-temperature thermodynamics of spin-$\frac{1}{2}$ heisenberg ladders. *Phys. Rev. B*, 54:R3714–R3717, Aug 1996. doi: 10.1103/PhysRevB.54.R3714. URL `https://link.aps.org/doi/10.1103/PhysRevB.54.R3714`.

[172] S. Liang, B. Doucot, and P. W. Anderson. Some new variational resonating-valence-bond-type wave functions for the spin-$\frac{1}{2}$ antiferromagnetic heisenberg model on a square lattice. *Phys. Rev. Lett.*, 61:365–368, Jul 1988. doi: 10.1103/PhysRevLett.61.365. URL `https://link.aps.org/doi/10.1103/PhysRevLett.61.365`.

[173] Steven A. Kivelson, Daniel S. Rokhsar, and James P. Sethna. Topology of the resonating valence-bond state: Solitons and high-T_c superconductivity. *Phys. Rev. B*, 35:8865–8868, Jun 1987. doi: 10.1103/PhysRevB.35.8865. URL `https://link.aps.org/doi/10.1103/PhysRevB.35.8865`.

[174] T. Barnes and J. Riera. Susceptibility and excitation spectrum of $(\mathrm{vo})_2\mathrm{p}_2\mathrm{o}_7$ in ladder and dimer-chain models. *Phys. Rev. B*, 50:6817–6822, Sep 1994. doi: 10.1103/PhysRevB.50.6817. URL `https://link.aps.org/doi/10.1103/PhysRevB.50.6817`.

[175] T. Barnes, E. Dagotto, J. Riera, and E. S. Swanson. Excitation spectrum of heisenberg spin ladders. *Phys. Rev. B*, 47:3196–3203, Feb 1993. doi: 10.1103/PhysRevB.47.3196. URL `https://link.aps.org/doi/10.1103/PhysRevB.47.3196`.

[176] M Reigrotzki, H Tsunetsugu, and T M Rice. Strong-coupling expansions for antiferromagnetic heisenberg spin-one-half ladders. *Journal of Physics: Condensed Matter*, 6(43):9235, oct 1994. doi: 10.1088/0953-8984/6/43/021. URL `https://dx.doi.org/10.1088/0953-8984/6/43/021`.

[177] Kazuo Hida. Haldane gap in the spin-1/2 double chain heisenberg antiferromagnet -numerical diagonalization and projector monte carlo study-. *Journal of the Physical Society of Japan*, 60(4):1347–1354, 1991. doi: 10.1143/JPSJ.60.1347. URL `https://doi.org/10.1143/JPSJ.60.1347`.

[178] D. G. Shelton, A. A. Nersesyan, and A. M. Tsvelik. Antiferromagnetic spin ladders: Crossover between spin s=1/2 and s=1 chains. *Phys. Rev. B*, 53:8521–8532, Apr

1996. doi: 10.1103/PhysRevB.53.8521. URL https://link.aps.org/doi/10.1103/PhysRevB.53.8521.

[179] S. P. Strong and A. J. Millis. Competition between singlet formation and magnetic ordering in one-dimensional spin systems. *Phys. Rev. Lett.*, 69:2419–2422, Oct 1992. doi: 10.1103/PhysRevLett.69.2419. URL https://link.aps.org/doi/10.1103/PhysRevLett.69.2419.

[180] M. Greven, R. J. Birgeneau, and U. J. Wiese. Monte carlo study of correlations in quantum spin ladders. *Phys. Rev. Lett.*, 77:1865–1868, Aug 1996. doi: 10.1103/PhysRevLett.77.1865. URL https://link.aps.org/doi/10.1103/PhysRevLett.77.1865.

[181] Yoshihiro Nishiyama, Naomichi Hatano, and Masuo Suzuki. Phase transition and hidden orders of the heisenberg ladder model in the ground state. *Journal of the Physical Society of Japan*, 64(6):1967–1979, 1995. doi: 10.1143/JPSJ.64.1967. URL https://doi.org/10.1143/JPSJ.64.1967.

[182] Leon Balents. Spin liquids in frustrated magnets. *Nature*, 464(7286):199–208, March 2010. ISSN 1476-4687. doi: 10.1038/nature08917. URL http://dx.doi.org/10.1038/nature08917.

[183] Claudine Lacroix, Philippe Mendels, and Frédéric Mila, editors. *Introduction to Frustrated Magnetism*, volume 164 of *Springer Series in Solid-State Sciences*. Springer Berlin, Heidelberg, 2011. ISBN 978-3-642-10588-3. doi: 10.1007/978-3-642-10589-0.

[184] Matthias Vojta. Frustration and quantum criticality. *Reports on Progress in Physics*, 81(6):064501, may 2018. doi: 10.1088/1361-6633/aab6be. URL https://dx.doi.org/10.1088/1361-6633/aab6be.

[185] J. Larrea Jiménez, S. P. G. Crone, E. Fogh, M. E. Zayed, R. Lortz, E. Pomjakushina, K. Conder, A. M. Läuchli, L. Weber, S. Wessel, A. Honecker, B. Normand, Ch. Rüegg, P. Corboz, H. M. Rønnow, and F. Mila. A quantum magnetic analogue to the critical point of water. *Nature*, 592(7854):370–375, April 2021. ISSN 1476-4687. doi: 10.1038/s41586-021-03411-8. URL http://dx.doi.org/10.1038/s41586-021-03411-8.

[186] J. Stapmanns, P. Corboz, F. Mila, A. Honecker, B. Normand, and S. Wessel. Thermal critical points and quantum critical end point in the frustrated bilayer heisenberg antiferromagnet. *Phys. Rev. Lett.*, 121:127201, Sep 2018. doi: 10.1103/PhysRevLett.121.127201. URL `https://link.aps.org/doi/10.1103/PhysRevLett.121.127201`.

[187] Y. Tokiwa, M. Garst, P. Gegenwart, S. L. Bud'ko, and P. C. Canfield. Quantum bicriticality in the heavy-fermion metamagnet ybagge. *Phys. Rev. Lett.*, 111:116401, Sep 2013. doi: 10.1103/PhysRevLett.111.116401. URL `https://link.aps.org/doi/10.1103/PhysRevLett.111.116401`.

[188] Indrani Bose and Saurabh Gayen. Hole motion in a coupled-chain model: Some exact results. *Phys. Rev. B*, 48:10653–10656, Oct 1993. doi: 10.1103/PhysRevB.48.10653. URL `https://link.aps.org/doi/10.1103/PhysRevB.48.10653`.

[189] Y. Xian. Rigorous results on a first-order phase transition in antiferromagnetic spin-1/2 coupled chains. *Phys. Rev. B*, 52:12485–12488, Nov 1995. doi: 10.1103/PhysRevB.52.12485. URL `https://link.aps.org/doi/10.1103/PhysRevB.52.12485`.

[190] XIAOQUN WANG. Low energy properties of a frustrated antiferromagnetic spin-1/2 ladder. *Modern Physics Letters B*, 14(09):327–335, 2000. doi: 10.1142/S0217984900000458. URL `https://doi.org/10.1142/S0217984900000458`.

[191] Zheng Weihong, V. Kotov, and J. Oitmaa. Two-chain spin ladder with frustrating second-neighbor interactions. *Phys. Rev. B*, 57:11439–11445, May 1998. doi: 10.1103/PhysRevB.57.11439. URL `https://link.aps.org/doi/10.1103/PhysRevB.57.11439`.

[192] S M Girvin and Daniel P Arovas. Hidden topological order in integer quantum spin chains. *Physica Scripta*, 1989(T27):156, jan 1989. doi: 10.1088/0031-8949/1989/T27/027. URL `https://dx.doi.org/10.1088/0031-8949/1989/T27/027`.

[193] Dave Allen, Fabian H. L. Essler, and Alexander A. Nersesyan. Fate of spinons in spontaneously dimerized spin-$\frac{1}{2}$ ladders. *Phys. Rev. B*, 61:8871–8877, Apr 2000. doi: 10.1103/PhysRevB.61.8871. URL `https://link.aps.org/doi/10.1103/PhysRevB.61.8871`.

[194] Oleg A. Starykh and Leon Balents. Dimerized phase and transitions in a spatially anisotropic square lattice antiferromagnet. *Phys. Rev. Lett.*, 93:127202, Sep 2004. doi: 10.1103/PhysRevLett.93.127202. URL https://link.aps.org/doi/10.1103/PhysRevLett.93.127202.

[195] Guang-Hua Liu, Hai-Long Wang, and Guang-Shan Tian. Existence of dimerized phases in frustrated spin ladder models. *Phys. Rev. B*, 77:214418, Jun 2008. doi: 10.1103/PhysRevB.77.214418. URL https://link.aps.org/doi/10.1103/PhysRevB.77.214418.

[196] Hsiang-Hsuan Hung, Chang-De Gong, Yung-Chung Chen, and Min-Fong Yang. Search for quantum dimer phases and transitions in a frustrated spin ladder. *Phys. Rev. B*, 73:224433, Jun 2006. doi: 10.1103/PhysRevB.73.224433. URL https://link.aps.org/doi/10.1103/PhysRevB.73.224433.

[197] Eugene H. Kim, Ö. Legeza, and J. Sólyom. Topological order, dimerization, and spinon deconfinement in frustrated spin ladders. *Phys. Rev. B*, 77:205121, May 2008. doi: 10.1103/PhysRevB.77.205121. URL https://link.aps.org/doi/10.1103/PhysRevB.77.205121.

[198] Toshiya Hikihara and Oleg A. Starykh. Phase diagram of the frustrated spin ladder. *Phys. Rev. B*, 81:064432, Feb 2010. doi: 10.1103/PhysRevB.81.064432. URL https://link.aps.org/doi/10.1103/PhysRevB.81.064432.

[199] G. Barcza, Ö. Legeza, R. M. Noack, and J. Sólyom. Dimerized phase in the cross-coupled antiferromagnetic spin ladder. *Phys. Rev. B*, 86:075133, Aug 2012. doi: 10.1103/PhysRevB.86.075133. URL https://link.aps.org/doi/10.1103/PhysRevB.86.075133.

[200] Xi-Hao Chen, Sam Young Cho, Huan-Qiang Zhou, and Murray T. Batchelor. The antiferromagnetic cross-coupled spin ladder: Quantum fidelity and tensor networks approach. *Journal of the Korean Physical Society*, 68(9):1114–1119, May 2016. ISSN 1976-8524. doi: 10.3938/jkps.68.1114. URL http://dx.doi.org/10.3938/jkps.68.1114.

[201] Cong Fu, Hui Zhao, Yu-Guang Chen, and Yong-Hong Yan. Ground-state phase diagram of the dimerized spin-1/2 two-leg ladder*. *Chinese Physics B*, 30(8):087501,

jul 2021. doi: 10.1088/1674-1056/abec31. URL https://dx.doi.org/10.1088/1674-1056/abec31.

[202] Yan-Chao Li and Hai-Qing Lin. Quantum phase diagram of the frustrated spin ladder with next-nearest-neighbor interactions. *New Journal of Physics*, 14(6):063019, jun 2012. doi: 10.1088/1367-2630/14/6/063019. URL https://dx.doi.org/10.1088/1367-2630/14/6/063019.

[203] Temo Vekua and Andreas Honecker. Quantum dimer phases in a frustrated spin ladder: Effective field theory approach and exact diagonalization. *Phys. Rev. B*, 73:214427, Jun 2006. doi: 10.1103/PhysRevB.73.214427. URL https://link.aps.org/doi/10.1103/PhysRevB.73.214427.

[204] Rui Wen, Guang-Hua Liu, and Guang-Shan Tian. Quantum phase transitions and dimerized phases in frustrated spin ladder. *Communications in Theoretical Physics*, 55(6):1102–1108, June 2011. ISSN 0253-6102. doi: 10.1088/0253-6102/55/6/26. URL http://dx.doi.org/10.1088/0253-6102/55/6/26.

[205] D. C. Cabra, A. Honecker, and P. Pujol. Magnetization curves of antiferromagnetic heisenberg spin- $\frac{1}{2}$ ladders. *Phys. Rev. Lett.*, 79:5126–5129, Dec 1997. doi: 10.1103/PhysRevLett.79.5126. URL https://link.aps.org/doi/10.1103/PhysRevLett.79.5126.

[206] O. V. Derzhko, T. E. Krokhmalskii, and J. Richter. Quantum heisenberg antiferromagnet on low-dimensional frustrated lattices. *Theoretical and Mathematical Physics*, 168(3):1236–1245, September 2011. ISSN 1573-9333. doi: 10.1007/s11232-011-0101-3. URL http://dx.doi.org/10.1007/s11232-011-0101-3.

[207] Masaki Oshikawa, Masanori Yamanaka, and Ian Affleck. Magnetization plateaus in spin chains: “haldane gap” for half-integer spins. *Phys. Rev. Lett.*, 78:1984–1987, Mar 1997. doi: 10.1103/PhysRevLett.78.1984. URL https://link.aps.org/doi/10.1103/PhysRevLett.78.1984.

[208] C. N. Yang and C. P. Yang. One-dimensional chain of anisotropic spin-spin interactions. iii. applications. *Phys. Rev.*, 151:258–264, Nov 1966. doi: 10.1103/PhysRev.151.258. URL https://link.aps.org/doi/10.1103/PhysRev.151.258.

[209] P. M. Chaikin and T. C. Lubensky. *Principles of Condensed Matter Physics*. Cambridge University Press, 1995.

[210] Michael E. Fisher and David R. Nelson. Spin flop, supersolids, and bicritical and tetracritical points. *Phys. Rev. Lett.*, 32:1350–1353, Jun 1974. doi: 10.1103/PhysRevLett.32.1350. URL `https://link.aps.org/doi/10.1103/PhysRevLett.32.1350`.

[211] J. M. Kosterlitz, David R. Nelson, and Michael E. Fisher. Bicritical and tetracritical points in anisotropic antiferromagnetic systems. *Phys. Rev. B*, 13:412–432, Jan 1976. doi: 10.1103/PhysRevB.13.412. URL `https://link.aps.org/doi/10.1103/PhysRevB.13.412`.

[212] Till D. Kühner, Steven R. White, and H. Monien. One-dimensional bose-hubbard model with nearest-neighbor interaction. *Phys. Rev. B*, 61:12474–12489, May 2000. doi: 10.1103/PhysRevB.61.12474. URL `https://link.aps.org/doi/10.1103/PhysRevB.61.12474`.

[213] Shengtao Jiang, Judit Romhányi, Steven R. White, M. E. Zhitomirsky, and A. L. Chernyshev. Where is the quantum spin nematic? *Phys. Rev. Lett.*, 130:116701, Mar 2023. doi: 10.1103/PhysRevLett.130.116701. URL `https://link.aps.org/doi/10.1103/PhysRevLett.130.116701`.

[214] Patrick A. Lee and Xiao-Gang Wen. Spin-triplet p-wave pairing in a three-orbital model for iron pnictide superconductors. *Phys. Rev. B*, 78:144517, Oct 2008. doi: 10.1103/PhysRevB.78.144517. URL `https://link.aps.org/doi/10.1103/PhysRevB.78.144517`.

[215] Emilian M. Nica, Rong Yu, and Qimiao Si. Glide reflection symmetry, brillouin zone folding, and superconducting pairing for the $p4/nmm$ space group. *Phys. Rev. B*, 92:174520, Nov 2015. doi: 10.1103/PhysRevB.92.174520. URL `https://link.aps.org/doi/10.1103/PhysRevB.92.174520`.

[216] H. Yamaguchi, Y. Tominaga, A. Matsuo, S. Morota, Y. Hosokoshi, M. Hagiwara, and K. Kindo. Ladder-based two-dimensional spin model in a radical-co complex. *Phys. Rev. B*, 107:174422, May 2023. doi: 10.1103/PhysRevB.107.174422. URL `https://link.aps.org/doi/10.1103/PhysRevB.107.174422`.

[217] Yoshihiro Nishiyama, Naomichi Hatano, and Masuo Suzuki. Hidden orders and rvb formation of the four-leg heisenberg ladder model. *Journal of the Physical Society of Japan*, 65(2):560–568, 1996. doi: 10.1143/JPSJ.65.560. URL `https://doi.org/10.1143/JPSJ.65.560`.

[218] Anders W. Sandvik. Finite-size scaling of the ground-state parameters of the two-dimensional heisenberg model. *Phys. Rev. B*, 56:11678–11690, Nov 1997. doi: 10.1103/PhysRevB.56.11678. URL `https://link.aps.org/doi/10.1103/PhysRevB.56.11678`.

[219] Juraj Hasik and Federico Becca. Optimization of infinite projected entangled pair states: The role of multiplets and their breaking. *Phys. Rev. B*, 100:054429, Aug 2019. doi: 10.1103/PhysRevB.100.054429. URL `https://link.aps.org/doi/10.1103/PhysRevB.100.054429`.

[220] P. W. Anderson. The resonating valence bond state in La_2CuO_4 and superconductivity. *Science*, 235(4793):1196–1198, 1987. doi: 10.1126/science.235.4793.1196. URL `https://www.science.org/doi/abs/10.1126/science.235.4793.1196`.

[221] Patrick A. Lee, Naoto Nagaosa, and Xiao-Gang Wen. Doping a mott insulator: Physics of high-temperature superconductivity. *Rev. Mod. Phys.*, 78:17–85, Jan 2006. doi: 10.1103/RevModPhys.78.17. URL `https://link.aps.org/doi/10.1103/RevModPhys.78.17`.

[222] Didier Poilblanc, Philippe Corboz, Norbert Schuch, and J. Ignacio Cirac. Resonating-valence-bond superconductors with fermionic projected entangled pair states. *Phys. Rev. B*, 89:241106, Jun 2014. doi: 10.1103/PhysRevB.89.241106. URL `https://link.aps.org/doi/10.1103/PhysRevB.89.241106`.

[223] N. Read and Subir Sachdev. Large-n expansion for frustrated quantum antiferromagnets. *Phys. Rev. Lett.*, 66:1773–1776, Apr 1991. doi: 10.1103/PhysRevLett.66.1773. URL `https://link.aps.org/doi/10.1103/PhysRevLett.66.1773`.

[224] X. G. Wen, Frank Wilczek, and A. Zee. Chiral spin states and superconductivity. *Phys. Rev. B*, 39:11413–11423, Jun 1989. doi: 10.1103/PhysRevB.39.11413. URL `https://link.aps.org/doi/10.1103/PhysRevB.39.11413`.

[225] Andrey V. Chubukov and Th. Jolicoeur. Dimer stability region in a frustrated quantum heisenberg antiferromagnet. *Phys. Rev. B*, 44:12050–12053, Dec 1991. doi: 10.1103/PhysRevB.44.12050. URL https://link.aps.org/doi/10.1103/PhysRevB.44.12050.

[226] R. Haghshenas and D. N. Sheng. $U(1)$-symmetric infinite projected entangled-pair states study of the spin-1/2 square $J_1 - J_2$ heisenberg model. *Phys. Rev. B*, 97:174408, May 2018. doi: 10.1103/PhysRevB.97.174408. URL https://link.aps.org/doi/10.1103/PhysRevB.97.174408.

[227] Subir Sachdev and R. N. Bhatt. Bond-operator representation of quantum spins: Mean-field theory of frustrated quantum heisenberg antiferromagnets. *Phys. Rev. B*, 41:9323–9329, May 1990. doi: 10.1103/PhysRevB.41.9323. URL https://link.aps.org/doi/10.1103/PhysRevB.41.9323.

[228] H. J. Schulz and T. A. L. Ziman. Finite-size scaling for the two-dimensional frustrated quantum heisenberg antiferromagnet. *Europhysics Letters*, 18(4):355, feb 1992. doi: 10.1209/0295-5075/18/4/013. URL https://dx.doi.org/10.1209/0295-5075/18/4/013.

[229] Rajiv R. P. Singh, Zheng Weihong, C. J. Hamer, and J. Oitmaa. Dimer order with striped correlations in the J_1-J_2 heisenberg model. *Phys. Rev. B*, 60:7278–7283, Sep 1999. doi: 10.1103/PhysRevB.60.7278. URL https://link.aps.org/doi/10.1103/PhysRevB.60.7278.

[230] Luca Capriotti and Sandro Sorella. Spontaneous plaquette dimerization in the J_1-J_2 heisenberg model. *Phys. Rev. Lett.*, 84:3173–3176, Apr 2000. doi: 10.1103/PhysRevLett.84.3173. URL https://link.aps.org/doi/10.1103/PhysRevLett.84.3173.

[231] R. Darradi, O. Derzhko, R. Zinke, J. Schulenburg, S. E. Krüger, and J. Richter. Ground state phases of the spin-1/2 J_1-J_2 heisenberg antiferromagnet on the square lattice: A high-order coupled cluster treatment. *Phys. Rev. B*, 78:214415, Dec 2008. doi: 10.1103/PhysRevB.78.214415. URL https://link.aps.org/doi/10.1103/PhysRevB.78.214415.

[232] R. L. Doretto. Plaquette valence-bond solid in the square-lattice J_1-J_2 antiferromagnet heisenberg model: A bond operator approach. *Phys. Rev. B*, 89:104415, Mar 2014. doi: 10.1103/PhysRevB.89.104415. URL `https://link.aps.org/doi/10.1103/PhysRevB.89.104415`.

[233] Shou-Shu Gong, Wei Zhu, D. N. Sheng, Olexei I. Motrunich, and Matthew P. A. Fisher. Plaquette ordered phase and quantum phase diagram in the spin-$\frac{1}{2}$ J_1-J_2 square heisenberg model. *Phys. Rev. Lett.*, 113:027201, Jul 2014. doi: 10.1103/PhysRevLett.113.027201. URL `https://link.aps.org/doi/10.1103/PhysRevLett.113.027201`.

[234] L. Isaev, G. Ortiz, and J. Dukelsky. Hierarchical mean-field approach to the J_1-J_2 heisenberg model on a square lattice. *Phys. Rev. B*, 79:024409, Jan 2009. doi: 10.1103/PhysRevB.79.024409. URL `https://link.aps.org/doi/10.1103/PhysRevB.79.024409`.

[235] Matthieu Mambrini, Andreas Läuchli, Didier Poilblanc, and Frédéric Mila. Plaquette valence-bond crystal in the frustrated heisenberg quantum antiferromagnet on the square lattice. *Phys. Rev. B*, 74:144422, Oct 2006. doi: 10.1103/PhysRevB.74.144422. URL `https://link.aps.org/doi/10.1103/PhysRevB.74.144422`.

[236] Ken'ichi Takano, Yoshiya Kito, Yoshiaki Ōno, and Kazuhiro Sano. Nonlinear σ model method for the J_1-J_2 heisenberg model: Disordered ground state with plaquette symmetry. *Phys. Rev. Lett.*, 91:197202, Nov 2003. doi: 10.1103/PhysRevLett.91.197202. URL `https://link.aps.org/doi/10.1103/PhysRevLett.91.197202`.

[237] Ji-Feng Yu and Ying-Jer Kao. Spin-$\frac{1}{2}$ J_1-J_2 heisenberg antiferromagnet on a square lattice: A plaquette renormalized tensor network study. *Phys. Rev. B*, 85:094407, Mar 2012. doi: 10.1103/PhysRevB.85.094407. URL `https://link.aps.org/doi/10.1103/PhysRevB.85.094407`.

[238] Luca Capriotti, Federico Becca, Alberto Parola, and Sandro Sorella. Resonating valence bond wave functions for strongly frustrated spin systems. *Phys. Rev. Lett.*, 87:097201, Aug 2001. doi: 10.1103/PhysRevLett.87.097201. URL `https://link.aps.org/doi/10.1103/PhysRevLett.87.097201`.

[239] Francesco Ferrari and Federico Becca. Gapless spin liquid and valence-bond solid in the J_1-J_2 heisenberg model on the square lattice: Insights from singlet and triplet excitations. *Phys. Rev. B*, 102:014417, Jul 2020. doi: 10.1103/PhysRevB.102.014417. URL https://link.aps.org/doi/10.1103/PhysRevB.102.014417.

[240] Wen-Jun Hu, Federico Becca, Alberto Parola, and Sandro Sorella. Direct evidence for a gapless Z_2 spin liquid by frustrating néel antiferromagnetism. *Phys. Rev. B*, 88:060402, Aug 2013. doi: 10.1103/PhysRevB.88.060402. URL https://link.aps.org/doi/10.1103/PhysRevB.88.060402.

[241] Wen-Yuan Liu, Shaojun Dong, Chao Wang, Yongjian Han, Hong An, Guang-Can Guo, and Lixin He. Gapless spin liquid ground state of the spin-$\frac{1}{2}$ $J_1 - J_2$ heisenberg model on square lattices. *Phys. Rev. B*, 98:241109, Dec 2018. doi: 10.1103/PhysRevB.98.241109. URL https://link.aps.org/doi/10.1103/PhysRevB.98.241109.

[242] Satoshi Morita, Ryui Kaneko, and Masatoshi Imada. Quantum spin liquid in spin 1/2 J_1–J_2 heisenberg model on square lattice: Many-variable variational monte carlo study combined with quantum-number projections. *Journal of the Physical Society of Japan*, 84(2):024720, 2015. doi: 10.7566/JPSJ.84.024720. URL https://doi.org/10.7566/JPSJ.84.024720.

[243] Yusuke Nomura and Masatoshi Imada. Dirac-type nodal spin liquid revealed by refined quantum many-body solver using neural-network wave function, correlation ratio, and level spectroscopy. *Phys. Rev. X*, 11:031034, Aug 2021. doi: 10.1103/PhysRevX.11.031034. URL https://link.aps.org/doi/10.1103/PhysRevX.11.031034.

[244] Didier Poilblanc and Matthieu Mambrini. Quantum critical phase with infinite projected entangled paired states. *Phys. Rev. B*, 96:014414, Jul 2017. doi: 10.1103/PhysRevB.96.014414. URL https://link.aps.org/doi/10.1103/PhysRevB.96.014414.

[245] Yang Qi and Zheng-Cheng Gu. Continuous phase transition from néel state to Z_2 spin-liquid state on a square lattice. *Phys. Rev. B*, 89:235122, Jun 2014. doi: 10.

1103/PhysRevB.89.235122. URL https://link.aps.org/doi/10.1103/PhysRevB.89.235122.

[246] Johannes Richter, Ronald Zinke, and Damian J. J. Farnell. The spin-1/2 square-lattice J_1-J_2 model: the spin-gap issue. *The European Physical Journal B*, 88(1), January 2015. ISSN 1434-6036. doi: 10.1140/epjb/e2014-50589-x. URL http://dx.doi.org/10.1140/epjb/e2014-50589-x.

[247] Ling Wang and Anders W. Sandvik. Critical level crossings and gapless spin liquid in the square-lattice spin-1/2 $J_1 - J_2$ heisenberg antiferromagnet. *Phys. Rev. Lett.*, 121:107202, Sep 2018. doi: 10.1103/PhysRevLett.121.107202. URL https://link.aps.org/doi/10.1103/PhysRevLett.121.107202.

[248] Ling Wang, Didier Poilblanc, Zheng-Cheng Gu, Xiao-Gang Wen, and Frank Verstraete. Constructing a gapless spin-liquid state for the spin-1/2 $J_1 - J_2$ heisenberg model on a square lattice. *Phys. Rev. Lett.*, 111:037202, Jul 2013. doi: 10.1103/PhysRevLett.111.037202. URL https://link.aps.org/doi/10.1103/PhysRevLett.111.037202.

[249] Guang-Ming Zhang, Hui Hu, and Lu Yu. Valence-bond spin-liquid state in two-dimensional frustrated spin-1/2 heisenberg antiferromagnets. *Phys. Rev. Lett.*, 91:067201, Aug 2003. doi: 10.1103/PhysRevLett.91.067201. URL https://link.aps.org/doi/10.1103/PhysRevLett.91.067201.

[250] Wen-Yuan Liu, Shou-Shu Gong, Yu-Bin Li, Didier Poilblanc, Wei-Qiang Chen, and Zheng-Cheng Gu. Gapless quantum spin liquid and global phase diagram of the spin-1/2 j1-j2 square antiferromagnetic heisenberg model. *Science Bulletin*, 67(10):1034–1041, 2022. ISSN 2095-9273. doi: https://doi.org/10.1016/j.scib.2022.03.010. URL https://www.sciencedirect.com/science/article/pii/S2095927322001001.

[251] Jiale Huang, Xiangjian Qian, and Mingpu Qin. Plaquette-type valence bond solid state in the $J_1{-}J_2$ square-lattice heisenberg model. *Phys. Rev. B*, 110:195111, Nov 2024. doi: 10.1103/PhysRevB.110.195111. URL https://link.aps.org/doi/10.1103/PhysRevB.110.195111.

[252] Wen-Yuan Liu, Shou-Shu Gong, Wei-Qiang Chen, and Zheng-Cheng Gu. Emergent symmetry in quantum phase transition: From deconfined quantum critical

point to gapless quantum spin liquid. *Science Bulletin*, 69(2):190–196, 2024. ISSN 2095-9273. doi: https://doi.org/10.1016/j.scib.2023.11.057. URL `https://www.sciencedirect.com/science/article/pii/S2095927323008393`.

[253] Kingshuk Majumdar. Magnetic phase diagram of a spatially anisotropic, frustrated spin- heisenberg antiferromagnet on a stacked square lattice. *Journal of Physics: Condensed Matter*, 23(4):046001, jan 2011. doi: 10.1088/0953-8984/23/4/046001. URL `https://dx.doi.org/10.1088/0953-8984/23/4/046001`.

[254] A. A. Nersesyan and A. M. Tsvelik. Spinons in more than one dimension: Resonance valence bond state stabilized by frustration. *Phys. Rev. B*, 67:024422, Jan 2003. doi: 10.1103/PhysRevB.67.024422. URL `https://link.aps.org/doi/10.1103/PhysRevB.67.024422`.

[255] Ulvi Kanbur, Hamza Polat, and Erol Vatansever. Thermal properties of rung-disordered two-leg quantum spin ladders: Quantum monte carlo study. *Phys. Rev. E*, 102:042104, Oct 2020. doi: 10.1103/PhysRevE.102.042104. URL `https://link.aps.org/doi/10.1103/PhysRevE.102.042104`.

[256] A S Ovchinnikov, V E Sinitsyn, I G Bostrem, Y Hosokoshi, and K Inoue. Magnetization and spin gap in two-dimensional organic ferrimagnet bipnnbno. *Journal of Physics: Condensed Matter*, 24(30):306003, jul 2012. doi: 10.1088/0953-8984/24/30/306003. URL `https://dx.doi.org/10.1088/0953-8984/24/30/306003`.

APPENDIX A – RUNG OPERATORS ALGEBRA

The rung operators $\hat{\mathbf{S}}_i = \hat{\mathbf{S}}_{i,1} + \hat{\mathbf{S}}_{i,2}$ and $\hat{\mathbf{D}}_i = \hat{\mathbf{S}}_{i,1} - \hat{\mathbf{S}}_{i,2}$ are defined for each rung i, where $\hat{\mathbf{S}}_{i,1}$ and $\hat{\mathbf{S}}_{i,2}$ are the spin$-\frac{1}{2}$ operators on the two legs of the rung. Their commutation relations are derived as follows:

$$[\hat{\mathbf{S}}_i, \hat{\mathbf{S}}_j] = [\hat{\mathbf{D}}_i, \hat{\mathbf{D}}_j] = [\hat{\mathbf{S}}_{i,1}, \hat{\mathbf{S}}_{j,1}] + [\hat{\mathbf{S}}_{i,2}, \hat{\mathbf{S}}_{j,2}], \tag{A.1}$$

$$[\hat{\mathbf{S}}_i, \hat{\mathbf{D}}_j] = [\hat{\mathbf{S}}_{i,1}, \hat{\mathbf{S}}_{j,1}] - [\hat{\mathbf{S}}_{i,2}, \hat{\mathbf{S}}_{j,2}]. \tag{A.2}$$

Since spin operators on different sites commute, cross-leg commutators vanish for $i \neq j$:

$$[\hat{\mathbf{S}}_{i,1}, \hat{\mathbf{S}}_{j,2}] = [\hat{\mathbf{S}}_{i,2}, \hat{\mathbf{S}}_{j,1}] = 0, \tag{A.3}$$

For spins on the same leg, the standard spin$-\frac{1}{2}$ commutation relations apply:

$$[\hat{S}^{\alpha}_{k,1}, \hat{S}^{\beta}_{j,1}] = i\delta_{kj}\epsilon_{\alpha\beta\gamma}\hat{S}^{\gamma}_{k,1}, \quad [\hat{S}^{\alpha}_{k,2}, \hat{S}^{\beta}_{j,2}] = i\delta_{kj}\epsilon_{\alpha\beta\gamma}\hat{S}^{\gamma}_{k,2}, \tag{A.4}$$

where δ_{kj} is the Kronecker delta, $\epsilon_{\alpha\beta\gamma}$ is the Levi-Civita symbol, and $\alpha, \beta, \gamma \in \{x, y, z\}$. Combining these, the rung operator commutators simplify to:

$$[\hat{S}^{\alpha}_i, \hat{S}^{\beta}_j] = i\delta_{ij}\epsilon_{\alpha\beta\gamma}\hat{S}^{\gamma}_i, \quad [\hat{D}^{\alpha}_i, \hat{D}^{\beta}_j] = i\delta_{ij}\epsilon_{\alpha\beta\gamma}\hat{S}^{\gamma}_i, \quad [\hat{S}^{\alpha}_i, \hat{D}^{\beta}_j] = i\delta_{ij}\epsilon_{\alpha\beta\gamma}\hat{D}^{\gamma}_i. \tag{A.5}$$

where $\hat{S}^{\gamma}_i = \hat{S}^{\gamma}_{i,1} + \hat{S}^{\gamma}_{i,2}$ and $\hat{D}^{\gamma}_i = \hat{S}^{\gamma}_{i,1} - \hat{S}^{\gamma}_{i,2}$. These relations show that $\hat{\mathbf{S}}_i$ and $\hat{\mathbf{D}}_i$ form a closed algebra under commutation.

Each rung, comprising two spin$-\frac{1}{2}$ sites, has a local Hilbert space spanned by four states: one singlet state $|s\rangle$ and three triplet states $|t_0\rangle$, $|t_+\rangle$, and $|t_-\rangle$, corresponding to total spin $S = 0$ and $S = 1$ with z-components $m = 0, +1, -1$, respectively. The action of the rung operators $\hat{\mathbf{S}}_i$ and $\hat{\mathbf{D}}_i$ on these basis states is summarized in Table 1.

Table 1 – Action of the rung operators on the basis states.

	$\hat{S}^z_i$	$\hat{S}^+_i$	$\hat{S}^-_i$	$\hat{D}^z_i$	$\hat{D}^+_i$	$\hat{D}^-_i$
$\lvert s\rangle_i$	0	0	0	$\lvert 0\rangle_i$	$-\sqrt{2}\lvert +\rangle_i$	$\sqrt{2}\lvert -\rangle_i$
$\lvert 0\rangle_i$	0	$\sqrt{2}\lvert +\rangle_i$	$\sqrt{2}\lvert -\rangle_i$	$\lvert s\rangle_i$	0	0
$\lvert +\rangle_i$	$\lvert +\rangle_i$	0	$\sqrt{2}\lvert 0\rangle_i$	0	0	$-\sqrt{2}\lvert s\rangle_i$
$\lvert -\rangle_i$	$-\lvert -\rangle_i$	$\sqrt{2}\lvert 0\rangle_i$	0	0	$\sqrt{2}\lvert s\rangle_i$	0

Source: The author (2025)